LEABHARLANN CHOLÁISTE NA TRÍONÓIDE, BAILE ÁTHA CLIATH | TRINITY COLLEGE LIBRARY DUBLIN
Ollscoil Átha Cliath | The University of Dublin

Terms and Conditions of Use of Digitised Theses from Trinity College Library Dublin

Copyright statement

All material supplied by Trinity College Library is protected by copyright (under the Copyright and Related Rights Act, 2000 as amended) and other relevant Intellectual Property Rights. By accessing and using a Digitised Thesis from Trinity College Library you acknowledge that all Intellectual Property Rights in any Works supplied are the sole and exclusive property of the copyright and/or other IPR holder. Specific copyright holders may not be explicitly identified. Use of materials from other sources within a thesis should not be construed as a claim over them.

A non-exclusive, non-transferable licence is hereby granted to those using or reproducing, in whole or in part, the material for valid purposes, providing the copyright owners are acknowledged using the normal conventions. Where specific permission to use material is required, this is identified and such permission must be sought from the copyright holder or agency cited.

Liability statement

By using a Digitised Thesis, I accept that Trinity College Dublin bears no legal responsibility for the accuracy, legality or comprehensiveness of materials contained within the thesis, and that Trinity College Dublin accepts no liability for indirect, consequential, or incidental, damages or losses arising from use of the thesis for whatever reason. Information located in a thesis may be subject to specific use constraints, details of which may not be explicitly described. It is the responsibility of potential and actual users to be aware of such constraints and to abide by them. By making use of material from a digitised thesis, you accept these copyright and disclaimer provisions. Where it is brought to the attention of Trinity College Library that there may be a breach of copyright or other restraint, it is the policy to withdraw or take down access to a thesis while the issue is being resolved.

Access Agreement

By using a Digitised Thesis from Trinity College Library you are bound by the following Terms & Conditions. Please read them carefully.

I have read and I understand the following statement: All material supplied via a Digitised Thesis from Trinity College Library is protected by copyright and other intellectual property rights, and duplication or sale of all or part of any of a thesis is not permitted, except that material may be duplicated by you for your research use or for educational purposes in electronic or print form providing the copyright owners are acknowledged using the normal conventions. You must obtain permission for any other use. Electronic or print copies may not be offered, whether for sale or otherwise to anyone. This copy has been supplied on the understanding that it is copyright material and that no quotation from the thesis may be published without proper acknowledgement.

Power and Position-Oriented Process Monitoring of Freeform Abrasive Machining

Emma Brazel, B.Sc. (Ing.)

Department of Mechanical and Manufacturing Engineering
University of Dublin

A thesis submitted to the University of Dublin in partial fulfilment of the requirements for the degree of Doctor in Philosophy

April 2013

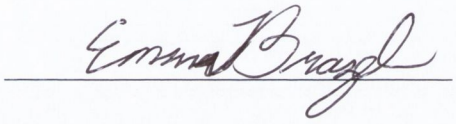
Supervisor
Dr. Garret E. O'Donnell

TRINITY COLLEGE
2 4 MAY 2013
LIBRARY DUBLIN

Thesis 9897

Declaration

I declare that the work in this thesis is, unless otherwise stated, entirely my own work and has not been submitted as an exercise for a degree at this or any other University. I agree that Trinity College Library may lend or copy this thesis upon request.



Emma Brazel

April 2013

Summary

Abrasive machining is used for the generation of freeform femoral implant surfaces in the biomedical industry. The abrasive machining operation is typified by high speed material removal in multiple axes, difficult-to-machine material and the use of hard abrasives on toroidal shaped grinding wheels. Such machining operations are often inefficient due to conservative choices of machining parameters, which are based upon trial-and-error approaches in order to maintain workpiece surface integrity. Process monitoring is necessary to achieve process optimisation, through the identification and avoidance of process disturbances, which could cause poor surface integrity at chosen machining parameters.

The aim of this thesis is to develop a platform for process monitoring and characterisation of the abrasive machining process for freeform surfaces. Two main aspects are addressed in this work. Internal machine signals are utilized as a more robust and flexible alternative to external sensors for process monitoring. The selection and characterisation of a suitable internal machine signal for process monitoring is addressed. The development of a position-oriented monitoring and analysis method is also explored. This is in order to assist in determination of process characteristics that allow for the identification of the origin of process disturbances in relation to the toolpath position over the surface of the component.

The sensitivity of the internal machine power signal towards changes in process parameters is an important consideration if the signal is to be utilised for process monitoring. Experiments were carried out in order to assess the sensitivity of the active power signal for flat surface grinding. The investigations showed that cutting power was sensitive to changes in process parameters of depth of cut, feed rate, wheel speed and tool wear, illustrating that cutting power is a suitable quantity for monitoring and characterisation of the abrasive machining process, as well as for identifying the onset of tool wear.

A position-oriented analysis method was developed to enable a distinct determination of process characteristics by combination of position and power/tool-

workpiece engagement data. The developed method was applied and tested under different machining parameters with two feed rates and radial offset/tool path spacing.

Internal machine signals of position and power were combined and evaluated over the course of an abrasive machining toolpath. This revealed an inter-positional dependency between the two quantities. Power was shown to increase significantly with increasing tool-workpiece engagement and feed rate. Regions of high cutting power over the toolpath could be attributed to the changing engagement conditions due to the part geometry.

In order to further understand the process characteristics it is necessary to quantify the material removed during the process. To this end, a custom laser profile monitoring system was developed which measured the difference in material before and after abrasive machining. Results showed that material varied considerably over the surface of the implant, with more material being removed in areas such as the patella track and the casting gates, and less material at the femoral condyles which could be attributed to the tool-workpiece engagement conditions at these regions.

A model based on laser measurements of the part before and after abrasive machining was developed in order to estimate tool-workpiece engagement conditions over the course of the freeform toolpath. Results for tool-workpiece engagement showed the majority of calculated values to be in the range of 0.01 – 1 mm^2, with areas of high engagement found similar to the laser measurement results. The calculations for engaged area provided the basis for determination of specific energy in the process.

Specific energy was shown to decrease with increasing engaged area and feed rate, by an approximate average value of 44% and 16% respectively. Specific energy was also found to be highly positional-dependent. The results of the specific energy analysis indicate specific energy could potentially be reduced in certain regions through an increase in material removal rate in order to increase machining efficiency.

This thesis has demonstrated the advantage of applying a position oriented approach towards analysis of internal machine signal power and material removal data from laser measurements, where process disturbances and machining characteristics can be identified and investigated in a more comprehensive manner. The research has also highlighted that the position-oriented monitoring approach with internal machine signals can serve as a basis for process monitoring, control and optimization in the future.

Acknowledgements

I would first like to offer my sincere thanks to my supervisor, Dr. Garret O'Donnell. He gave me the opportunity of pursuing a PhD, and since then has supervised my work with much enthusiasm, patience, guidance and constructive advice. I have learnt a lot from him over the years and his support is both gratefully acknowledged and appreciated.

I would also like to thank those at DePuy Ireland, particularly Ruairi Cullinane, John Quinn, Dr. Ray Hanley and the rest of the team in the Innovation Centre. Their support has been invaluable and it has been a very rewarding experience collaborating so closely with industry these past few years.

I would also like to acknowledge that this project has been funded by the Irish Research Council for Science, Engineering and Technology and DePuy Ireland under the Enterprise Partnership scheme.

Special thanks also to Prof. Andrew Torrance, Prof. John Monaghan and Mr. Kevin Kelly, for valuable advice at different times during the project, and to all the staff of the Department of Mechanical and Manufacturing Engineering, Trinity College Dublin, especially the technicians who have always been a great help.

To all the postgrads, past and present: Paul E, Paul H, Kev, Stuart, Barry, Jeff, Emily, Aoife, Dave, Niamh, Paul McD, Ivor, Kate, Oana, Eoin, Rory, Peadar and Gio. Thank you for all the friendship, encouragement, technical support/proofreading and general banter over the years, and I wish you all the best for the future.

Thanks also to my sister Ailbhe, and my two brothers Sam and Matthew for their support and refreshing sense of humour. And finally, I owe my deepest gratitude to my mother and father, Deborah and Colm. Their endless support, love and encouragement, has helped me get to where I am now, so thank you for everything.

"Out of clutter, find simplicity;
From discord make harmony;
In the middle of difficulty lies opportunity."

- A.Einstein

This work is dedicated to my parents, Colm and Deborah Brazel.

Contents

Contents i

Nomenclature iv

Chapter 1 Introduction 1

1.1 Research background 2

1.2 Motivation and challenges in abrasive machining of femoral components 3

1.3 Research objectives 5

Chapter 2 Literature review 7

2.1 Process characteristics 7

2.1.1 Abrasive machining 7

2.1.2 Freeform abrasive machining 9

2.1.3 Material removal, forces and specific energy 15

2.1.4 Temperature and velocity effects 22

2.1.5 Wheel wear and super-abrasives 32

2.2 Process monitoring 41

2.2.1 Forces, vibration, acoustic emission & temperature measurement 43

2.2.2 Power measurement 47

2.2.3 Internal machine signal measurement 59

2.2.4 Position-oriented analysis 65

2.2.5 Laser displacement measurement 70

2.3 Summary and context 77

Chapter 3 Experimental methodology 79

3.1 Machine tool 79

3.1.1 Machine description 79

3.1.2 Machine-side data acquisition 80

3.1.3 Tooling: Electroplated CBN wheel 82

3.2 Workpiece materials 83

3.2.1 Workpiece characterisation: Cobalt Chrome alloy 83

3.2.2 Planar grinding workpiece 88

3.2.3 Experimental setup 88

3.2.4 Femoral component workpiece 89

3.3 Workpiece surface and tool wear characterisation 90

3.3.1 Workpiece surface roughness measurement 90
3.3.2 Tool wear measurement 91
3.4 Laser measurement 95
3.4.1 Laser measurement rig 95
Chapter 4 Process characterisation through power monitoring 98
4.1 Evaluation of signal: power monitoring and material removal 98
4.2 Establishing key process metrics 112
4.2.1 Experimental setup: Taguchi L16 test array 112
4.2.2 Results and discussion 114
4.3 Feed rate effect 124
4.4 Summary 125
Chapter 5 Development of position-oriented-process monitoring methodology for freeform surfaces 127
5.1 Laser measurement 128
5.2 Engagement analysis 137
5.2.1 Engagement analysis results 141
5.3 Position-oriented power monitoring 145
5.4 Estimation of specific energy 149
5.5 Summary 150
Chapter 6 Application of position-oriented monitoring approach for freeform surfaces 152
6.1 Design of experiment with position-based analysis 152
6.2 Laser measurement results 154
6.3 Engagement analysis results 158
6.4 Power measurement results 160
6.5 Estimate of specific energy 165
6.6 Summary 170
Chapter 7 Conclusion 172
7.1 Process characterisation through power monitoring 172
7.2 Development of position-oriented process monitoring methodology 174
7.3 Application of position-oriented monitoring approach for freeform surfaces 176
7.4 Concluding remarks 178
7.5 Recommendations for future work 179
Appendix I Freeform abrasive machining investigations 181
AI.1 Macro surface roughness 181
AI.2 Energy cost estimate 182

AI.3 Grinding burn marks 184
Appendix II Flat surface grinding with toric wheels 186
AII.1 Temperature investigations 186
Appendix III Machine Signal Evaluation 192
Appendix IV Machined surface 3D topographic maps 193
References 194

Nomenclature

Symbol	Definition
a	depth of cut (mm)
A	wear flat area (%)
a,b,b',c	points of intersection between toolpath n, n+1, and cast curve
A_1,A_2	areas of engagement between toolpath n+1 and cast curve (mm^2)
A_s	tool-workpiece engaged area (mm^2)
A_{Total}	total calculated area of tool-workpiece engagement (mm^2)
A_w	tool-workpiece engaged area (mm^2)
b	contact width (mm)
C	Carbon
CBN	Cubic Boron Nitride
C_o	areal packing density (grains/mm^2)
Co	Cobalt
cos (φ)	power factor
Cr	Chromium
d	Euclidean distance (mm)
d_0	offset radius from centre of machining arbour (mm)
DF	degrees of freedom
D_{ICP}	transformed cast laser point cloud
d_{RMS}	overall root mean square distance between the cast laser scan and the post-machined scan (mm)
d_s	major toric wheel diameter (mm)
d_s	distance between cast and post-machined laser scans (mm)
Exp SS	expected sums of squares
F	F-test
HRC	Rockwell hardness
I	electric current (Ampere)
l_g	contact length (mm)
M	reference post-machined laser point cloud
$M = [x_1\ y_1\ z_1]$	cast laser curve matrix
$M_2 = [x_2\ y_2\ z_2]$	post-machined laser curve matrix
Mo	Molybdenum
n	sample size
NC	numerical control
P	cutting active power (Watt)
P	probability value

Symbol	Definition
$P_{air\ cut}$	recorded active spindle power for air cut or spindle idling (Watt)
P_c''	area specific power (Watt/mm^2)
PCR	per cent contribution ratio
P_{total}	total recorded active spindle power (Watt)
R	minor toric wheel radius (mm)
r	minor toric wheel radius taken as offset radius (mm)
R_a	average surface roughness (μm)
rpm	rotations per minute
R_w	local workpiece radius (mm)
rx	angle of desired rotation (radian)
S	apparent power (Volt-Ampere)
s	toolpath spacing (mm)
s	standard deviation
Sa	3D surface roughness (μm)
Sdq	RMS surface slope
Sds	summit density (grains/mm^2)
Seq SS	sequential sums of squares
s_h	scallop height or macro surface roughness (mm)
S_n	cubic spline curve
u	specific energy (J/mm^3)
u_{ch}	specific energy for chip formation (J/mm^3)
V	electric potential difference (Volt)
$v = M_2 - M$	vector distance from laser curve to post-machined curve
v_f	feed rate (mm/s)
v_s	wheel speed (m/s)
v_w	feed rate (mm/s)
w	machined track width (mm)
x_1, y_1, z_1	Cartesian coordinates of laser curve n from cast implant (mm)
x_2, y_2, z_2	Cartesian coordinates of laser curve n from post-machined implant (mm)
y_c	known centre of rotation for A-axis of laser holder (mm)
y_{dist}	triangulated distance from laser to object (mm)
θ	angle of rotation of A-axis of laser holder (°)
θ	angle of rotation of A-axis of machine arbour (°)
μ	sample mean
φ	phase of voltage relative to current (°)

Chapter 1

Introduction

The manufacturing sector in high-wage countries is characterised by the production of high value components with technologically intensive processes. This type of manufacturing process however entails considerable cost through energy and material consumption [1]. In order to maintain a competitive advantage, the manufacturing process must be as resource and energy-efficient as possible. Process monitoring and control is key to enabling high-efficiency production.

Process monitoring can increase performance and efficiency of machining through the avoidance of and compensation for process disturbances as well as prevention of workpiece damage [2]. The scope of process monitoring can include tool condition, process condition, workpiece surface integrity and chatter detection [3]. Examples of sensors currently used for process monitoring include force dynamometers, accelerometers, power meters, acoustic emission sensors, thermocouples and strain sensors.

New challenges however are facing the reliability and applicability of such sensor systems for tool condition and process monitoring, as machining operations become more complex with multiple axes, increased velocities and freeform machining. Monitoring of the entire process condition and the resulting part quality is gaining more importance with new capabilities such as machine tool diagnostics and in- process quality control [4]. However, dissatisfaction has been expressed with not enough process, workpiece or tool condition monitoring knowledge making the transition from research environments to real industrial machining applications [5, 6].

There is a necessity for sensor systems to be integrated directly with the machine tool, without the lengthy setup times and modifications to the machine tool structure characteristic of some typical sensor solutions currently available. Modern machine control systems allow open access to internal signals in the numerical controller providing the opportunity to measure and record these signals via the Human Machine Interface (HMI).

However, as this technology is relatively new in application, there is a need to investigate the sensitivity of internal signals as well as their potential towards application for complex freeform machining operations [3].

1.1 Research background

A key sector in Irish industry currently facing high-end manufacturing challenges is the orthopaedic manufacturing industry. Due to the worlds aging population and the effects of degenerative joint disease, the market for orthopaedic implants is growing [7]. Femoral implants are needed as a result of joint arthritis, osteoporosis and fracture, and the main function of the implant is to replace the weight-bearing surfaces of the knee joint in order to relieve debilitating pain. Femoral implants typically comprise of a Cobalt Chrome femoral head component which articulates on a low-friction polyethylene platform resting on a Cobalt Chrome tibial tray, as illustrated in Figure 1.1.

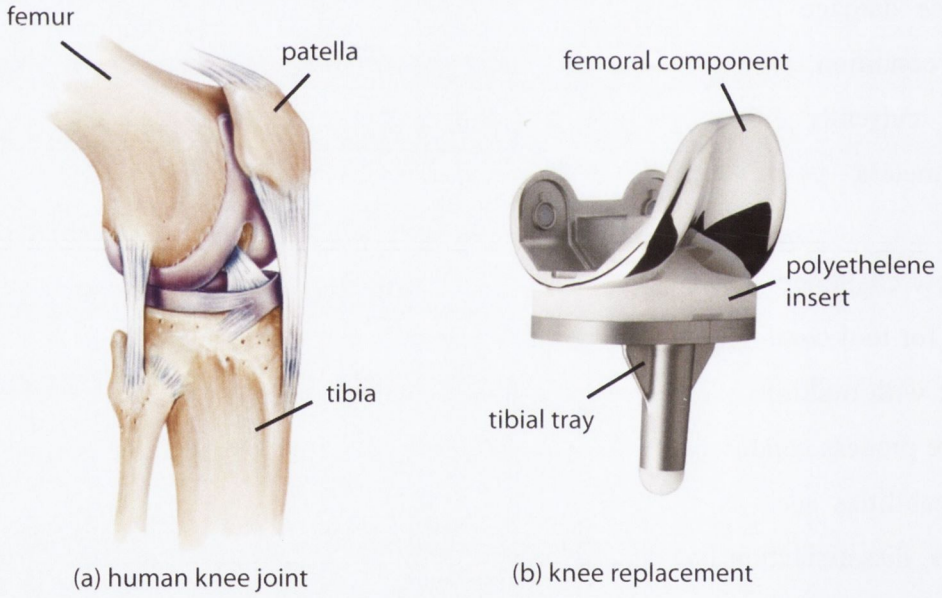


Figure 1.1: (a) The normal anatomy of a human knee, anterolateral view, (b) example of an orthopaedic femoral implant [Source: DePuy, Johnson & Johnson]

The focus of this research lies with the manufacture of the femoral component. Such components are subject to high dimensional quality standards to ensure minimum wear and efficient transfer of load through the articulating surface when in vivo [8]. Machining operations must guarantee the highest quality of parts in order to maintain appropriate part

quality. At the same time, process efficiency must be achieved while maintaining flexibility to adapt to changes in product types.

Manufacturing of the femoral component takes place in four main stages; casting, abrasive machining, milling and polishing as illustrated in Figure 1.2. The implant is first investment cast based on a wax negative mold. Due to stringent dimensional requirements, this process alone is not sufficient to generate the final profiled surface; therefore the casting is to near-net shape and is followed by material removal operations of abrasive machining and milling. Abrasive machining is responsible for the majority of the material removal and the generation of the final surface profile, while milling is used to trim the edges of the implant. The final stage in the process is polishing where the implant surface roughness is reduced through belt lapping and robotic arm controlled cloth polishing of the surface [9].

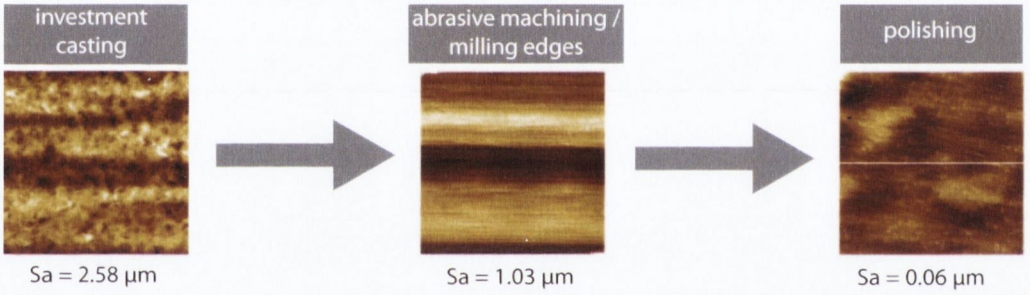


Figure 1.2: Implant manufacturing process chain illustrating surface area roughness, Sa, with example surface topographic images at different stages in the process

1.2 Motivation and challenges in abrasive machining of femoral components

Cobalt Chrome alloys have excellent properties for biomedical implants including high strength, hardness, wear resistance, and biocompatibility [8, 10]. This, however, makes the alloy difficult to machine. The abrasive machining process therefore involves the use of sophisticated machinery including high speed spindles, three or more axes machining and the use of hard abrasives of Cubic Boron Nitride (CBN) on electroplated steel wheels. Toric shaped grinding wheels are also typically employed in the abrasive machining process of the implants due to their freeform profiles [11].

Although advances in cutting technology make it possible to machine such alloys nowadays, the material removal process places significant demands on the technology. Oliveria et al. outlined some of the industrial challenges faced with grinding [12].

These include;

- Surface integrity and process reliability
- Robust grinding process monitoring and control
- Grinding process energy efficiency improvement

Surface integrity and process reliability are important for ensuring that critical components such as those for aerospace, or biomedical applications can cope with the increasing demands of performance and reliability during the components life. Major issues that can be encountered in the grinding process that affect the surface integrity include chatter vibration, grinding burn, residual stresses, profile errors and surface roughness deterioration [13].

In order to guarantee the required surface integrity, production grinding processes have traditionally been developed using experimental trial-and-error approach with extensive surface evaluations. These processes are often very conservative in terms of process parameters with low material removal rates. One of the ways of achieving efficiency in a process is by increasing the material removal rate. However, it is critical to understand the effects of changing operating parameters before new grinding/abrasive machining strategies can safely be implemented [12]. Process monitoring is key towards identifying grinding machining process disturbances that could induce poor surface integrity. In addition to disturbance detection, information regarding the measured process quantities obtained with the monitoring system can be used for optimizing the process [14].

Recording of internal machine signals is a promising technique for process monitoring of freeform abrasive machining of femoral implants without unwanted interference within the machining envelope or structure. Active power can therefore be monitored from the machine, along with servo drive position. However, before this technique can be successfully applied, there is a need for evaluation and characterisation of the signal in response to varying process parameters [15].

In freeform machining, the workpiece and tool engagement situation is constantly changing therefore making determination of process characteristics through power or other sensors particularly difficult. A position-oriented analysis presents an opportunity to assist in determination of process characteristics and allow for identification of process disturbances in relation to the toolpath position over the surface of the component [16].

Process disturbances can therefore be more reliably determined and the source of the disturbance investigated with this type of analysis.

Another challenge is the lack of knowledge surrounding the exact quantity of material removed during the process. In order to understand how the power signal is affected by different machining parameters, it is necessary to quantify this variable. There are a number of measuring techniques currently used for measurement of freeform shaped parts including coordinate measuring machines, stationary optical systems, interferometric systems and profilometry [17]. The most cost effective and flexible solution for this application is laser profilometry. Measurements of the material removed during the process using this profile measurement technique, combined with position-oriented power monitoring, form a process monitoring platform that can serve as a basis for future process optimisation through offline adaptive control.

1.3 Research objectives

The aim of the present research is to investigate the characteristics of the freeform grinding process with respect to power monitoring applied to the process. Two aspects were investigated, first characterization of the internal machine power signal, and second, application of a position-oriented analysis strategy towards freeform grinding. The objectives and tasks of the project may be stated as:

- To examine the application of and sensitivity of the internal machine motor power signal applied to flat surface and freeform grinding.
- To characterise the material removed during freeform grinding and to investigate the tool-workpiece engagement during freeform grinding.
- To characterise the freeform grinding process through a position-oriented analysis.

The internal machine signal of active power of a spindle during surface grinding of Cobalt Chrome alloy was monitored under various conditions through a machine-NC-based application. The sensitivity of the power signal towards material removal and tool wear was investigated. The effects of changes in feed rate, wheel speed, depth of cut and tool condition were also investigated through Taguchi experimental design.

A laser measurement system was developed to determine the material removed during a freeform abrasive machining process for femoral implants of Cobalt Chrome alloy. Based on these measurements, a tool-workpiece engagement model was developed to estimate the engagement over the course of the toolpath. A position-oriented analysis method was developed to correlate machine internal power and position signals with model-based engagement over the full surface of the implant. In order to form an estimate of the efficiency of the process the specific energy parameter was calculated over the course of abrasive machining of the freeform surface.

A case study involving the application of the position-oriented analysis strategy was undertaken. The position-oriented analysis strategy was applied under different machining parameters with two feed rates and radial offset/tool path spacing tested for abrasive machining of femoral implants. The sensitivity of the analysis strategy to changes in process parameters was illustrated for process power, model-based tool-workpiece engagement and specific energy over the surface of the implant.

Chapter 2

Literature review

In the biomedical and aerospace industry freeform surfaces are often generated by abrasive machining of difficult-to-cut materials. The abrasive process is typically geometrically complex, energy intensive and hard-wearing on tooling. Due to the high process energy and forces and constantly changing tool-workpiece engagement conditions it is difficult to specify optimal process parameters. The implementation of process monitoring leads to a better understanding of process characteristics and engagement conditions, which are directly related to surface integrity of the component as well as the efficiency of the process. This chapter therefore reviews work on characterisation of the abrasive process with a particular focus on process power monitoring.

2.1 Process characteristics

2.1.1 Abrasive machining

Abrasive machining is a process defined by the tools geometrically undefined cutting edges [18]. Typically, the machine tool is either of the form of a wheel comprised fully of abrasive grit, or with the grits adhered to the wheels periphery. During the process both the wheel and the workpiece move at high speed relative to each other. With high speed operations the combined cutting speed can reach anywhere between 1200 m/min up to 15000 m/min, and material removal rates up to 2500 cm^3/min and above can be achieved during the cutting process. The material removal rate Q_w however does depend to a large extent on the cutting technology, workpiece material properties and the required geometry and surface finish of the component [5].

As a result the grinding used in modern day manufacturing can be distinguished between two types of processes. Precision grinding typically involves depths of cut in the tens of microns range, with which a high surface finish/low surface roughness and excellent form accuracy can be obtained. Abrasive machining on the other hand seeks to remove large volumes of material at high material removal rates whilst maintaining

excellent form accuracy within tight tolerances [19]. A high surface finish is not the main goal of the process as further finishing operations usually follow. Therefore the depths of cut in abrasive machining are greater, ranging from the hundreds of microns to tens of millimetres. Abrasive machining is particularly suitable for difficult-to-machine materials such as high alloy steels, Titanium, Cobalt Chrome and nickel base alloys.

Much research has been carried out on abrasive processes in recent years, and novel techniques have been developed, notably; Creep Feed Grinding (CFG), its use highlighted in the production of deep slots and fir tree patterns in turbine blade roots, and High Efficiency Deep Grinding (HEDG), a process capable of delivering both high wheel and workpiece feed rates with large depths of cut, typically used for the machining of profiles in parts [20]. Table 2.1 shows some typical grinding parameters for the various techniques, where the specific removal rate is the product of the depth of cut and the workpiece speed as shown in Equation 2.1.

$$Q'_w = av_f \tag{2.1}$$

Parameters	Reciprocating Grinding	Creep-feed Grinding	HEDG
Depth of cut, a	Low 0.001 – 0.05 mm	High 0.1 – 30 mm	High 0.1 – 30 mm
Workpiece speed, v_f	High 1 – 30 m/min	Low 0.05 – 0.5 m/min	High 0.5 – 10 m/min
Wheel speed, v_s	Low 20 – 60 m/s	Low 20 – 60 m/s	High 80 – 200 m/s
Specific removal rate, Q_w'	Low 0.1 – 10 mm^2/s	Low 0.1 – 10 mm^2/s	High 50 – 2000 mm^2/s

Table 2.1: Typical grinding parameters for common grinding techniques [21]

The advantages of high speed grinding in abrasive machining can only be utilised in an effective manner if the machine exhibits certain requirements for this high performance grinding technology. When working with high rotational speeds the grinding wheel/spindle/motor system must run extremely accurately and with a minimum amount of vibrations. A high level of rigidity is therefore required for the entire machine system. Additionally, precise balancing of the grinding wheel is necessary. In terms of the tool, the wheel used for high speed grinding should be strong

enough such that the centrifugal force does not lead to a breakage in the high speed operation range. Therefore superabrasive electroplated wheels with a steel hub are particularly suitable for this type of application. Lighter wheels are also in development and increasingly becoming available, the use of Carbon Fiber Reinforced Polymer (CFRP) can enable wheel speeds of up to 200 m/min to be realised [22]. Along with a rigid and precise machine structure, in high performance grinding the machine often includes sophisticated pieces of equipment incorporating high speed spindles, several grinding wheels, dressing devices, custom built coolant delivery systems and workpiece on-line measurement.

2.1.2 Freeform abrasive machining

As technology has evolved the occurrence of complex shaped parts and freeform part surfaces has become more frequent. Freeform surfaces are now used in the aviation industry for turbine blades, in medicine for knee prostheses, and in the automotive industry for car body tool dies [23-25]. In order to facilitate the generation of these surfaces by material removal, modern grinding machines typically utilise 3 to 6 axes of movement for high volume metal removal and difficult-to-machine materials.

An example of a 5-axis machine for the grinding of turbine blade profiles is shown in Figure 2.1. Such multi-axis machines are often complemented with latest generation control units that are capable of high speed interpolation of tool paths between the axes as well as open controller architecture where machine variables may be used for process monitoring [26].

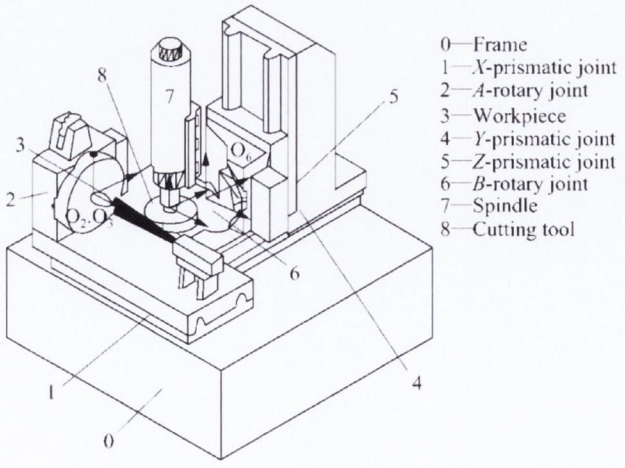


Figure 2.1: 5-axis turbine blade grinding machine [27]

All complex 3 – 5 axis grinding processes have been derived from the two traditional main classes of grinding; flat surface grinding and cylindrical grinding. Figure 2.2 describes these basic processes.

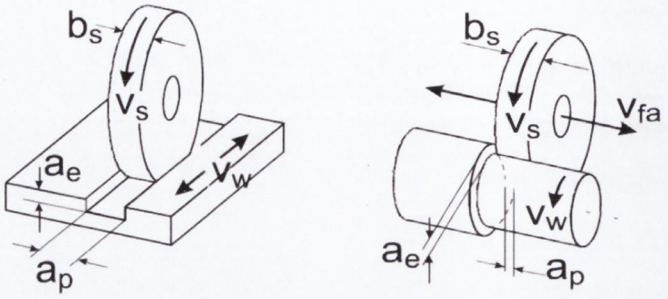


Figure 2.2: Surface grinding (left), external cylindrical grinding (right) [18]

In surface grinding the wheel moves orthogonally to the workpiece by a depth of cut a_e. If traversing across the workpiece the wheel is moved by the amount a_p between grinding paths. In external cylindrical grinding the workpiece is rotated between centres, the grinding wheels peripheral surface engages with the outside of the round workpiece and the feed direction of the grinding wheel goes alongside the workpiece rotation axis.

The basic grinding processes and its many subdivisions have been fundamentally distinguished according to the German standard DIN 8589 [18]. For complex parts with freeform geometries however the relatively basic type of movement as described by surface and cylindrical grinding are not sufficient to generate the required surfaces. Shape grinding instead is used where a contoured wheel moves across the part in a number of non-linear paths generated through NC code.

Toric grinding wheels

Toric shaped grinding wheels, a form of wheel with a minor and major radius for reaching the contours of curved surfaces, have been increasingly employed in the last decade to generate these types of complex shapes through multi-axis machining. First reports in the literature of torus shaped grinding wheels appeared in the early 1990's. Aspheric shaped mirrors were previously manufactured using conventional grinding to obtain a rough shape then polished with loose diamond abrasive while repeatedly performing measurements and shape inspections. This was a lengthy process taking

days to manufacture a single lens. With the advent of superabrasives, a Cast Iron Fiber Bond Diamond (CIFB-D) wheel could be used. This standard wheel was then shaped to a toroid cross-section by using a diamond dresser to cut the profile in the wheel. These newly-shaped toric wheels were then employed to machine precisely and quickly aspheric shaped ceramic mirrors while keeping surface roughness and form error to a minimum [28]. In order to maintain form accuracy and a low surface roughness a further method was developed where the axis of the wheel was inclined at 30° and the entire width of the wheel was used over the aspheric mirror, effectively changing the grinding point across the wheel from left to right as it moved across the part. It was found that a wide range of profiles could be ground using this method, and wheel wear was kept to a minimum as the entire width of the wheel was effectively used, thereby wearing the wheel in an even and efficient manner [29].

Further research was carried out for a similar application where non-axisymmetric aspherical lenses were ground using toroid shaped wheels which had been trued with a diamond dresser. Okuyama et al. investigated the effect of form deviations of the wheel surface, noting that both the waviness and amplitude of the toroid shape trued wheel surface had a significant effect on workpiece quality. The inner toric radius was found to be most influential on form error, as the full wheel circumference error was generally compensated for through the influence of both wheel and feed speed. It was also noted that the form deviation of a grinding wheel surface must be smaller than the objective machining accuracy to generate a surface without significant form deviation [30].

Other applications of machining with toroid-shaped wheels have included rake grinding of a taper ball end mill, where previously the conical surface or edge of a standard wheel would have been used for this application. Feng et al. found that the curved geometry of a torus-shaped grinding wheel tool was particularly suitable for generating a constant helical angle and constant normal rake angle on the spiral rake surface of a taper ball-end mill as the toroid-shaped wheel produced minimum gouging and an accurate profile [31].

More recently, NC shape grinding for the machining of complex freeform shaped parts has been investigated by Jansen et al. [32]. A simulation of the grinding process with toroid shaped wheels was developed to address the issue of geometrical grinding errors in the process as illustrated in Figure 2.3. In this simulation a wheel-workpiece contact area was determined through a finite element geometric-kinematic simulation

for force prediction in conjunction with a model of the process/machine dynamics. From this, grinding forces were predicted and profile errors from grinding were estimated with the surface of the workpiece after the grinding process being the main output [33-35].

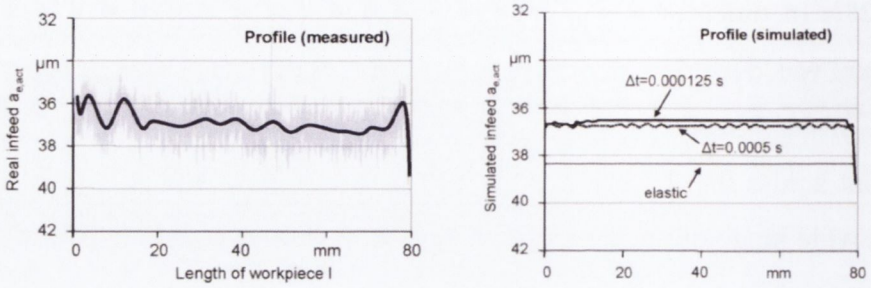


Figure 2.3: The simulated and measured workpiece surface [32]

Although this simulation encompassed the main interactions between the grinding machine structure and the process, there were some limitations – notably the depth of cut had to be known for the simulation, and increasing complexity resulted in increasing computational cost. In the context of the current work, machining with toroid shaped wheels in line by line paths is referred to as 'shape grinding'. In the shape grinding process the toroid shaped wheel is moved in several toolpaths across the workpiece as shown in Figure 2.4.

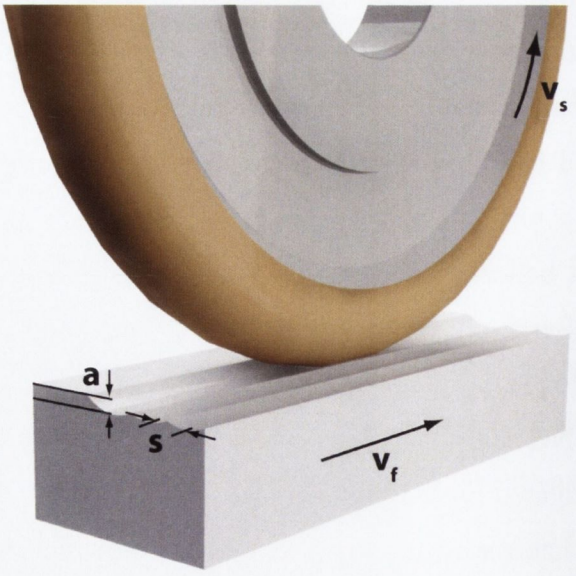


Figure 2.4: Schematic of toroidal wheel and planar workpiece

This movement and tool shape allows for a large degree of flexibility in the workpiece form. With a freeform workpiece, the material removal rate can vary both along the path and between two consecutive paths. The desired surface can be produced by multidimensional relative motions between grinding wheel and workpiece, as shown in Figure 2.5. The contact area between the grinding wheel is therefore complex and varying. Investigations of three-axis grinding of freeform surfaces with toric grinding wheels have also shown that contact conditions between the grinding wheel and workpiece significantly influence the shape accuracy [23]. The limits for the shape of the workpiece are given geometrically by the radius of the grinding wheel profile and by the grinding wheel radius. The smallest producible concave radius on the workpiece is given by the respective tool radius.

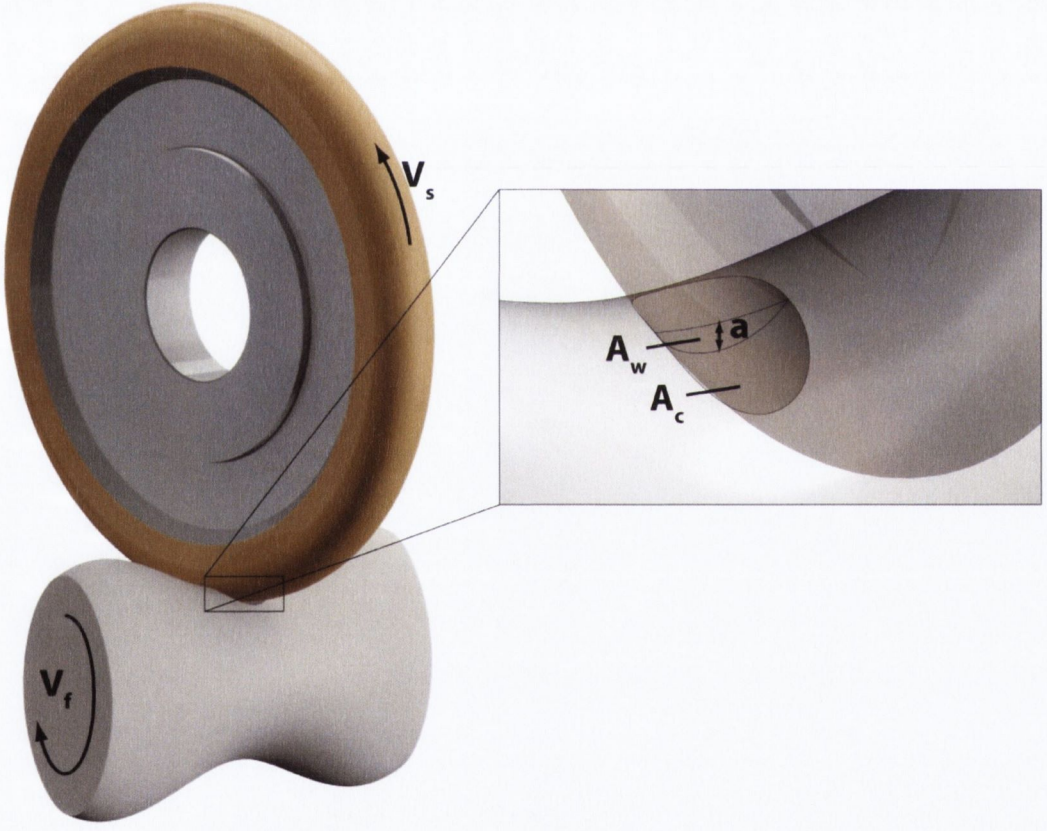


Figure 2.5: Freeform NC shape grinding with toroidal wheel

An analytical model was developed by Denkena et al. for analysis of tool-workpiece engagement for prediction of surface roughness [36]. The geometrical contact width of the tool b_g, the engagement area A_w and the specific material removal rate Q_w' over the depth of cut a_e in convex and concave machining were estimated

through a mathematical representation of the contact conditions as illustrated in Figure 2.6. The contact width b_g and the material engagement area A_w were found to be higher for concave than for convex surfaces. The engagement calculation for the second toolpath was also noted to be of high importance as this toolpath represents the majority of the contact conditions.

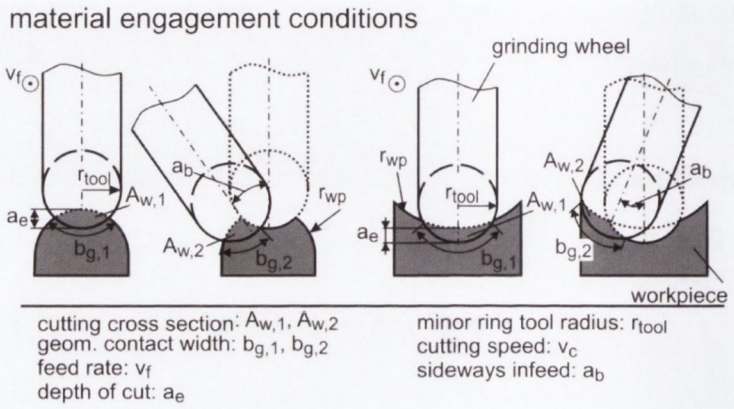


Figure 2.6: Engagement of the grinding wheel on differently curved surfaces [23]

Denkena et al. applied the analytical model for contact conditions in order to predict surface roughness for machining of ceramic implants with small toric shape grinding tools [37]. The model was then further developed by Denkena et al. for frontal grinding at an inclined lead angle in the feed direction [11, 38]. The objective was to determine the height of the roughness peaks between the feed grooves, otherwise known as scallop height or macro surface roughness, as illustrated in Figure 2.7. The theoretical macro surface roughness was found to match well with the measured surface roughness in grinding trials, with any underestimate of the surface roughness being due to micro-surface roughness variations in the feed direction for frontal grinding conditions. The developed model is useful for predicting changes in surface roughness when grinding parameters are altered in an attempt to optimise the process.

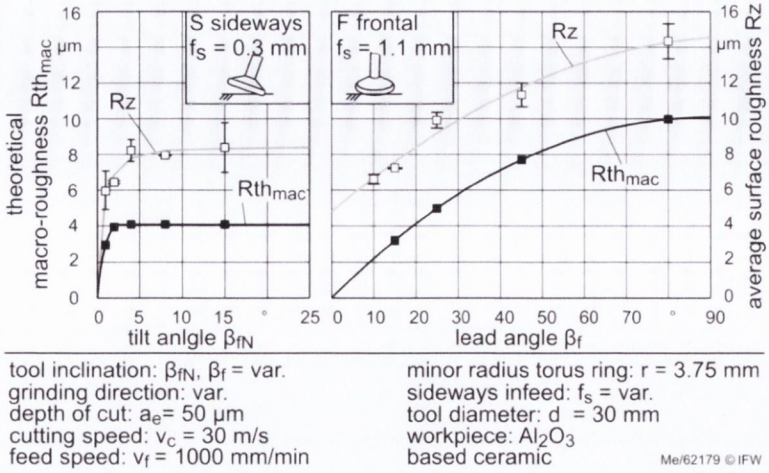


Figure 2.7: Macro surface roughness for sideways and frontal grinding with toric pins [38]

2.1.3 Material removal, forces and specific energy

Grinding wheels are generally composed of either primarily abrasive grits or grits embedded in a secondary bond material. The grits provide the cutting action for material removal during the grinding process. Grit materials are typically crystalline in nature and tend to have predominantly negative rake angles up to $\alpha = -75°$, as illustrated in Figure 2.8 [39].

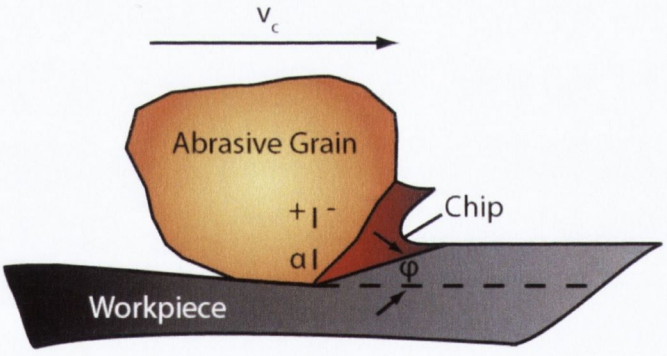


Figure 2.8: Abrasive grain with a negative rake angle generating a chip, adapted from [40]

During the material removal process, grits move along cutting arcs or paths in a track bound manner, as shown in Figure 2.9. Each grit may have one or more cutting edges. The material removal action itself is initiated through these cutting edges engaging with the workpiece and forming chips that are removed from the work surface.

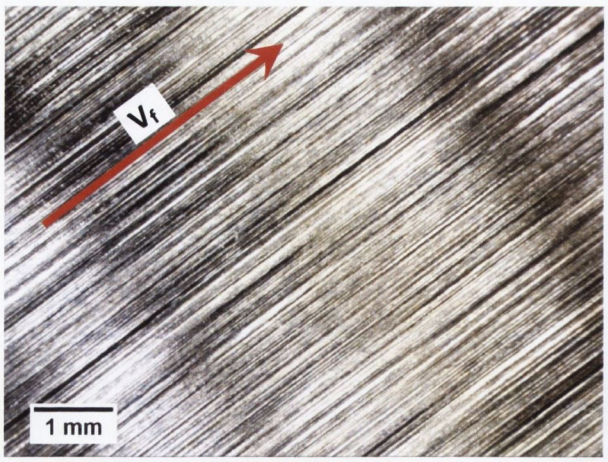


Figure 2.9: Optical micrograph of grinding tracks visible for new wheel on Cobalt Chrome alloy

The cutting force acting upon the individual grit during a cutting edge engagement can be broken down into a component F_t in the tangential direction of the cutting speed and a component F_n in the direction normal to this. The tangential force component is generally responsible for the cutting chip removal, while the normal force acts to press the cutting edge into the workpiece and may be responsible for material deformation. For grinding with non-symmetrical profiles there may be an additional force component present in a direction parallel to the wheel axis which may be denoted as F_a [18, 40].

$$F_c = F_t + F_n + F_a \tag{2.2}$$

In the early fifties strain gauges were primarily used to analyze forces in surface grinding by Marshall and Shaw [14, 41]. More recently, force dynamometers with piezo-electric force transducers have been used to measure the tangential and normal forces in order to characterize the process [42, 43].

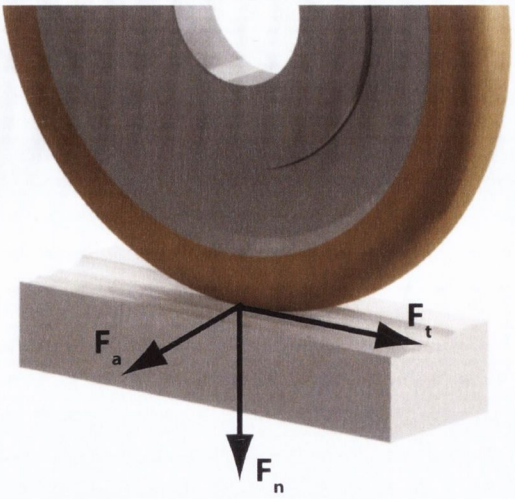


Figure 2.10: Forces in grinding

A related analysis method, which can sometimes be a more practical solution in industrial settings, is to measure the power expended in grinding. Since in grinding the feed rate is usually much smaller than the wheel speed, $v_f << v_s$, the total grinding power, P, associated with the normal and tangential force components in surface grinding can be written as [20]:

$$P = F_t v_s \tag{2.3}$$

A key fundamental metric related to the power consumed in the process is known as the specific energy, u, which is defined as the energy per unit volume of material removed.

$$u = \frac{F_t v_s}{a b v_f} = \frac{P}{Q_w} \tag{2.4}$$

The specific energy of the cutting process is an important quantity for a variety of reasons. It is the work required to convert a cubic volume of metal into chips, and is approximately independent of other variables. It is also a function of the work material and the mean chip size, and is generally proportional to the toughness of the metal being ground. Specific energy can also be used as a general metric to describe the efficiency of the machining process.

Specific energy in grinding of steels has previously been measured and found to be as high as 20-60 J/mm^3 and even higher for fine grinding. For difficult-to-machine

materials this may be even higher. When compared to other material removal processes, such as turning, for example, specific travelling energy e''_c dissipating into the workpiece was compared for external traverse cutting and grinding and found to be 0.056 J/mm² and 16.5 J/mm² respectively [44]. The grinding process typically involves high wheel/workpiece velocities and large strains. With such high speeds there should not be sufficient time for a significant amount of heat generated by the plastic flow of the materials and chip to be conducted away into the workpiece during the chip generation process. Therefore the chip formation process should be close to adiabatic. The upper bound or limit on the energy per unit volume in such a process should therefore be the energy necessary to melt a unit volume of material, in order to generate a chip. The melting energy per unit volume of iron is 10.5 J/mm^3 and this value is generally representative of steels [40]. However, specific energy values recorded for grinding are typically much higher than this. It is clear that there are other mechanisms at work in the process responsible for expending energy in ways other than pure chip generation.

The actual engagement between the grit and work surface has been found to take place in three defined phases [45]. Removal of the workpiece material is achieved through chip formation. Chip formation is initiated through a plastic shearing action when the cutting edge has penetrated to a critical depth of cut, T_μ [46]. The critical depth of cut is highly variable, and factors which can affect it include the sharpness of the cutting edge or wheel wear, the cutting face orientation, its rake angle, radius and the friction coefficient [18, 40].

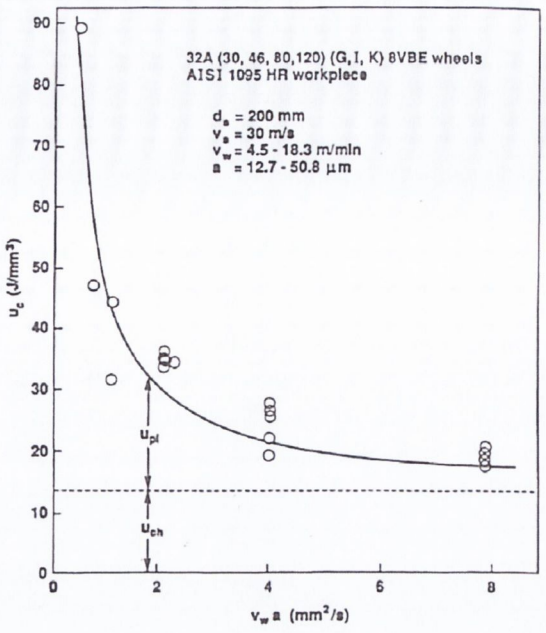


Figure 2.11: Specific energy versus volumetric removal rate per unit width in straight plunge grinding [40]

In Figure 2.11 the specific energy for chip formation during plunge grinding of steel is shown to decrease to a value of 13.8 J/mm^3. This value is markedly higher than the melting energy for iron at 10.5 J/mm^3. The reason for this originates with Merchant's classic model of chip formation, where according to the model 75% of the chip-formation energy is typically associated with shearing, and the remaining 25% with chip-tool friction [47]. This implies a value of 10.4 J/mm^3 for the shearing component of 75% of u_{ch} which is remarkably similar to the corresponding melting energy of iron of 10.5 J/mm^3. The other 25% of the minimum energy input is expended by rake face friction between the chip and the abrasive grain. This correlation between grinding and melting energies has been found for a wide range of materials, as shown in Figure 2.12.

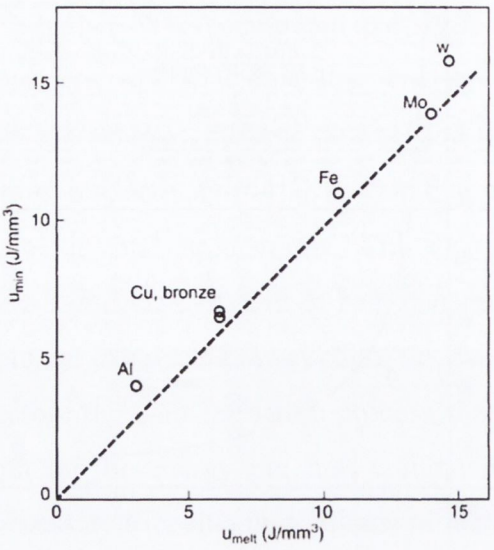


Figure 2.12: Minimum specific energy, u_{min} versus melting energy, u_{melt} for various metallic materials [48], [40]

When the specific cutting energy is evaluated at various removal rates it can be seen that for slower material removal rates, which correspond to smaller chip thicknesses, the specific cutting energy becomes extremely large. This is commonly referred to as the 'size effect'.

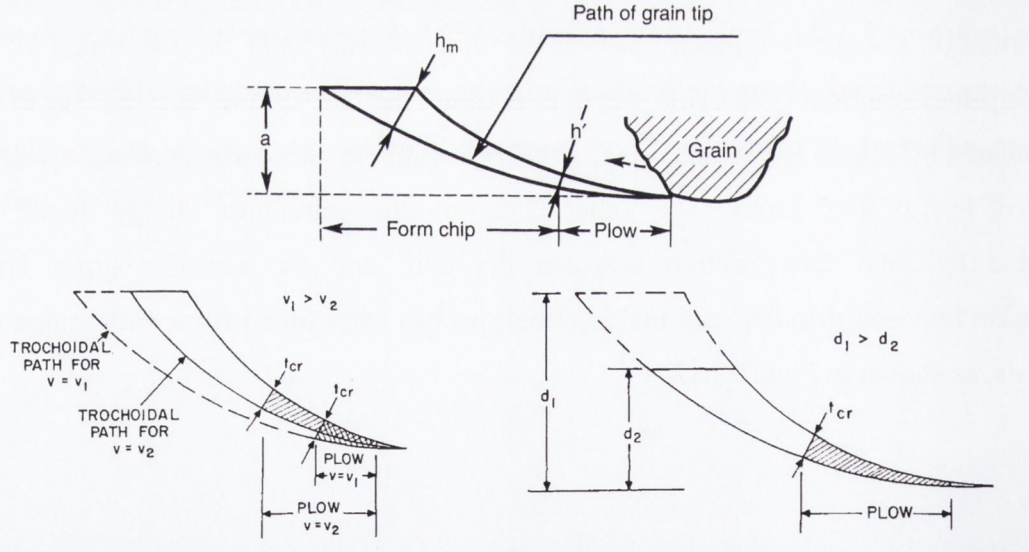


Fig. 20 Illustration of the effect of table speed on the transition from plowing to chip forming at a critical undeformed chip thickness

Fig. 21 Illustration of the effect of downfeed on the transition from plowing to chip forming at a critical undeformed chip thickness

Figure 2.13: Illustration of plowing and chip formation, where a is the depth of cut, also referred to here as the downfeed, d, h_m is the maximum undeformed chip thickness, also referred to as t, and h' is the critical depth of cut where chip formation commences, also referred to as t_{cr} [40, 49]

The size effect is due to energy dissipation between a combination of plowing, sliding and chip formation mechanisms due to the interaction between the abrasive grain and the work surface. After the initial phase of elastic deformation when the cutting edge of the grain has first made contact with the workpiece, and before chip formation occurs, plastic flow or plowing of the workpiece material takes place [40, 50]. During plowing material flows to the sides of the engagement zone forming ridges, but it may also flow beneath the cutting edge of the abrasive grain to its flank face. The energy expended due to plowing contributes to the observed 'size effect'. The relative amount of plowing can be decreased through an increase in the material removal rate, where an increase in the feed rate or depth of cut will enlarge the undeformed chip volume, so that the relative amount of material plowed aside before reaching h' decreases relative to that provided afterwards by chip formation, as illustrated in Figure 2.13 [49].

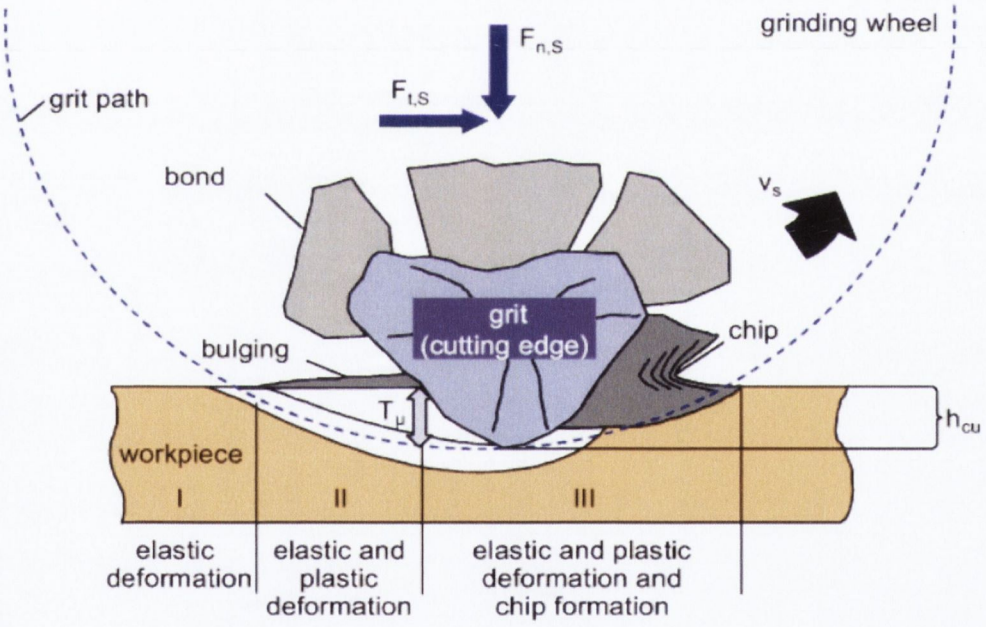


Figure 2.14: Zones of elastic and plastic deformation in chip removal [18]

The third mechanism that can contribute to the overall large magnitude of specific energy in grinding is referred to as sliding. At times the cutting edges can fail to penetrate the workpiece, instead rubbing or sliding across the workpiece surface without generating any chips [51]. This sliding mechanism is as a result of wheel wear, where the grits are dulled or flattened to such a degree that they are no longer removing

material during the process. The dulled flattened abrasive tips are commonly referred to as 'wear flats' and are caused by attritious wear of the grinding wheel [52]. This mechanism can expend little to no energy for a perfectly sharp wheel, however as the wheel wears down the energy due to sliding increases. The total energy in the process is therefore split between the three grinding mechanisms described above as described in Equation 2.5.

$$u = u_{ch} + u_{pl} + u_{sl} \tag{2.5}$$

Power forces and temperature are all highly influenced by the degree of sliding, plowing and cutting energy in the process. There will always be a minimum process energy level needed for the energy necessary to generate a chip, which roughly corresponds to the energy needed to melt a unit volume of that material [48]. Typically though, the energy necessary for cutting is higher than this base level of energy, and most of this remaining energy expended through plowing and sliding is dissipated as heat into the workpiece and abrasive cutting tool [47].

2.1.4 Temperature and velocity effects

Due to the high velocities and relatively small uncut chip thickness, the process of abrasive machining gives rise to many challenges. The issues of main concern are typically thermal damage of the workpiece and tool wear.

In grinding, most of the mechanical energy is dissipated as heat at the wheel-workpiece contact zone [47]. In this zone the heat is then dissipated between the grinding wheel, q_s, the workpiece, q_w, the chips, q_{span}, and the cooling lubricant, q_{kss}, as illustrated in Figure 2.15 [18]. Most of the heat generated during cutting is caused by friction at the tool face, chip surface and during chip cropping. A small portion of the heat generated is due to friction of the grinding wheel bond material against the workpiece.

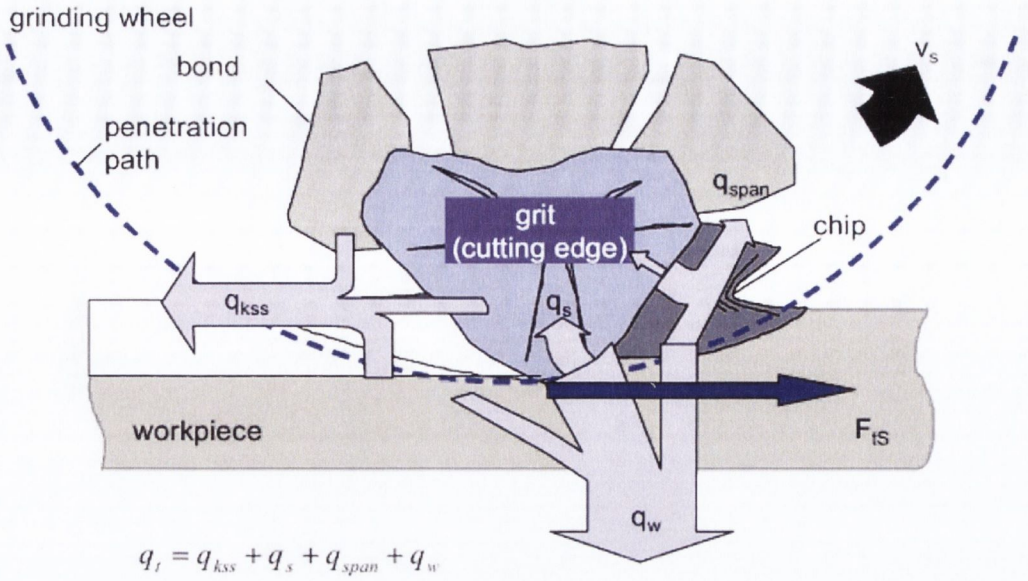


Figure 2.15: Energy distribution and heat flow during cutting edge penetration [18]

Heat is also generated through plastic deformation of the workpiece. This can result in the generation of high temperatures which can cause various types of thermal damage to the workpiece, such as burning, metallurgical phase transformations, softening or tempering of the surface layer with possible rehardening, unfavourable residual tensile stresses, cracks and reduced fatigue strength. Furthermore, thermal expansion of the workpiece during grinding can lead to residual stresses and contribute to inaccuracies and distortions in the workpiece [53, 54]. An example of damage of the surface integrity of a ground workpiece of a steel gear due to grinding burn is shown in Figure 2.16. The thermal damage is visible in this image with nital acid etching of the surface. As a result of high temperatures during the process the martensitic phase in the gear is transformed to cementite and the hardness in the surface layers is reduced. High tensile stresses occur as a result of the thermal damage and as a consequence cracks appear on the gears surface [55].

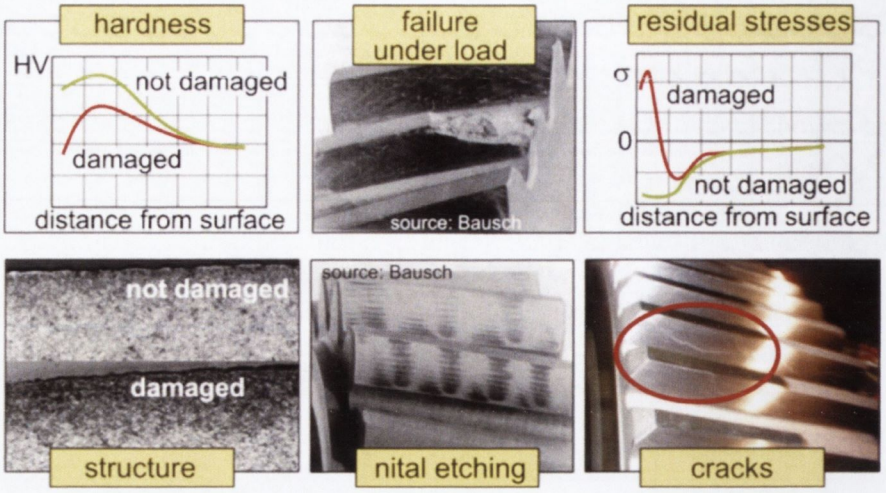


Figure 2.16: Possible grinding errors on a gear [55]

The application of coolant can help prevent such issues from arising through conduction of some of the thermal energy into the fluid instead of the workpiece, however the fluid film burnout limit is a limitation for the effectiveness of coolant in such applications. This is because as the temperature increases the boiling mechanism can progress to film boiling where a vapour film is developed between the workpiece and the fluid. The vapour acts as an insulator and prevents heat transfer to the fluid. As a result, the workpiece temperature quickly rises and surface burning of the material may occur [56].

The temperatures in grinding may be approximated by the application of moving heat source theory where the grinding zone is modeled as a source of heat that moves across the surface of the workpiece. Temperatures of the workpiece surface are typically estimated through calculation of the total heat flux, q_t, and subtraction of the grinding wheel, q_s, chips, q_{span}, and cooling lubricant, q_{kss}, components. The fraction of the total energy for each of these components is estimated through calculation of the heat or energy partition ratio. The energy partition ratio depends on the type of grinding, the wheel and workpiece materials, and the operating conditions.

A sliding heat source solution was first developed based upon Carslaw and Jaeger's early work [57, 58]. This solution was later applied analytically for thermal analysis of fine grinding based upon a sliding heat source at the shear plane in dry grinding. More recent applications of heat source theory have been extended to oblique shape heat source solutions for shallow-cut and deep grinding [59], and a circular arc

shaped heat source for HEDG grinding [60]. The inclined heat source model is suited to large depths of cut and high speeds and is illustrated in Figure 2.17.

This model gives a clear insight into why the HEDG grinding process is so efficient; with large depths of cut and high speeds a situation arises where part of the heat entering the grinding zone is not conducted downwards, instead it is convected out across the workpiece to the advancing material. That heated material is then quickly removed with the chips during the process thereby reducing the maximum temperature where the newly ground surface is generated.

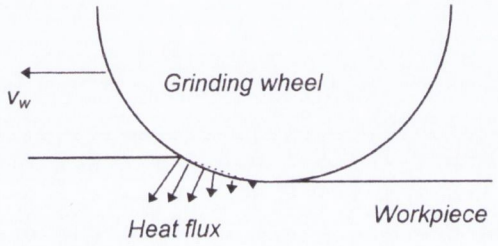


Figure 2.17: Inclined heat source [59]

Energy partition ratios can also vary significantly depending on the type of grinding, fluid application conditions, and wheel condition. Stephenson and Jin reported that the heat partition to the workpiece with increasing Q_w' was reduced, primarily due to the contribution of heat removal by the grinding chips. This effect is illustrated in Figure 2.18 where the finished temperature of the workpiece remains low with increasing specific removal rate [61]. A considerable amount of further work has been done on modeling temperatures in grinding, much of which is described in detail in two recent CIRP keynote papers [53, 62].

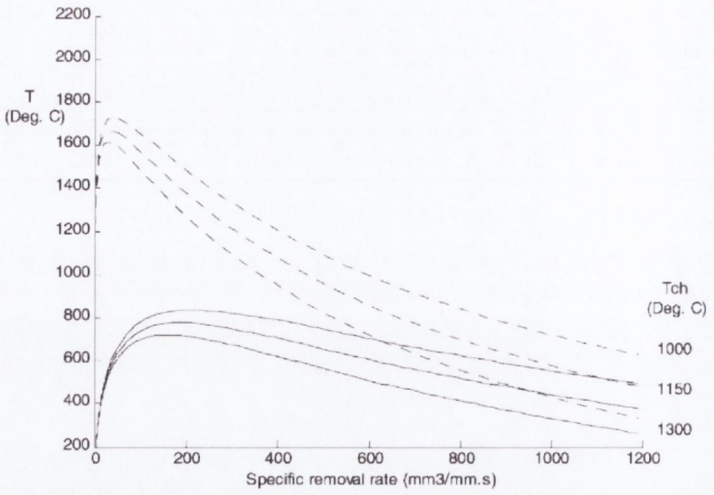


Figure 2.18: Predicted grinding temperatures on finished surface of workpiece (wheel speed 150 m/s, a_e = 3 mm, wheel diameter d_e = 200 mm, mineral oil as grinding fluid; solid line: h_f =23,000 W/m2 K, dotted line: h_f = 0) [61]

Residual stress is a type of elastic stress which is present in a material even when no external force is being applied. Residual stress can have a significant effect on the way a component behaves, adding or subtracting from applied stress. The magnitude of thermal energy entering the workpiece has a significant impact on the magnitude of residual stresses within a part. Grinding causes residual stresses in the vicinity of the surface layers of a workpiece. Both tensile and compressive stresses can be induced by grinding. Residual compressive stresses are induced by localized plastic flow due to the mechanical interaction of abrasive grains with the workpiece.

Residual compressive stresses are considered to have a beneficial effect on mechanical strength properties, whereas residual tensile stresses are considered to be detrimental. Since fatigue cracks always occur under tensile loading, the surface with the residual tensile stresses will always be the most prone to fatigue cracking. Residual tensile stresses are caused mainly by thermally induced stresses and deformation associated with the grinding temperature and its gradient from the surface into the workpiece. The influence of residual stresses has been found to be relatively more pronounced with higher strength brittle materials. Severe grinding conditions on high-strength steels and aircraft alloys are typically responsible for larger residual tensile stresses thereby leading to reduced fatigue strength [53].

Brinksmeier et al. suggested that the generation of residual stresses in a component from grinding are primarily caused by [63]:

- machining conditions
- topography and specification of the grinding wheel including wear
- cooling conditions

Chen et al. went on to suggest that thermal expansion and contraction in the grinding process was one of the most significant factors in the generation of tensile residual stresses. The emphasis of their research was therefore to determine the grinding temperature for the onset of tensile residual stress, tensile residual stresses were found to develop after the grinding temperature reached a critical level at approximately 200°C for En9 medium carbon steel. It was also found that the critical temperature for tensile residual stresses was highly dependent on a materials properties, particularly its yield strength [64].

In a contribution to a CIRP keynote paper, Brinksmeier investigated the relationship between residual stresses and specific grinding power for grinding operations of case hardened steel as shown in Figure 2.19. It was found that it was possible to induce compressive stress if the specific grinding power was sufficiently low. The higher heat conductivity of CBN grinding wheels was also found to produce lower specific grinding power and hence reduced thermal load, leading to less tensile residual stress in the workpiece [14].

As the generation of residual stresses in the part is related to the temperatures experienced in the process, the detection of the onset of grinding burn is a useful way of avoiding residual stresses and thermal damage in the part. Since the grinding zone temperature is a function of the energy introduced during the grinding process, the threshold temperature for burning of the workpiece surface should be related to the specific grinding energy.

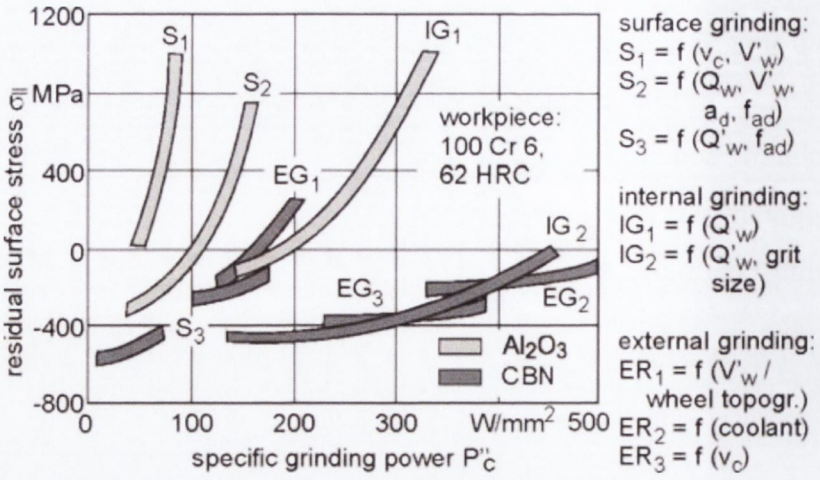


Figure 2.19: Residual stress as a function of specific grinding power, diagram contributed by Brinksmeier to CIRP keynote paper on process monitoring in grinding [14]

Based on Jaeger's thermal model, Malkin developed burn threshold diagrams that consider the critical specific grinding energy for the on-set of thermal damage, an example of which is shown in Figure 2.20 [62]. The increasing gradients of the lines correspond to increasing critical temperatures, and the horizontal axis relates to a relationship between the effective wheel diameter, depth of cut and work speed.

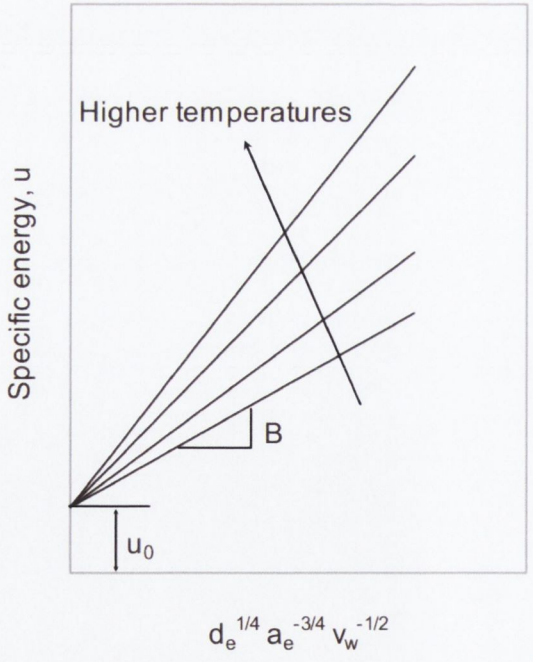


Figure 2.20: Lines of constant maximum grinding zone temperatures [53]

A more recent example of a burn threshold diagram generated for HEDG of cast iron is illustrated in Figure 2.21. In this the maximum surface temperature calculation has been modified to take into account the high percentage of the total grinding energy removed with the chip (up to 95%) due to the increased speeds in HEDG as compared to Malkin's previous estimate for a shallow cut regime of 55% [65]. If the specific energy remains below the temperature threshold line shown then grinding burn can be avoided. The difficulty in applying this method in process control is the necessity for application first of a thermal model followed by experimental validation of the results.

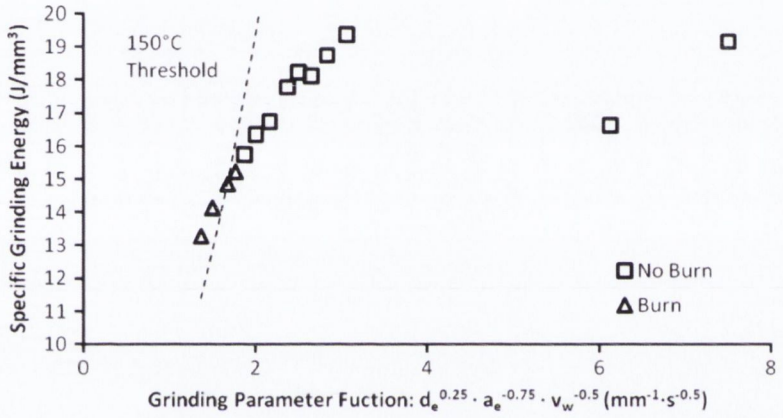


Figure 2.21: Burn threshold diagram demonstrating a limiting threshold for a temperature rise of 150°C for wheel speeds of 100 m/s for SG cast iron [65]

An increase in the material removal rate is generally understood to result in both lower specific cutting energy and increased power and process forces [21, 66]. This is an important consideration for increasing efficiency of the grinding process. Neugebauer et al. discussed high performance cutting and the opportunities associated with exploiting velocity effects in production processes in order to extend process limits [67, 68]. An increase of feed rate and depth of cut in high performance cutting operations typically results in lower specific cutting forces and energy, but higher cutting forces and power consumption. For example, Rowe et al. found that at low workspeeds the specific energy of the process was higher and the onset of thermal damage tended to occur at lower workspeeds. Increases in the base temperature and bulk heating could be avoided through increases in the workspeed with high speed grinding [69].

From a quality and economic point of view the removal rate is the main criterion for the selection of cutting speed, feed and depth of cut. The application of increased removal rates has some clear benefits, however there are some limitations involved, namely:

- risk of thermal damage due to exceeding the critical temperature
- shorter tool life reducing productivity and efficiency
- surface quality reduction at higher feeds and larger depths of cut

Therefore the machining conditions should be carefully optimized in order to provide high performance and efficient machining. This relationship is illustrated in Figure 2.22.

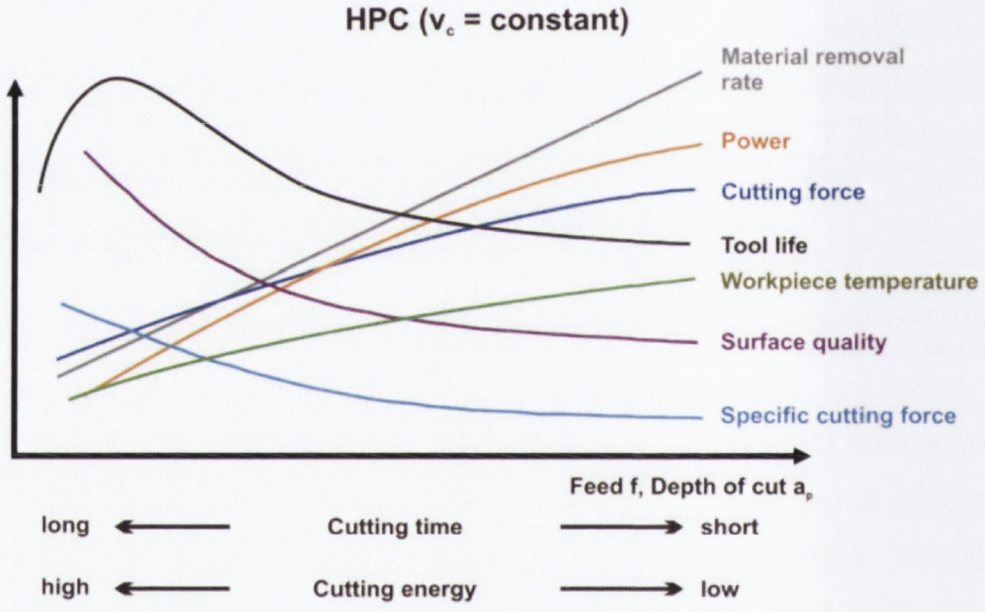


Figure 2.22: Effect of high speed cutting and increased cutting speed and depth of cut on the machining process [67]

Linke et al. discussed the implications of high speed grinding showing the positive influence of higher cutting speeds on surface integrity [70]. AISI 52100 hardened steel was ground with vitrified bonded CBN grinding wheels. Specific energy was estimated from tangential force readings from a force dynamometer and temperature from a pyrometer. Experimental results for grinding demonstrated that the

increased feed rates resulted in decreased specific energy and workpiece temperature, as shown in Figure 2.23.

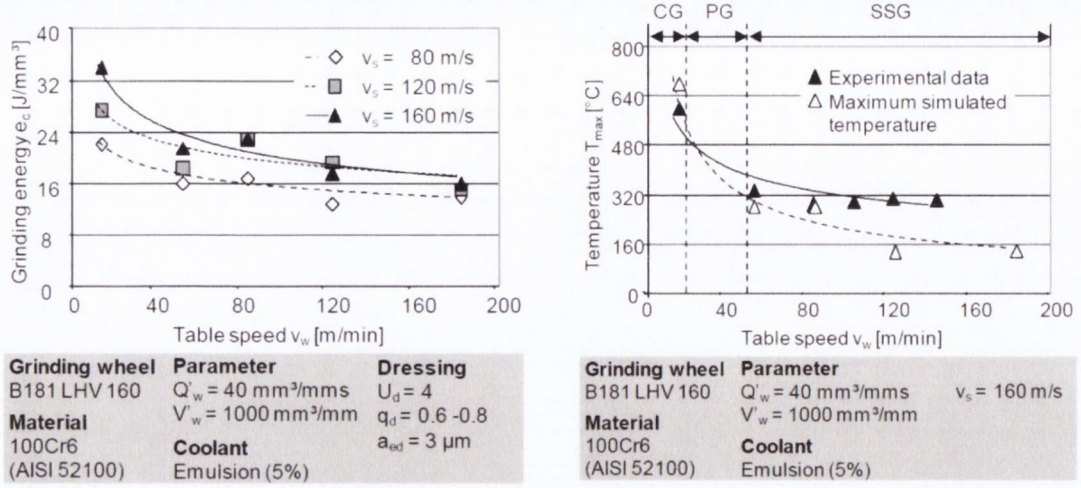


Figure 2.23: Specific energy as a function of table speed and grinding wheel speed (left) and measured and simulated temperature as a function of table speed for v_s = 160 m/s (right) (CG: conventional grinding, PG: pendulum grinding, SSG: speed stroke grinding) [70]

Comley et al. highlighted the benefits of high speed cylindrical grinding in the production of steel and cast iron camshafts [71]. Specific grinding energy was found to reduce as the specific material removal rate increased. As the material removal rate increased a greater proportion of the energy is removed by the grinding chips, this effect was demonstrated with a peak followed by a reduction in the finished surface temperature. Tool wear was not adversely affected with spindle power remaining at a stable value. These results demonstrate that with careful selection of process parameters significant achievements in reduction of cycle time and process sustainability can be made.

2.1.5 Wheel wear and super-abrasives

The wear of a grinding wheel is usually expressed as a volumetric loss of material. The G-ratio or 'Grinding Ratio' is a performance parameter used for describing the wheel wear resistance. It is the ratio of the volume of workpiece material removed per unit volume of wheel wear, as given by Equation 2.6.

$$G = \frac{V_w}{V_s} \tag{2.6}$$

The lower the G-ratio is, the more wheel wear that occurs. Figure 2.24 shows a typical relationship between volumetric wheel wear versus the accumulated workpiece material removed for an external cylindrical plunge grinding operation where the slope of the graph is the grinding ratio. The rate of wear is an important consideration when seeking to optimize a process. If an abrasive is chosen that wears too quickly, or machining parameters chosen that result in excessive wheel wear, any savings made through process optimization could be offset through having to replace the wheel too soon.

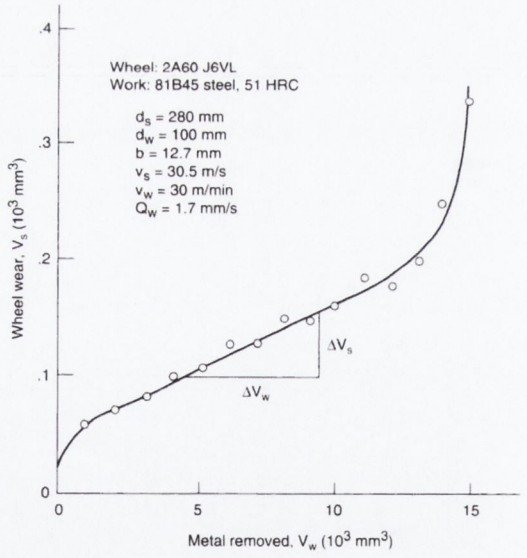


Figure 2.24: Volumetric wheel wear versus accumulated material removal [40]

Wheel wear mechanisms

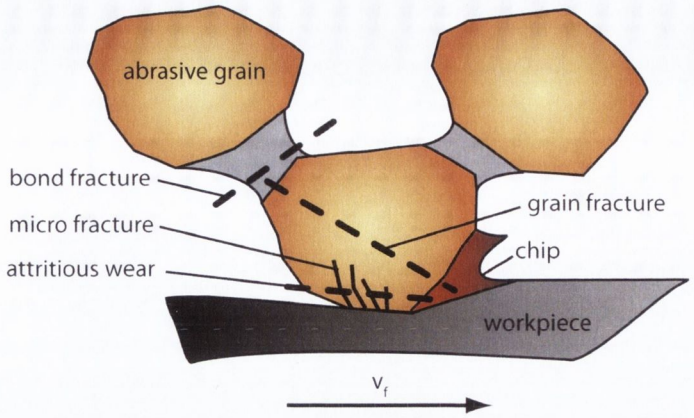


Figure 2.25: Mechanisms of wheel wear, adapted from [40]

The prevailing mechanisms of wear in the grinding process have been quantified through numerous research studies since the 1970's [72, 73]. High temperatures and pressures in the grinding contact zone can result in microscopic wear in the abrasive grain and the wheel bond. Wear of the abrasive grains during grinding with both Al_2O_3 and CBN wheels can be attributed to three main mechanisms of wear as illustrated in Figure 2.25 [40] :

- Attritious wear
- Grain fracture
- Grain pullout/bond fracture

Attritious wear begins in the crystalline layers lying near the surface of the abrasive grain. Extreme pressures and temperatures in these layers from friction against the workpiece cause this layer to soften and become more susceptible to abrasion [18]. This results in dulling of the abrasive grain, and the growth of 'wear flats' [40]. Attritious wear has a significant effect on the grinding forces, increasing them through the generation of friction as the dulled grains drag across the workpiece. In the case of grain fracture, alternating mechanical and thermal fatigue stresses can cause cracks in the abrasive crystals and eventually lead to fracture of the abrasive grain. When fragments of the grain break off, the area of wear is reduced and the grain is effectively sharpened.

As the wear flat area is reduced so too are the grinding forces and power [40, 74]. Grain microfracture can also take place where very small sections of the grain break off the grit. Grain pullout refers to the dislodging of the abrasive grains from the bond material. This mechanism has a similar effect to that of grain fracture, whereby the amount of possible wear flat area is reduced through the removal of grains from the bond, thus the forces are somewhat reduced as a result.

Conventional Abrasives and CBN

In industry, one of the most commonly used abrasive materials is aluminium oxide, or Al_2O_3. Aluminium oxide is a ceramic abrasive typically used in the machining of steel and other ferrous, high-strength alloys. Another commonly used ceramic abrasive is Silicon carbide, or SiC. SiC is harder than Al_2O_3 however it is not as tough. Silicon carbide is typically used for the grinding of metals such as aluminium, brass, stainless steels as well as cast iron and some ceramics [75]. SiC does show reactivity or solubility with iron, showing high attritious wear grinding ferrous materials due to chemical and diffusion reactions with the workpiece forming carbides and silicides. This can limit SiC's use for grinding ferrous materials, however, despite this, SiC is still the abrasive of choice in industry based in part on abrasive cost but more on ease of use, especially for dressing of forms critical for aerospace and medical applications, while being able to generate acceptable workpiece quality [76].

Typical Knoop hardness values range from 1370 – 2260 kg/cm^2 for aluminium oxide, to 2500 kg/cm^2 for SiC [74]. Abrasives with a much higher hardness value, such as CBN (Cubic Boron Nitride) or diamond, are known as superabrasives. Diamond has a Knoop hardness value of approximately 6500 kg/cm^2, and is typically used for machining hard abrasive materials such as ceramics, cemented carbides and glass. CBN has a Knoop hardness value of around 4500 kg/cm^2, and is typically used for the machining of hard materials such as hardened tool steels and aerospace alloys [74].

Cubic Boron Nitride (CBN)

Cubic Boron Nitride was invented by the General Electric Research Laboratory in 1957 [77]. CBN is a synthetic material that is composed of cubic boron nitride grain and

a special ceramic binder, an example of CBN grain is illustrated in Figure 2.26. CBN has the same structure as diamond and is the second hardest abrasive material next to diamond [5, 78].

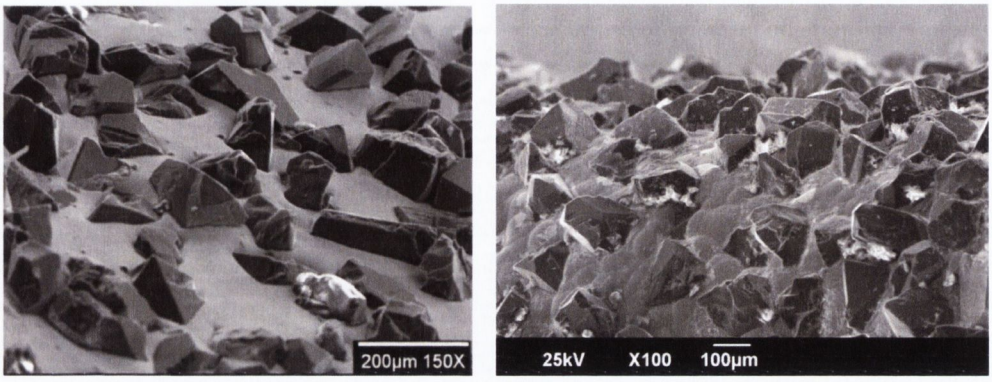


Figure 2.26: SEM images of new electroplated CBN wheel 120 grit, left, from [79], and right, worn electroplated CBN wheel surface courtesy of J.Badger, 2010

As well as for its high hardness, CBN is also noted for its high thermal stability up to temperatures in excess of 1300°C. However, CBN is susceptible to chemical reaction at temperatures above 800°C with alkali and water, therefore the use of straight oil-based coolant is preferable when grinding with CBN [80]. Another chemical related benefit with CBN is that, unlike diamond, CBN is non-carbon based, and therefore does not experience high wear rates when grinding steel. Diamond tends to experience high wear rates during grinding of steel due to diamond's carbon solubility in ferrous materials [77]. CBN is also relatively wear resistant; Aspinwall et al. studied machining with small diameter profiled single layer electroplated CBN and diamond grinding wheels during grinding of a nickel-based superalloy, Udimet720, where lower absolute wear values were observed for CBN than for the diamond abrasive used [81].

Oliveria et al. observed that although CBN superabrasive is rather expensive when compared to conventional abrasives, most economic analyses indicate that the added cost of CBN wheels pays off in terms of enhanced productivity and workpiece quality [12]. For example, Rowe et al. demonstrated for grinding of Inconel 718, vitrified CBN wheels used at high speed gave better quality with a lower cost than conventional abrasives, as illustrated in Figure 2.27 [82]. Liu et al. investigated the performance of Al_2O_3 and superabrasive wheels for grinding on a nickel-based alloy. Their main finding was that the performance of a CBN wheel was found to be better overall than

the Al_2O_3 wheel, regardless of whether the wheels were used for finishing or roughing operations [83].

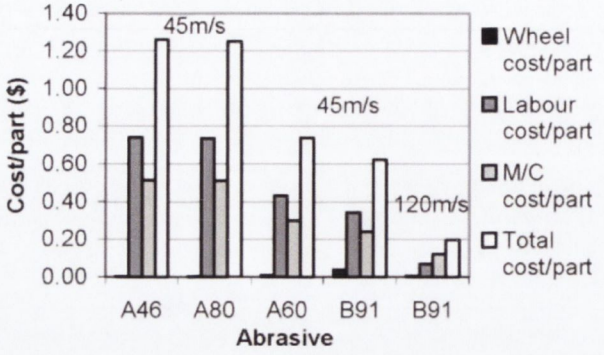


Figure 2.27: Comparison of costs per part when grinding Inconel 718, where the A represents Al_2O_3 and the B represents CBN [82]

Rowe also noted that the main caveat to using CBN in grinding operations is the high material removal rates necessary to justify the high associated costs of the abrasive and to avoid excessive wheel wear. Therefore it should only be considered to use CBN wheels on a suitable machine that provides good mechanical dampening and suitable strength in the spindle for such wheels [82].

Metallic Electroplated Bonds

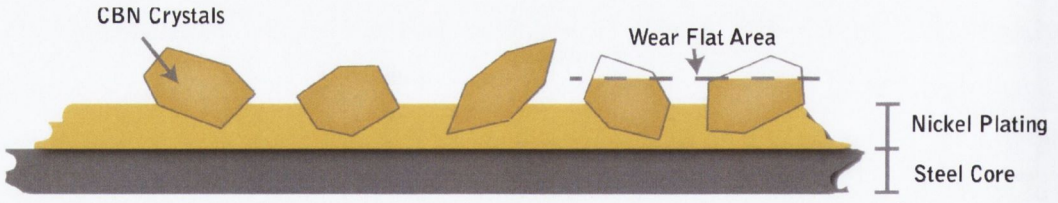


Figure 2.28: Cross-section of electroplated CBN wheel, adapted from [79, 84]

Electroplated, or galvanically bonded, CBN wheels consist of a single layer of CBN crystals held in place on a metal hub by an electroplated nickel binder. Figure 2.28 shows the surface of an electroplated CBN wheel with abrasive grain tips protruding above the electroplated nickel. Electroplated CBN wheels represent the largest share of the single-layer market, especially in the automotive and aerospace applications and are central to most high speed grinding applications [85]. Electroplated CBN wheels are generally less expensive than bonded types due to there only being a single layer of

superabrasive on the wheel. Much of the expense of the wheel is associated with precise machining of the steel hub, which can usually be reused. The depth of nickel plating is typically equal to about 30% of the grain dimension. Plating thickness can be increased for added bond strength for grinding tough materials, and the grit height distribution can be improved to ensure most abrasive grains are active and cutting during grinding [85].

Upadhyaya & Fiecoat investigated the effect of CBN crystals toughness and nickel wheel plating thickness on grinding performance [86]. Wheels with tougher CBN crystals were found to wear at a slower rate, and therefore remove more material and require less power. Furthermore, wheels with thinner plating layers were found to wear less and remove more material despite significant crystal loss up to wheel failure. This suggests that the wear rate depends more on crystal exposure than on active grain density [86], where active grain density refers to the density of grains at the surface of the wheel that perform the cutting operation [87].

Wear and Electroplated CBN

Wheel wear has more significant economic consequences for grinding with superabrasive wheels, owing to the high abrasive costs involved. Initial investigations by Shi and Malkin set out to examine the mechanisms of wear for electroplated CBN through the measurement of spindle power and wheel topography [88]. Net grinding power was measured during the grinding of hardened steel and wheel topography was measured after the tests. Attritious wear causes dulling of the abrasive grains by rubbing against the workpiece, and also increases the active grain density leading to a smoother workpiece and higher forces. Grain pullout resulted in less active grains, thereby reducing the active grain density for grinding. Grain fracture was also found to be an important factor in reducing the wear flat area on the wheel, thereby directly reducing the power and forces for grinding due to the reduced sliding friction involved [88]. The key difference between conventional bonded abrasive and electroplated CBN is that when grain pullout takes place there are no grains left to replace those that have been removed due to the single layer of abrasive.

The changes in grinding behaviour over an electroplated CBN wheels' life was subsequently investigated by Shi and Malkin [79]. Wheels with different grit sizes were observed over a wide range of grinding conditions. One of their main findings was that

radial wheel wear could be characterized for a grinding cycle by an initial transient at a progressively decreasing wear rate to a steady state wear regime at a nearly constant rate as illustrated in Figure 2.29. This is important to note when monitoring wheel wear either through power measurement or wheel topography measurement, the power recorded for the first few tests is usually significantly lower than power recorded after the transient wear state of the wheel has passed. Grain pullout was found to dominate the initial transient wear, whilst wheel wear in the steady state regime was found to be dominated by grain fracture. Grinding power was found to increase mainly by dulling of grains by attritious wear and fine scale grain fracture.

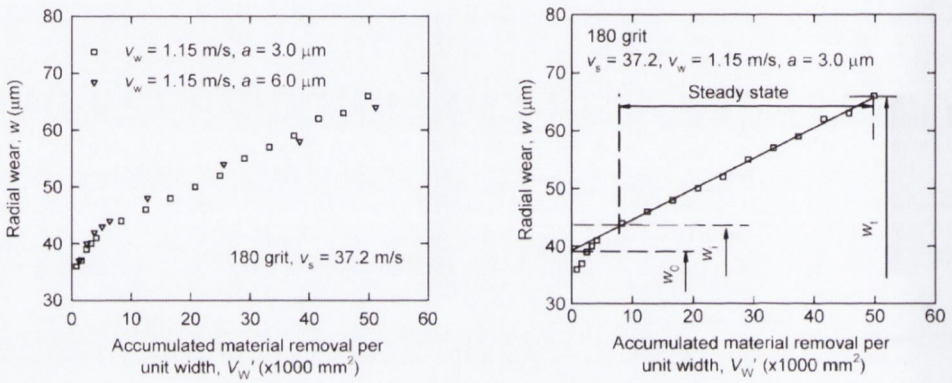


Figure 2.29: Radial wheel wear consisting of initial transient and steady states [79]

Wear of electroplated CBN was further investigated by Guo et al. in 2007 [89]. Straight surface grinding tests were conducted using 120-mesh plated CBN wheels on nickel base alloy blocks, with wheel diameters ranging from 12.7 to 25.4 mm and wheels speeds of 12 to 60 m/s. Results for spindle power and surface roughness are shown in Figure 2.30 for a 120-grit wheel, where the transient and steady-state stages for grinding power are illustrated as the accumulated volume of material removed increases. Using these results a model was developed to predict the wear flat area and power increase as the volume of material removed increased with model coefficients obtained through numerous empirical tests measuring forces during grinding at different process parameters [89].

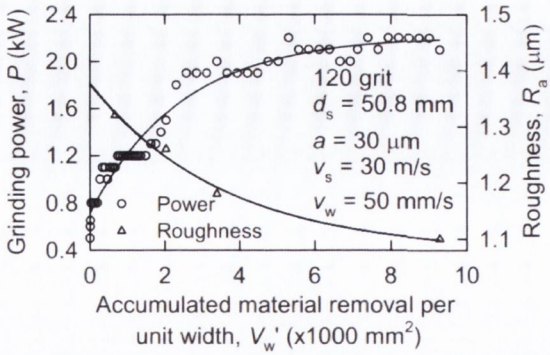


Figure 2.30: Transient power and surface roughness [89]

Thermal Aspects of Wear and Electroplated CBN

As compared with shallow cut grinding using conventional aluminum oxide wheels, Malkin and Guo found that lower temperatures and less thermal damage arises for cutting with CBN. This can be attributed to the very high thermal conductivity of the abrasive grains so that more grinding heat is conducted to the grinding wheel rather than to the workpiece. The thermal conductivity of CBN grain is approximately 35 times that of aluminum oxide, resulting in a much larger fraction of the grinding heat being transported to the grain instead of to the workpiece, in other words a lower energy partition to the workpiece. The energy partition to the workpiece is typically about 20% for CBN, and can be even lower with vitrified and electroplated CBN wheels due to the added benefit of cooling by the fluid at the grinding zone [53, 90].

Upadhyaya and Malkin found energy partitions ranging from 3% to 8% for grinding of hardened bearing steel with a 120 grit electroplated CBN wheel at temperatures below the burnout limit for the oil coolant of approximately 130°C. It should be noted that cooling by the fluid may be effective only if the grinding zone temperature is below the burnout limit. Figure 2.31 (a) illustrates maximum temperatures during grinding of hard steel measured using thermocouples embedded in the workpiece. Temperatures are shown to increase with radial wheel wear, and as the fluid burnout limit is reached the temperature rises rapidly. Figure 2.31 (b) demonstrates the corresponding increase in specific energy derived from measured spindle power with increased wheel wear. Two main effects are illustrated by these findings -: as specific energy increases as a result of wheel wear, so too does the temperature experienced in the workpiece, and once the fluid burnout limit is reached the coolant is no longer effective at removing heat from the grinding zone [84].

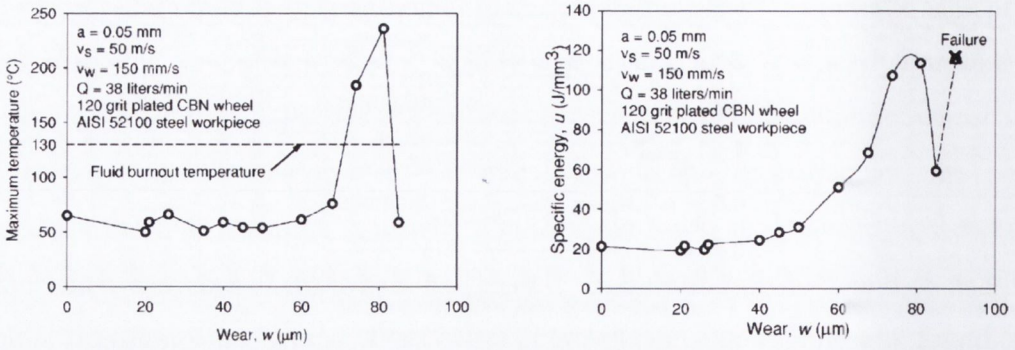


Figure 2.31: Left, effect of radial wheel wear on maximum workpiece temperature, right, specific energy versus radial wheel wear [84]

Residual Stresses with CBN Grinding

As workpiece temperature tends to increase with wheel wear it can be safely inferred that residual stresses also increase with the onset of tool wear. A poor choice of grinding conditions can lead to the generation of increased cutting temperatures which can contribute to the creation of tensile residual stresses in the workpiece. Brinksmeier et al. reported compressive residual stresses to be more prevalent when grinding with CBN abrasive. This can be attributed to the high hardness of CBN which results in less wear leading to less heat arising in the cutting zone, with the consequence that mostly compressive residual stresses are produced [63]. Similar findings were observed by Matsuo et al. for surface grinding of thin annealed steel workpieces with CBN wheels, where a plastically deformed layer on the surface of the workpiece along with a convex warp was found confirming the presence of mainly compressive residual stress after grinding with CBN [91].

Tonshöff et al. reported a correlation between the magnitude of residual stresses and workpiece surface temperature estimated through a grinding power model [92]. Chen et al. observed a similar linear relation between residual stresses and grinding temperature rise through a temperature heat model, and noted that a transitional temperature exists between compressive and tensile residual stresses with higher grinding temperatures inducing the onset of tensile stresses in the part [64]. Duscha et al. investigated the effect of increased velocities on residual stress for CBN grinding of hardened steels. They found that for increasing feed rate of 12 m/min – 180 m/min coupled with a constant specific removal rate of $Q'_w = 40$ mm^2/s that more compressive residual stresses were observed due to a more mechanical impact with lower temperatures [93].

2.2 Process monitoring

As suggested in the previous section, abrasive processes are considered to be highly complex, dependant on a large number of input variables and non-stationary, in that process mechanisms such as wheel condition change with time [14]. In order for a manufacturing enterprise to remain competitive it is necessary to ensure the manufacturing process is as efficient, precise and productive as can be. For industries typified by intensive machining operations such as abrasive machining, this can be achieved through process monitoring and optimization [3]. The role of a monitoring system in grinding can be summarized with two key tasks;

- Process disturbance detection
- Process optimization

Monitoring systems for an abrasive process should be capable of detecting disturbances such as process instabilities in the process, and be able to provide an opportunity to prohibit the disturbances. Major issues encountered in the grinding process are chatter vibration, grinding burn, residual stresses, profile errors and surface roughness deterioration. These issues can occur as a result of selection of unsuitable process parameters or as a result of excessive tool wear. These issues must be identified and corrected for in order to maintain workpiece quality as well as machine equipment functionality.

Expensive damage and outage of the production system caused by disturbances can be significantly reduced through implementation of a good process monitoring strategy [13, 94]. In addition to disturbance detection, information regarding the measured process quantities obtained with the monitoring system can be used for optimizing the process. Optimization can be in terms of total cycle time or cost. The information obtained from a process monitoring system can also be used to establish a database as part of an intelligent system [13, 14]. This can be achieved through offline optimization or adaptive control systems.

Figure 2.32 from Klocke et al. illustrates a general procedure for development of process monitoring and control systems [2]. In order to generate a process monitoring and control system that produces reliable and useful results particularly in industry, the process challenges and commonly encountered disturbances must first be specified.

Process parameters that affect the disturbances should then be identified and studied so that suitable sensors can be chosen that will pick up the relevant disturbances. After selection of suitable sensors, process characterization can then take place by running tests at different process parameters and analysing the resulting process behaviour. A prototype monitoring solution can then be developed and subsequently transitioned into a real production situation if significant industrial interest and backing can be secured.

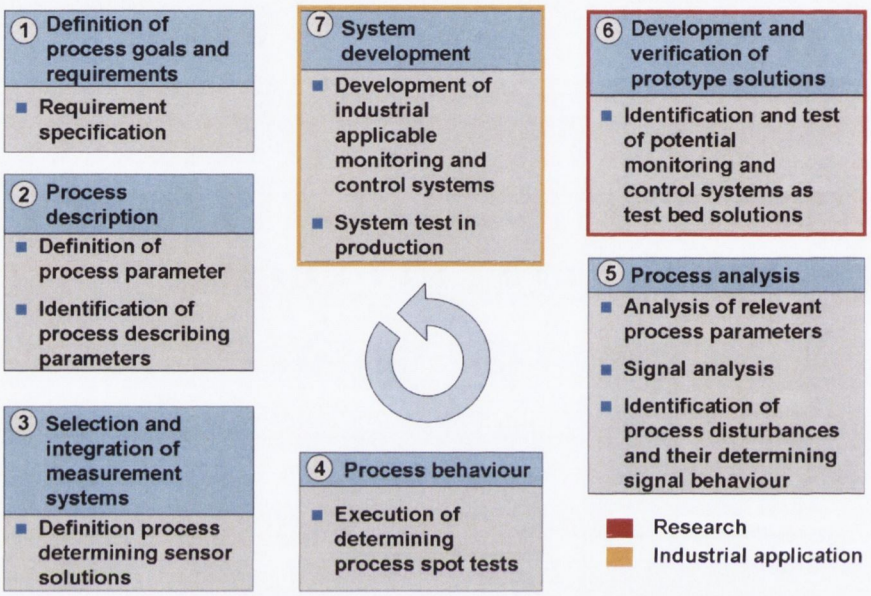


Figure 2.32: Procedure for the development of monitoring and control systems [2]

Over the past decade, extensive research has been carried out in process monitoring of machining [14, 95]. Through advances in sensing technologies numerous physical quantities are now measurable and can assist in tool condition monitoring and control, including, for abrasive machining [14] -:

- Power
- Force
- Wheel topography
- Temperature
- Acoustic emission
- Vibration

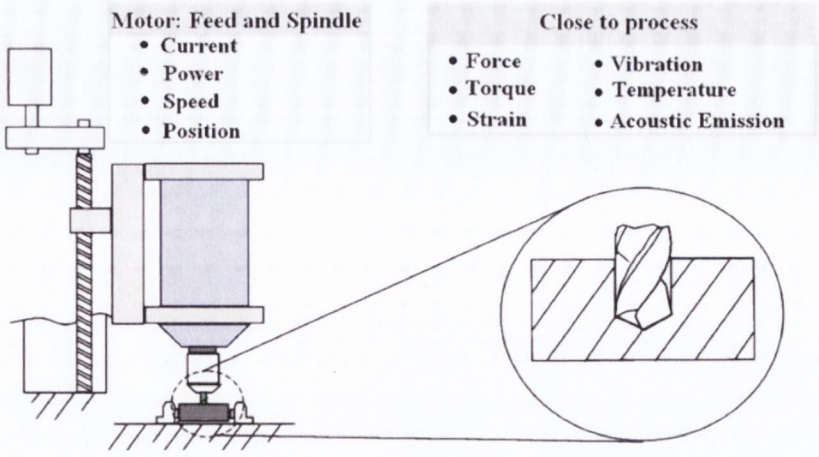


Figure 2.33: Measurable phenomena for online sensor monitoring [3]

A recent CIRP keynote paper by Teti et al. describes the state-of-the-art in sensor technologies as well as signal processing and decision making strategies for process monitoring [3]. Measurement techniques can be classified into two approaches; direct and indirect, as illustrated in Figure 2.33. The direct approach to process monitoring is where the actual quantity of the variable is measured and employed to derive useful information in relation to a process, for example in the case of tool wear; machine vision. With the indirect measurement approach a process is assessed through auxiliary quantities such as power or cutting force component, and the actual quantity is subsequently deduced through correlation through empirical means [96]. The indirect method of assessing a process through auxiliary quantities such as power is a more appropriate approach in industry, where ease of use, space, setup time and maintenance issues are important considerations.

2.2.1 Forces, vibration, acoustic emission & temperature measurement

A considerable amount of research has been conducted in the field of tool condition monitoring where sensors for power, force, vibration, acoustic emission and temperature measurement have been utilized. This work has been comprehensively reviewed in a number of keynote papers on process and tool condition monitoring over the past two decades, namely [3, 4, 14, 95, 97, 98].

According to Dimla et al. cutting forces and vibration are considered to be the most widely applicable parameters for tool condition monitoring during any metal-cutting operation [99]. Force monitoring typically takes place through the use of a force

dynamometer, an example is shown in Figure 2.34 (a). The first attempts to measure grinding forces date back to the early 1950's and were based on strain gauges [14, 41]. With the introduction of piezo-electric quartz force transducers more accurate force sensing solutions have been realized. Over the past two decades force dynamometers with piezo-electric force transducers have been used to measure the tangential and normal forces in order to characterize the process [42, 43]. In a keynote paper on tool condition monitoring in 1995, Byrne et al. noted that commercial dynamometers consisting of four three-component force transducers fitted under high preload in a plate arrangement provide the most accurate measurement of cutting forces [4].

More recent novel applications of force monitoring include force control for rotational grinding of substrates for micro-fabrication of semiconductor integrated circuits where normal force was monitored and controlled in a position feedback loop, a significant reduction in surface roughness was observed using this control strategy [100]. Other examples of integration of force sensors into the machine structure have included integration of force sensing rings into the machining spindle for monitoring of a drilling operation [101], and testing of a prototype force measurement system comprising of a Kistler high speed rotating cutting force (RCD) dynamometer for process monitoring of a blisk milling process [102]. While these applications can provide significant insight into the process forces and characteristics, the main drawback for use of force sensors in industry is their prohibitive cost and the necessity for significant modification to the machining setup for installation.

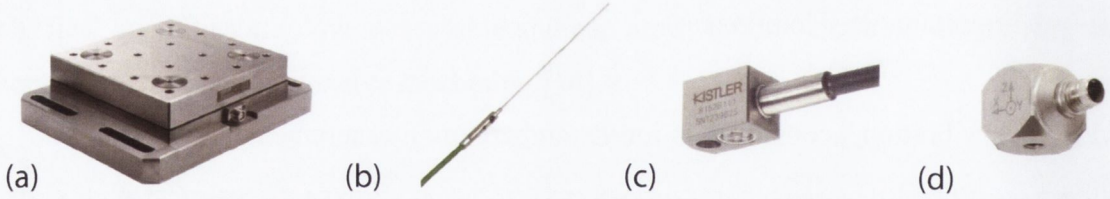


Figure 2.34: Sensors for process monitoring, (a) force dynamometer, (b) thermocouple, (c) acoustic emission sensor, (d) accelerometer [Source: Kistler and Omega Engineering]

Much work has also been done on monitoring and identification of vibration and chatter in grinding. For example, Inasaki et al. provided a comprehensive review of chatter origins and suppression in their keynote paper, while Quintana et al. provided a recent review of research in chatter in machining processes [103, 104]. Typically piezoelectric accelerometers are used for vibration monitoring in machining operations,

where they can be used to detect chatter or tool unbalance [97]. An example of a recent application of vibration monitoring studied the onset of chatter with difficult to grind materials with a vitrified CBN wheel including Inconel and Silicrome using a test setup with an electro-dynamic shaker and an accelerometer. Results showed that induced random vibration had a significant influence on wheel wear [105]. Vibration monitoring has also been successfully applied in a position-oriented-monitoring strategy for the manufacturing of blisk geometry with the objective of identifying certain unwanted frequencies responsible for dimensional deviations in the finished product [106].

Many other sensor types have been the subject of research including temperature measurement, acoustic emission and strain measurement. Temperature measurement is of particular interest for the analysis of thermal effects in the cutting zone for the hopes of correlation with issues such as thermal damage, including grinding burn and microstructural changes resulting in changes of hardness of the workpiece, and the onset of wheel wear. Limitations of temperature measurement however include the requirement for considerable research in each application in order to account for changes in the boundary conditions such as tool geometry and the use of coolant, and the distance from the sensor to the cutting zone in order to obtain the best prediction of the tool-workpiece temperature [95].

Davies et al. provided a comprehensive review of temperature measurement in machining operations, and noted that for grinding, the most commonly used methods of temperature measurement include thermocouples, both embedded and machinable, as well as radiance techniques including IR pyrometers [107]. Xu et al. compared methods for measurement of temperatures in grinding, comparing the performance of an embedded thermocouple, infrared detector and a foil/workpiece grindable thermocouple to each other and concluded that all three methods provided reasonable results, while the foil/workpiece thermocouple proved to be the most sensitive picking up 'flash' temperatures during grinding [108].

In 2005, Brinksmeier et al. investigated the potential of embedded thermocouples and miniature force sensors in the grinding wheel. Thermocouples in the form of type K thin-film sensors of Chromel and Alumel layer were deposited on silicon by evaporation techniques, thermowire sensors were also used. The sensor signal was transmitted by wireless means to a data acquisition system at a rate of 40 kHz. The thin film thermocouple wires showed the highest response rate, while the thermowire wire

pair sensors displayed a more stable signal [109]. The thermocouples were not calibrated, however the technology shows potential for the future in integration of wheels, though cost and wheel stability may be a prohibitive factor when considering the use of such technology in industry.

Acoustic emission is another widely used method for process monitoring in grinding [14]. A primary application of acoustic emission in grinding is to detect changes in the structural integrity of the workpiece, such as grinding burn, while other applications have included recognition of the start of grinding contact as well as collision monitoring [13]. Acoustic Emission (AE) refers to the generation of transient elastic waves generated by the rapid release of energy by a sudden redistribution of stress in a material [110]. The mechanisms leading to AE generation include deformations through dislocations and distorted lattice planes, phase transformations, friction and crack formation and propagation [14].

A recent example of an application of AE in grinding has featured determination of the contact length during grinding to assist in temperature modelling, where AE was monitored during wet plunge surface grinding of hardened 55 HRC high speed steel workpieces using a vitrified-bonded aluminum oxide wheel. The AE signal was acquired using a Kistler 8152B sensor with a response frequency range of 50–400 kHz, and the sensor was magnetically clamped to the vice holding the workpiece. Spikes at the start and end of the signal were correlated with entry and exit of the workpiece which corresponded to the correspond to the actual wheel–work contact length in grinding [111].

Another recent application of AE investigated detection and prediction of wheel wear in grinding. White fused alumina wheels were used to grind carbon steel at a rotational speed of 30 m/s, with an oil-based coolant. The grinding process was monitored by an acoustic emission sensor with a frequency range of 60–400 kHz mounted on the side face of the worktable through magnetic force. Worn and sharp wheel conditions were distinguished from the AE signal using genetic algorithm classification methods, after removing noise in the signals with a high-pass filter with cut-off frequency of 90 kHz. Experimental results showed that the system was able to classify the wheel state as sharp or worn with an accuracy of up to 99.39% with a depth of cut of 10 μm [112]. Though the AE signal has proven to be a useful tool in research for identifying physical phenomena such as grinding burn, workpiece contact and wheel

wear, the potential for application of this sensor in industry is limited due to the necessity for mounting of the sensor close to the workpiece [13].

Another sensor currently under development with high potential for process monitoring is the surface acoustic wave wireless passive strain, or SAW sensor [113]. SAW based strain sensing involves electrically inducing a surface acoustic wave into a piezoelectric material and then reconverting the energy of the wave back into an electrical signal, where the frequency of the wave is dependent on the amount of strain the material is experiencing. A significant advantage of SAW devices is their low power consumption due to the wireless interrogation. Promising results have been observed for oblique cutting of aluminium with a carbide tool and spindle speed of 600 rpm, where the SAW sensor response was found to correlate well with the active axis signal response with a Kistler force dynamometer. The sensor was also able to discern tool condition with increased amplitude observed in the sensor signal for a worn tool. The SAW technology shows clear potential for cost effective process and tool condition monitoring, however it may be some time before the technology becomes widely available.

2.2.2 Power measurement

Power measurement is becoming more commonly used in process monitoring for two reasons; first, power can be used as an indirect sensor for cutting force, and second, the measurement apparatus for power measurement does not disturb the machining operation [3, 114]. The current and therefore the effective, or active power of the main spindle is in direct relation to the torque delivered at the shaft of the motor where every event at the shaft is thus mirrored by the power input of the motor drive [18, 115].

As illustrated in Figure 2.35 there is a relation between the active power also known as real power, the reactive power, and the apparent/complex power. Active power is measured in Watts (W) and is the product of voltage and current through the resistance in a circuit. Active power is the power responsible for doing work or producing heat. In the monitoring application described in this research active power is recorded. Reactive power is power stored in and discharged by inductive motors, transformers and solenoids. Reactive power generates reactance in the circuit and is measured in Volt-amperes reactive (VAR). Apparent power is measured in volt-amperes (VA), and is the product of line voltage and all the line current in the circuit,

apparent power is also the vector sum of the active and reactive power. The angle θ is the angle by which the input voltage leads the input current.

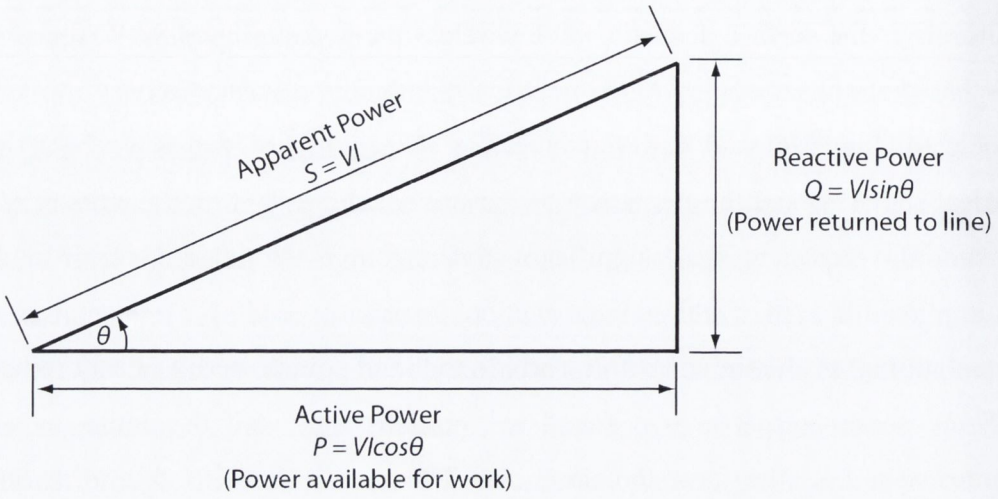


Figure 2.35: Power triangle and relevant formulae

The motors used for spindles in high-powered industrial numerical control applications are typically alternating current servo motors due to their high accuracy, small size and lower cost. While single phase DC power is the electrical power equal to the current by the voltage, three phase AC power is calculated using Equation 2.7.

$$P = \sqrt{3}VI\cos\theta \tag{2.7}$$

An example of a typical power metering configuration is illustrated in Figure 2.36. Spindle power is the most suitable machine power signal for measurement when investigating cutting power and forces, as this is the power signal that is closest to the actual cutting process. Spindle power can be a useful parameter in detecting machining problems such as tool breakages, collisions and tool wear. A typical power meter records voltage through crocodile clips on exposed wire, and current through the use of Hall-effect sensors [14, 97]. Hall effect sensors comprise of current transformers which are clamped around the insulated copper wire. The sensors produce an electromagnetic field (EMF) in the direction perpendicular to the current and the field, the resulting measured voltage (Hall voltage) across the output is proportional to the vector cross product of the current (I) and the magnetic field (B) [116].

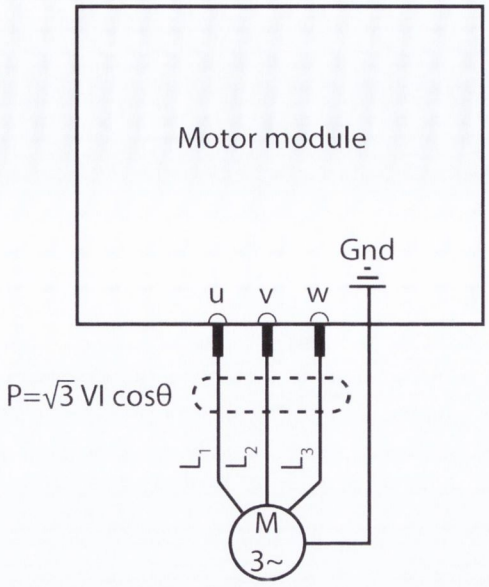


Figure 2.36: Motor power measurement for a three phase motor, adapted from [148]

An early study by Mannan et al. in 1989 investigated the feasibility for cutting process monitoring through the measurement of motor current and power [117]. A custom designed instrument utilizing a Hall-effect transducer was used to monitor power and current on electric motors with different drives for turning, drilling and milling. Investigations showed that tool breakage could be successfully detected by motor current monitoring. Tool wear could also be identified via motor current during milling of stainless steel and drilling with a 15 mm diameter tool at speeds of 36 m/min and 30 m/min respectively.

Li and Tso later analysed the effects of tool wear and cutting parameters on the cutting current signal in drilling [118]. Tests were performed for a range of drill diameters from 4.6 to 7.4 mm and a range of different speeds from 4 to 18 m/min for drilling of quench steel. Spindle motor and feed motor current was found to increase as tool wear increased with an almost linearly incremental relationship, thereby allowing drill flank wear state to be reliably identified using this method.

Al-Sulaiman et al. used a custom-made differential current detector box to measure machining power during the drilling of mild steel and evaluated the signal as a means of detecting tool wear for the drilling process [119]. Tests were performed at a number of different drill diameters from 6.35 mm to 12.7 mm during drilling of glass resin and Kevlar polyester fiber. Similar to the results shown by Mannan et al. and Li and Tso, an increase in power was shown as the tools wore down, as shown in Figure 2.37, illustrating the effectiveness of monitoring power for detection of tool wear.

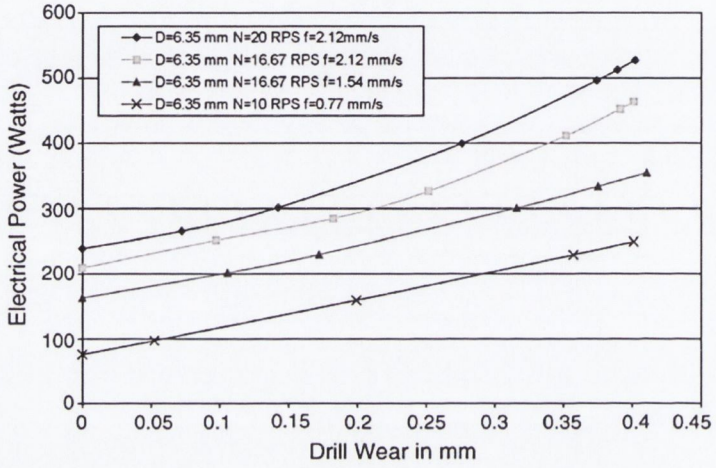


Figure 2.37: The effect of wear for 6.35mm drill and mild steel on power for different feed rates and cutting speeds [119]

At times it may be difficult or unsafe to measure the voltage through exposed wires. As the electrical voltage is preset at the motor, the required power in some cases can be sufficiently captured by the current signal alone [18]. For NC milling, Lee et al. determined that the sensitivity of the feed drive motor current was sufficient for the characterization of tool breakage in NC milling of steel with a spindle speed of 140 to 360 rpm and a depth of cut of 3 mm [120].

Kim et al. developed a filter to extract the cutting force component out of measured drive current signals during a contour NC milling process [121]. Current was measured from the servo motors of a Fanuc CNC 15m. A steel workpiece was used with a 20 mm milling cutter at speeds of 600 rpm and feedrates of 300 and 600 mm/min. Using an artificial neural network the current signals were processed to remove the friction component. Cutting signals from measured current matched closely with force traces measured by a force dynamometer during the machining process for circular

interpolated contour milling, with an axial depth of cut 1 mm and feed rate of 600 mm/min.

Axinte and Gindy reported on the effectiveness of a spindle power signal for tool condition monitoring in milling, drilling and turning. Solid carbide drill bits were used on a nickel-based alloy, Inconel 718 [122]. Axinte and Gindy concluded that spindle power was comparable in sensitivity to force signals from a dynamometer in the detection of tool wear in milling. Chipping of the milling cutter during the milling process however proved difficult to detect using spindle power. The spindle power signal was sufficient in sensitivity for both turning and drilling processes to detect both the chipped tool and gradual tool wear. Filtering of the spindle power signal for critical frequencies was noted to improve the ability to detect chipping and other small events during milling.

Diaz et al. observed an increase in cutting power for a corresponding increase in the material removal rate for endmilling of a low carbon steel for various machining parameters [123]. Power was measured with a Hall effect power meter on a Mori Seiki NV1500. The width of cut was varied between 1 – 7 mm, the spindle speed between 5426 – 7060 rev/min and feed rate between 330 – 860 mm/min. The average air cutting power demand of 1510 W was subtracted from the average total power demand. An almost parabolic trend was observed for cutting power as a function of the MRR of the cutter.

An example of a typical power profile for an internal cylindrical grinding machine is shown in Figure 2.38 where Herrmann and Thiede investigated a methodology for achieving energy efficiency in a manufacturing production environment [124]. The fixed energy profile is illustrated where the basic power for machine operation is shown with the power for machining. The basic power level for spindle operation should always be subtracted from the total power level for the machining time for calculation of the actual power for cutting.

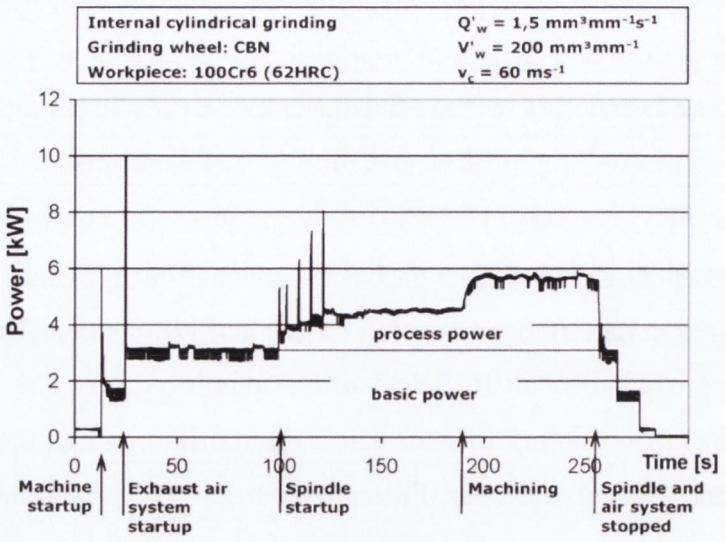


Figure 2.38: Energy profile of Studer grinding production machine [124]

Early investigations were conducted by Brinksmeier and Minke on characterisation of the CBN grinding process through power process monitoring for grinding during different cutting speeds [125]. A CBN wheel was used on hot work tool steel with cutting speeds ranging from 120 m/s to 180 m/s. Total grinding power was found to increase almost linearly with increasing cutting speeds, and with increasing specific material removal rate as shown in Figure 2.39. Another interesting finding was that the power demand increased with an increase in coolant flow. This was likely due to the braking effect that increased coolant flow has on the spinning of the grinding wheel. Kwak et al. observed similar results for external cylindrical grinding of Chromium–Molybdenum steel, where power was measured through three Hall effect sensors on the electric cables of the spindle motor. Power was observed to increase at varying degrees with increasing depth of cut, workpiece speed and traverse speed [126].

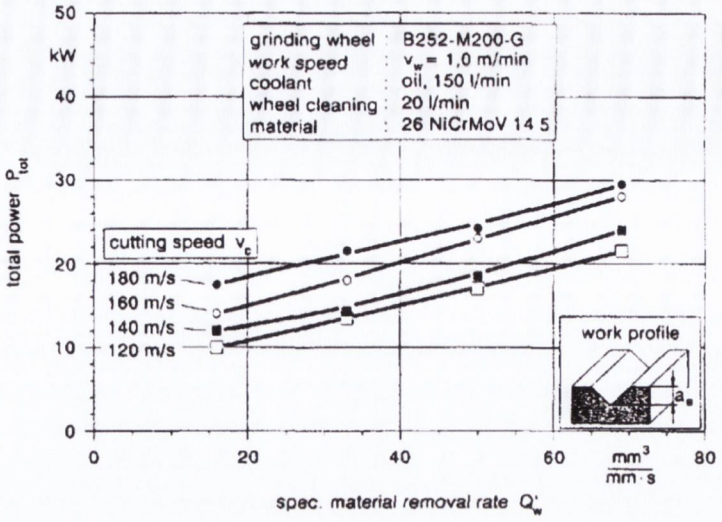


Figure 2.39: Total spindle power depending on specific material removal rate for different cutting speeds [125]

The surface condition of a traditional grinding wheel changes considerably with progressing machining time, the wheel dulls and dressing of the wheel becomes necessary in order to restore its sharpness. Determination of the wheel life is important as too frequent dressing wastes expensive abrasive as well as valuable operation time. Early investigations by Inasaki showed that monitoring the power consumption was useful in the determination of the grinding wheel life, as the calculated time constant from the derivative of the grinding power over time showed a steady increase in magnitude with corresponding increase of material removed with the wheel [127].

Subrahmanya and Shin employed a selection of sensors including acoustic emission, power metering, piezoelectric accelerometers and a capacitance probe for displacement measurements during chatter to monitor a plunge grinding operation. In these experiments an aluminium oxide grinding wheel was used to grind hardened steel alloy workpieces at a wheel speed of approximately 28 m/s. Experimental results and a decision-support algorithm illustrated that AE signals were most sensitive to grinding burn, and chatter, vibration signals from accelerometers were found to be the next senstivive towards burn and chatter, however both sensors had issues with repeatability. Spindle power consumption was deemed to be the most sensitive and robust sensor used towards wheel wear [128].

Investigations into the detection and effects of grinding burn through the use of power monitoring were conducted for a grinding of spiral bevel ring gears utilizing a vitreous bond CBN grinding wheel [13]. Monitoring of grinding power revealed an

almost linear increase in power with accumulated material removal, as illustrated in Figure 2.40. Grinding burn was detected for the first time using nital etching at a rate of 8100 mm^3/mm for the 28^{th} part. In previous work Inasaki also identified grinding burn through power readings using Al_2O_3 wheels on mild steel, and subsequently confirmed the presence of burn using nital etching [127].

Karpuschewski and Inasaki commented that for medium or large-scale production in the automotive industry, using grinding wheels with lifetime power monitoring is a very effective way to avoid thermal damage of the gear workpiece and also to avoid use of the environmentally harmful etching process [13, 55]. Other authors have also noted that monitoring of grinding power through the use of Hall Effect sensors on the spindle motor in order to calculate specific energy for use with a thermal model, can provide the basis of an adaptive strategy for the prevention of thermal damage in grinding [66, 129, 130].

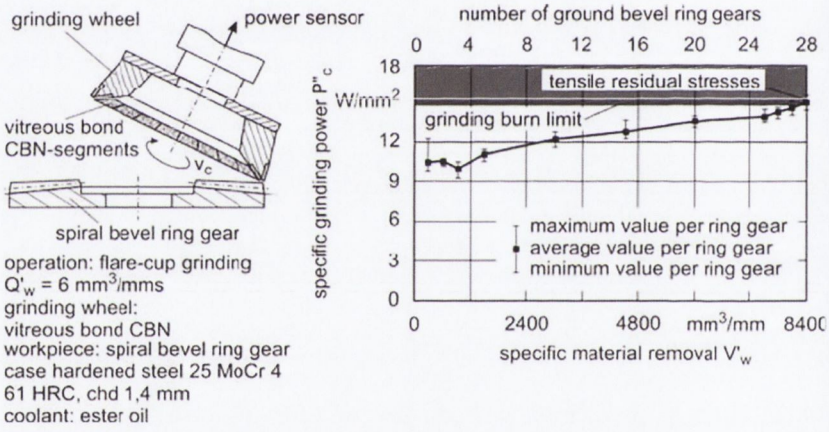


Figure 2.40: Power monitoring in spiral bevel gear grinding to avoid grinding burn [13]

The use of power monitoring in combination with other sensors for avoidance of thermal damage as well as optimisation of the grinding process is becoming more frequent. For example Guo and Malkin have investigated optimisation of the grinding of turbine blade root profiles using continuous dress creep-feed form grinding (CDCF) [131]. In CDCF grinding a profiled wheel is continuously dressed as it machines the blade with a diamond roll to maintain the required profile geometry and wheel sharpness. In order to optimize the cycle time and remain below damaging thermal heat-flux limits in grinding, force and power models were developed. Measured grinding

power and forces from a 3D force dynamometer were used to calibrate models. The process was then optimized to achieve reduced cycle time with respect to adjusting the workpiece speed and dress infeed per wheel revolution. A 40% reduction in cycle time was achieved using this method and process anomalies could be detected by using calculated control limits from the power model [132]. Guo and Malkin also investigated the implementation of pc-based optimization software for cylindrical plunge grinding with models derived from force and wear flat area as well as energy partition relationships with power for the prediction of thermal damage. Simulated power usage was found to agree with measured power [133].

Guo et al. performed research into an optimization strategy for five-axis grinding with CBN wheels [134]. The contact geometry between the wheel and workpiece was analysed as a stack of discrete sub-wheels for which the physical process parameter such as forces, power, and temperature were predicted using the contact data. The interpreted geometrical data was then used with empirical grinding models to predict physical process parameters such as forces, power and heat flux. Some model parameters were found previously and then taken as decision variables in a multi-constraint optimization [89]. By varying the workspeed to suit certain geometrical interactions, the process could be optimized and cycle time reduced. Further experimental validation work is needed for this model.

Recently, Guo investigated modelling and simulation of mold and die CBN grinding [135]. A model was constructed based on the previous model described in [134] utilising empirical results for power and grinding forces in order to predict process parameters of forces, power and heat flux. Results from grinding a half bottle shaped mold illustrated that by varying the workspeed cycle time could be reduced by 50% while achieving reduced grinding forces and power.

Another area where power monitoring and analysis can be useful is for the detection of unproductive 'air grinding', or when no material removal is taking place. An issue to keep in mind however when performing this kind of analysis is that the signal delay must be taken into account, especially the switch from a rapid feed rate to contact feed rate just before machining contact [14].

Power monitoring has also been demonstrated to be a useful parameter in the investigation of wheel 'collapse' during grinding of HSS steel with vitrified Al_2O_3 grinding wheels. Collapse, according to Badger, is a phenomenon where power

increases gradually with attritious wear until a critical value is reached, at this point wheel wear is rapid and then suddenly drops down to a steady-state value. Post-collapse power was found to be in the order of 80% of the pre-collapse power. Wheel collapse was mainly attributed to large mechanical forces causing grit and bond fracture, caused by increased forces from wear or dulling of the grits [136].

Recently Murray et al. investigated power monitoring of a grinding operation for Cobalt Chrome femoral implants [137]. The focus of the investigation was to conduct a life cycle analysis of the grinding process. The CNC grinding machine used for the case study was a Huffman HS-155R Multi-Axis Superabrasive Grinding System. The machine had a 20.9 kW spindle motor, five-axis configuration and two CBN-plated stainless steel grinding wheels. A fluid handling system was attached to the grinding system consisting of a 11.2 kW coolant pump, two 0.37 kW coolant filtration pumps and a 0.745 kW mist filtration pump. The energy used by the grinding system was measured using a Fluke 1735 power logger, and average active power was recorded in 0.5 s intervals for the filtration system, the main power of the grinding machine, the servos used to control movement of the fixture and grinding wheel, and the spindle motor. The mass of the implant was also measured before and after the grinding process where it was found that the average mass of material removed for each part was found to be 0.05 kg. The power consumed by the spindle motor was found to be the only piece of equipment that significantly altered the total power consumption of the grinding process, an example of recorded spindle power is shown in Figure 2.41.

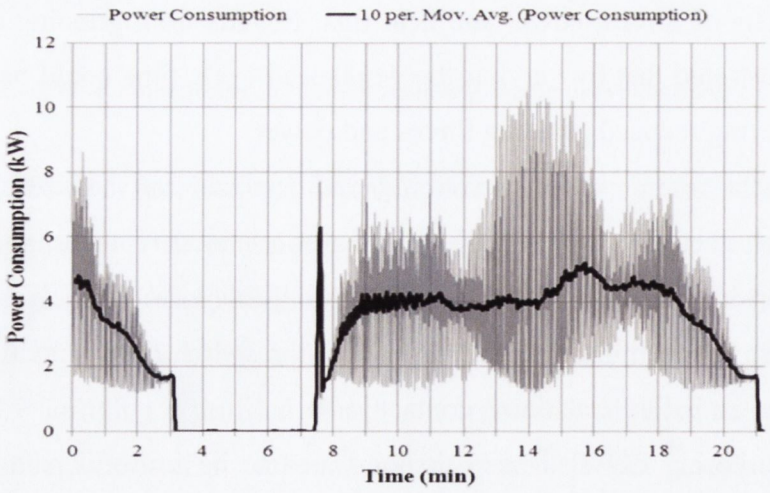


Figure 2.41: Power consumption of the spindle motor for grinding of femoral implant [137]

Murray et al. noted that the variation in required power could be attributed to changes in the material removal rate caused by the tolerance variations of the casting process for the femoral implants [137]. In terms of the carbon footprint of the process, it was found that energy use in the form of input electricity accounted for 55.9%, while scrap production accounted for 34.6% and the CBN wheel plating accounted for 7.6%. Furthermore, a summary of the energy use of different functions for the manufacture of 5000 implants revealed that the spindle accounted for 47% of process energy use, while coolant was 34% and the other 19% was due to auxiliary processes including filtration. This indicates that increasing the energy efficiency of the grinding process of femoral implants by increasing process efficiency and reducing the amount of scrapped parts could potentially do more than any other measure to reduce the carbon footprint of the grinding process in a sustainable manner. The limitation of this study in the context of the current work is that the variation of the spindle power consumption due to the alternating tool-workpiece machining conditions was not investigated and correlated with measured spindle position. Power monitoring was also performed through an external handheld power metering device with a low 0.5s sampling interval, and machining parameters were not varied.

The benefits of power monitoring have been reiterated by Byrne et al. who noted that drive power of motors is one of the most important sensor systems for indirect continuous measurement as it is a derivative of the cutting force components which are the characteristic variables for the process [4]. While sensors to measure current or effective power of feed drives or the main spindle represent the simplest alternative to force dynamometers in technical terms, and are also quite simple to retrofit, there are however some disadvantages to using such sensors, namely [4] -:

- The friction component in the drive guideways is contained in the measuring signal, this may be quite large and may fluctuate with lubrication state and traversing rate
- Actual cutting forces are only a fraction of the main power
- Spindle power is proportional to the resultant cutting force in the direction of the primary motion, and depending on the type of grinding involved and the abrasive-workpiece engagement conditions, this may result in the power being a less sensitive parameter in the monitored forces

Power monitoring for the grinding process and the associated difficulties were further discussed by Tonshoff et al. [14]. Tonshoff et al. concurred with Byrne et al. indicating that the moment of friction as well as current variations due to rotational speed changes must be eliminated first before analysing the power signal in grinding. Fixed power demands for a process must also be subtracted from the total process power in order to obtain the cutting power component for further analysis.

Ketteler observed that the amount of power consumed by the spindle motor is not only determined by the torque that is needed by the tool to cut the material, but also by other sources [138]. The main influences on the sensor signal were identified as;

- Tool: tool wear, tool material and geometry
- Cutting process: cutting conditions, coolant
- Workpiece: dimensions, state, failures of cast parts
- Machine tool: friction of the spindle bearings, friction in the gear box, friction in the guideways, efficiency of the motor

Investigations into the efficiency of the motor by Kettler showed that the power consumption of the main spindle motor idling at a constant speed could change by 12%, depending upon whether the machine tool is cold or has already been machining for a certain period of time [138]. As Tonshoff et al. also noted, these variations must be taken into account when analysing spindle motor power signals.

Another factor to take into consideration when inferring cutting force through the use of a power signal is that it is crucial the relationship between input current/power and output force/torque is linear and understood. The performance of current/power sensors can be improved by developing a model of the distortion introduced by the sensor within the mechanical/electro-mechanical system [3].

Another important consideration for motor power and current monitoring is the sensitivity and dynamic bandwidth of the sensor [3]. The bandwidth of the power measurement must be considered as the sampling rate for the current should be high enough to provide meaningful information about the process characteristics. Stein and Wang noted that the bandwidth of the spindle motor servo imposes limiting factors to the combination of spindle speed and number of cutting edges on the tool [139]. This is particularly relevant for tool condition monitoring of milling, as the bandwidth of the

hall effect sensor should be higher than the frequency of the applied cutting force, i.e. the tooth passing frequency, in order to measure the periodic cutting force [121]. Bandwidth frequencies of 60 – 100 Hz have been noted for current measured from feed drive and spindle motors [140, 141]. If the sensor frequency is not high enough to detect a periodic cutting force suitable for tool condition monitoring of individual milling tooth cutters for high spindle speeds it may be still be suitable for helping to maintain a constant material removal rate during machining, as a mean value of the cutting force can be inferred. For example, Kim et al. used spindle motor current measurement for a fuzzy logic control loop where a constant mean cutting force was maintained during milling by adjusting the feed rate in real time for varying depths of cut [142].

Despite the difficulties outlined already with using the motor power signal as an indirect sensor of cutting force, monitoring of spindle power remains one of the least obtrusive and most promising of all the machining process monitoring strategies available for an industrial environment.

2.2.3 Internal machine signal measurement

Monitoring of internal drive signals can be an excellent alternative to measuring power with current probes and voltage clips, as internal machine signals provide the ability to monitor important machine parameters without the use of external sensors.

Recently, Rivero et al. utilized internal machine signals to identify tool wear during the high-speed milling of aerospace aluminium alloy [143]. Experiments were carried out on a high-speed horizontal Fatronik three-axis machining centre with linear motor drives, Fidia numerical control and Simodrive 611 for the spindle control. The spindle had a maximum speed of 24,000 rpm and 27 kW nominal power. Cutting power consumption was measured by the internal current of the motors closed-loop controls at 3 kHz, where the internal current was then converted to voltage outputs by the motor drives and collected using a signal amplifier with a National Instruments DAQ card at a sampling rate of 25 kHz. The voltage was related to cutting forces through a conversion based on the maximum rated voltage of 5 V. Cutting speeds of 1200 m/min and feeds of 5000 mm/min were used with a 16 mm two-tooth carbide milling cutter of 16 mm diameter on aerospace alloy Al 7075-T6. Analysis revealed that cutting power and axial force signals undergo significant variation after milling for an extended period of time due to the effects of tool wear. Therefore the internal machine current signals for the

spindle and z-axis were deemed to be sensitive to tool wear during dry milling of aluminium alloys [143].

Other applications of sensorless monitoring have illustrated the potential for tool failure monitoring during drilling operations [144, 145]. Franco-Gasca et al. performed drilling tests on as cast pearlitic iron, using a CNC Baker-422 drilling machine with 53 mm diameter drills. The current signal was monitored from the servomotor spindle driver using a data acquisition system with an analogue to digital converter with a sampling frequency of 256 Hz. The collected data was processed and a low-pass 8^{th} order filter removed noise components from the data. Drill wear was estimated with high reliability under different drilling conditions using the developed filtering and wavelet transform algorithm for the internal machine current signals.

Kim et al. employed a similar strategy where the spindle load meter within the NC controller of the machine was used to estimate the drilling torque and corresponding drill wear [146]. HSS drills of 4 and 6 mm were used on a mild steel S45C workpiece and progressive flank wear of the drill was consecutively measured with a Nikon tool microscope after a specified number of holes were drilled. During drilling the NC load meter signal during drilling was passed through a low pass filter to eliminate high frequency noise then subsequently sampled at 500 Hz and stored in a cassette for offline analysis. The acquired data was then used to estimate the drilling torque and drill wear, where it was shown that the spindle motor power provided a reliable indication of the onset of drill wear.

Verl et al. investigated the recording of drive variables for the use of prediction of necessary maintenance due to time-related wear and tear in a machine [147]. Tests were performed on a custom machine table comprising of a ball screw drive with a working range of 800 mm. The position signal from servo motors linear and rotary encoders were monitored and the development of wear was identified in the form of positional error in a long term machining test.

Open architecture control & data acquisition

Sensorless monitoring is one of the least intrusive of power monitoring strategies for machining. Open architecture controllers are a modern enabler of sensorless process monitoring by allowing for the collection of machine data via numerical control. The machine controller hierarchy for internal machine signal monitoring of a typical Siemens

numerical control machine tool is described in Figure 2.42. A typical machine tool consists of a panel for the operator known as the human machine interface, or HMI, which can either come in the form of a proprietary panel or a windows pc-based interface. The HMI sits on top of a PLC or NC controller, depending on the make of the machine. In Siemens based control, the HMI usually resides on top of the numerical control, in this case the 840D sl. The NC passes on commands to the drive controllers, which control the state of the drive motors of the machine tool spindles and workpiece axes drives. Siemens equipment communication is based on the Profibus standard protocol.

In order to obtain data directly from the drives such as position, feed, speed and power consumption the controller needs to be 'open'. If the drive is open user variables be set up within the HMI interface for the collection of machine data. The concept of such open control is a relatively recent development, and is referred to as 'open architecture control'.

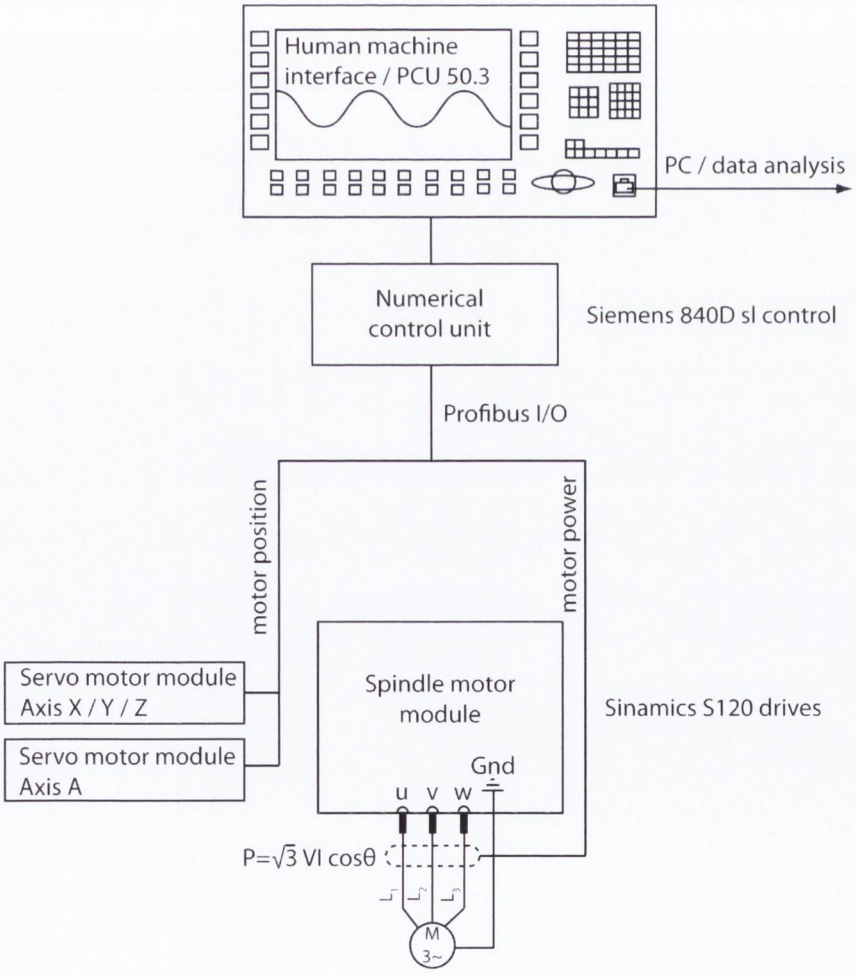


Figure 2.42: Internal machine signal measurement, adapted from [148, 149]

Open architecture control is a concept derived from the flexibility requirement for systems concerning process monitoring and control [150]. Open interfaces and configuration methods are provided in a vendor-neutral, standardized environment and can enable users to design their own controls according to a given configuration [151]. A related benefit of open architecture control is that software developed for open control can be reused and user-specific algorithms can be deployed. In particular, open numeric controls offer an opportunity for getting access to drive and control signals [152]. Drive signals contain information on the mechanical behaviour of the drive chain components; therefore the use of internal machine signals is a reliable and cost effective approach for process monitoring of machining operations [153].

Currently, the majority of available commercial process monitoring and control systems including Prometec, Artis, Comara KG, Montronix and Dittel, systems remain as add-on external hardware modules integrated with the machine tool and utilize Profibus communication [149]. The trend in both commercial solutions and academic research is set to continue towards more flexible software applications that can integrate into the higher HMI level on machine tools [154].

The Siemens 840Dsl is a system-wide open and interconnectable multi-axis digital numerical control system currently found in many modern machine tools [149]. The open nature of the 840D controller has led to research work on monitoring internal drive signals on machine tools with Siemens control.

An example of a structure for remote monitoring of a Hermle C600U milling machine with a Siemens Sinumerik 840D controller is described by da Silva et al. [155]. Machine data including axes position was collected through a data acquisition system consisting of a Siemens PCI board CP5611, internet server and data acquisition software developed in C++. Whilst the research described by da Silva et al. focuses on remote web-based monitoring of the overall machine condition, nonetheless it illustrates a feasible way of extracting machine data from a Siemens control.

Hardware Tracing on Siemens 840D control

A proprietary solution that can be used for hardware tracing on modern Siemens 840D control is the SinuCom NC Trace tool. The SinuCom NC Trace tool forms part of a commissioning tools bundle for the 840D controller [156]. It is interesting to note

there are similar trace systems available for other modern numerical controls including the Cycle Time Analyzer by Bosch, TNCscope by Heidenhain and OPC. Perhaps underutilized as a basic commissioning tool for machine builders, NC Trace for Siemens 840D control has only recently been discovered as a useful tool for researchers in process monitoring. NC Trace provides the ability to record internal control data in interpolation cycle time or control loop cycle time of typically 1.5 ms. Furthermore, the tool has the ability to trace OPC data with a cycle time of approximately 100 ms, depending on the number of selected trace values. The signals of importance for process monitoring and analysis are: time, axis positions, spindle and drive power, velocities, acceleration and jerk of the axes, and velocity of the tool centre point and the current of the drives. In addition to process raw data, the trace tool can also record the command line of the NC program that is active when the trace data is acquired [157, 158]. The ability to monitor machine variables directly from the controller without any additional hardware presents an opportunity for a process monitoring strategy and software developed through research that can feasibly be transitioned directly to an industrial machining application.

An adaptive logging module for process monitoring utilizing the NC trace tool to monitor control digital drive signals was designed by Brecher and Rudolf [159]. Signals acquired through the NC Trace module for tool wear monitoring included feed drive speed and position, feed drive current, main spindle rotational speed and main spindle current with a typical sample rate of two milliseconds. However, before the data was analysed to detect the state of tool wear, the disturbance effects of friction and acceleration in the machine drives were first eliminated. As mentioned by Byrne et al. [5] disturbances, especially friction component in guideways may be contained in the measured signal, and if possible they should be eliminated before obtaining meaningful data from the signal. In the adaptive logging module the frictional and acceleration effect was compensated for through the use of friction field models and analysis of the control loop. Tool wear could then be identified through the increasing amplitude of the torque generating moment [159]. The compensation for friction in the guideways is perhaps more relevant for monitoring of the current of feed drives where the change in amplitude of current is small relative to process disturbances such as tool wear. To obtain meaningful data from spindle power the basic fixed power demand for idling or

air cut power is subtracted from the total recorded power, thus providing the power due to cutting alone which can be used for analysis of the process.

Brecher and Rudolf applied the concept of monitoring of digital drive signals through development of an application for the Siemens HMI based on an artificial neural network for surface roughness average parameter (Ra) predictions [15]. The machine tool used was a three-axis vertical EmcoMill E900 with Siemens 840Dsl numerical control. Internal machine signals were recorded using Siemens SinuCom NC Trace. C45 steel was milled within +/-20 % of a spindle speed of 2018 rpm, cutting speed of 265 m/min and axial depth of cut of 1 mm. An example of recorded digital drive signals recorded at a sample rate of 2 ms is illustrated in Figure 2.43. On the left-hand side, the torque-generating current signals of the feed drive axis and the main spindle are shown while the right-hand side represent the position signals and the rotational speed. A HMI GUI was developed in order to facilitate the interaction between the operator and the NC kernel. Surface roughness was estimated based upon the recorded digital drive signals, where it was noted that an increase of the material removal rate of 20% could be achieved with optimised process parameters as calculated by the artificial neural network.

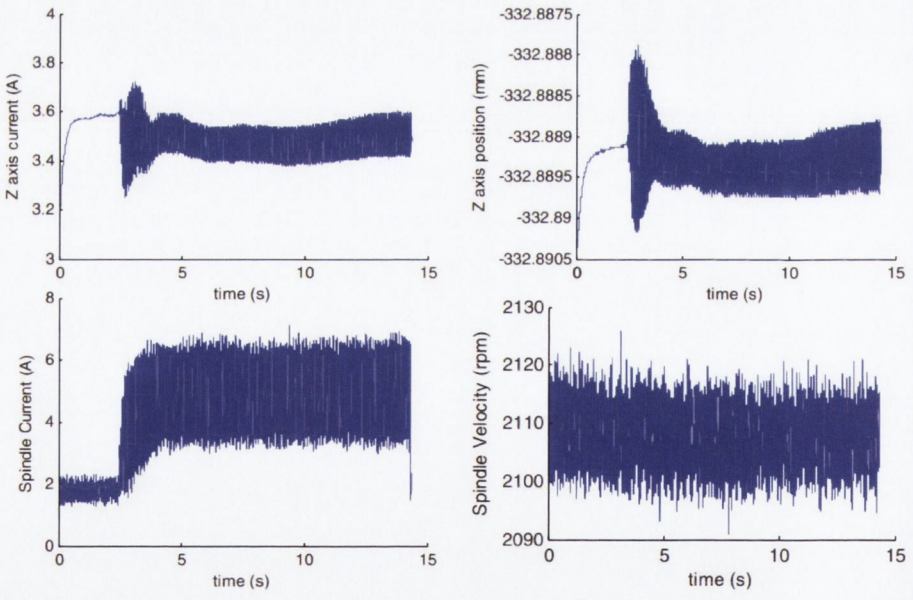


Figure 2.43: Digital drive signals obtained from NCU kernel for z axis and main spindle [15]

The capabilities of NC kernel data and external sensor data captured with piezoelectric accelerometers were compared in similar work by Quintana et al. for indirect evaluation of surface roughness in vertical milling operations using the same

experimental setup described previously by Brecher and Rudolf [15, 160, 161]. Vibration was monitored during the experiments with two unidirectional piezoelectric accelerometers placed following the machine tool X and Y axes directions with one residing in the spindle and the other on the machine tool table. Internal machine signals of current, position and velocity for the spindle and feed drives were monitored through SinuCom NC Trace. The internal machine signal data for surface roughness prediction through artificial neural networks was shown to be clearly reliable as well as a convenient approach for sensorless process monitoring. The results presented a slightly higher correlation factor in the case of the data acquired from the internal machine signals of R=0.95947 than with a neural network using accelerometer data of R=0.94353.

Additionally, it was noted that accelerometers must be installed in a fixed place on the machine tool and the signal can be affected by several levels of noise or dissipation due to the varying distance between the point of origin of the vibration and the point where the vibration is captured. In comparison, the control drive's internal data signals are digitalized and pre-processed in the numerical kernel control and power amplifier and evaluation of the signal is based on the mean value of the digital drive signals, therefore the influences of noise are decreased to a minimum for the internal drive signals. Furthermore, while the internal machine current signals are measured directly at the drives this is still not at the cutting tool interface so it should be taken into account that it is possible for friction of the guideways in the drives to affect the signal, as described previously by Brecher and Rudolf [15].

Brecher and Rudolf concluded that monitoring of internal machine signals has proven to be just as effective as the use of external accelerometer sensors and as a result is a significantly more time-effective, flexible and cost effective solution for process monitoring as shown in this application and potentially in many other machining applications.

2.2.4 Position-oriented analysis

The alternating machining conditions during the machining of freeform surfaces can make determination of machining characteristics extremely difficult. Correlation of process power and forces with tool position can provide a positional dependent analysis of the process characteristics. This can assist in determination of the root cause of

process disturbances thus improving the monitoring abilities in a freeform grinding process.

De Lacalle et al. investigated the correlation between cutting forces and their actual point of generation during the machining process [162]. High speed milling was used in the manufacturing of molds of hardened steel. Slender tools were used due to the high depth and low fillet radii of the cavities. Cutting forces therefore produced tool deflection in this case and as a result deviations in the tolerances of the machined part were generated. A three component quartz dynamometer Kistler 9255B was used during tests. The positions of the three axes of the CNC machine tool were collected from the internal programmable controller (iPLC) using an analog/digital data acquisition board controlled through Labview with a sampling frequency of 208 kHz per channel. Position and force data were correlated and matched within a 20 ms time window where for a given point in x, y and z the corresponding maximum value of Fx, Fy and Fz are taken within a 20 ms time window of the recorded position.

Figure 2.44 shows an example of a stamping die for a car body component where the same experimental setup used in [162] was used in further work by de Lacalle et al. in order to measure the positional and cutting force information during machining [163]. The post-processed result of the cutting forces are illustrated, where the colour map shown is the cutting force component including the maximum Fy value given as a function of position (up), and (down) two vector graphs (Fx,Fy,Fz). De Lacalle noted that some conclusions could be drawn from this analysis including; the cutting force was very stable, and was highly dependent on the slope of the workpiece. Also, while in zone A, a higher value of the force was observed to correspond with an excess of material left by the semi-finishing operation. De Lacalle observed that the position-oriented approach generates more information than classical linear-machining tests in which forces are only recorded as a function of time which therefore lose their relation with the part geometry. This approach is particularly useful in attributing the cause of process disturbances to machining conditions encountered during the process. A force dynamometer was also used in the demonstrated approach, however de Lacelle pointed out that this method could be easily adapted to internal machine signal monitoring where the spindle current consumption could be collected instead of cutting forces.

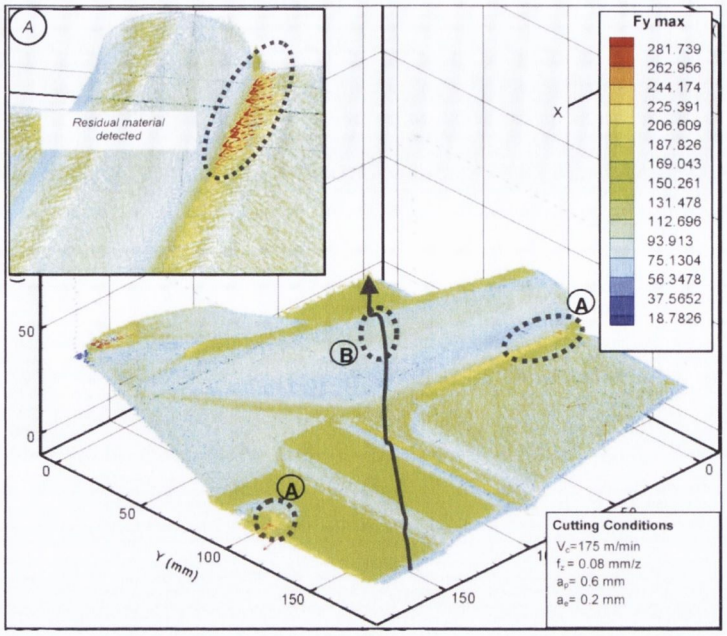


Figure 2.44: Real cutting force map of the superfinishing operation of a stamping die (GGG70L), while the zoomed area (A) shows the increase in forces due to residual material on the die [163]

De Lacalle et al. investigated further application of the force and position monitoring solution for optimization of surface quality through adaptation of toolpath and cutter orientation [164]. An 8 mm diameter ball-endmill was used for milling of a freeform surface comprised of hardened tool steel. Cutting parameters of 6000 rpm and a feed rate of 600 m/min were used. Cutting forces were measured with a Kistler dynamometer, while the tool axes position was measured through a data acquisition device on the machine as described in [163]. Dimensional errors of the workpiece were measured using a coordinate measurement machine. The toolpath was varied with different inclinations and directions as illustrated in the last row in Figure 2.45. Test 1 was a conventional toolpath, while Test 2 was a basic application of a toolpath based on a three axis cutting force estimation model, Test 3 was the same toolpath however with more control points, and Test 4 was a five axis milling toolpath based on the cutting force estimate toolpath. Results are shown in Figure 2.45 where Test 3 provided the highest accuracy with errors under 10 μm in most of the milled areas. Deflection force was also observed to be at a minimum with the toolpath used in Test 3. The findings by de Lacalle et al. illustrate the application of position oriented monitoring for evaluation of process characteristics and cutting conditions for adapted toolpath strategies.

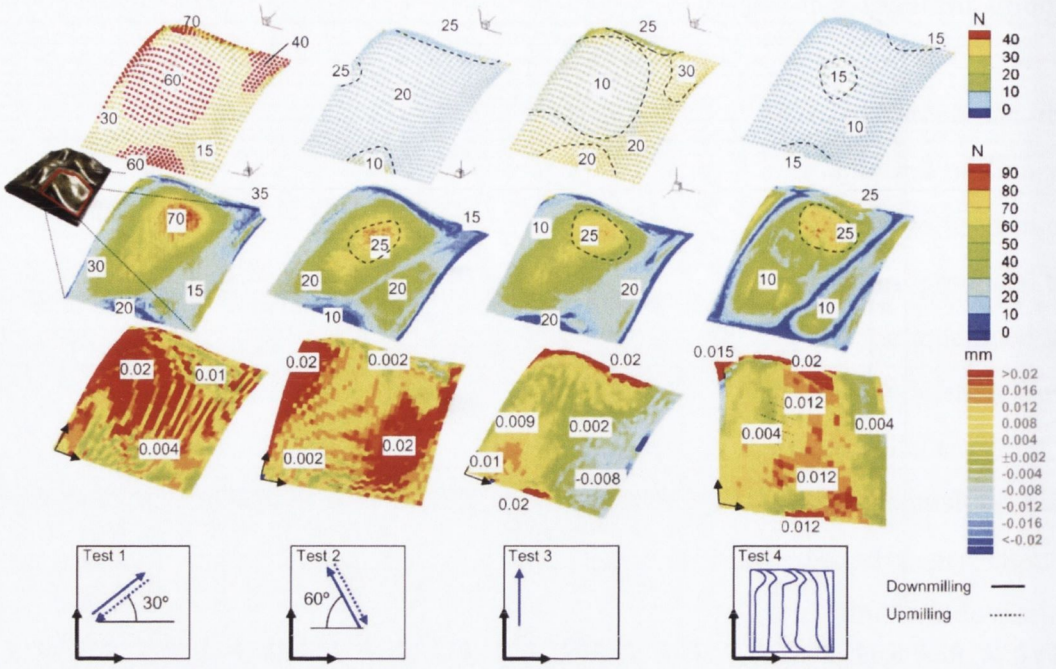


Figure 2.45: (Top) Predicted deflection forces, (Centre) Measured deflection forces, (Bottom) Dimensional errors measured in a CMM [164]

Position orientated analysis of cutting forces has also been investigated by Klocke et al. during freeform milling of an impeller blade [16, 165]. Position information was acquired from a Chiron FZ15 machine centre equipped with a phase-shifted sinusoidal encoder. Signals from the rotary encoder were converted using an interpolation unit to transistor transistor logic (TTL), then de-noised using an opto-coupler and the final signal acquired with a National Instruments PCI 6602 counter card. The measurement chain used to quantify process forces consisted of a stationary three-component dynamometer Kistler 9255B mounted onto the machine table, along with a rotary force dynamometer Kistler 9123C applied to measure the tool forces. Signals from the force dynamometer were conditioned to output voltage signals of +/-10 V and acquired via a National Instruments DAQ card. Force platform dynamometer, rotary force dynamometer and machine position signals were correlated based upon calculating the time delay between each of the signals based on values for signal conversion and transmission delays, with a 21.7 % delay shift of one spindle revolution observed. The positional measurement accuracy was also verified to within 0.004 mm. Forces during surface finishing of an impeller's blade were then examined using position-orientated process monitoring. During the finishing process a signal anomaly of the resultant force was observed after approximately 25 seconds of machining and this is illustrated in

Figure 2.46. The increase in forces at this point can be attributed to the tool's changeover to the backside of a blade, due to the thin-walled configuration of the blade. Reaching the leading edge; the tool initiates vibrations into the work piece, which results in the observed increase in the force measurement. Klocke et al. observed that as the evidence of the demonstrated signal anomaly is strongly position-related, this application illustrates the potential for position-oriented analysis of signals in freeform machining where workpieces and processes can be analysed towards anomalies and disturbances in consideration to their origin.

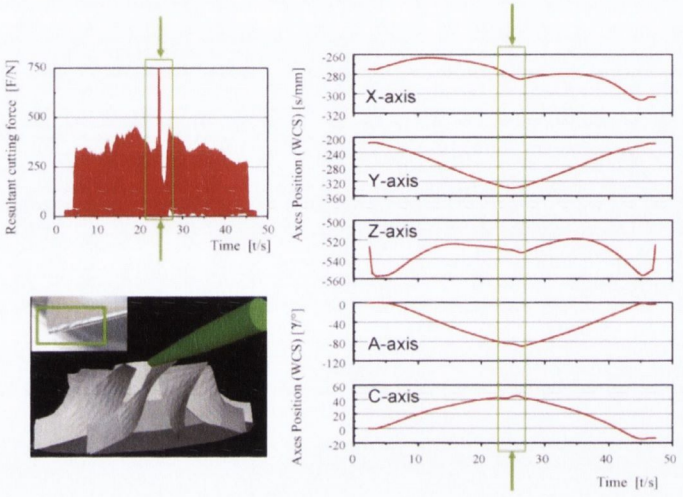
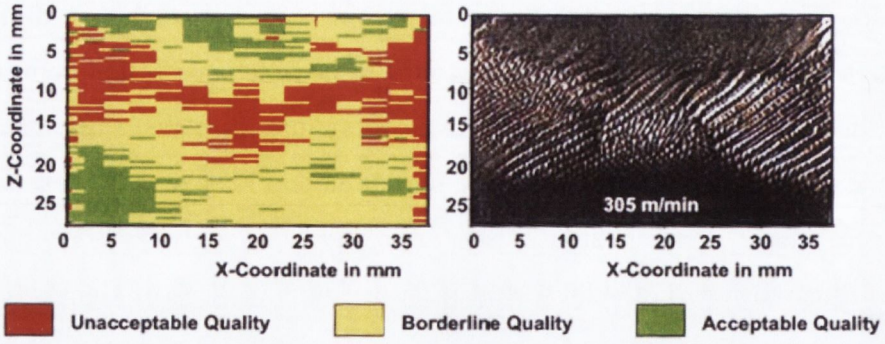


Figure 2.46: Position orientated monitoring during finishing of an impeller blade [16]

More recently, Kratz has explored position-oriented monitoring of vibrations during finish milling of thin-walled components [94, 106]. Accelerometers were based on the spindle housing and the resulting vibration signals were analysed with a joint time frequency map method developed by Kratz. The frequency map method is calculated by determining joint time frequency analysis of each machined line parallel to the x-direction, then extracting the amplitude value of the specified frequency in combination with the positional information of each FFT and charting this information in the parts coordinate system. A result of a sample finishing operation for machining of a thin-walled, 36mm overhanging cantilever is shown in Figure 2.47, where each line of cut's frequency content has been analysed in segments and rated based upon the frequency content with status set red yellow or green according to the processes stability.



Trial parameter	
Work piece: Material, Width, Height, Thickness in mm	TiAl6V4, 40, 36, 2
Tool: Type, Diameter d in mm, Number of teeth n	Tapped Ball, 10, 8
Cutting speed in m/min	140, 260, 305
Feed rate in mm/tooth, Depth of cut a_e, Width of cut a_p in mm	0.0125, 0.1, 0.4
Lead angle β_f, Tilt angle β_{fn} in deg	0, 80

Figure 2.47: Validation of monitoring solution algorithm [106]

Process instability highlighted in red on the left of Figure 2.47 corresponds to the dimensional deviation on the part shown on the right. This analysis shows that amplitudes of certain frequencies are assignable to resulting dimensional deviations and the surface roughness of the thin-walled component. A limitation of this approach however, is the requirement for accelerometers, which while integrated into the spindle housing still require modification to the machine structure as well as improved cross-correlation between recorded sensor signals for freeform machining.

2.2.5 Laser displacement measurement

Freeform surfaces with a complex geometry have been recognised as important design forms for modern components. Examples of freeform shapes found in industry include airplane wings and fuselage, optical parts and mirrors, car body parts including stamping dies, as well as turbine blades, impellers and blisks. Freeform parts are considered to be advanced surfaces, and may have no axes of rotation or translational symmetries. The geometry of freeform surfaces cannot be described by a single universal equation, as is the case for a spherical surface, but require a myriad of equations including toroidal, biconic and microstructures as well as NURBS [166].

Inspection of free-form surfaces has traditionally involved skilled technical personnel who inspect the surface using a number of mechanical gauges and templates. This is still common practise in industry for certain stages of inspection during the

process where the use of go/no-go gauges is common practise [167]. There is considerable scope for improvement and automation of inspection methods in industry which could eliminate the need for manual inspection while introducing a robust form of traceability into the process.

In a recent CIRP keynote paper Savio et al. describe the state of the art in metrology of freeform shaped parts [17]. Currently, the most important general-purpose instrument for the inspection and dimensional verification of freeform shapes in industry is the Coordinate Measuring Machine (CMM), due to the CMM's flexibility and high accuracy for measuring different shaped parts. CMM's can be equipped with both contact and non-contact probes. Contact probes are the most commonly used systems and acquire detailed dimensional data by moving a sensing probe device along the work-piece surface. Scanning probing systems are preferred over touch trigger systems as they provide a continuous deflection output that can be combined with the machine position to derive the location of the surface. Optical CMM-based probes are also gaining acceptance in industry, with their advantages including the non-contact nature of the measurement system where the dangers of surface damage associated with contact metrology are avoided, the fast acquisition rate for large numbers of points, and the high degree of associated flexibility with measurement settings. Optical probing systems comprise of distance triangulation sensors that can be classified into three basic types, depending on the number and position of points that are measured at the same time: point sensors, line or stripe sensors, and area sensors. Examples of commercially available non-contact laser measurement probes include Nikon Metrology CMM-based laser scanners as well as Faro laser robotic arm scanners.

Laser scanning is achieved through the principle of laser triangulation [168]. The main components of a triangulation sensor are a collimated light source, generally a laser diode, and a detector unit consisting of an imaging lens and a position-sensitive detector, either a CCD line or position- sensitive diode (PSD), as illustrated Figure 2.48. The optical axes of the light source and the imaging lens form a fixed angle, the so-called triangulation angle. Triangulation refers to the measurement of distance through calculation of the triangulation angle. In laser measurement the laser diode projects a laser spot onto the object to be measured. The object surface is positioned sufficiently close to the point in which both the light source and imaging lens axes intersect and the diffuse reflection of the light spot on the workpiece surface is imaged onto the detector.

Distance to the measurement object is calculated by the sensor through the position of the light spot on the detector and from the distance of the transmitter to the receiving element. Typical measurement ranges for triangulation-based sensors are 2 mm to 200 mm; while resolutions up to 10^{-4} mm can be achieved.

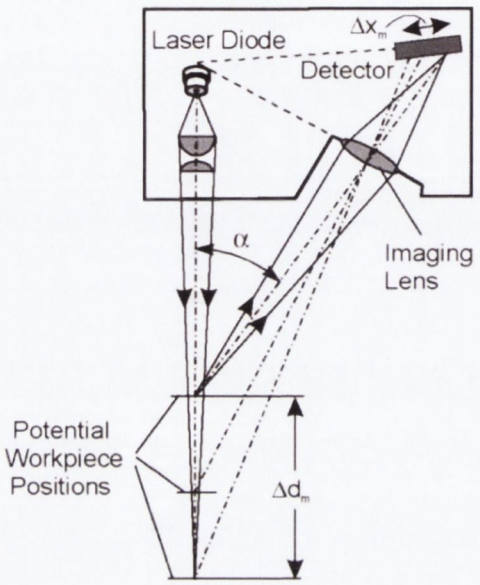


Figure 2.48: Principle of the laser triangulation sensor [168]

The main source of error for laser measurement tends to be related to the optical characteristic of the workpiece surface where very smooth surfaces can provide insufficient diffusely reflected light. However, this error can be compensated for by controlling the laser intensity and the sensitivity of the detector. Other common errors can be induced by the slope of the surface which can produce direct reflections to the detector, volume scattering particularly for plastic material, an inhomogeneous surface texture, specular reflections or ridges left by machining [17, 168].

Laser measurement data analysis methods

There are a number of steps that must be performed before evaluation of acquired laser measurements for freeform surfaces is possible and these are stated in Figure 2.49. Filtering of the data may be necessary if there is considerable noise present in the signal dependent on the acquisition device used. Registration of the acquired point clouds is usually necessary for laser measurements of freeform surfaces as the measured part

coordinates typically do not match exactly with the coordinates of the part with which the measurements are to be compared to. The part for comparison can take the form of a CAD model or a second point cloud of another or the same part pre- or post-machining. Coarse alignment refers to matching of the point clouds through coordinate transformation and/or basic alignment based on surface feature matching.

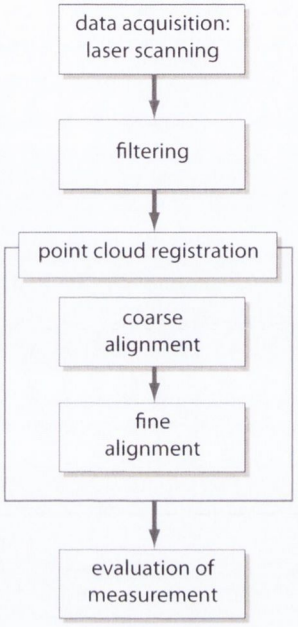


Figure 2.49: Overall laser measurement and analysis strategy, adapted from [17]

method commonly used for further fine alignment registration is the Iterative Closest Point (ICP) algorithm [167, 169, 170]. The algorithm works through calculation first of the closest Euclidean distance between each corresponding point. A transformation matrix that minimizes the sum of square errors between the measurement point set and the correspondent set is then calculated. The transformation matrix is then applied, and the first step repeated and the algorithm iterated until the objective value decreases to less than the threshold value.

An efficient method of implementing the ICP algorithm is through the use of kD-tree searching. A k-Dimensional tree is a way of organising many points such that they can be efficiently searched through in order to determine, for example, the nearest neighbours of points. Each node on the k-D tree contains a multidimensional point with N coordinates and also has an axis member which defines the split plane dimension. Each node also has a Left and Right neighbour and Parent link as illustrated in Figure 2.50.

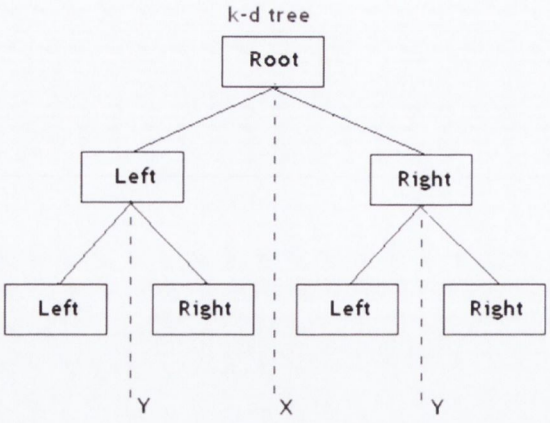


Figure 2.50: Illustration of kD-tree algorithm [171]

The split dimensions are rotated from the first to the N-th, or 3rd in this case, meaning that the nodes from the first level of the tree are split to left and right with respect to the first dimension, x, the second level with respect to the second dimension ,y, and the third level with respect to the third dimension. When the N-th level is reached the split plane index is set again to zero. For example, for a 2D space with points x and y, if x_node < x_parent, the node is placed to the left, otherwise the node is placed to the right. For the second level the only difference is that the split plane is y, if node_y < parent_y the node is placed to left otherwise it is placed to the right [171]. Once the kD tree is built the data can be searched for the multidimensional nearest neighbour using the minimum Euclidean distance between points.

If two point clouds of X-Y-Z data are to be compared by selecting similar curves from each dataset, it is important that they lie on the same plane so that they can be compared accurately. If the 3D curves which have been projected onto the same plane are then rotated to a 2D plane, then the difference between the two curves can be calculated easily. Principal component analysis (PCA) has been widely used in system identification and dimensionality reduction in dynamic systems. The technique has been used previously to extract features from multiple sensory signals treated as a high-dimensional multivariate random matrix, composed of several vectors formed by the signals [3]. This was used in the identification of tool wear in broaching from two perpendicular cutting force signals [172]. Principal component analysis identifies the most influential similarities or differences in a given data set. The method involves first calculating the mean of the data set, then subtracting the mean to centre the data. The covariance matrix must then be calculated; where the covariance is a measure of how

much the dimensions vary from the mean with respect to each other. The eigenvectors and eigenvalues of the covariance matrix are then calculated and analysed, where the eigenvector with the highest eigenvalue is the principle component of the data set [173]. The Matlab princomp() function returns the principal components for a given data set, where the first two define vectors that form a basis for the plane of best fit [174]. The data set can then be projected onto this plane by multiplying by the principal component transformation matrix.

Laser measurements of freeform components are typically evaluated by calculation of the deviations from the nominal or comparison model. An example of a map of deviations calculated from measurements for a femoral implant is illustrated in Figure 2.51, where the material removed from machining is clearly illustrated.

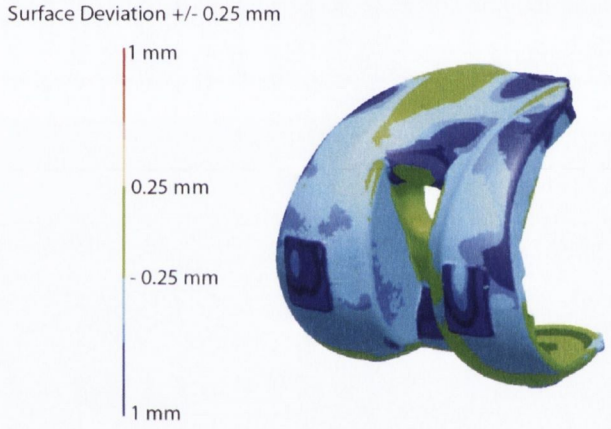


Figure 2.51: Example of map of deviations for laser scan comparison of femoral implant casting and post-machined, measured with a Metris LC-60D CMM based laser scan head [175]

Martinez et al. compared contact and non-contact laser scanning methods for dimensional measurement to determine if both methods could produce the same reliable results [176]. A TP20 Renishaw touch-trigger probe with a 2 mm tip diameter was compared against the performance of a LC50 Metris laser scanner system; a line scanning triangulation sensor capable of capturing a line segment of approximately 750 digitized points. Both systems were mounted on the same Brown & Sharpe global CMM base. Martinez et al. found that both measurement methods produced similar results with deviations found in the range of 7 – 15 μm for laser and touch probe results. More recently, Besic et al. compared the two measurement methods investigated first by Martinez et al. of a touch-trigger contact probe and optical laser sensor. A filtering

technique applied to the laser point cloud to remove noise from the data was noted to further improve the measurement results for the Metris LC50 laser scanner, with measurement errors below 7 μm for flatness, and 6 μm for parallelism observed for the filtered data [177].

While it has been noted that CMM-based laser scanners can provide comparable accuracy and resolution to that of traditional touch-probe techniques, one of the main drawbacks of measurement with a CMM is that the part must be first carefully placed, then held stationary during inspection, and inspection time can also be relatively slow. Another drawback for measurement using CMM's is the lack of potential for integration into an automated process chain due to the fact that CMM's are typically large and expensive machines.

Laser measurement with CMM-based laser scan heads also typically involves substantial human involvement in laser scan path planning and selection of measurement settings [167]. Such processes are not cost effective and lack flexibility. While automated solutions are being investigated for laser scanning path planning there is still a need for a fully automated inspection solution that is flexible enough to be integrated into a production process and can replace the need for manual gauge inspection.

Alternatives to CMM based laser measurement systems are currently being researched. One such example is a novel vision system designed by Brosed et al. which consists of a laser triangulation sensor with a motorised stage for inspection of complex geometry parts [178]. Results for repeatability and accuracy were compared for the robotic arm. A CMM using a heat exchanger as a reference part with several elements to be verified set in various positions and orientations. Repeatability errors for the robot arm laser system were found to be in the range of 20 to 75 μm in the worst of cases, indicating significant potential for the use of a robot arm non-contact inspection system particularly suitable for geometry that is difficult to reach with conventional probe CMM systems.

Another example of robotic-based laser measurement was used for determination of the volume and position of material to be removed for robotic belt grinding process for aero engine blades [179]. In order to choose optimum machining parameters it is useful to know the material that must be removed from a workpiece. A 3D scanning system with an ABB robotic arm fitted with a RobotScan H-200 laser scanner was

tested for this purpose. Laser measurements were performed on the semi-finished blade ready for robotic belt grinding. The point cloud data was then registered and compared to the CAD design model through an iterative closest point (ICP) algorithm. The material to be removed from the semi-finished blade by the following belt grinding process could then be determined through calculation of the Euclidean distance between the design model and the semi-finished blade laser scan around the surface of the blade.

There is considerable potential in applying laser measurement to inspection of freeform surfaces, as well as for assisting in the determination of the varying material removed over the surface of the femoral implant from abrasive machining. If this quantity can be determined optimisation of the abrasive machining process is then possible, as without knowledge of the material removal and machining characteristics effective process monitoring and optimisation cannot be achieved.

2.3 Summary and context

The manufacture of high value components with complex, freeform surfaces entails considerable cost through time, energy and material consumption. Achieving efficiency of such machining processes is important in order to ensure long term competitiveness and economic sustainability. Efficiency of the abrasive machining process through increases of material removal rates can only be achieved if a suitable process monitoring platform is available in order to fully understand the underlying process characteristics so that surface integrity of the workpiece can be maintained [66, 68].

Advances in sensors and machine numerical control enable process monitoring of machining operations through monitoring of internal machine signals including position and process power [3]. However, as this is a relatively recent development only a limited amount of research has been performed surrounding the sensitivity and potential of the signals for application in high performance machining operations [15, 159, 161].

A position-oriented evaluation of sensor signals has been noted to be of benefit in evaluation of the process behaviour as process anomalies can be attributed to their root cause during machining [16, 94]. A new area of research with considerable potential for application in an industrial setting is in using position oriented monitoring in conjunction with internal machine signal monitoring applied to freeform machining.

Usually in order to fully understand machining characteristics the volume and location of material removed in the process must first be known. Offset toolpaths are

used for machining freeform surfaces and so the depth of cut during the process is unknown. Laser measurement is gaining importance as a viable inspection method for freeform surfaces [17, 168]. However there are few papers published in using laser measurement to determine the quantity of material removed during a process, and few solutions available that are flexible enough to allow for future integration into a process monitoring chain.

Authors have acknowledged that alternating machining characteristics can arise as a result of the complex contact conditions during grinding of freeform surfaces with toric shape wheels [23]. Previous work on the modelling of engagement conditions during grinding with toric wheels has featured known depths of cut and has focused mainly on the prediction of surface roughness and process forces [11, 32, 36]. Estimating tool-workpiece engagement based on real measurements of material removal and power during the process could provide significant insights into process behaviour during grinding of freeform surfaces with toric grinding wheels and indicate ways of improving process efficiency.

Chapter 3

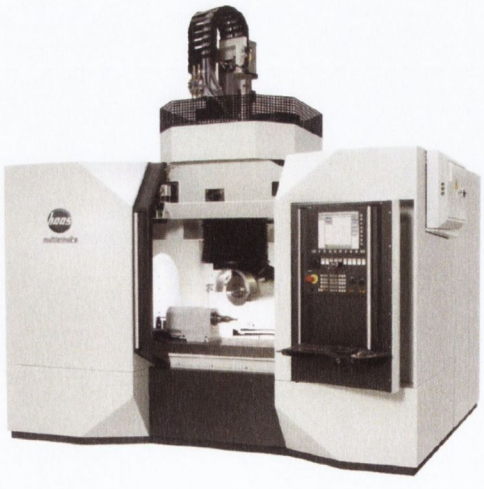
Experimental methodology

In this chapter the workpiece material, test specimens, tooling, machining equipment and experimental and process monitoring protocols are described.

3.1 Machine tool

3.1.1 Machine description

The Haas Multigrind CB is a 5-axis CNC machine tool used for grinding and milling in specialised sectors such as biomedical devices. The high powered spindle has a variable speed of up to 10,000 rpm for milling, and 8,000 rpm for grinding, with a corresponding maximum feed speed of 30 m/min. The spindle is a two-end spindle, with the maximum power rating for both spindle ends at 29 kW. The machine is fitted with a custom fixturing unit for holding femoral implants. A full specification of the machine is shown in Figure 3.1.



Multigrind CB Technical Data	
Grinding Spindle - Two Ends	
Reccommended continuous power rating	23 kW
Maximum power rating	29 kW
Rotation speed standard	8000 rpm
Travel	
X-axis	700 mm
Y-axis	410 mm
Z-axis	500 mm
A-axis	320°
Accuracy/Feed rates	
Linear axis resolution	0.0005 mm
Feed rate linear	30,000 mm
Rotary axis resolution	0.001°
Feed rate rotart A axis	2600 rpm
Control	
Siemens Sinumerik	840 Dsl

Figure 3.1: Haas multigrind CB 5-axis machine [Source: Haas Multigrind]

3.1.2 Machine-side data acquisition

The Multigrind CB used in this research was equipped with a Siemens 840D sl numeric control. Siemens Sinucom NC software was installed during machining commissioning at HAAS Schleifmaschinen GmbH in Germany in order to interface with the numeric control. The Siemens 840D sl numeric control system provides direct or indirect access to drive data such as torque-generating currents and power signals or position. This signal information can be acquired synchronously to the interpolation cycle time, servo controller loop cycle time. The Sinucom Trace software installed on the Human Machine Interface (HMI) enables acquisition and logging of control data and drive signals with a real time connection to the Siemens 840D sl controller as shown in Figure 3.2.

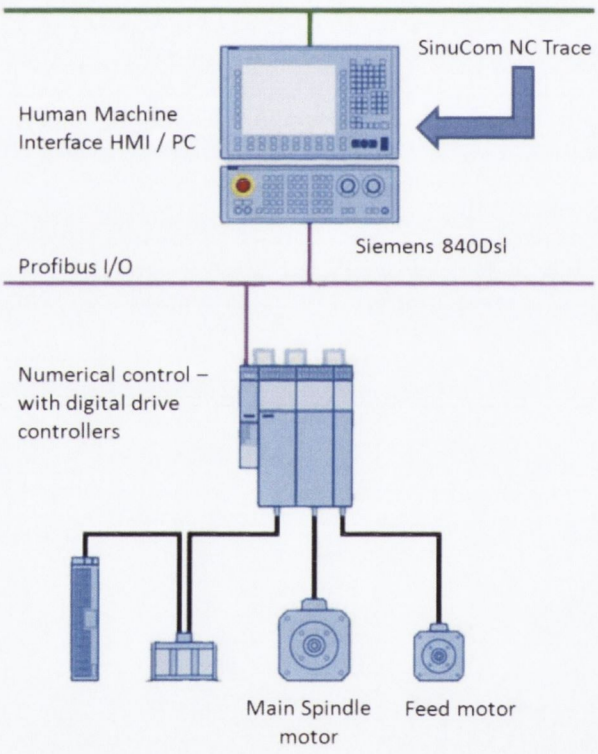


Figure 3.2: Siemens 840D schematic, adapted from [156]

Machine and servo data variables for the monitoring of active power in Watts, current in Amps and tool base position in inches were all monitored from the Siemens Sinucom Trace software for the purposes of this research. Variables monitored and their definitions are listed in Table 3.1. Active power is the power as defined by Equation

3.1, which takes into account the power factor and the actual line current and voltages, and is the power responsible for doing work in the process.

Variable Name	Description	Units
nckServoDataActPower32	Active power actual value, monitored for machining spindle and axes drives	Watts
nckServoDataActCurr32	Torque-generating current actual value, monitored for machining spindle and axes drives	Amps
actToolBasePos	Tool-base position, monitored for axis drives X,Y,Z and A	Inches (subsequently converted to Metric mm)

Table 3.1: Siemens 840D sl machine variables and Sinamics S120 servo variables

$$P = \sqrt{3}VI\cos\theta \tag{3.1}$$

The sample rate used in this research was the maximum available at 333 Hz, with a sampling interval of approximately 3ms which corresponds to the position controller loop cycle time. An example of a digital drive active power signal recorded from Sinucom Trace is shown in Figure 3.3. The spindle was rotated at 8,000 rpm with machining parameters of 0.5 mm depth of cut and 59 mm/s feed rate for flat surface grinding of Cobalt Chrome alloy.

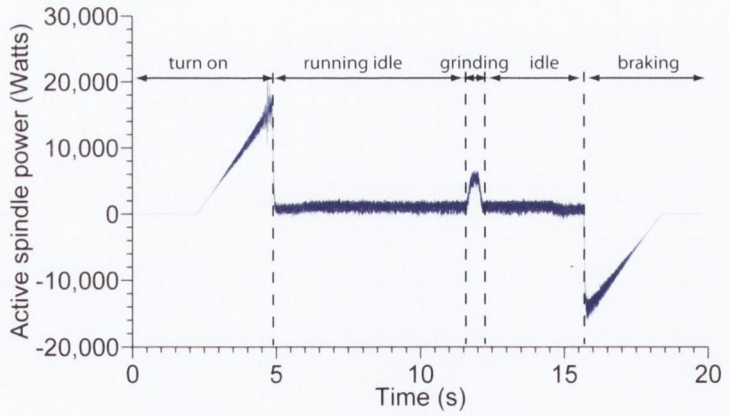


Figure 3.3: Active power signal recorded from the main spindle for flat surface grinding

When material removal is monitored using active power as the metric, a point either side of where material removal takes place is selected, for example in Figure 3.3 either side of the region denoted by material removal or grinding. The mean of this region is then calculated and used as the active total power value for the corresponding test. In order to calculate the power required for material removal alone, the power

drawn without material removal, also known as an air cut, as illustrated by the spindle running idle in Figure 3.3, is subtracted from the total active power reading, P, as given by Equation 3.2.

$$P = P_{total} - P_{air\ cut} \tag{3.2}$$

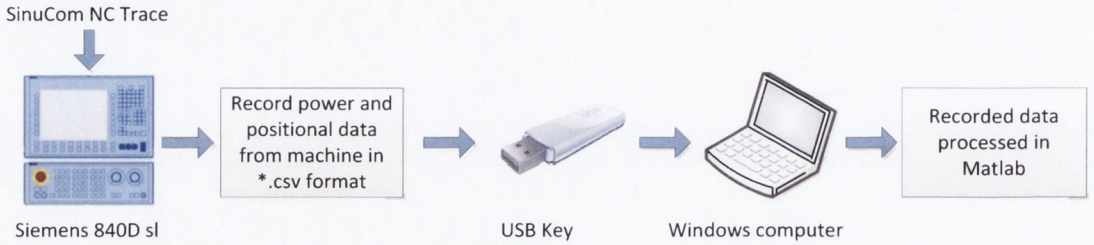


Figure 3.4: Internal machine signal data acquisition chain

Data was recorded from the Sinucom Trace software in the form of *.csv files as illustrated in Figure 3.4. The files were stored on the machine pc during testing, and were subsequently downloaded via usb key after the tests were finished. Each csv file was opened in Microsoft Excel 2010, the file header was deleted, variables were renamed and then saved as a standard text file (*.txt). Each text file was then imported into Matlab where the data was subsequently processed.

3.1.3 Tooling: Electroplated CBN wheel

The wheels used in this research were electroplated CBN contoured wheels on a steel body and were produced by Günter Effgen GmbH. The CBN grit size in all cases was B301, which is the CBN designation for a grit size of approximately 301 μm. The wheels had a major radius of 100 mm with a minor contoured radius of 12 mm. Figure 3.5 and Figure 3.6 show the wheel and its dimensions. The presence of the 12 mm contour radius is to enable the wheel to machine femoral implant profiles. The electroplated CBN coating covered the 12 mm radiused sides with a surplus 1 mm on each side. Wheels were balanced in the machine with the assistance of a Dittel M600 balancing module and counterbalance weights.

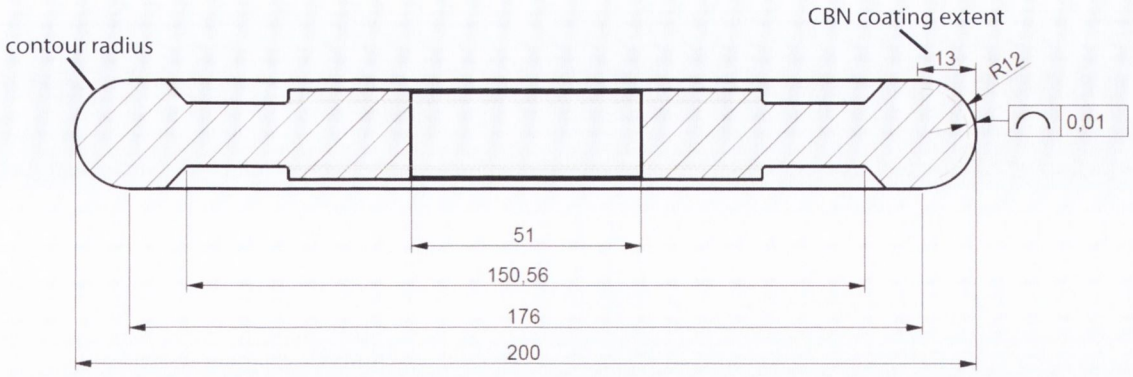


Figure 3.5: Effgen electroplated CBN B301 wheel with contoured radius of 12mm and full wheel diameter of 200mm

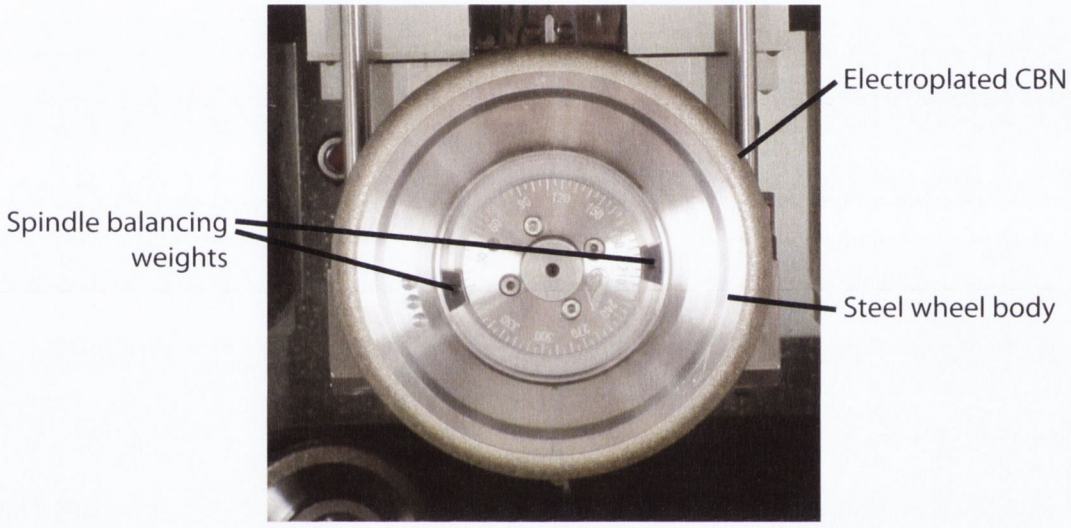


Figure 3.6: Electroplated CBN B301 wheel in place in machine with counter-balance weights

Oil-based cutting fluid was applied through high-pressure 20 bar 1 mm diameter nozzles surrounding the spindle and rotary axis. A Henkel oil, Multan CR10, was used for coolant in this research. The coolant oil had a boiling point of 260°C [180].

3.2 Workpiece materials

3.2.1 Workpiece characterisation: Cobalt Chrome alloy

Cobalt Chrome alloy is widely used in the orthopaedic implant industry for both femoral components and tibial trays. Typically the alloy comprises of a high percentage of Cobalt, Chromium in combination with Molybendum and Carbon resulting in an alloy with high strength, hardness, elastic modulus and wear resistance. Cobalt Chrome alloy also has a high resistance to corrosion due to its chromium and molybdenum

content [10, 181]. The standard Cobalt Chrome alloy used in investment casting of biomedical implants is designated as ASTM F75, and comprises of 27 – 30% Chromium, 5 – 7% Molybdenum and 0.35% Carbon [182].

Implant Alloy	ASTM Designation	Elastic Modulus (GPa)	Yield Strength (MPa)	Ultimate Strength (MPa)	Fatigue Strength (MPa)	Hardness (Vickers Hardness)	Elongation at Fracture (%)
Stainless steel							
	ASTM F138	190	792	930	241-820	130-180	43-45
CoCrMo alloys							
	ASTM F75	210-253	448-841	655-1277	207-950	300-400	4-14
	ASTM F90	210	448-1606	1896	586-1220	300-400	10-22
Ti alloys							
Ti-6Al-4V	ASTM 136	116	897-1034	965-1103	620-689	310	8
cpTi	ASTM F67	110	485	760	300	120-200	14-18

Table 3.2: Material properties of biomedical alloys [181]

The properties of the alloy are described in Table 3.2. Commonly used commercial/proprietary names to describe this alloy include Vitallium and Haynes Stellite-21. When Cobalt Chrome alloy is investment cast, the alloy is melted at 1350 to 1450°C and then poured into ceramic moulds of the desired shape. The moulds are made by fabricating a wax pattern to near-final dimension and then coating the pattern with a special ceramic. A ceramic mould remains after the wax is melted out. The molten metal is then poured into the mould. The molten metal is then poured into the mould. Once the metal has solidified into the shape of the mould, the ceramic mould is cracked away and the cast implant can then be machined to its final dimensions [183].

Cobalt undergoes a structure transformation at 450°C and is face centred-cubic ,fcc, above this temperature and hexagonal close-packed, hcp, below it. Mixtures of both structures usually exist at room temperature. As-cast Cobalt Chrome alloy typically consists of an alpha phase Cobalt-rich matrix , plus interdendritic and grain-boundary carbides, primarily $M_{23}C_6$ where M represents Cobalt, Chromium, or Molybdenum. The precipitates have been noted to be the main strengthening mechanisms which help to increase the abrasive wear resistance in these types of alloys [183-186]. The alpha phase grains of Cobalt Chrome alloy are also quite large and can be seen in Figure 3.7 along with the interdendritic phase [183, 185].

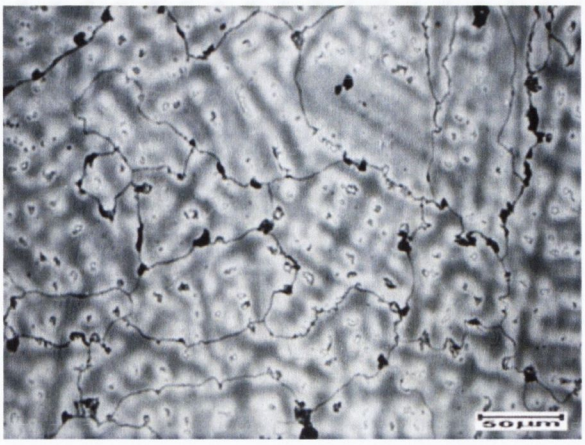


Figure 3.7: As-cast microstructure showing features at grain boundaries and interdentritic regions (optical micrograph) [185]

Many of the attributes that contribute to Cobalt Chrome alloy being an excellent biomaterial also contribute to making the alloy difficult to cut, necessitating the use of tough abrasives such as CBN [8]. Aluminium Oxide wheels, Al_2O_3, have been found to wear at a faster rate during grinding of Cobalt Chrome alloy. One of the best attributes of Cobalt Chrome alloy is corrosion resistance, which is related to its high chromium content and the surface oxide, nominally Cr_2O_3 [183]. However, this surface oxide has been found to strongly adhere to aluminium oxide owing to the mutual solubility of these two oxides [40]. This effect may have an increase on the rate of attritious wear of the aluminium oxide wheel due to the affinity of alumina for metal oxides. In comparison, the wear process was found to be mainly physical during grinding with CBN wheels, since CBN is more stable at high temperatures [187].

Metallurgical examinations of Cobalt Chrome material

Metallurgical examinations were carried out in order to examine the microstructure of the supplied investment cast femoral Cobalt Chrome material. Samples were cut by means of wire electrical discharge machining from three as-cast implants and three post-machining implants near the patella track and just to the left of the casting gate on the femoral condyle. The samples were then mounted in epoxy resin and polished in three stages; first with 320 grit paper, then 1200 grit paper, and finally polished with a diamond suspension solution to a 1 µm surface finish.

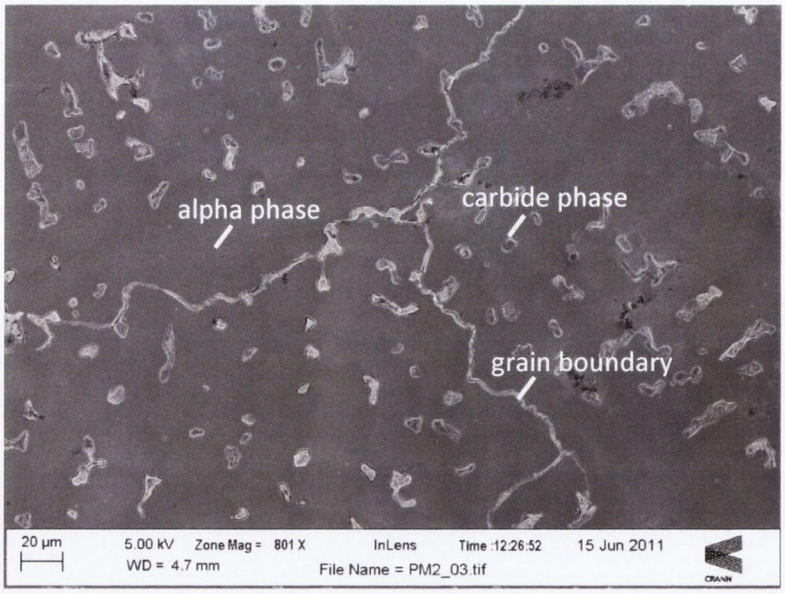


Figure 3.8: SEM image of Cobalt Chromium F-75 alloy from femoral implant

A Zeiss Supra Variable Pressure Field Emission Scanning Electron Microscope was used for examination of the etched surfaces. Figure 3.8 and Figure 3.9 show a SEM image taken near the patella track. The carbides present in the material and grain structure are clearly visible. Carbide phases form with the added carbon in the alloy and act to reduce the wear rate of the Cobalt Chrome alloy through their increased hardness [186, 188].

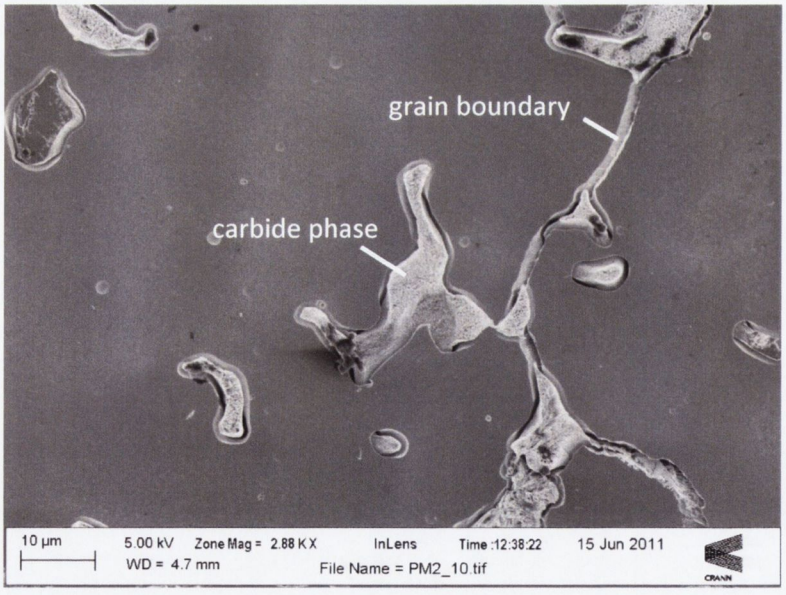


Figure 3.9: SEM image of carbide phase in Cobalt Chrome alloy from femoral implant

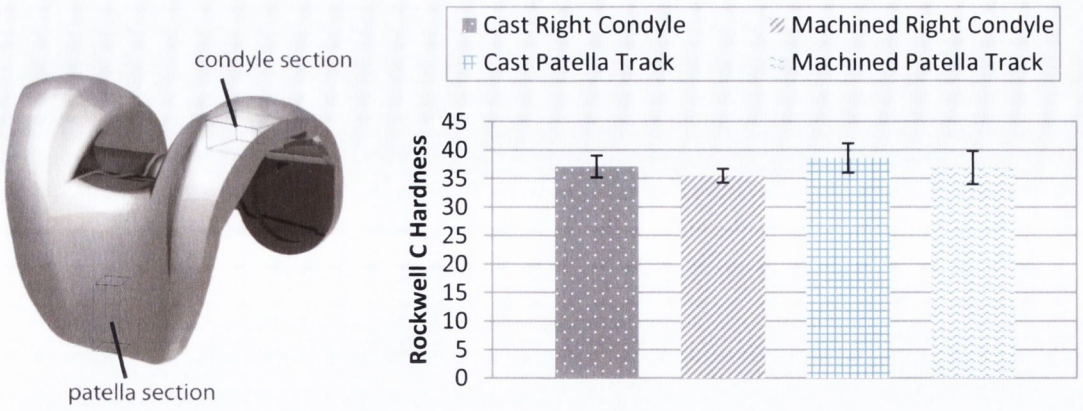


Figure 3.10: Microhardness measurements of Cobalt Chrome alloy femoral implant sections

Microhardness measurements of the workpiece were taken using a Mitutoyo hardness testing machine at a load of 1 kg and 15 s indent duration with a Vickers indenter. Microhardness results are shown to be similar for the various implant sections with a mean of approximately 37 HRC, as shown in Figure 3.10.

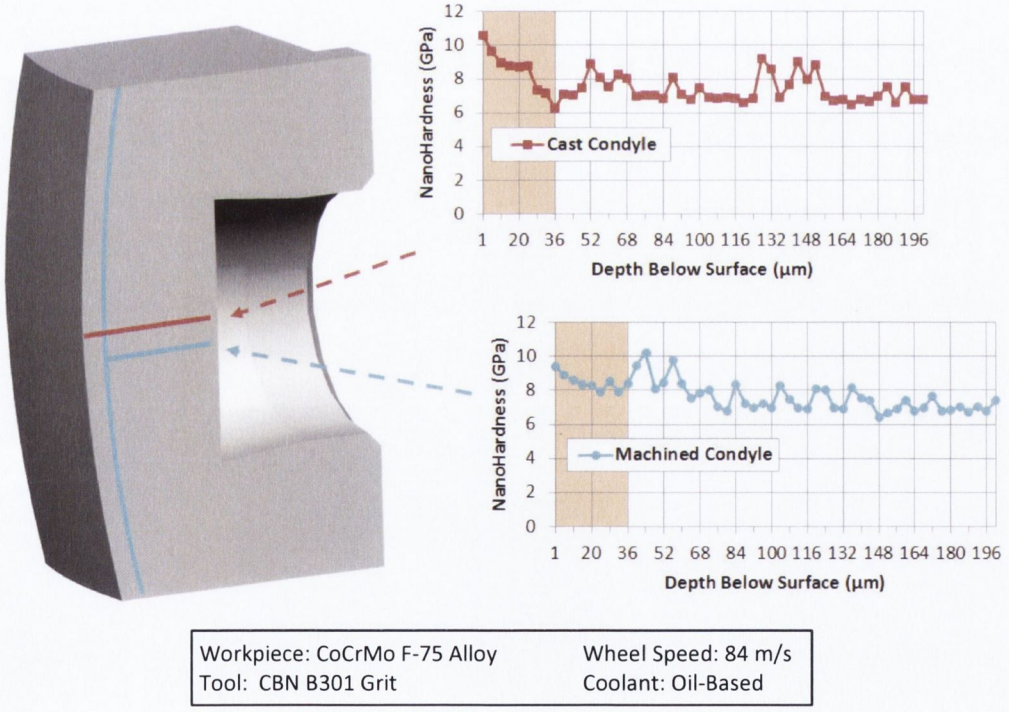


Figure 3.11: Nanoindentation hardness values for an as-cast and post-grinding condyle section

Nanoindentation hardness tests were also performed on the samples. A MTS nanoindenter XP with a diamond Berkovich indenter was used to perform the tests. An example of nanoindentation results is shown in Figure 3.11, where nanoindentation was

performed over the depth of the sample from the surface to a depth of 196 μm with a spacing of 4 μm. Comparable values of nanohardness have been found by Warren et al. to be 8.8 GPa for the ground surface of AISI 52100 steel [189]. The seemingly random increases in nanohardness can be attributed to the carbide phase content of the alloy. An indication of the hard casting skin is illustrated in the graph for the cast section of the femoral condyle, where the hardness is at its maximum at the surface, and decreases through the depth of the sample until a depth of approximately 36 microns where the hardness then levels off. Typical depths of cut during grinding of the femoral implant ranged from approximately 0.1 mm to 2 mm, therefore it can be assumed that the cast skin layer was removed after grinding. An interesting finding in terms of the grinding process is also shown in Figure 3.11 where some indication of grinding-induced hardness is shown near the surface over approximately the first 20 μm of the sample. This implies that if significant temperatures are present in the process workpiece hardness could be induced by the process.

3.2.2 Planar grinding workpiece

Workpiece material was supplied for the planar grinding tests in the form of investment-cast bars of Cobalt Chrome alloy. Test parts in the shape of T-bars were then sectioned and milled from the cast bars with thickness of 8 mm, flat surface area of 68 mm x 25 mm, designed to fit in the machine fixture, as shown in Figure 3.12. The bulk hardness of the Cobalt Chrome alloy used in these tests was measured and found to be approximately 37 HRC.

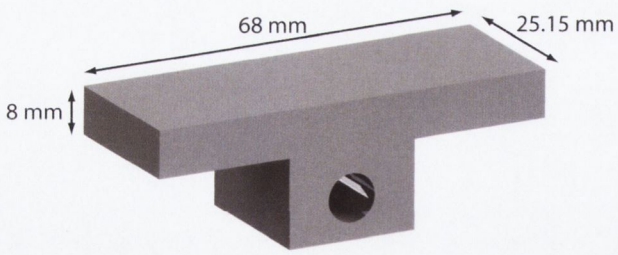


Figure 3.12: Schematic of workpiece dimensions

3.2.3 Experimental setup

The Cobalt Chrome alloy specimens used in the planar grinding tests were held in the machining arbour with an additional clamp in order to provide stability in the Y-

direction and in order to prevent excessive chatter vibrations during machining. Figure 3.13 shows the clamping arrangement and design.

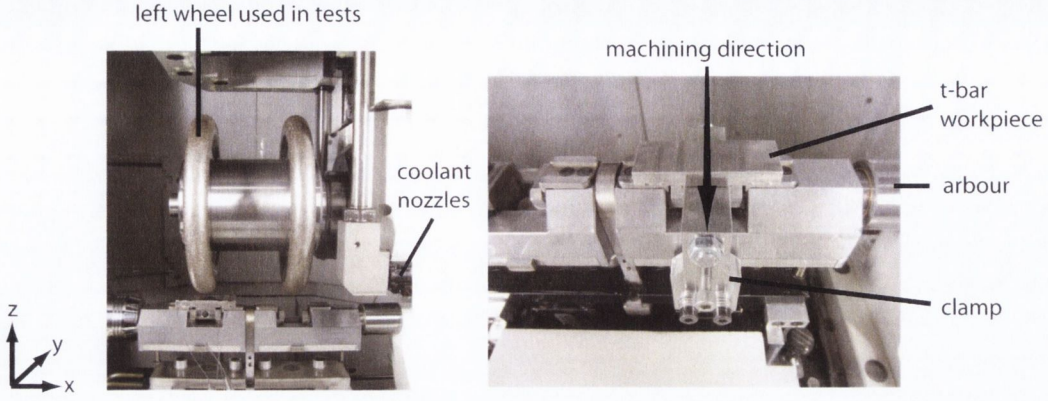


Figure 3.13: (a) Clamp and workpiece (b) Clamp and workpiece installed on arbour

Surface grinding tests took place in the Y-direction. The spindle was a two-end spindle with two wheels installed; all tests were performed using the wheel on the left as illustrated in Figure 3.13. The left and right wheels were distinguished by an 'X' and 'XX' laser mark on the steel wheel body respectively. This also enabled identification when the wheel set was unmounted from the spindle.

3.2.4 Femoral component workpiece

Femoral implant castings were used for the machining trials, an example is shown in Figure 3.14 where some key part dimensions are illustrated. An interesting feature to note is that the radii over the freeform surface vary between 15 – 25.4 mm. The height of the casting gates is not included in this schematic which can extend up to 2 mm above the surface of the implant.

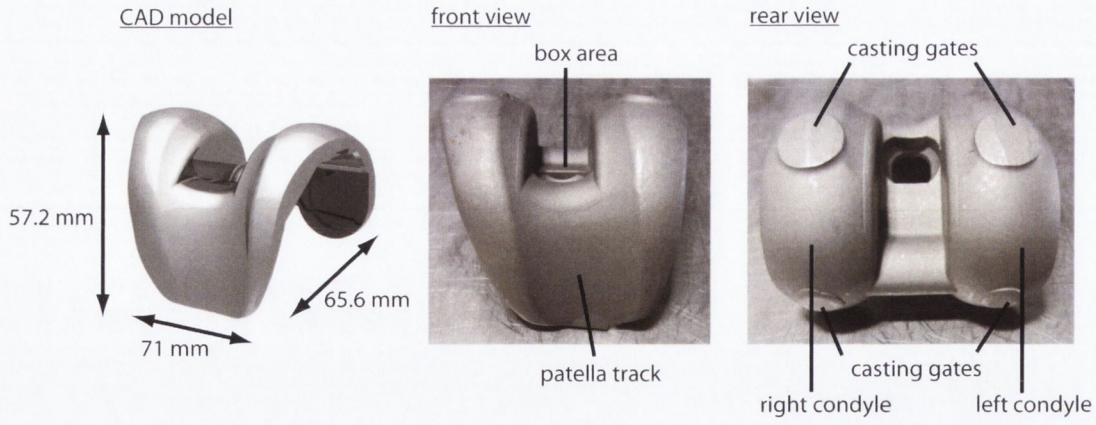


Figure 3.14: Schematic of implant dimensions and photograph of typical implant casting used in tests

Figure 3.15 illustrates the femoral implants held in place on the machine arbour. A post-machined implant is shown on the left and an implant casting is shown on the right. During abrasive machining of femoral implants the A-axis rotates and the spindle moves up and down in the Z-direction for each toolpath line perpendicular to the X-direction. The toolpath spacing is the amount by which each toolpath line is separated by in the X-direction.

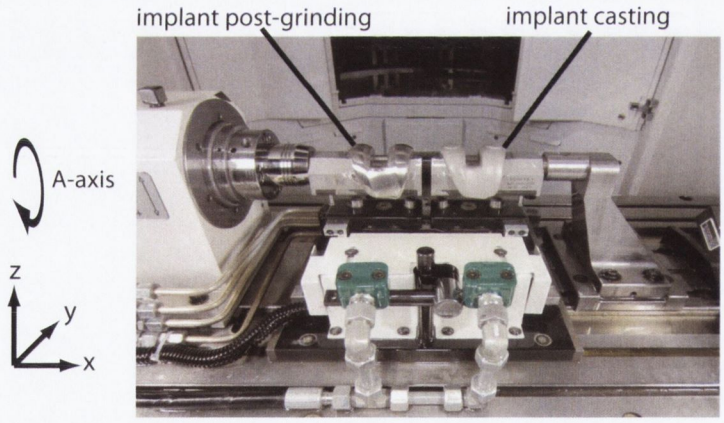


Figure 3.15: Experimental setup with machine axes

3.3 Workpiece surface and tool wear characterisation

3.3.1 Workpiece surface roughness measurement

The surface roughness profilometer used to measure the surface roughness average, *Ra*, for the Taguchi array tests in Phase 1 was a Mitutoyo Suftest SJ-400 profilometer with a 5 μm nominal stylus tip. The evaluation length was 2.5 mm, the cut-

off length, λc, was 2.5 mm, and the traverse speed was 0.5 mm/s. The average roughness parameter was measured 5 times along each tool path in order to obtain the mean value. No curvature compensation was used.

3.3.2 Tool wear measurement

The wheels used in this particular application are B301 electroplated CBN wheels. Electroplated CBN wheels are characterized by a single layer of grits electroplated to the steel wheel hub with a nickel alloy. According to the supplier, the thickness of the electroplated layer is typically half that of the grit size, as the grit size in this application is 301μm the electroplated layer therefore has an approximate thickness of 150μm. As there is only one layer of CBN grit present, the wear that occurs during the grinding process is typically micro wear where the individual grains wear down or are dislodged from the bond, as opposed to the macro wear with significant wheel diameter reduction that would appear with resin bonded or conventional grinding wheels.

Wear of grinding wheel grits has always been difficult to measure due to the various different angles and orientations of the individual grits and the large quantity of grits present [40]. A number of methods were attempted in this research in order to quantify wheel wear, however, optical microscopy with a USB camera as well as wheel replication utilizing an optical microscope proved to be the most effective methods for the quantification of wheel wear.

Optical microscopy

Optical micrographs were taken of the wheel surface using a 5MP usb polarized microscope camera, Dinolite AM7013MZT, at 20x and 200x magnification. The grinding wheel was held on a granite base for stability and the USB microscope was clamped on a Mitutoyo stand perpendicular to the wheel surface. The areal packing density, or grains per unit area, for 10 images of an area of 16 mm^2 for both the new and worn wheel was measured [88]. The count was performed manually by identifying and recording the number of grains with ImageJ image processing software.

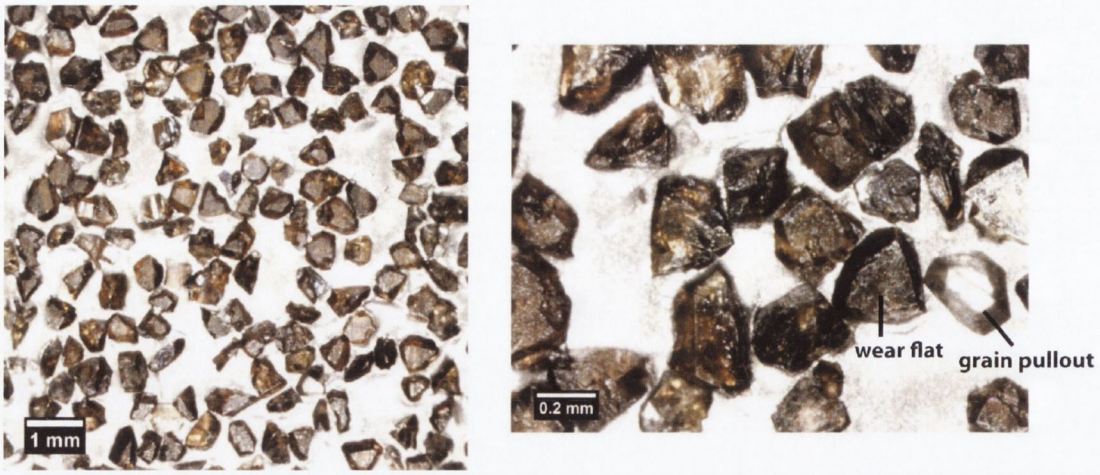


Figure 3.16: Example of optical micrograph from USB microscope for a worn electroplated wheel surface with wear flats visible, left: 20x magnification of 16mm^2 area for areal packing density measurement, right: 200x magnification

Wheel surface replication

After the machining tests were completed, replicas of both the new and worn wheel were taken using Microset 101TH material at 5 arbitrary locations around the wheel surface. Replicas of the wheel surface were taken in order to avoid cutting a section out of the steel hub which could still be replated and reused. Microset 101TH is a two-part synthetic rubber compound specified to have a resolution of 0.1 μm and exhibit high contrast characteristics. Cai et al. found that out of three different replicate materials tried including; Microset 101, Thixoflex and Contrast T which are both addition-curing silicone-based impression materials, Microset 101 was the best replicate material tried due to Microsets 101 high resolution and easy application. Also, for a test using vitrified CBN wheels, the Rt surface roughness of the replica was found to be approximately 60%-90% of the values for the wheel depending on the surface roughness of the wheel, while the error using Microset replica was estimated to be less than 20% for fine-grain wheels [190].

Before application the wheel surface was cleaned with alcohol to remove any traces of the oil-based coolant and debris. The replicate material was then applied to an area on the wheel surface with an application gun. Before the material set, a microscope slide was placed on top of the material with a small weight to ensure that (a) the replicate material penetrated down to the electroplated nickel layer of the wheel surface and (b) that there was a flat backing on the material to enable examination under the microscope. The replicate material was then left for an hour to cure, and subsequently

peeled from the wheel surface when ready. An example of the replicate material examined under the SEM is shown in Figure 3.17, where the difference between new sharp CBN grains and a worn wheel surface with an example of grain pullout can be seen.

Optical micrographs were taken of the replicas with a Leica DMLM microscope fitted with a 5MP Canon Powershot S50 camera. Images taken at 10x magnification of the replicas reveal flat reflective areas which represent the wear flats on the active grains. Subsequently the wear flat area, A, which is the percentage of the wheel surface consisting of wear flats, was estimated by calculating the wear flat by overlaying a fine grid on the optical micrographs [40]. The image processing and grid construction was conducted using ImageJ software.

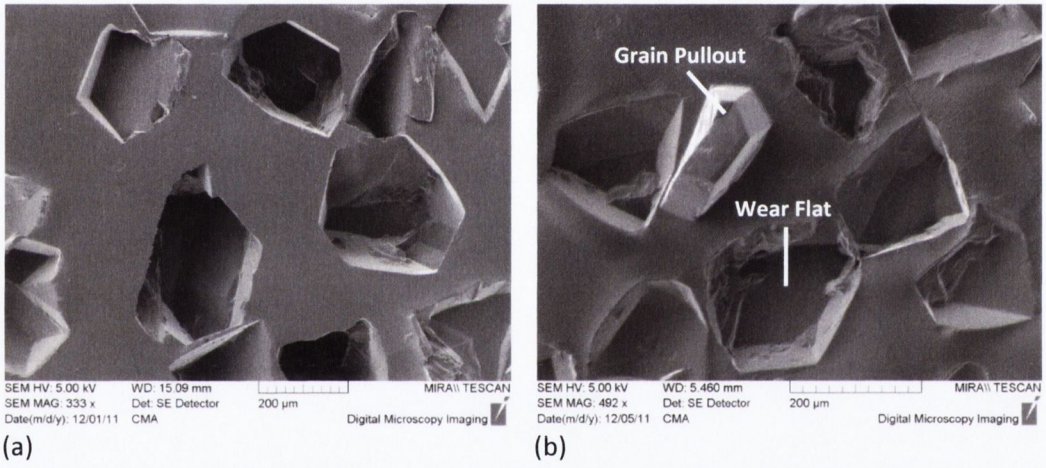


Figure 3.17: SEM images of wheel replicas (a) New and (b) Worn

White light interferometry

The surface of the replicas as well as certain workpiece samples were also examined with an Omniscan MicroXam white light interferometer. Three dimensional surface topography plots were produced from three replicas each of the worn and new wheel. The topography plots were processed and curvature-compensated for in SPIP 6 software. The plots were then analysed using MountainsMap 6.2 and the 3D surface topography parameters calculated as shown in Table 3.3.

The 3D surface topography parameters Sa and Sdq are part of the 12 S-parameter set in the ISO standard 25178-2 (2012) Geometrical Product Specification (GPS) – Surface Texture Areal – Part 2 [166]. Sa is a height parameter describing the arithmetical mean height while Sdq is a hybrid parameter which describes the root mean

square gradient of the surface. Sds is another spatial parameter which is the number of summits of a unit sampling area, useful for describing the density of grain summits on a grinding wheel. SSc is a hybrid parameter which describes the average of the principle curvatures of the summits within the sampling area, which can provide an evaluation of the average radius of the grits which describes the sharpness of the grits [191]. An example of results obtained from white light interferometry detailing the average surface roughness, *Sa*, of the surface area is shown in Figure 3.18.

For examination of the surface roughness parameters for the replicas of the wheel surface, some processing of the data was applied in SPIP Image Metrology software. Any obvious outliers in the data from light scattering in the z-direction were first removed. A three degree polynomial plane correction was then applied to the data. A selective threshold Fourier filter, a function in the SPIP software, which is a combination of a low-pass or smoothing filter, and a high-pass filter to detect contrast with a threshold, set to 20 % in this case, was then applied to the data in order to remove noise from light scattering.

Parameter	Description	Units
Sa	Surface area roughness	µm
Sds	Density of peaks	mm^{-2}
SSc	Mean summit curvature	mm^{-1}
Sdq	Root mean square value of surface slope	

Table 3.3: Surface Topography Parameters

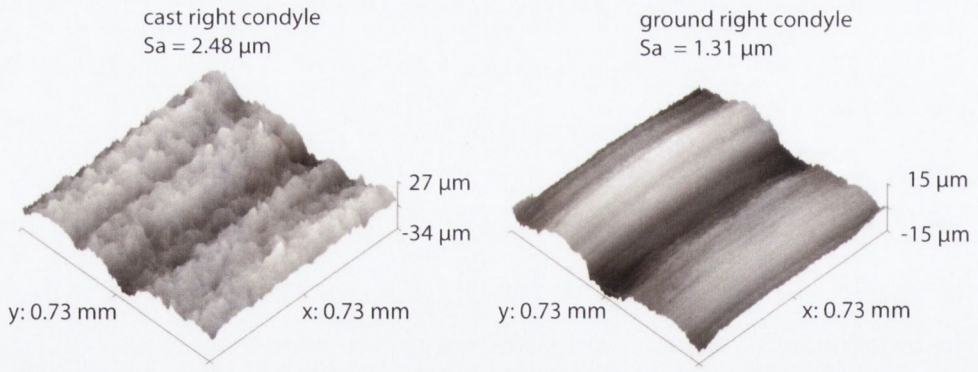


Figure 3.18: Example of white light surface roughness values for cast and post-abrasive machining for condyle section of femoral implant

3.4 Laser measurement

3.4.1 Laser measurement rig

During abrasive machining depths of cut of between approximately 0.1 mm and 2 mm can occur, based upon measurements taken between castings before and after machining. The thin layer of material removed can be detected using a laser sensor that measures displacement through the principle of optical triangulation. A special purpose laser measurement rig was designed in order to measure the material removed during abrasive machining, as detailed in Figure 3.19. The laser sensor used, MicroEpsilon ILD-1700-50, provides a linear measuring range of 50 mm and a resolution of 3 μm, where the resolution refers to the smallest possible change of a quantity which can be reliably measured by the sensor.

The specified linearity of the sensor for the full scale output is +/- 0.08% or 40 μm, where linearity is the largest deviation from a best-fit straight line over the measurement range created by data from the sensor with reference taken from a true distance scale. The spot diameter at midrange for the laser was 55 μm, the distance between all measurements taken with the laser displacement sensor were greater than this value in order to prevent overlapping of the laser spot.

A resolution of 10,000 pulses per rotation is used for the servo-motors in this application. A linear slide provides the X-axis travel and the associated screw lead is 2.54 mm with a linear resolution of 0.00254 mm, which is close to the resolution of the laser displacement sensor. The backlash, where backlash is the axial distance the nut can be moved without turning the lead screw, and the lead screw accuracy were examined by the suppliers for a 12.7 mm lead screw and a 3 kg load and were found to be < 0.003 mm and 0.0006 mm/mm respectively.

For the purposes of this testing and verification stage a static measurement strategy is employed. This is in order to avoid the risk of associated error with dynamic data acquisition during movement of the motors. Distance measurements along the profile of the implant are accomplished through the following measurement strategy; the laser is fired, displacement is recorded, the motor moves the part by a set step along the X-direction, the laser is fired and the procedure repeats until a full profile scan is acquired, as described in the schematic shown in Figure 3.20. As movement in the linear X-axis took place in one direction the risk of backlash was minimized.

Once a full profile scan is acquired the implant is then rotated by a set value and the procedure is repeated until the full implant surface has been scanned. This procedure is controlled through Labview 2011 and associated VI's.

Laser Measurement System Technical Data	
Control	
National Instruments Labview 2011	
Servo motors	
RP Mechatronics RCM-23L30-RT3	
Torque	0.87 Nm
Encoder resolution	50,000 pulses / rotation
Maximum rotational speed	2000 rpm
Travel	
Reliance Cool Motion Stage RCMS23L-0100	
X-axis linear slide	304.8 mm
Linear slide resolution	2.54 µm
Based on 12.7mm lead with a 3kg load	
Backlash	<0.003 mm
Lead accuracy	0.0006 mm/mm
Laser sensor	
MicroEpsilon ILD-1700-50	
Linear measuring range	50 mm
Spot diameter at midrange	55 µm
Resolution	3 µm
Linearity (FSO)	40 µm or +/- 0.08 %

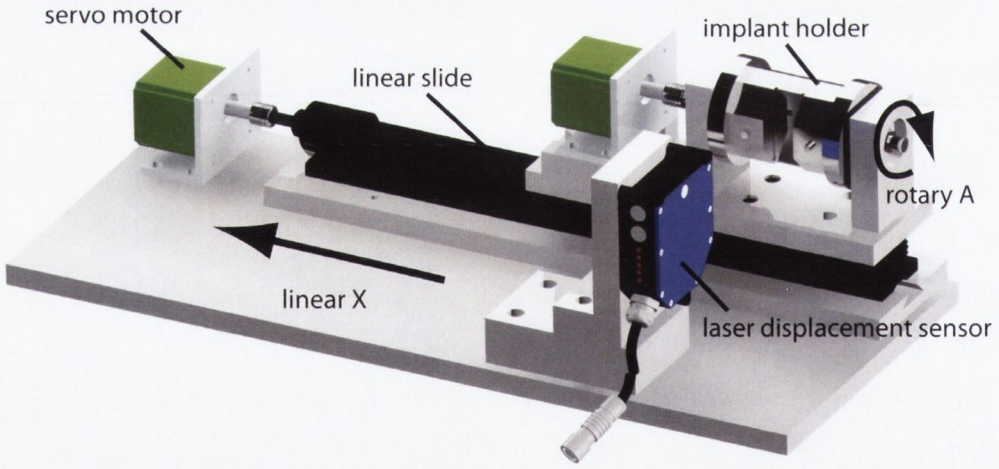


Figure 3.19: Schematic of developed laser measurement system and associated technical data, FSO – Full Scale Output/full range

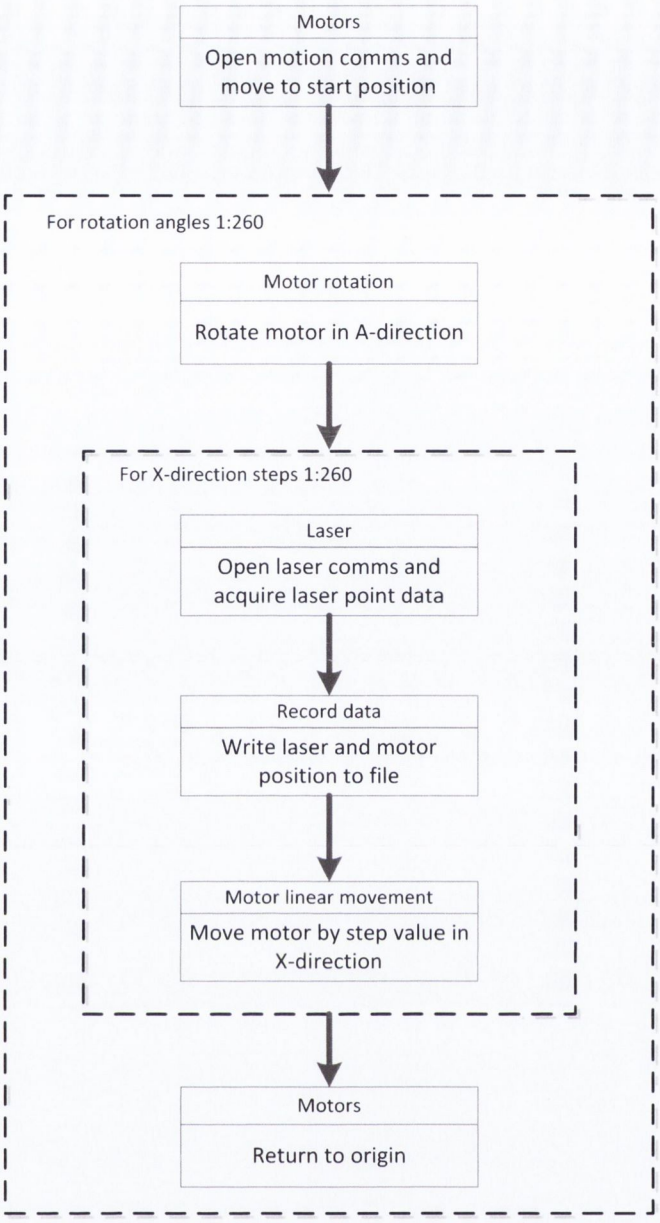


Figure 3.20: Labview schematic of laser measurement labview control system

Chapter 4

Process characterisation through power monitoring

Internal machine signals can be a useful means of monitoring a cutting process, as indicated in Chapter 2. Spindle power is related to grinding process energy, forces and heat generation in the workpiece. The magnitude and rate of energy transfer in the process determines to an extent the occurrence of form deviations, thermal damage and residual stresses of the workpiece. Power expended during abrasive machining is primarily influenced by operational parameters, tool wear and the machinability of the workpiece. The sensitivity of the internal machine power signal to changes in process parameters is an important consideration if the signal is to be utilised for process monitoring. Therefore, it is necessary to understand how changes in cutting velocity, depth of cut and tool condition affect the power signal, and the sensitivity of the internal machine signal to these process changes. This has been studied in a limited fashion for the milling process previously [143, 161]; however, the characterisation of internal machine signals for abrasive of Cobalt Chrome alloy with electroplated CBN wheels has not yet been investigated.

This chapter therefore aims to:

(a) Characterise the machine internal power signal

(b) Investigate the power signal response with respect to varying grinding parameters

4.1 Evaluation of signal: power monitoring and material removal

The first step in utilising a power signal as a process metric is to quantify the power response without material removal. This is the base level of power drawn by the spindle necessary for rotation at the set speed. Spindle active power was measured at a variety of speeds up to the maximum machine rated rotational value of 8000 rpm whilst

holding the grinding spindle stationary, an example raw data plot is illustrated in Figure 4.1.

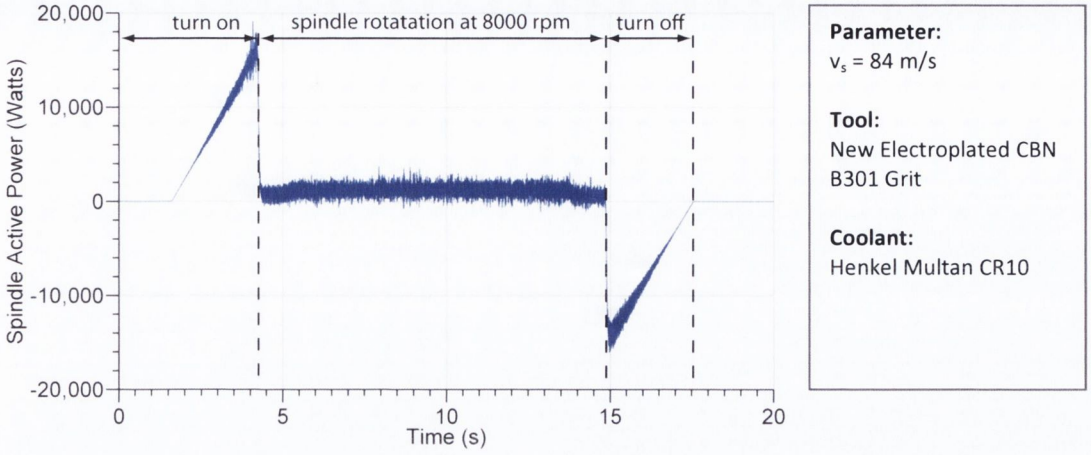


Figure 4.1: Example raw data plot for spindle active power rotating at 8000 rpm

As shown in Figure 4.2 there is a relatively linear increase in power until 7000 rpm is reached, past this point at 8000 rpm spindle power is shown to drop slightly. This departure from the increasing trend is likely related to the efficiency of the motor; a measure of how well input electrical energy is converted into mechanical output energy. Constant losses in the motors circuit can be due to friction, windage and iron losses. Since constant losses are essentially independent of load, whilst stator and rotor losses depend on the square of the load current, the overall efficiency of a typical induction motor can be significantly low at low load levels [192, 193]. Typically motors run more efficiently closer to their rated power, usually in the range of 50-100% [194]. This may go some way towards explaining the lower power draw at the fastest rotational speed of 8000 rpm, where at 8000 rpm, the highest load level without machining, the circuit is more efficient at converting electrical to mechanical energy, and therefore less power is required at this setting.

The effect of applying coolant in the process is also illustrated in Figure 4.2. The coolant fluid fed in under pressure exerts a braking effect on the grinding wheel surface, thus the magnitude of the spindle power is increased significantly when the coolant supply is turned on. The hydrostatic pressure from the coolant can be seen to have an increased braking effect as the spindle rotational speed is increased [125].

Another interesting feature from Figure 4.2 is the difference in trendlines shown for spindle current and power. This can be attributed to the voltage from the frequency

inverter stepping up as the rotational speed is increased [195]. As the voltage can change depending on the rotational speed of the drive it is generally better to monitor the power as this quantity takes both the voltage and current into account.

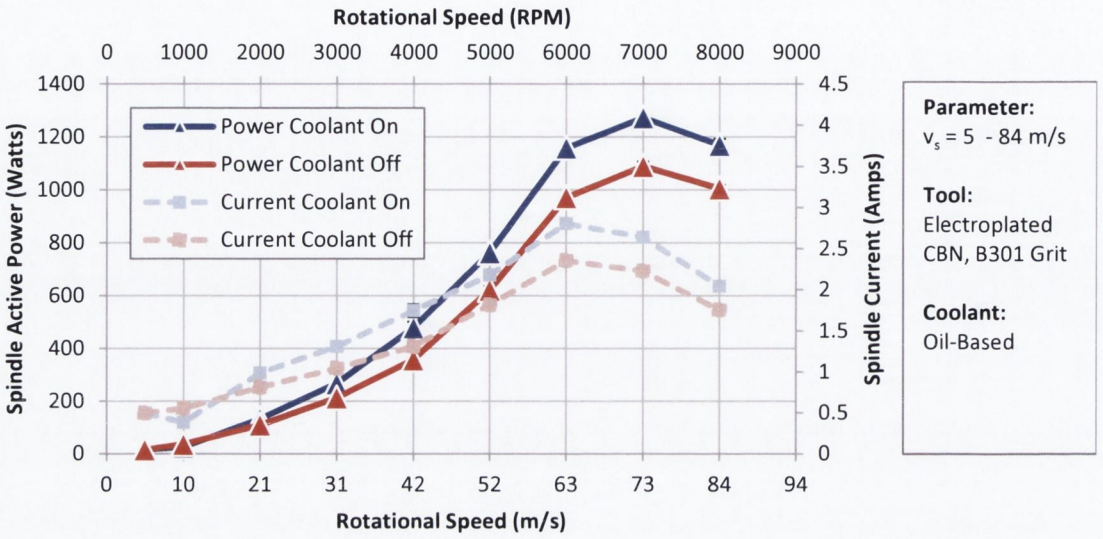


Figure 4.2: Mean spindle power consumption versus rotational speed

An example of a frequency domain plot for a spindle speed of 84 m/s is shown in Figure 4.2. The main spindle rotational frequency of 133.2 Hz can be detected in the spindle power signal with a further harmonic frequency of 66.7 Hz.

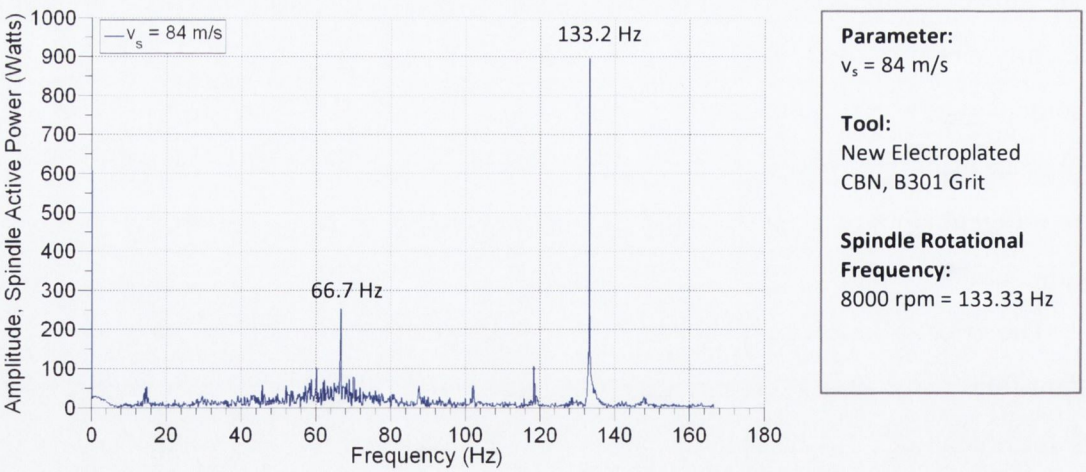


Figure 4.3: FFT example plot for spindle rotation at 8000 rpm

The frequency component responsible for spindle rotation determined through Fast Fourier Transform of the data is illustrated in Figure 4.3. The amplitude of the

corresponding signal noise for the active spindle power is also illustrated in Figure 4.4, where it can be seen that as the rotational speed of the spindle increases so too does the 'noise' component related to the frequency for powering the rotation of the spindle. This component needs to be subtracted from the main signal in order to obtain the power due to material removal.

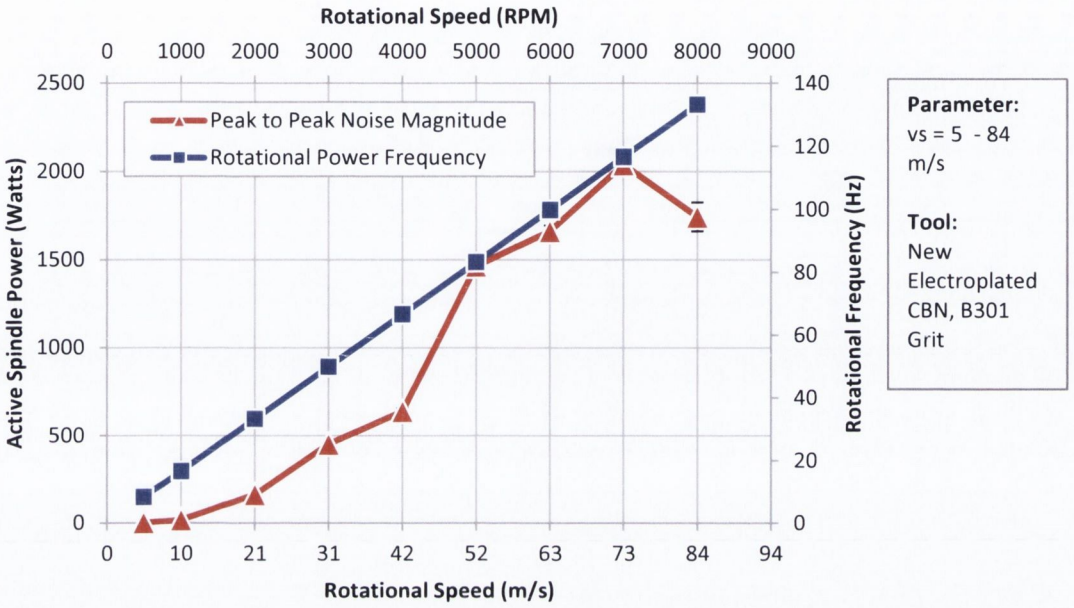
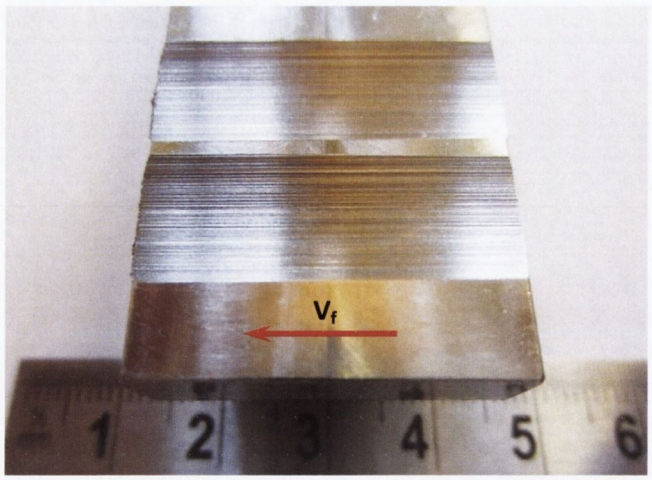


Figure 4.4: Spindle rotational frequency response

The frequency component of the spindle power data related to rotational speed presents a linear trend, whilst the peak to peak noise associated with the rotational frequency resembles a trend similar to that shown in Figure 4.1 for the mean spindle power and current values. The maximum rated rotational speed at 8000 rpm presents a relatively efficient speed in terms of both spindle active power consumption as well the associated noise component.

The next stage in examining the power signal was to characterise the power expended during the material removal process. Flat surface grinding was performed on workpiece specimens of Cobalt Chrome alloy. Operational parameters that may be encountered during a typical abrasive machining operation of a femoral implant were selected. An example of a cut from abrasive machining across a Cobalt Chrome alloy T-bar shaped workpiece is shown in Figure 4.4. The grinding tracks across the ground surface typical of a new sharp electroplated CBN wheel are visible.



Parameter:
a = 0.8 mm
v_s = 84 m/s
v_f = 55 mm/s

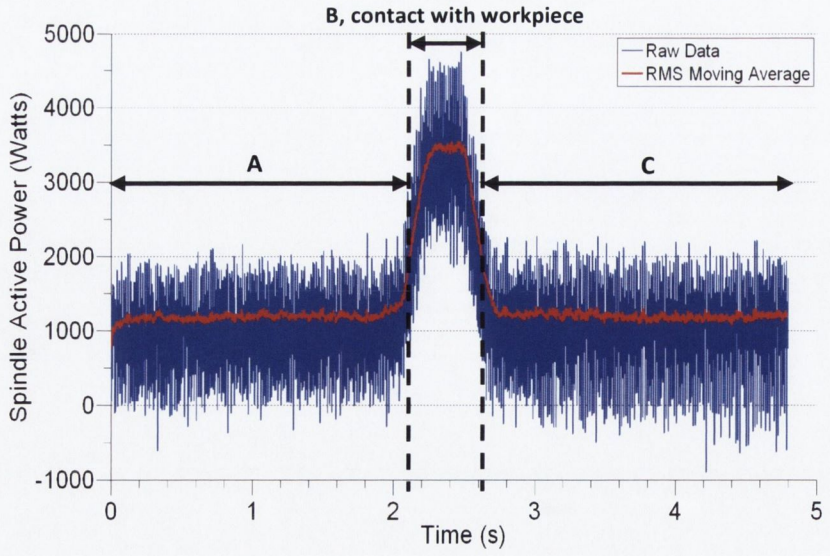
Material:
CoCrMo F-75 Alloy

Tool:
New Electroplated CBN
B301 Grit

Coolant:
Henkel Multan CR10

Figure 4.5: Example of two ground tracks across T-bar shaped workpiece

An example of a spindle power trace for surface grinding with a new wheel and 0.8 mm depth of cut is presented in Figure 4.5. Both the raw data and RMS moving average are illustrated. The region denoted by A shows the power consumed as the wheel approaches the workpiece. This is the power necessary for spinning the wheel at the required speed with coolant turned on. Region B denotes the power consumed during abrasive machining of the workpiece. A significant increase in power can be seen here over the duration of wheel-workpiece contact. At a feed rate of 55 mm/s, the time taken to traverse the workpiece of length 25.15 mm is 0.46 seconds; which is approximately the duration of increased power corresponding to wheel-workpiece contact shown in Figure 4.5. Region C denotes the power consumed where the wheel has exited the workpiece.



Parameter:
a = 0.8 mm
v_s = 84 m/s
v_f = 55 mm/s

Material:
CoCrMo F-75 Alloy

Tool:
New Electroplated CBN
B301 Grit

Coolant:
Henkel Multan CR10

Figure 4.6: Spindle power trace example

The corresponding spindle current trace recorded during the same abrasive machining operation is shown in Figure 4.6. As expected, spindle current exhibits the same trend as spindle power shown in Figure 4.5.

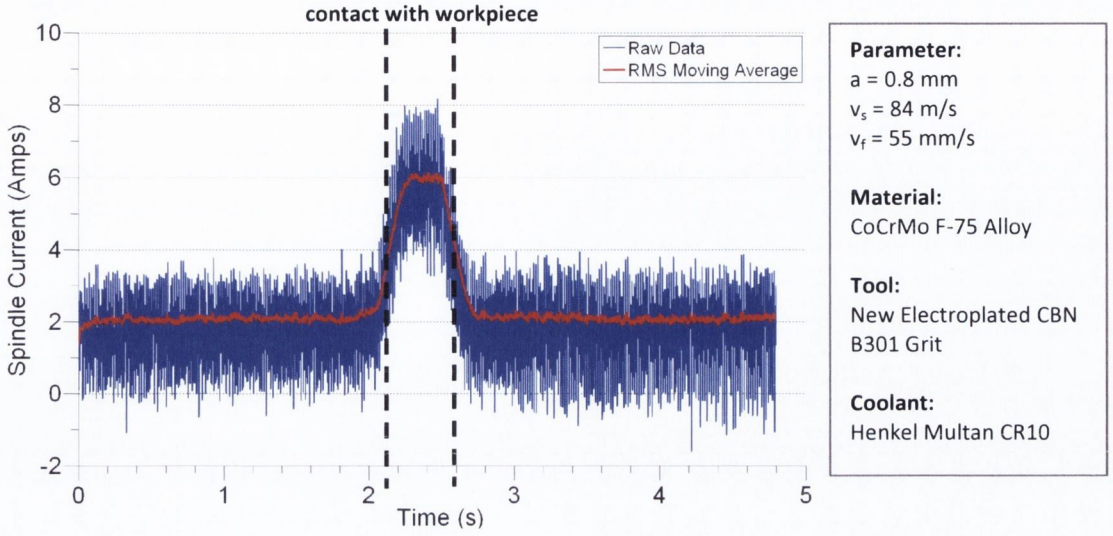


Figure 4.7: Spindle current trace example

Certain feed axes are also sensitive to the grinding process. During a surface grinding operation, the spindle, operating on *X*, *Y* and *Z* axes approaches the workpiece, as shown in Figure 4.7. The grinding wheel then moves across the workpiece in one toolpath across the Y-axis, at a fixed X and Z value. The rotary arbour A-axis is also held stationary during this operation.

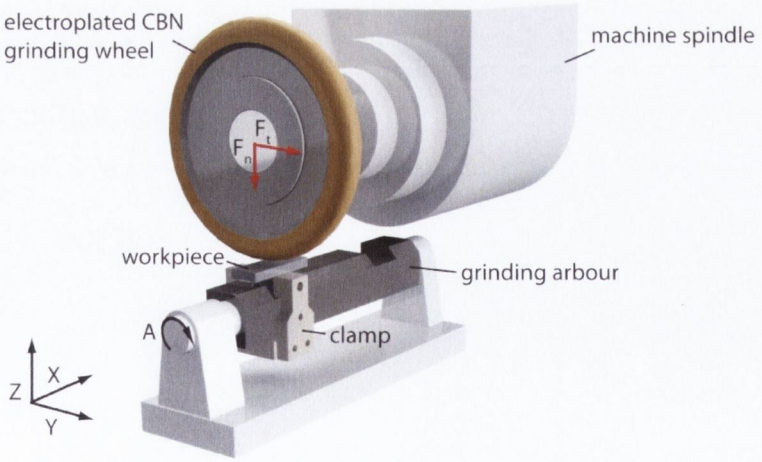


Figure 4.8: Schematic of experimental setup

Despite the fact that the A-axis is held stationary during surface grinding, a negative current response is still observed in both the vertical Z-axis and the rotary A-axis, where the dynamic current response is illustrated in Figure 4.8, for the same operation as shown in Figures 4.5 and 4.6.

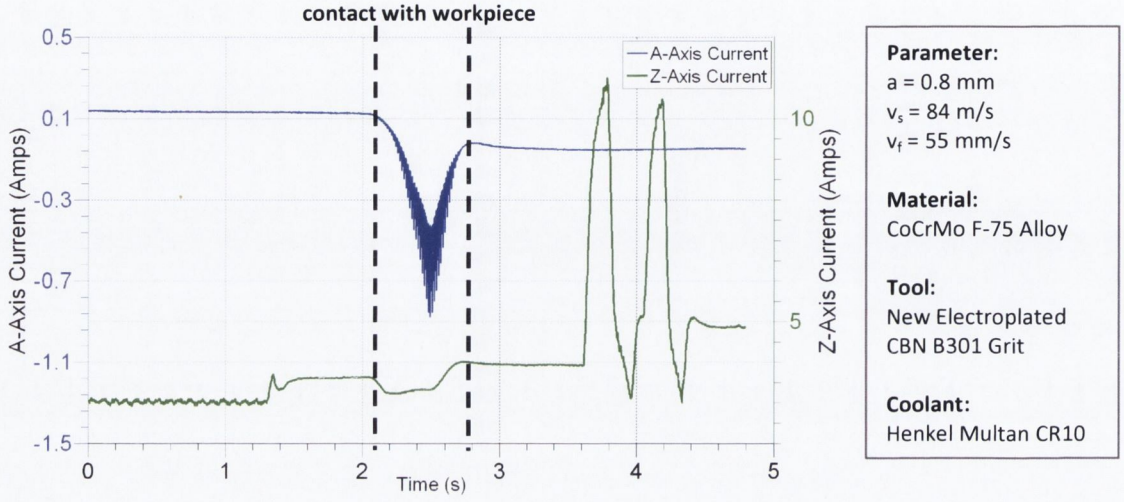


Figure 4.9: Feed axis A and Z response during grinding

The resultant force in the vertical *Z* direction is realised as a small drop in current as the tool and spindle are effectively supported by the workpiece for a short period of time during the abrasive machining operation. The A-axis response is also shown as a drop in current, however, the response is a sharp one in contrast and appears to be compensated for rather quickly through a resulting increase in current after the machining event. This can be attributed to the drive's servo-mechanism, whereby a change in position is corrected for through a change in pulse width modulation of the voltage, resulting in a change of the current value. In order to further examine the digital feed drive current signal behaviour, current was recorded during a basic oscillating movement of back and forth and up and down of the corresponding feed axes. Current traces for the rotary *A* and linear *Z* axes are illustrated in Figure 4.10 and Figure 4.11.

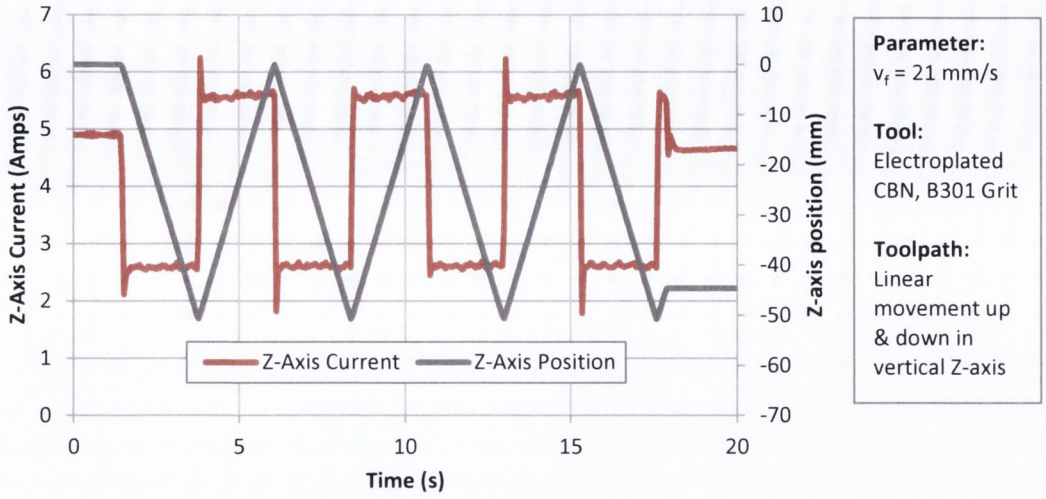


Figure 4.10: Typical movement trace in Z-Axis

A change in direction of current is shown to result in a change of direction of the axes movement. The feed rate is dependent on magnitude of the current. Current remained at an unchanged value when the axis was held stationary. Referring back to Figure 4.9, during abrasive machining, the change in current magnitude with fixed A and Z-axis position can be attributed to the large forces experienced during the grinding operation.

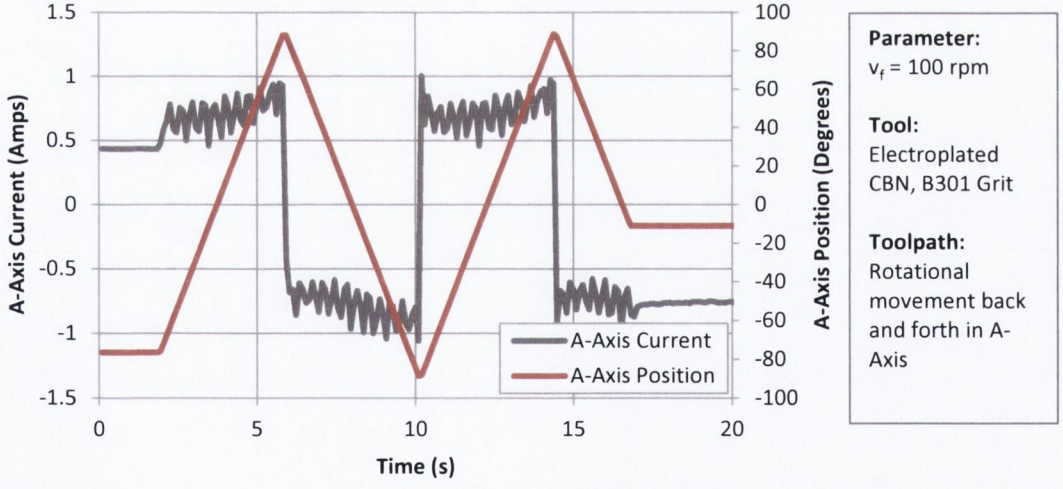


Figure 4.11: Typical movement trace in A-Axis

Tests were carried out to examine the power signal's sensitivity towards material removal. An experiment was carried out to record spindle active power at various depths of cut during abrasive machining of Cobalt Chrome alloy. Parameters selected were analogous to those typically used during the abrasive machining of Cobalt Chrome alloy femoral implants. Power was shown to increase in a relatively linear manner as

depth of cut was increased, as shown in Figure 4.12. This result indicates that the spindle power signal is a sufficiently sensitive parameter to detect changes in depth of cut during abrasive machining of Cobalt Chrome alloy. This trend is also in line with previous findings in the literature where spindle power was found to increase almost linearly with increasing depth of cut during high speed milling [196].

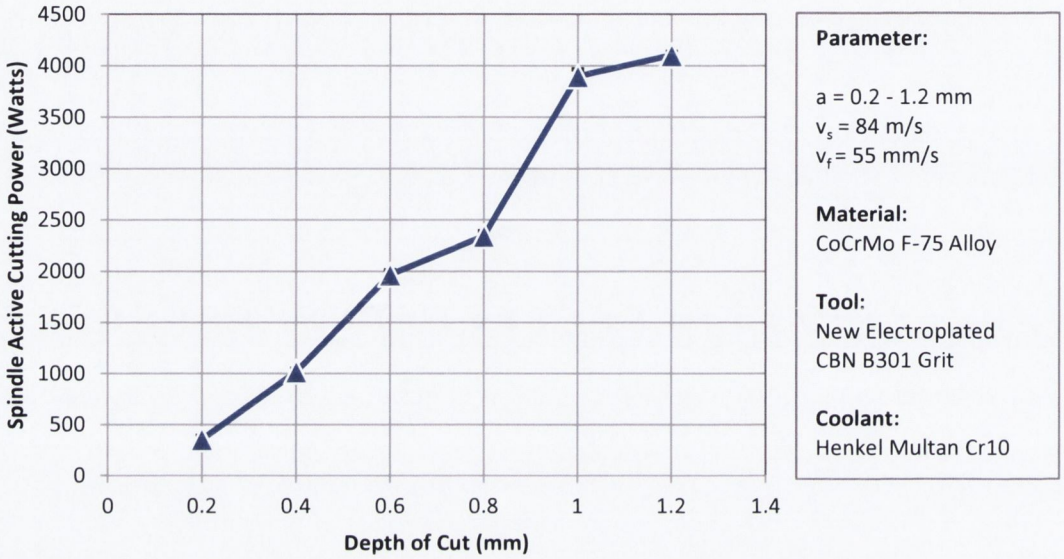


Figure 4.12: Spindle active cutting power for various depths of cut

However, if the grinding wheel geometry is considered, a reasonable expectation would be a non-linear relationship between depth of cut and spindle power, due to the circular cross-section of the wheel. Indeed, with increasing depth of cut the relationship with engaged tool-workpiece area is non-linear, as given by Equation 4.1 and further illustrated with the curve in red in Figure 4.13. The range of depths of cut evaluated in this experiment where, a = 0.2 – 1.2 mm, go some way towards explaining this behaviour, where it can be seen that within this range the trend is almost linear, thus giving rise to the approximately linear increase in power with depth of cut in experimental results, as shown in Figure 4.11. With depths of cut below approximately 0.2 mm and above approximately 1.2 mm it is interesting to note that the trend becomes highly non-linear with increased cross-sectional area of engagement.

$$A_s = R^2 cos^{-1}\left(\frac{R-a}{R}\right) - (R-a)\sqrt{2Ra-a^2} \tag{4.1}$$

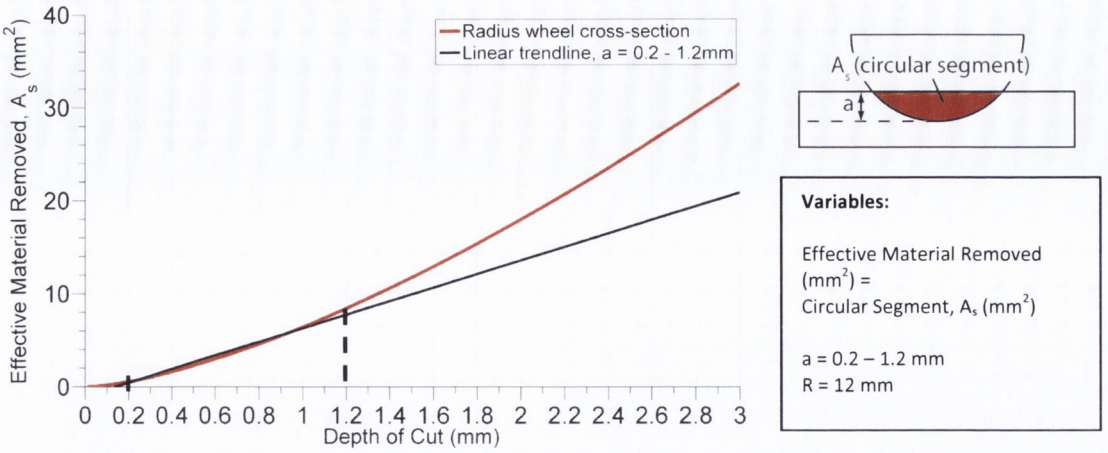


Figure 4.13: Effective wheel cutting area cross-section versus depth of cut

An experiment was performed in order to investigate the limit to which depth of cut could be detected through power monitoring with a new wheel. Cutting power is shown in Figure 4.14, where for a 0.1 mm depth of cut, the mean value for three tests is 231 Watts. The increase in power for values less than a = 0.1 mm, with a corresponding cross-sectional engaged area, $A_s = 0.21$ mm^2, become difficult to detect above the noise level responsible for wheel rotation when grinding with a new wheel. Although the rotary A-axis was held at a fixed value of 0 degrees throughout the tests, the impact of machining was still detectable through the change in current recorded for the axis. Figure 4.15 illustrates the effect of changes in depth of cut with a change in current of 0.26 Amps for a 0.1 mm depth of cut. The results indicate that the feed A-axis is suitable for use as a secondary process monitoring metric in conjunction with spindle power.

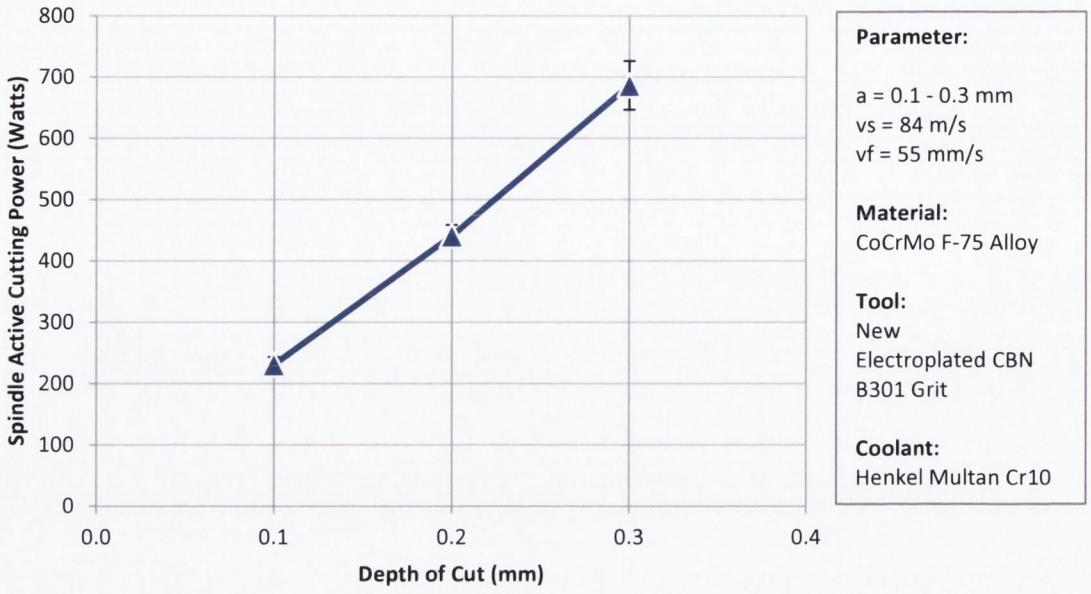


Figure 4.14: Depth of cut limit tests

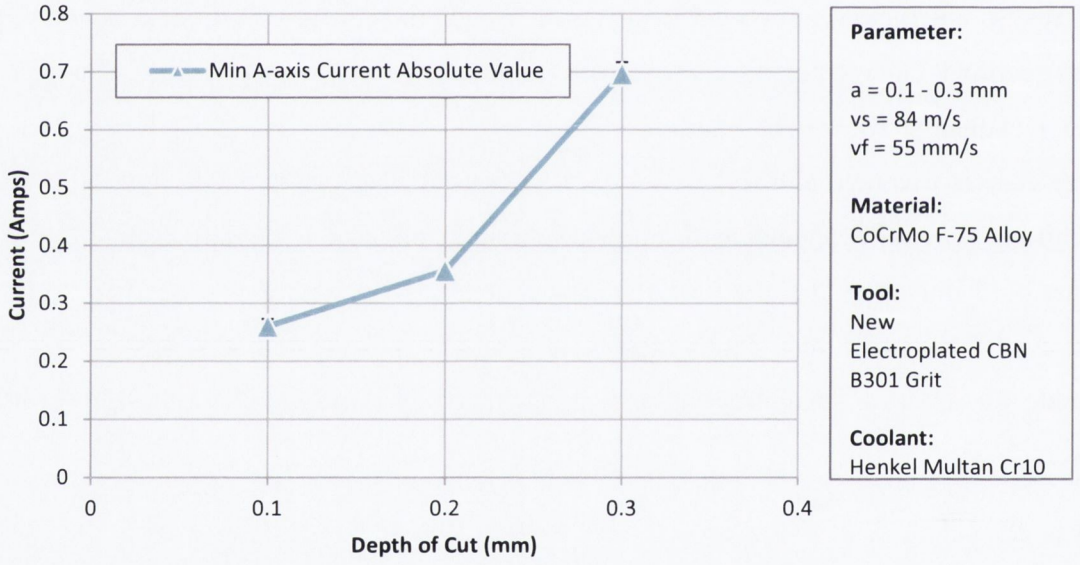


Figure 4.15: Depth of cut limit tests

As mentioned in Section 2.1.3, tool wear can give rise to excessive process forces and heat, which may in turn be detected through power monitoring. An experiment was designed to determine if a difference in spindle power consumption could be detected between a new and worn tool during abrasive machining of Cobalt Chrome alloy. The depth of cut parameter was varied while feed rate and wheel speed were maintained at a constant value based on standard values for femoral abrasive machining. A new wheel

and a wheel considered to be in a worn state were evaluated. Spindle active power was measured during machining.

Depth of Cut (mm)	Wheel Condition
0.4	New
0.6	Worn
0.8	

Table 4.1: Test parameters to evaluate the effect of wheel wear

Surface area roughness, *Sa*, of the machined tracks in the workpiece was examined through white light interferometry. Cutting power for both a new and worn wheel is illustrated in Figure 4.16, while the corresponding workpiece surface roughness measurements are illustrated in Figure 4.17.

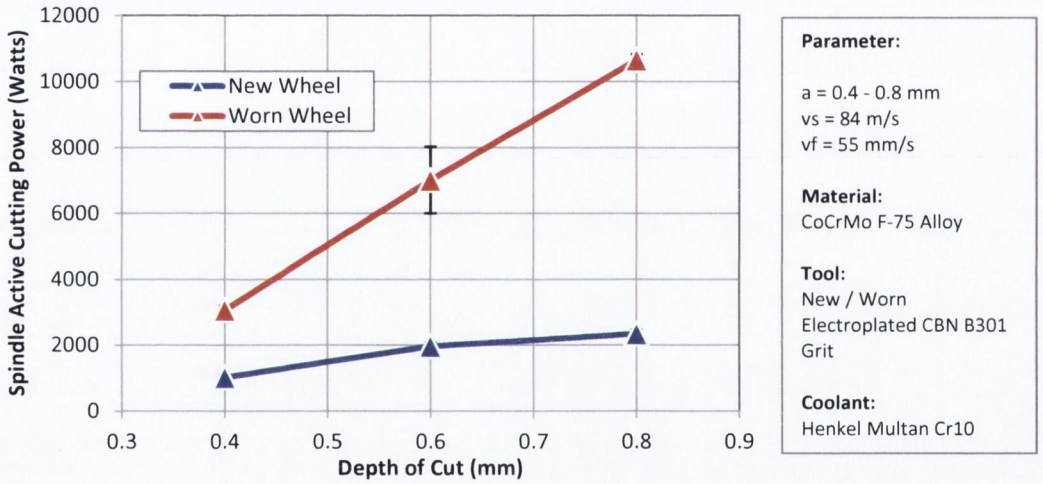


Figure 4.16: Cutting power for new and worn wheel

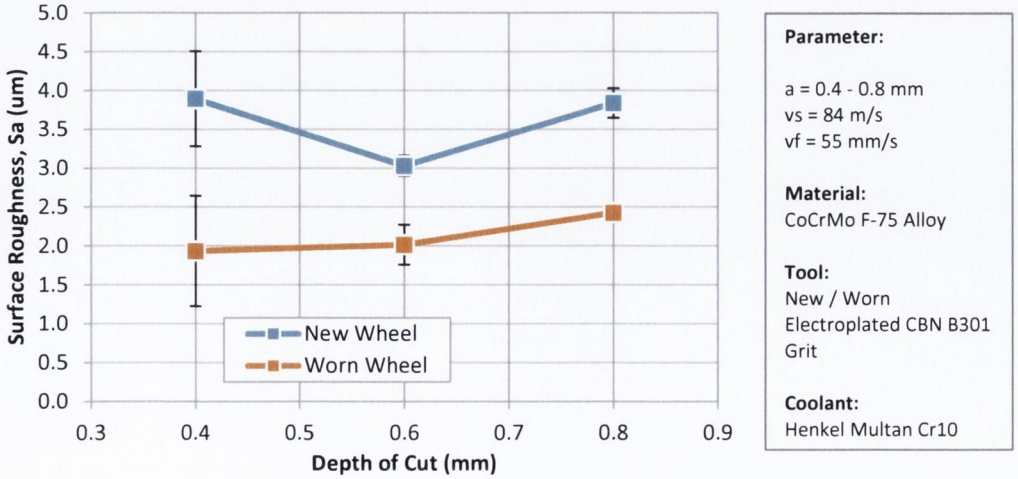


Figure 4.17: Workpiece surface roughness for new and worn wheel

The lower value of *Sa* for the workpiece machined with the worn wheel, as shown in Figure 4.17, indicates a quantifiable difference in wheel condition between the new and worn wheels. The difference in cutting power between the two wheels is significant with the worn wheel consuming considerably more power on average during abrasive machining than the new wheel. This is similar to findings by Guo et al. where spindle power measured by a universal power meter was found to increase with a corresponding decrease in surface roughness as the wheel was worn down and the volume of material removed increased [89]. The increase in spindle power as the wheel wears as shown in Figure 4.16 can be attributed to the increased forces and temperatures experienced when machining with worn CBN wheels [84].

Specific Energy and Area Specific Power

A key fundamental metric related to the power consumed in the process is known as the specific energy, u, which is defined as the energy per unit volume of material removed. The specific energy of the cutting process is the work required to convert a cubic volume of metal into chips, and can be used as a metric to describe the efficiency of most machining processes [197]. The specific energy includes the energy needed for chip formation, plowing, sliding as well as elastic deformation. Typically abrasive machining process incur more material deformation, both elastic and plastic, and as a result specific energy for abrasive processes is usually higher than for other machining processes such as milling or turning [198].To investigate further the impact of tool wear, specific energy, u, the energy expended per unit volume of material removal was calculated as follows:

$$u = \frac{P}{v_f A_s} \tag{4.2}$$

Where P is the cutting power, v_f, the feed rate and A_s, the area of material removal due to the toric shaped wheel, where R is the minor tool radius of 12 mm and a is the depth of cut, as given in Equation 4.1. A secondary energy-related process parameter is given by the area specific power, P_c'', calculated over the geometric contact length of the wheel, l_g [74, 93]. Area specific power is the power per unit area of material

removed and is also assumed to be equal to the heat q_t generated in the process. Area specific power, P_c'', is given by Equation 4.3:

$$P_c'' = \frac{P}{l_g b} \tag{4.3}$$

Where,

$$l_g = \sqrt{a d_s} \tag{4.4}$$

Where d_s is the wheel diameter of 200 mm and b is the contact width.

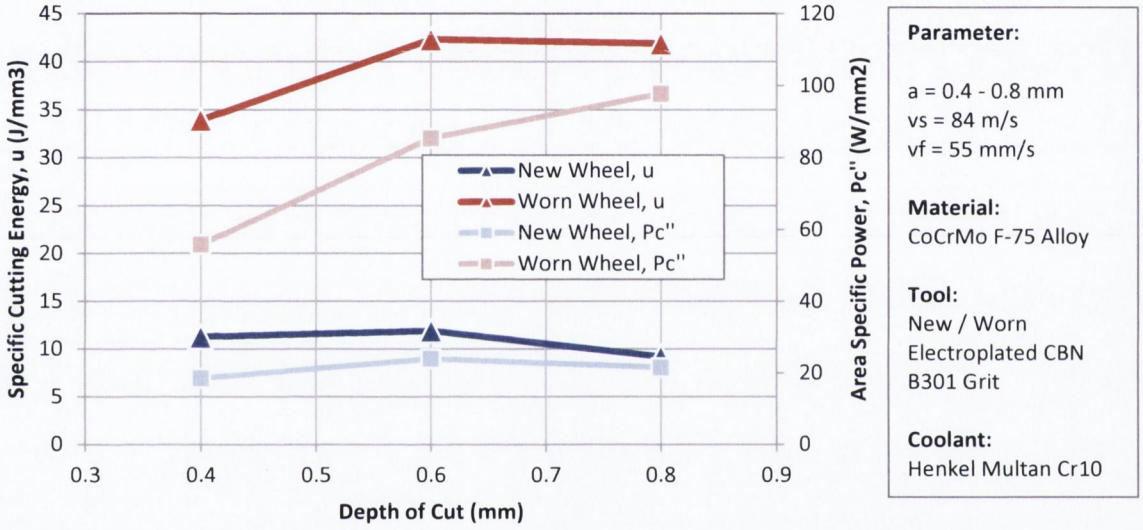


Figure 4.18: Specific energy, u, and area specific power, Pc''

A significant increase in specific energy was found with a worn wheel, as illustrated in Figure 4.18. As discussed in Section 2.1 the increase in specific energy for a worn wheel can be attributed to the sliding of wear flats against the workpiece surface. This constitutes a large portion of the total grinding energy as the wheel wears during its lifespan. In comparison, during abrasive machining with a sharp new wheel most of the specific energy can be attributed to cutting and plowing with little to no sliding occurring due to the absence of wear flats at the beginning of the wheels life. The magnitude of increase of specific energy of approximately 20 – 30 J/mm^3 with a worn wheel is quite high and this can have a significant effect on the process whereby as the wheel wears the risk of induced thermal damage increases. Figure 4.18 also shows area specific power calculated for the tests. The trend in area specific power, P_c'' was found

to be quite similar to that of specific energy, with a significant difference in area specific power for a new and worn wheel illustrated.

4.2 Establishing key process metrics

4.2.1 Experimental setup: Taguchi L16 test array

The next set of experiments aimed to establish the influence of a variety of process parameters and tool wear on key process metrics including power, specific energy and surface roughness. Taguchi methods can be used for screening purposes, when the experimenter is interested in addressing main effects in an efficient manner with a minimum of experimental tests. Taguchi test arrays are fractional factorial experiments. The fractional factorial design focuses on main effects and lower-order interactions while assuming that higher order interactions between the variables do not exist. Such designs are suitable for a screening process, where many parameter settings have to be selected and it is necessary to keep the study size at a minimum number of tests [199]. In the case of this abrasive machining process the existence of main effects and their associated magnitudes are of interest, rather than interactions between the factors as it is likely that the interaction effects are rather small in comparison to the main effects.

This study utilized a modified L16 Taguchi fractional factorial orthogonal array with analysis of variance (ANOVA). Modified refers to the fact that the array is customised based upon the number of levels each factor has, where in this case there are four levels for two of the factors, and two levels for the remaining two factors.

Analysis of variance involves partitioning of the total variability of a response into its individual components. The total sum of squares and degrees of freedom are broken up into components associated with the structure of the factorial data collection process. Analysis of variance essentially extends the two-sample t-test for testing the equality of two population means to a more general null hypothesis of comparing the equality of more than two means. One of the main results from an ANOVA table is the p-value. The p-value takes into account the mean difference, the sample variance and the sample size, and if the p-value is small the quantity likely has a main effect on the response variable [199-201]. The per cent contribution ratio, PCR, is calculated as [202]:

$$PCR = \frac{SS_A{}'}{SS_T} x\ 100 \tag{4.5}$$

Where;

$$SS_A' = SS_A - V_e \nu_A \tag{4.6}$$

Where SS_A' is the expected sum of squares for the main effect, A, SS_A are the calculated sum of squares, SS_T are the total calculated sum of squares V_e is the variance component for error and ν_A are the degrees of freedom for A. The percent contribution ratio is the pure sum of squares divided by the total sum of squares in order to express the impact of a factorial effect.

The test array is shown in Table 4.2, where each set of test parameters was replicated 3 times. The factor levels were chosen based on previous experience with a reasonable spread in values, for feed rate, wheel speed and depth of cut. In order to examine the effect of wheel condition a new wheel and a second wheel deemed to be near the end of its life was provided by the partner company for the duration of the test.

Test Number	Wheel Speed (m/s)	Feed Rate (mm/s)	Depth of Cut (mm)	Wheel Set
1	52	42	0.5	New
2	52	51	0.5	New
3	52	59	1	Worn
4	52	68	1	Worn
5	63	42	0.5	Worn
6	63	51	0.5	Worn
7	63	59	1	New
8	63	68	1	New
9	73	42	1	New
10	73	51	1	New
11	73	59	0.5	Worn
12	73	68	0.5	Worn
13	84	42	1	Worn
14	84	51	1	Worn
15	84	59	0.5	New
16	84	68	0.5	New

Table 4.2: Modified Taguchi L16 array

Tool wear was quantified through surface topography parameters. The areal packing density was measured using a 5MP usb polarized microscope at 20X magnification. The average of the areal packing density for 10 images of an area of $16mm^2$ for both the new and worn wheels was taken. Replicas of the wheel surface

were also taken and the wear flat area, A, was estimated from optical micrographs taken of the replicas. Surface topography measurements of the replicas were also taken using a white light interferometer, and the topography parameters of density of summits, *Sds*, summit curvature, *SSc*, and Root Mean Square Gradient, *Sdq,* which is the RMS-value of the surface slope within the sampling area, were calculated from the 3-Dimensional white light data.

Spindle active power was measured using the Sinucom Trace on the machine HMI, and cutting power data was processed in Matlab (version R2010a) with specific energy calculated for each test. The specific energy, u, was calculated through Equations 4.1 and 4.2 shown in Section 4.1, where R is the minor tool radius of 12 mm in this case and a is the depth of cut, as illustrated in Figure 4.19. For a depth of cut of 0.5 mm and 1 mm the machined track width, w, was approximately 6.8 mm and 9.6 mm respectively.

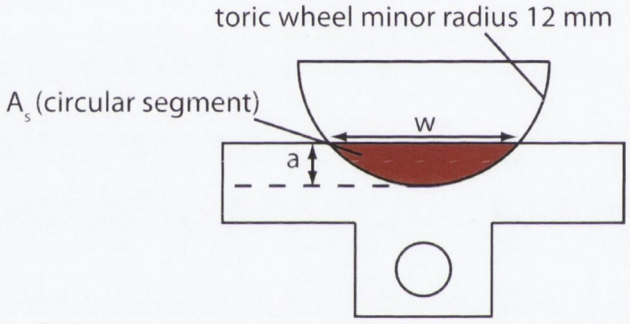


Figure 4.19: Diagram of wheel intersecting with workpiece

Surface roughness was measured with a Mitutoyo Surftest SJ-400 surface roughness profilometer. Minitab software (version 16.2) was used to design the test array, perform statistical analysis (ANOVA) and produce main effect plots.

4.2.2 Results and discussion

The test results for response variables of cutting power, specific energy and surface roughness including the mean and standard deviation of the three test replicates are shown in Table 4.3.

Test Number	Cutting Power (Watts)	Cutting Power Std. Dev. (W)	Specific Energy (J/mm^3)	Specific Energy Std. Dev. (J/mm^3)	Surface Roughness, Ra (μm)	Surface Roughness, Ra, Std. Dev. (μm)
1	2842	85	29.3	0.88	8.22	0.17
2	3227	99	27.7	0.85	8.15	0.19
3	12122	435	31.7	1.14	7.50	0.05
4	12599	246	28.8	0.56	7.63	0.09
5	7162	35	73.7	0.36	7.61	0.05
6	7187	37	61.7	0.32	7.54	0.05
7	7249	467	19.0	1.22	8.08	0.21
8	8545	281	19.6	0.64	8.18	0.11
9	7219	501	26.4	1.83	8.18	0.21
10	7399	66	22.6	0.20	8.13	0.07
11	8280	285	60.9	2.09	7.45	0.04
12	9831	519	63.2	3.34	7.60	0.04
13	13287	67	48.7	0.24	7.54	0.14
14	13667	240	41.7	0.73	7.64	0.12
15	3930	747	28.9	5.49	8.31	0.13
16	3694	250	23.8	1.61	8.05	0.23

Table 4.3: Taguchi L16 Array with results

Wheel Wear

Optical micrographs of the worn wheel surface taken with a USB microscope at 200X magnification, as shown in Figure 4.19 reveal wear on the CBN grains by attrition, grain fracture and grain pullout [79]. Surface topography parameter measurements are presented in Table 4.4. The areal packing density is calculated as 9.7 grains/mm^2 for the new wheel and 9.0 grains/mm^2 for the worn wheel. The difference between the two values indicates that a small amount of grain pullout has taken place during the wheels life.

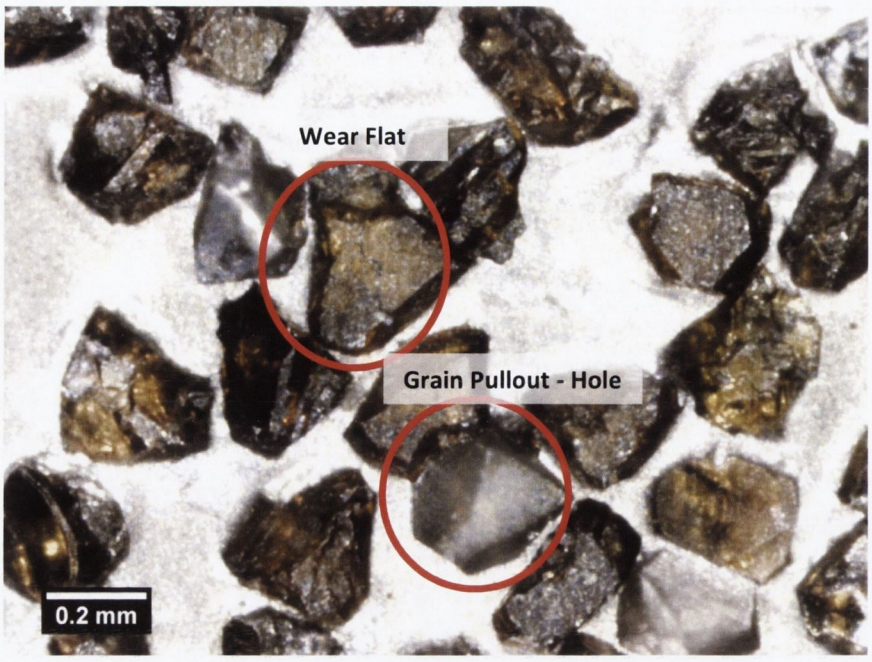


Figure 4.20: Micrograph of worn wheel surface taken with USB camera microscope at 200x magnification

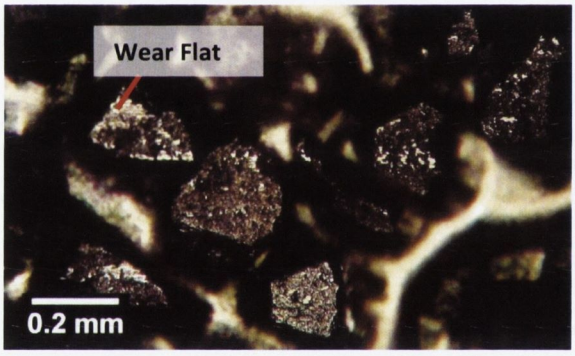


Figure 4.21: Example of wear flats taken from replica on worn wheel with Leica DNLM microscope

After the tests were completed, replicas of the wheel surface were taken using Microset 101TH material at 5 random locations around the wheel surface. Optical micrographs of the replicas were taken with a Leica DMLM microscope as shown in Figure 4.20. Subsequently the wear flat area, A, which is the percentage of the wheel surface consisting of wear flats, was estimated by calculating the wear flat by overlaying a fine grid on the optical micrographs of the replicas [40]. The average value for the wear flat area, A, was found to be 2.1% for the worn wheel. Any underestimation of wheel wear is likely to relate to inaccuracies of the replicate material.

Wheel Condition	Areal Packing Density, Co (Grains/mm^2)	Sds (Peaks/mm^2)	SSc (mm^{-1})	Sdq	Wear Flat Area (%)
New	9.7	66.2	56.2	1.01	
Worn	9.0	52.9	37.9	0.88	2.09

Table 4.4: Wheel wear metrics

Surface topography measurements of the replicas were taken using a white light interferometer. Figure 4.21 shows 3D topographic maps taken from replicas of both the new and worn B301 wheel. Topography parameters were calculated from the data and the results are shown in Table 4.5. The summit curvature parameter, *SSc,* is shown to be greater for the new wheel versus the worn. The value for the root mean square gradient, *Sdq*, was also comparatively larger, indicating that in general the summits on the new wheel had steeper slopes and a more pronounced curvature parameter, essentially implying that the new grains were sharper than the grains on the worn wheel. The density of summits parameter, *Sds,* indicates the presence of a greater number of sharp peaks per mm^2 for the new wheel than for the worn. This is in line with previous observations for 3D topography of wheel wear [203]. There is clearly a considerable difference between the new and worn wheels in terms of grain morphology, whereas the concentration of grains does not vary by a large amount.

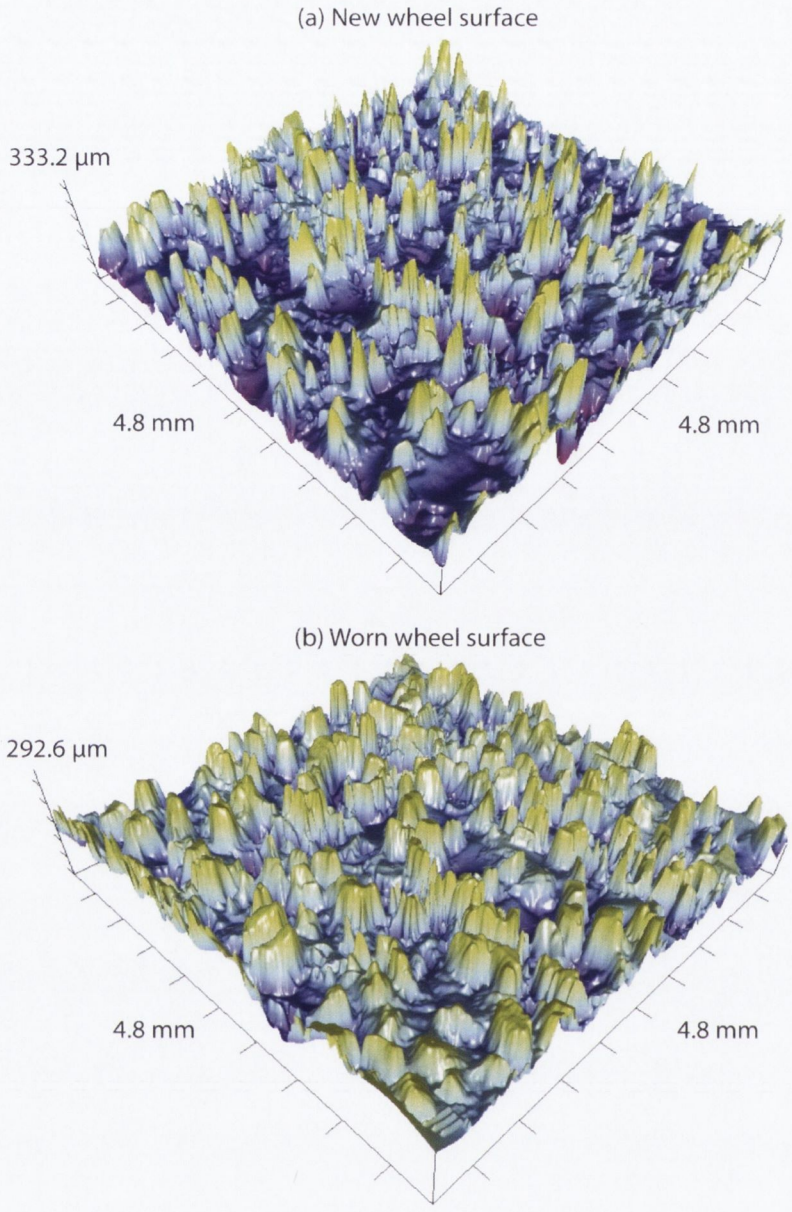


Figure 4.22: 3D Topographic maps of (a) New B301 grit wheel replica surface (b) Worn B301 grit wheel replica surface

Main Effect Plots and ANOVA

Figure 4.22 and Table 4.6 show the main effects plot and corresponding ANOVA results relating to means for cutting power for the duration of machining for the tests. In general, recorded cutting power for the various parameters varied between 3 kW and 13 kW. The analysis of variance p-value identified that for the cutting power response, all of the main factors were statistically significant for the alpha value of 5%. Wheel condition had the highest per cent contribution ratio (PCR) of 52.3% for cutting power.

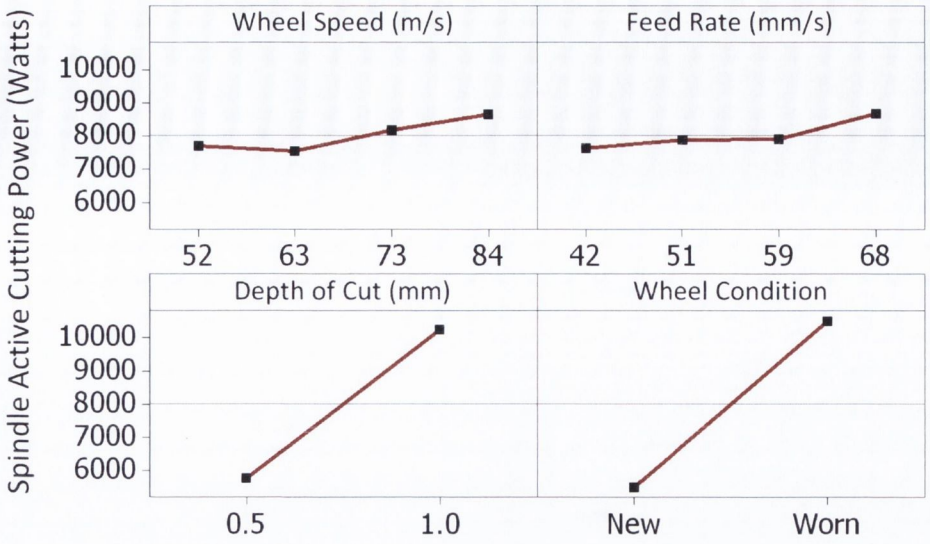


Figure 4.23: Main effect plot for cutting power

Source	DF	Seq SS	Exp SS	F	P	PCR (%)
Wheel Speed (m/s)	3	9054780	7932609	8.07	0.000	1.4
Feed Rate (mm/s)	3	7325870	6203699	6.53	0.001	1.1
Depth of Cut (mm)	1	242111238	241737181	647.26	0.000	42.1
Wheel Condition	1	300466576	300092519	803.26	0.000	52.3
Error	39	14588213				3.1
Total	47	573546677				

DF = Degrees of freedom
Seq SS = Sequential sums of squares
Exp SS = Expected sums of squares
F = F-test
P = Probability value
PCR = % contribution ratio

Table 4.5: ANOVA Results for cutting power

This is as expected, as power and forces have been shown previously to increase significantly with wheel wear, as illustrated in Section 4.1 [79, 89]. Depth of cut has the second highest PCR of 42.1%. Wheel speed, and feed rate both have a significant effect on the cutting power response, however their PCR values were much lower, at 1.4% and 1.1% respectively. The error level with a PCR of 3.1% was also quite low. These results show that spindle cutting power from the NC data is sensitive to a wide range of changes in process parameters, and that power monitoring in this case is a reliable indicator of tool wear over a variety of machining parameters.

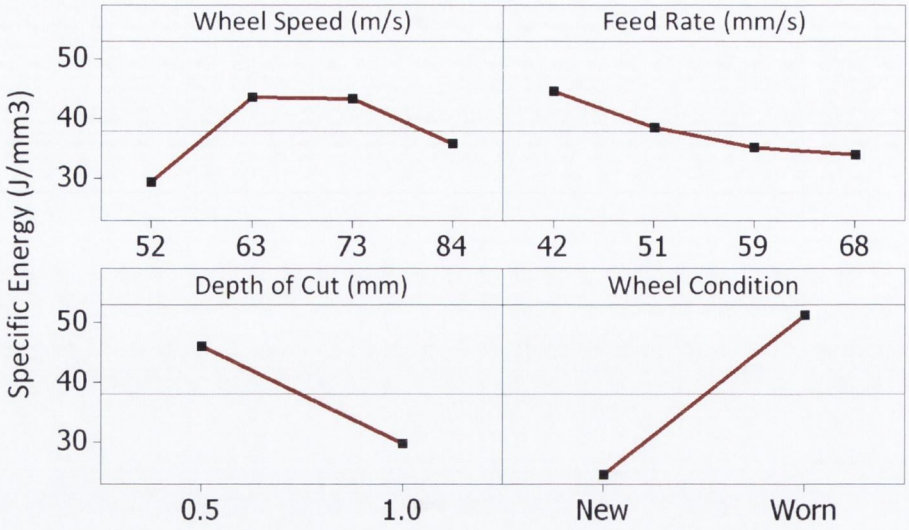


Figure 4.24: Main effect plot for specific energy

Source	DF	Seq SS	Exp SS	F	P	PCR (%)
Wheel Speed (m/s)	3	1648.8	1622.2	62.09	0.000	11.2
Feed Rate (mm/s)	3	818.9	792.3	30.84	0.000	5.4
Depth of Cut (mm)	1	3198.7	3189.8	361.39	0.000	21.9
Wheel Condition	1	8530.0	8521.1	963.73	0.000	58.6
Error	39	345.2				2.9
Total	47	14541.6				

Table 4.6: ANOVA results for specific energy

Main effect plots for means of specific energy are shown in Figure 4.24. As with cutting power, analysis of variance identified that all factors were significant at the 5% level. The increase in mean specific energy with tool wear as shown in Figure 4.24 to a value of over 50 J/mm^3 is particularly significant, with a PCR of 59%. This value is quite high, illustrating the extreme increase in energy entering the workpiece as the tool wears. The other contributing factors towards increased specific energy in the process are the wheel speed and feed rate. With a relatively slow wheel speed and feed rate of 63 m/s and 42 mm/s respectively, along with a depth of cut of 0.5 mm and a worn wheel, the specific energy is shown to rise to a maximum test value of 74 J/mm^3.

It is also interesting to note that as the depth of cut increases from 0.5 mm to 1 mm specific energy is shown to decrease. This becomes a significant issue in terms of efficiency in machining and reducing the effect of residual stress – with a larger depth of cut the energy is dispersed over a greater surface area and thus the specific energy is reduced. Temperatures generated during the grinding process are known to be a direct

consequence of the energy going into the process [40]. Consequently, specific energy has been used previously as a burn threshold method for avoiding thermal damage on the workpiece [65, 66, 204]. Ensuring that temperatures in the process are as low as possible is also beneficial in terms of avoiding residual stresses. Residual tensile stresses, which can be responsible for deformation of the workpiece after machining, are caused mainly by thermally induced stresses and deformation associated with the temperatures during the process [53]. Therefore lower specific energies during the process are desirable equally in terms of reducing the risk of thermal damage and of residual stresses.

Another interesting point to note is that an increase in feed rate results in a decrease in specific energy. This is in agreement with other publications for different metal alloys, where increased material removal rates have resulted in lower specific energy [66, 205]. The volumetric removal rates in this case ranged from 97 mm^3/s to 473 mm^3/s. The results therefore indicate the most optimal conditions for low specific energy would be to run the process with increased volumetric removal rates in order to avoid high specific energies during machining. This may be particularly beneficial when tool wear starts to become a significant factor as the wheel approaches the end of its useful life. Further work needs to be undertaken in order to determine the optimal volumetric removal rate with respect to specific energy and temperature. Maximum permissible forces in the machining clamp and spindle may also be an issue when considering an increase in volumetric removal rates.

Figure 4.25 shows the main effect plots for means of the average surface roughness, Ra value. The Ra values quoted are quite high, ranging from 7.5 μm and 8.1 μm. This is due to the geometric influence of the curved profile of the machined track. As expected, the workpiece surface roughness was shown to decrease with wheel wear, with a correspondingly high PCR of 79% [79]. A considerable difference in the Ra value is shown between the new and worn wheels of approximately 0.6 μm.

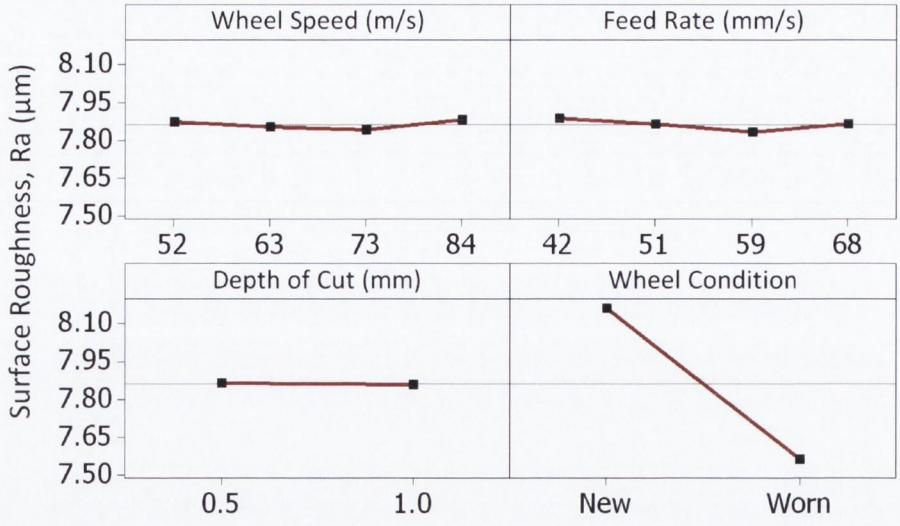


Figure 4.25: Main effect plot for surface roughness (µm)

Source	DF	Seq SS	Exp SS	F	P	PCR (%)
Wheel Speed (m/s)	3	0.01277	-0.06982	0.15	0.926	0.0
Feed Rate (mm/s)	3	0.01679	-0.0658	0.20	0.894	0.0
Depth of Cut (mm)	1	0.00035	-0.02718	0.01	0.911	0.0
Wheel Condition	1	4.30441	4.27688	156.36	0.000	79.1
Error	39	1.07364				20.9
Total	47	5.40797				

Table 4.7: ANOVA results for surface roughness (µm)

The level of error for the surface roughness ANOVA results is also high with a PCR of 21%. This is likely due to the highly variable surface produced by grinding with a relatively large mean grain diameter of 301 µm. The results for wheel speed, feed rate and depth of cut show little change in the surface roughness value between parameters. Therefore an increase in the material removal rate during machining could be achieved with minimal effect on surface roughness, which in turn could be beneficial in terms of avoiding high energy and temperatures.

Figure 4.26 and Figure 4.27 demonstrate the signal to noise ratio for cutting power and surface roughness. The signal-to-noise or S/N ratio in this case is defined as:

$$S/N = 10log_{10}\left(\frac{\mu^2}{\sigma^2}\right) \tag{4.7}$$

Where μ is the mean or average and σ is the standard deviation. The SN ratio is essentially the ratio of sensitivity to variability squared. The SN ratio is typically expressed in decibels, dB. Higher values of the signal-to-noise ratio, *S/N*, indicate control factor settings that minimize the effects of the noise factors. Often, Taguchi designs are used to identify optimal control factor settings that make the process or product robust, or resistant to variation from the noise factors. In terms of obtaining the best signal from the process, a new wheel affects the signal adversely for both the responses of cutting power and surface roughness. This is likely due to the cutting variability from the various sharp grains that can be found on a new tool. Increased values of feed rate and wheel speed also produce increased signal variation for cutting power.

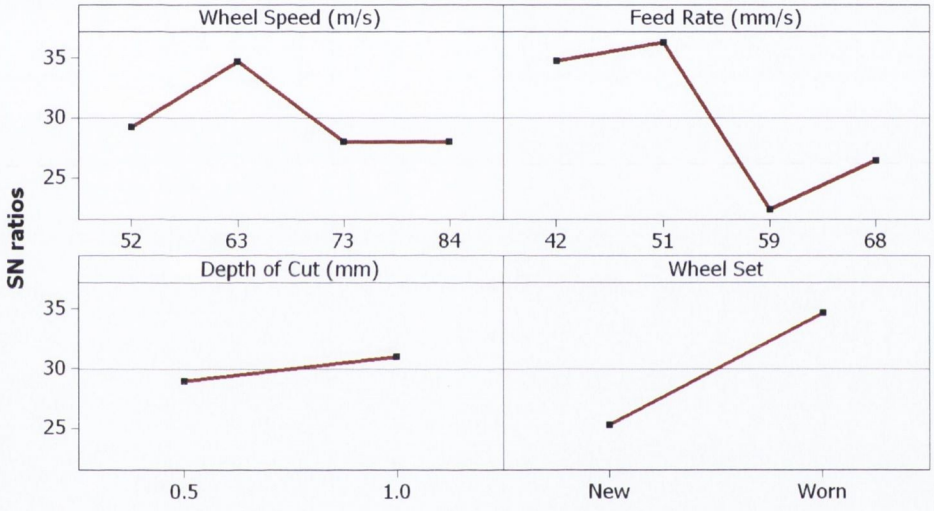


Figure 4.26: Spindle cutting power signal to noise ratio for Taguchi L16 array

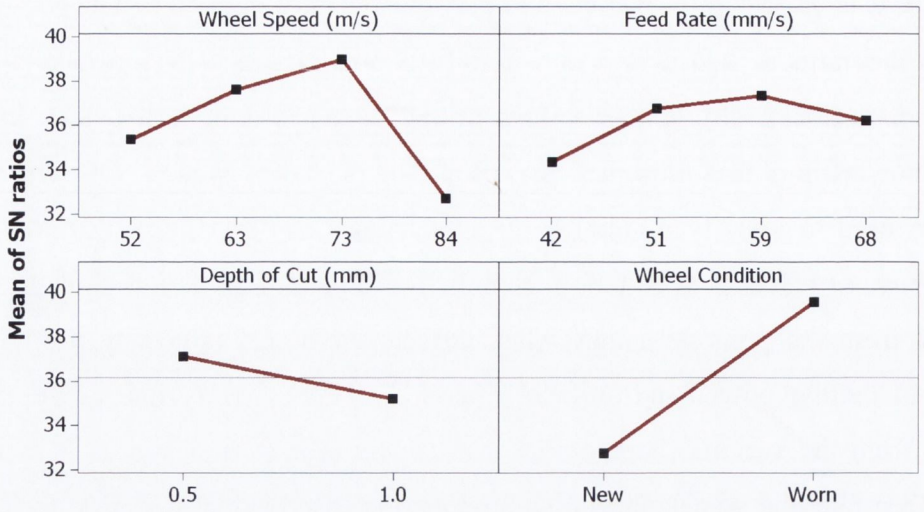


Figure 4.27: Surface roughness signal to noise ratio for Taguchi L16 array

4.3 Feed rate effect

Based on the results from Section 4.2 a test was designed to establish the specific energy values at increased volumetric removal rates. The effect of increased feed rate for a fixed wheel speed of 84 m/s and depth of cut of 0.8 mm is illustrated in Figure 4.28. The average of three tests was taken for each point. Figure 4.28 illustrates that even with a very large increase in feed rate, the specific energy remains at the same low value of approximately 10 J/mm^3. This result clearly illustrates the potential in the process for increasing feed rate without adversely affecting the specific energy.

The limit to this analysis is that it was performed for one depth of cut value. Depth of cut has a significant effect on the magnitude of specific energy in the process, and the collated results from various depth of cut tests in Figure 4.29 illustrate the effect of varying depth of cut at a set feed rate of 55 mm/s. It is evident that for lower depths of cut of $a < 0.3$ mm, there is a significant increase in specific energy. In order to maintain a low level of specific energy the overall volumetric removal rate, Q_w, would need to be kept constant during the process thereby necessitating a further increase in feed rate at low depths of cut.

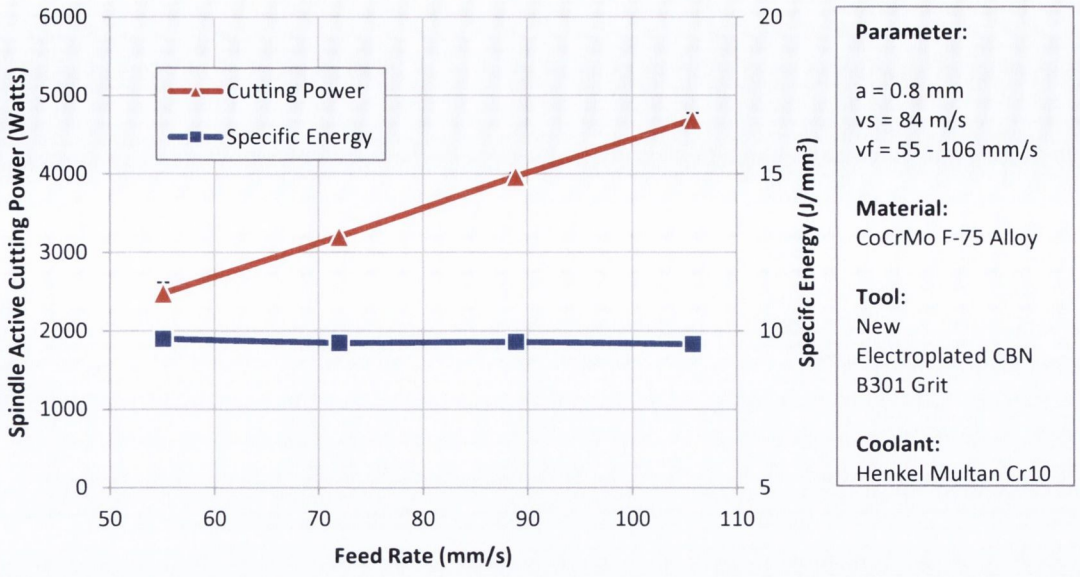


Figure 4.28: Cutting power and specific energy for increased feed rate

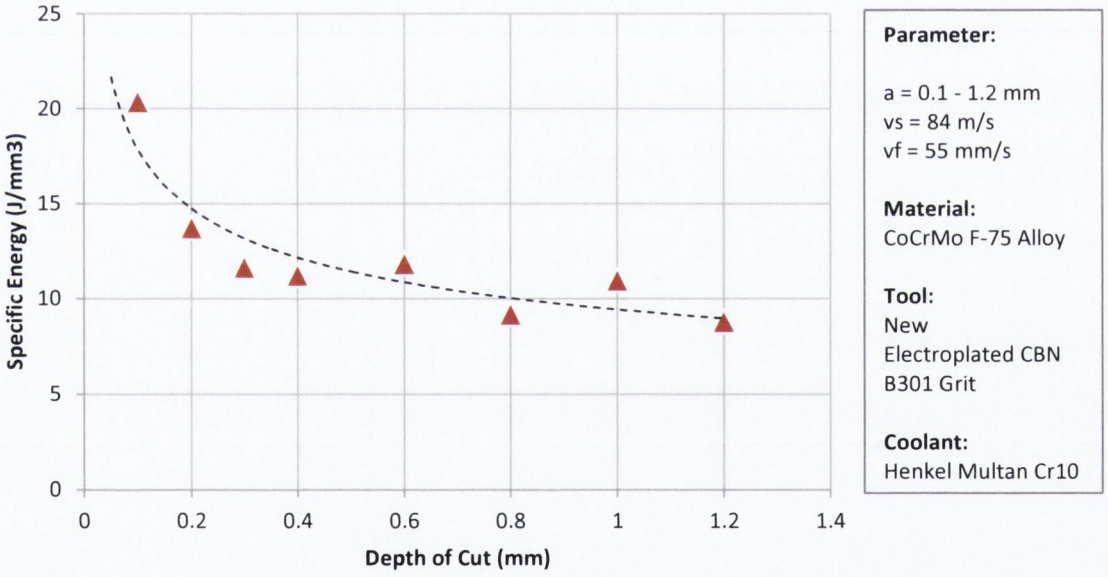


Figure 4.29: Collated specific energy depth of cut test results

4.4 Summary

Internal machine signals were used to monitor the abrasive machining process. Spindle cutting power was found to be the most appropriate signal for monitoring and characterisation of the grinding process and feed drive current was shown to be a useful indicator of the material removed in the process. Spindle cutting power was shown to

increase almost linearly with depth of cut for grinding of Cobalt Chrome alloy with a new electroplated CBN wheel between the depths of cut of 0.2 – 1.2 mm. A large increase in cutting power in the range of 2 – 7 kW was found when grinding with a worn wheel with a corresponding increase in specific energy of approximately 20 – 30 J/mm3 with machining parameters analogous to those typically used in the abrasive machining of femoral implants.

Through a Taguchi L16 design of experiment, all factors including depth of cut, wheel speed, feed rate and wheel wear were found to be significant main effects on the spindle cutting power signal. An increase in feed rate was shown to result in a decrease in specific energy of approximately 10 J/mm3. Wheel wear was shown to have a significant increase on specific energy in the range of 25 J/mm3. Wheel wear was finally shown to be the only main effect on workpiece surface roughness.

An increase in feed rate from 55 mm/s to 106 mm/s showed that at a constant depth of cut of 0.8mm and wheel speed of 84 m/s, despite an increase in spindle cutting power of approximately 2 kW, specific energy remained relatively unchanged at approximately 10 J/mm3.

Chapter 5

Development of position-oriented-process monitoring methodology for freeform surfaces

During abrasive machining of freeform surface alternating machining conditions can give rise to indeterminate machining characteristics. Abrasive machining characteristics of freeform surfaces can be better understood if a position-oriented approach is applied, where process monitoring metrics such as power, tool-workpiece engagement and specific energy are evaluated over the entire toolpath and machined surface. The following approach is therefore taken towards development of an analysis method to evaluate process monitoring quantities during freeform abrasive machining:

(a) Determination of the material removed in the process through a developed laser measurement system
(b) Development of an area-based tool-workpiece engagement model based upon laser distance measurements
(c) Development of a machine power and position data analysis method
(d) Development of a combined data analysis strategy with a position-oriented specific energy graph over the course of a freeform toolpath as an output metric

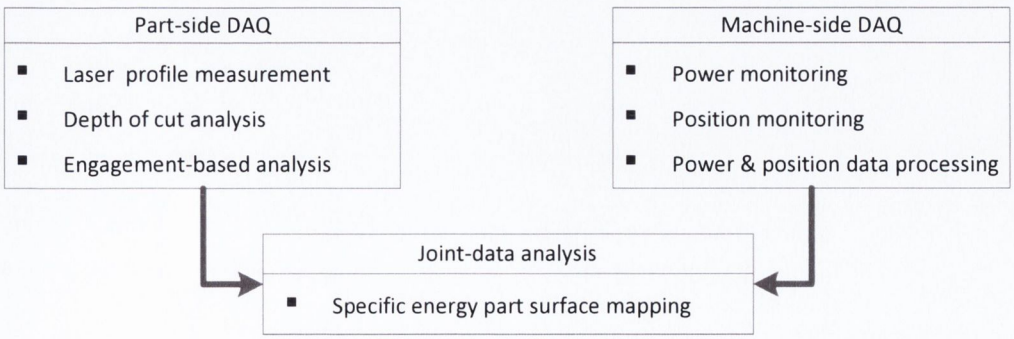


Figure 5.1: Schematic representation of position-oriented power monitoring strategy

5.1 Laser measurement

Due to the nature of the freeform surface and the use of a torus shaped grinding tool the engagement situation during abrasive machining is constantly changing. Typically, machining depths of cut parameters are specified along a toolpath dependant on the part to be machined and the tool that the machining is to be performed with. With freeform machining, the situation is more complex. In freeform machining the tool spindle follows coordinates based off a finished product CAD drawing. This type of toolpath is known as an offset or parallel toolpath [206].

Such toolpaths follow the contours of a final part shape regardless of what material may be encountered along the way. As a result, depending on the casting provided, the depth of cut can be highly variable and excess material or flashing left on the castings can further add to the variability in engagement. Furthermore, the variable contours and curves of a freeform surface and the constantly changing interaction between the curved surface of the grinding wheel add to the overall variability in the engagement situation.

As the tool-workpiece engagement has a large influence on process forces, power and machining efficiency, it is of benefit to undertake an analysis of the engagement situation during machining. It is difficult to perform such an analysis through purely geometric considerations. In order to ascertain the amount of material removed and the change in depth of cut over the surface of a freeform part it is more convenient to measure this quantity directly. This can be achieved through laser profile measurement of the part before and after machining.

The difference in material removed before and after abrasive machining can be detected using a laser sensor that measures displacement through the principle of laser triangulation [168]. The laser sensor used in this research provides a linear measuring range of 50 mm and a resolution of 0.003 mm. The associated screw lead is 25.4 mm with a linear resolution of 0.00254 mm, close to the resolution of the laser displacement sensor used. A CAD drawing of the laser measurement rig developed for this research is illustrated in Figure 5.2, specification and operation of the measurement rig is detailed previously in Section 3.5.

The lasers resolution was further examined by measuring the step change on an artefact part machined through surface grinding. Measurements were taken on each step and repeated 5 times. Measurements of the artefact step height were also taken with a

Mitutoyo dial gauge with a stated resolution of 0.01 mm. As shown in Figure 5.3 and Table 5.1 the measurements from the laser sensor indicate changes of depth of cut of approximately 0.05 mm can be detected. The standard deviation measured for the laser of between 0.008 - 0.015 mm is greater than the stated laser resolution of 0.008 mm, this may be due to machining errors in the surface of the part. The results suggest that changes in depth of cut over 0.1 mm should pose no problem for the laser to detect.

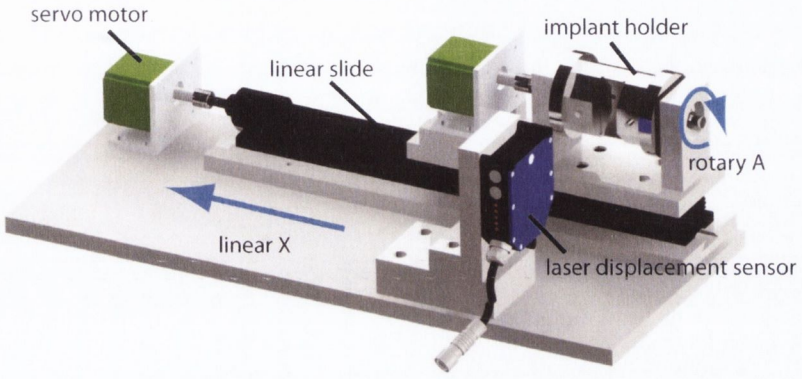


Figure 5.2: Laser measurement rig

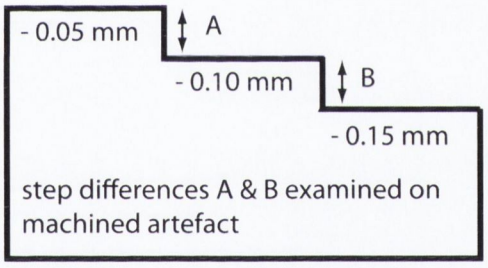


Figure 5.3: Laser artefact schematic with 0.05 mm steps of width 3mm ground into part

	Laser		Dial Gauge	
	A	B	A	B
Mean (mm)	0.040	0.039	0.044	0.050
Std. Deviation (mm)	0.015	0.008	0.005	0.000

Table 5.1: Mean and standard deviation of five measurements for artefact steps, A and B

The laser was subsequently tested on the curved freeform surface of a typical femoral implant. An example of three repeat scans over the same cross-section of the implant is shown in Figure 5.4. Figure 5.4 (left) shows the laser displacement signal recorded for three repeat passes over the same cross-section over the implant. This corresponds to a rotation of 192.6° of the holder. Figure 5.4 (right) shows the standard

deviation for the three repetitions along each X-position over the profile. The mean of the standard deviations for each point is approximately 0.0075 mm, with the standard deviation outlier of 0.07 mm shown in Figure 5.4 (right) removed.

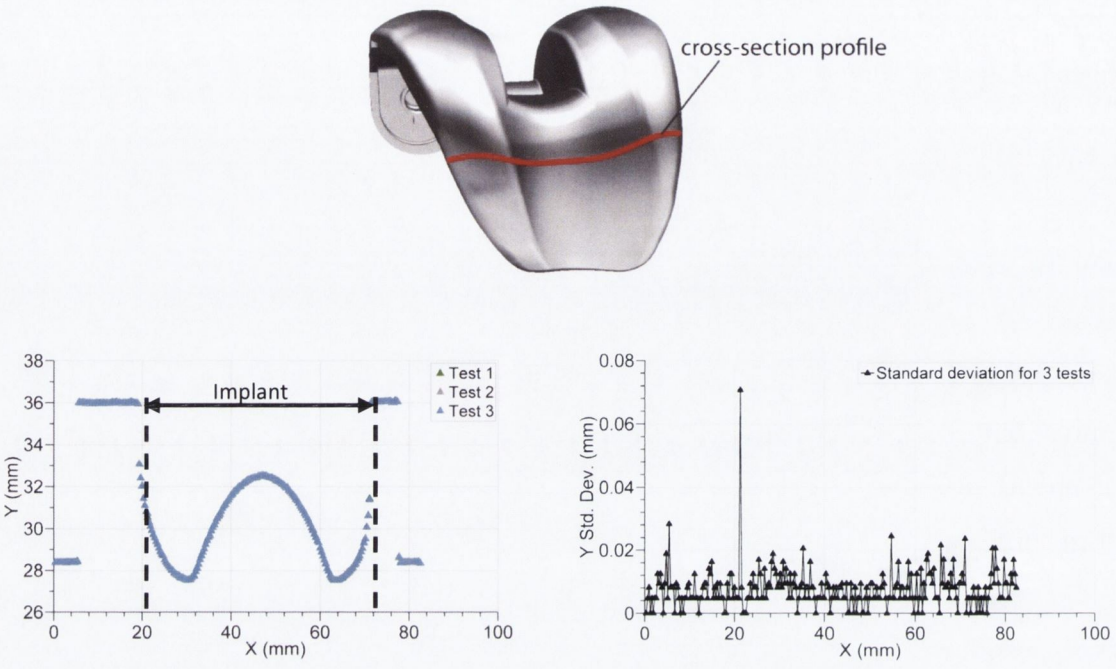


Figure 5.4: Repeat laser scans across selected implant profile (left), standard deviation of three repeat scans (right)

To examine the difference between the implant before and after machining it is necessary to acquire a full surface scan of the implant. A 3D point cloud of the implant surface was therefore acquired before and after abrasive machining. In order to obtain a point cloud representation of the whole implant approximately 260 line scans with a rotary A-axis spacing of 0.9 degrees were taken over the surface of the implant. This number of scans was determined to contain sufficient detail for an evaluation of the implant surface as it captured the geometric features of the surface as illustrated in Figure 5.5. The line scan spacing in the X-direction corresponded to a measured point every 0.3175 mm up to 82.55 mm which covered the surface of the implant and provided a sample size of 260 points in the X-direction. This resulted in a square matrix pointcloud of 260 x 260 Cartesian co-ordinates when the data was processed. The data was processed by saving to text files laser profile scans in the form of displacement in the X-direction, the laser displacement measurement in the Y-direction as well as the corresponding rotation in the A-direction and then subsequently processing the text files

in Matlab where the data was converted from Polar to Cartesian co-ordinates through the following formulae:

$$R = y_c - y_{dist} \tag{5.1}$$

$$y = R\cos\theta \tag{5.2}$$

$$z = R\sin\theta \tag{5.3}$$

The *X*, *Y* and *Z* coordinates were then rotated through 180° by multiplying by a Euclidean rotation matrix given in the form;

$$Rx = \begin{bmatrix} 1 & 0 & 0 \\ 0 & \cos rx & -\sin rx \\ 0 & \sin rx & \cos rx \end{bmatrix} \tag{5.4}$$

$$[x' \quad y' \quad z'] = [x \quad y \quad z]Rx \tag{5.5}$$

Figure 5.5 shows a surface plot of the rotated line scans from laser measurement of a cast implant (left) and the same implant post-abrasive machining (right).

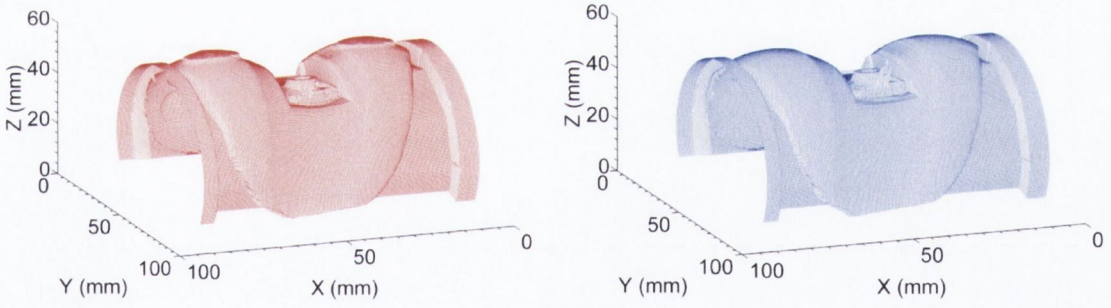


Figure 5.5: Laser measurements of cast implant (left), laser measurements of same implant post-grinding (right)

When a part is removed from the holder before machining and then replaced after machining, there is an associated error positioning the part in the same place. The part may have moved at a micron level depending on the accuracy of the clamping device, exactly the same homing position may not be achieved by the sensor between scans and there may be a slight change in environment and light scattering conditions. To minimise such error and ensure that the laser scans before and after machining match correctly a registration and data matching/transformation algorithm was developed. This

algorithm utilizes kD-Tree matching, based on an iterative closest point algorithm developed by Wilm which was used to match point cloud data from positron emission tomography (PET) and structured light scanning of the human face [207].

The algorithm developed here first structures the point cloud through a k-Dimensional tree, then minimizes the Euclidean distance between neighbouring points in the two data sets. The K-Nearest Neighbour search object and kD-Tree were initialized in Matlab through the Statistics toolbox [174, 208]. Figure 5.6 illustrates an overlaid matched cast and post-machined point cloud result. For the purposes of this application the highest 1% of distances between scans are disregarded by the algorithm in order to avoid a situation where matching is skewed by outlier points from laser light scattering.

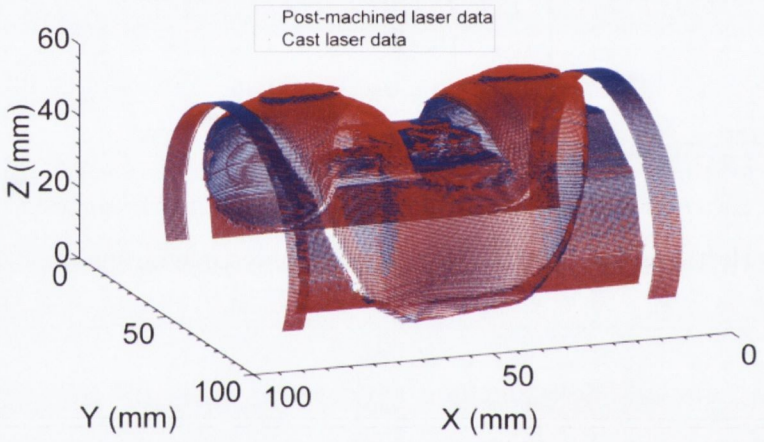


Figure 5.6: kD-Tree Algorithm Result

The RMS error, d_{RMS}, is defined as the overall root mean square distance between the cast laser scan and the post-machined scan where D_{ICP} is the cast-point cloud which the translation and rotation determined from the minimum distance direction from kD-tree matching is applied to, and M is the reference point cloud taken as the post-abrasive machining point cloud scan, as given by Equation 5.6.

$$d_{RMS} = \sum_{i=1}^{n} \|D_{ICP} - M\|^2 \tag{5.6}$$

Figure 5.7 shows the reduction in the RMS distance between a cast laser scan and a post-machined laser scan over number of iterations, n, through use of the kD-Tree

matching algorithm. The maximum overall RMS distance was reduced to approximately 0.24 mm over 20 iterations in this case.

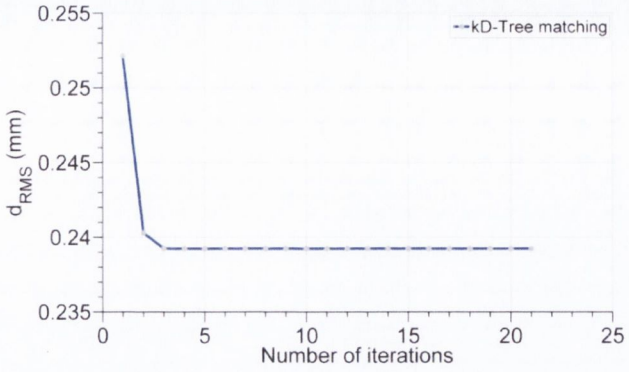


Figure 5.7: kD-Tree RMS distance results comparison

To visualize the material removed it was necessary to develop a way of determining the distance between the two acquired point clouds of the cast and post-machined implant. A known method of calculating the distance between point sets is the Euclidean distance metric, as calculated through Equation 5.7. This equation provides a positive distance between points for the set of real numbers, $\mathbb{R}^n$.

$$d = \sqrt{(x_1 - x_2)^2 + (y_1 - y_2)^2 + (z_1 - z_2)^2} \tag{5.7}$$

However, for more complex curved surfaces, it is necessary to calculate a signed distance, either positive or negative so that actual material removal can be identified.

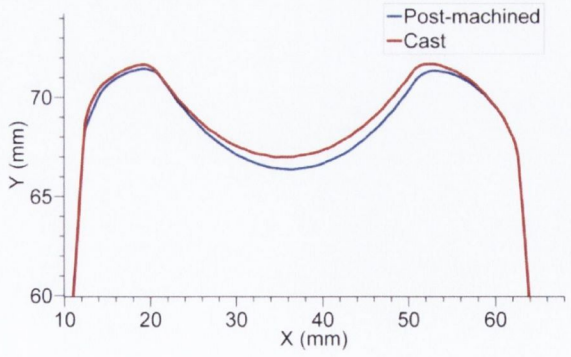


Figure 5.8: Example cast and post-machined laser measurement result

Due to the effect of rotation and translation point cloud matching through the kD-tree algorithm, the line scan profiles will not lie on exactly the same plane. In order to

obtain the laser measurements in the orientation illustrated in Figure 5.8 it is necessary to project the curves of interest onto the same plane. In order to achieve this a reference plane was first calculated for the post-machined laser line scan (M) through principle component analysis in Matlab. Principle component analysis is a well-known technique which identifies the most influential similarities or differences in a given data set. For example, principle component analysis has recently been used in conjunction with an iterative closest point matching method in order to generate statistical shape models to examine the major modes and differences of sizes and three-dimensional shape variation of male and female clavicle bones [209].

The Matlab princomp() function returns the coefficient set for the first two principal components which define vectors that form a basis for the plane of best fit. The third principal component is orthogonal to the first two, and its coefficients define the normal vector of the plane, n [173, 174, 210]. Letting U be a matrix which is the orthonormal basis for a subspace or plane W of $\mathbb{R}^n$ the projection vector for projection of a vector v onto a plane W is [211];

$$proj_w v = UU^T v \tag{5.8}$$

The null() function in Matlab provides an orthonormal basis for the null space of a matrix. The projection of M_2 onto the plane or subspace W given by M was therefore calculated as shown in Equation 5.10 where M_R is the resultant projected matrix onto the plane W. Figure 5.9 illustrates this.

$$proj_v M_2 = null(N)null(N)^T v \tag{5.9}$$

$$M_R = proj_v M_2 + M_2 \tag{5.10}$$

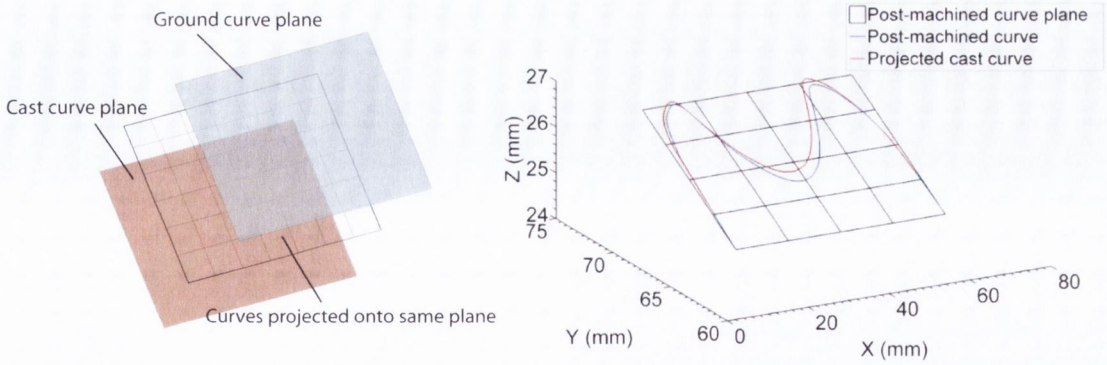


Figure 5.9: Projection of laser curves onto a common plane

In order to calculate the distance between line scans it was necessary to further rotate each curve such that it lies exclusively in the X-Y plane. The X, Y and Z coordinates were rotated by multiplying by a Euclidean rotation matrix given by Equations 5.4 and 5.5. The distance between points can then be calculated as given by Equation 5.11.

$$d_s = y_1 - y_2 \tag{5.11}$$

Figure 5.10 illustrates a post-machined implant laser scan with the colormap corresponding to the distance as calculated in Equation 5.11. The areas shown in brown illustrate a large difference between the cast and ground implant where a significant amount of material has been removed, whereas the areas shown in dark blue illustrate a difference of zero, for example on the implant holder, which does not move between scans therefore a difference of zero is expected. These results are encouraging and show that laser measurement is an ideal way to identify material removed where it is not specified for a process.

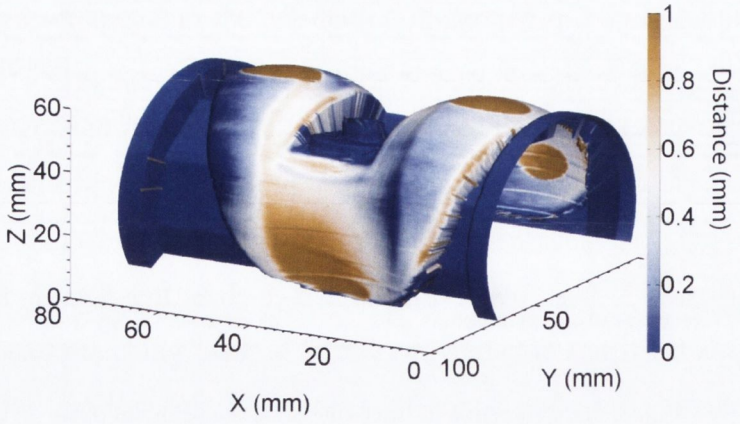


Figure 5.10: Cast and ground distance comparison, colormap corresponding to distance (mm)

In order to perform calculations directly on the implant surface it is necessary to perform segmentation on the laser data. Data segmentation was performed by deleting data at the edges of the scan in the X-direction. The edges of the implant surface were identified through calculating the slope between points along the X-direction, with the largest slopes identifying the edges of the implant and the corresponding points then deleted. Slopes were calculated between each point along the X-direction, with the largest slopes identifying the edges of the implant. The result of data segmentation is illustrated in Figure 5.11. As mentioned previously there is considerable variation present in the distance or depth of cut taken over the surface of the part. Figure 5.12 illustrates further the variation in depth of cut along the X-axis, where it can be seen there is a large distribution of values less than 0.5 mm.

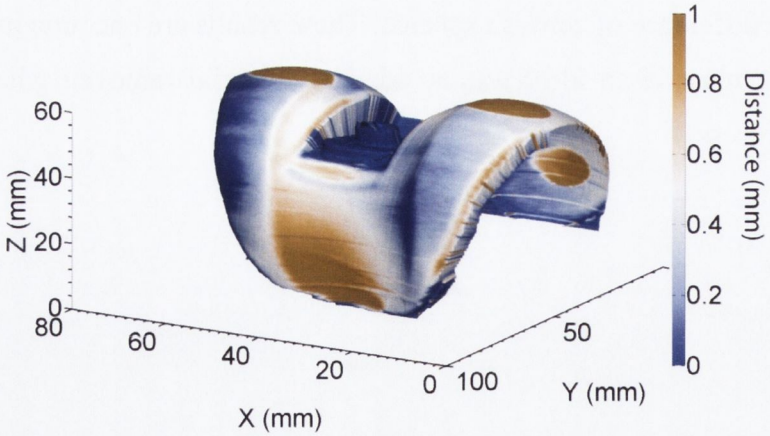


Figure 5.11: Segmented data, colourmap corresponding to distance (mm)

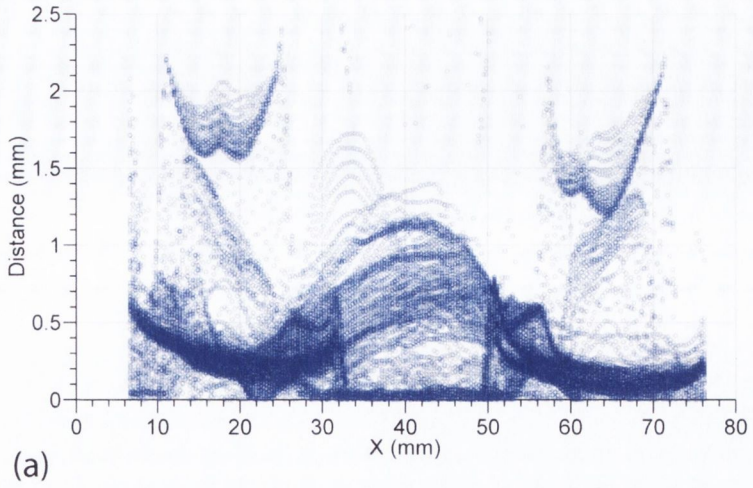


Figure 5.12: Depth of cut or distance shown over X-axis for femoral implant

While calculation of the distance between cast and post-machined laser scans in order to illustrate the material removed from abrasive machining is useful, calculation of the area of engagement between the tool and workpiece during machining is also necessary. This metric can then be used to calculate further parameters such as specific energy over the surface of the implant.

5.2 Engagement analysis

Engagement model based on laser distance measurements

In order to perform an engagement analysis utilizing the acquired laser data, it was necessary to reduce the 3-Dimensional problem to that of a 2-D problem. Figure 5.13 illustrates a grinding wheel. Of the two radii on the wheel the minor toric radius in the X-Z plane has a larger influence on form error and engaged area, relating to toolpath spacing and depth of cut and the shape of the workpiece whether it is convex, concave or planar. On the other hand the major toric radius is significantly influenced by the wheel speed and feed rate in that direction [30]. The following analysis focuses on estimation of engagement in the X-Z plane for calculation of the grinding specific energy.

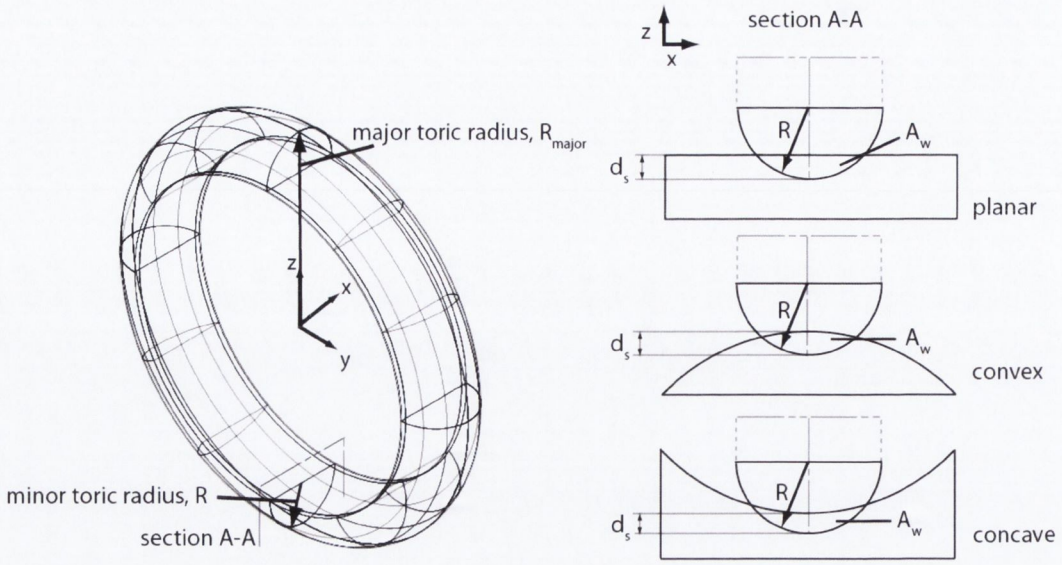


Figure 5.13: Wireframe illustration of grinding wheel and engagement conditions that may be encountered during freeform grinding, where d_s represents the distance between cast and post-machined laser scans, i.e. the depth of cut, R represents the minor toric radius and A_w represents the engaged area between wheel and workpiece

An outline of the algorithm developed to analyse 2D cross-sectional engagement of the minor torus tool radius based on laser measurement of the part is illustrated in Figure 5.14. Engaged area in this case refers to the amount of area intersected between the tool and workpiece for each toolpath line in the 2-Dimensional X-Z plane. Each laser line scan was first projected onto an exclusive X-Y plane using the method outlined in Section 5.1. Smoothing was applied to the laser measurement profiles through the smooth() function in Matlab utilizing a default span of 5. Smoothing was applied to the laser measurement profiles through the smooth() function in Matlab utilizing a default span of 5. The smooth filter in Matlab smoothes the data using a moving average lowpass filter with filter coefficients equal to the reciprocal of the span. The filter handles the endpoints through the following results vector, yy; where yy(1) = y(1) and yy(2) = (y(1) + y(2) + y(3))/3, and the following points are a moving average over the specified span of 5 in this case. The purpose of the smoothing was in order to avoid any possible self-intersection of generated parallel curves which can occur if jagged or irregular points exist, for example near the edges of the implant.

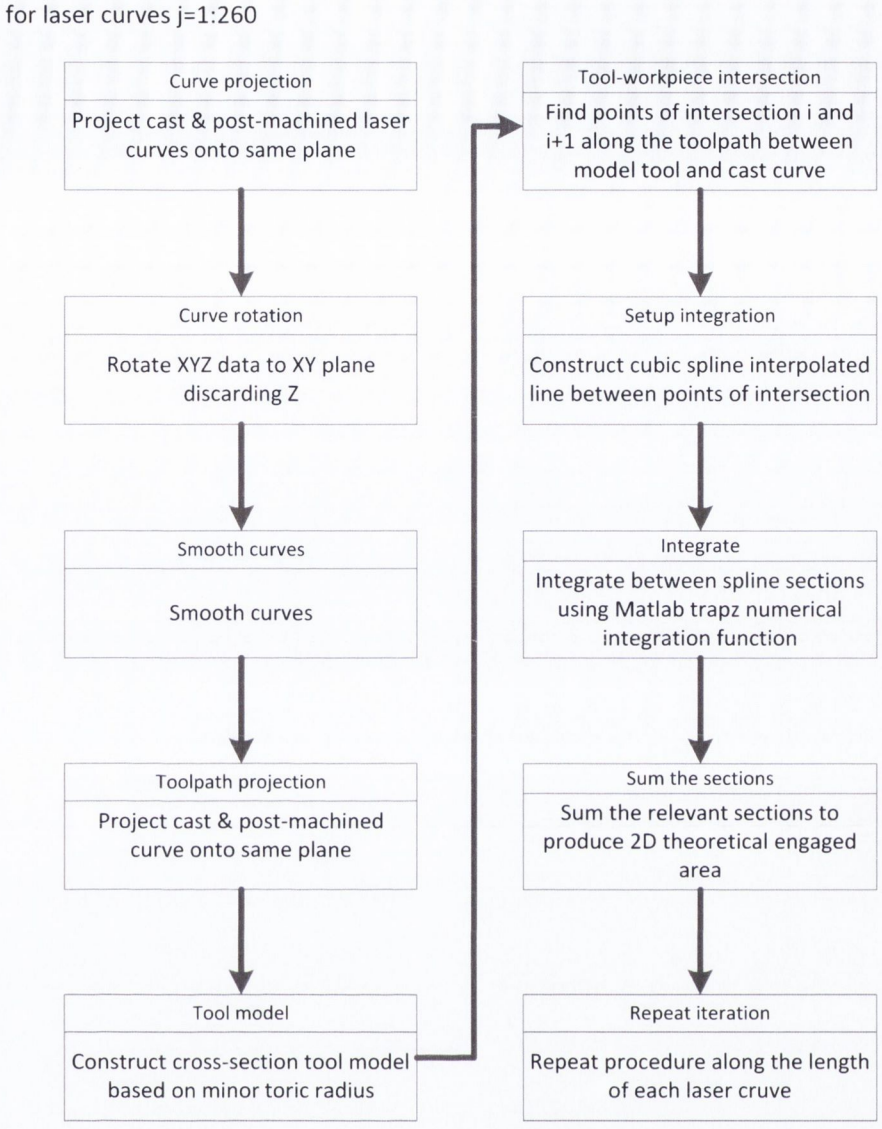


Figure 5.14: Outline of algorithm for calculating area of intersection between tool and workpiece

Parallel curves, otherwise known as 'offset' curves, are curves which are displaced from a base curve by a constant offset, either positive or negative, in the direction of the curve's normal [206]. Given a planar parametric curve, $C(t) = (x(t), y(t))$, the offset curve with an offset radius R is defined by $C_R(t) = C(t) + RN(t)$, where $N(t)$ as given by Equation 5.12 is the unit normal of $C(t)$.

$$N(t) = \frac{(y'(t), -x'(t))}{\sqrt{x'^2(t) + y'^2(t)}} \tag{5.12}$$

An offset curve was generated using the post-machined laser curve as a base curve. This was based on the assumption that the ground/post-machined laser curve provides a representation of the depth of cut that took place during abrasive machining across the corresponding implant cross-section, as well as providing a trace of the contours the machine toolpath had to follow to generate the finished surface. The offset curve is a constant distance of 12 mm corresponding to the minor tool radius, R, away from the base post-machined curve. Each point in the offset curve was separated by a distance corresponding to the set machine parameter toolpath spacing, s. Taking each point in the offset curve as a centre-point, a parametric curve was generated representing the minor tool radius circular cross-section, as illustrated in Figure 5.15 and Figure 5.16.

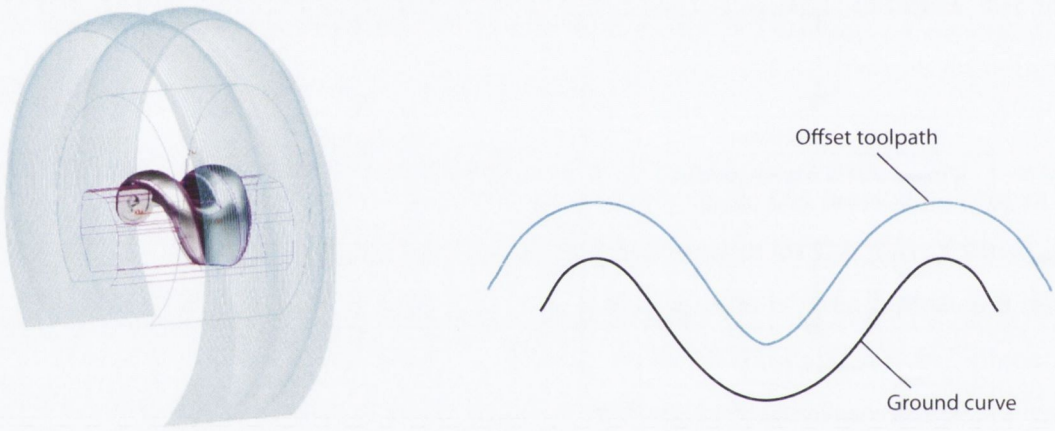


Figure 5.15: Example of an offset toolpath created in Unigraphics NX 7

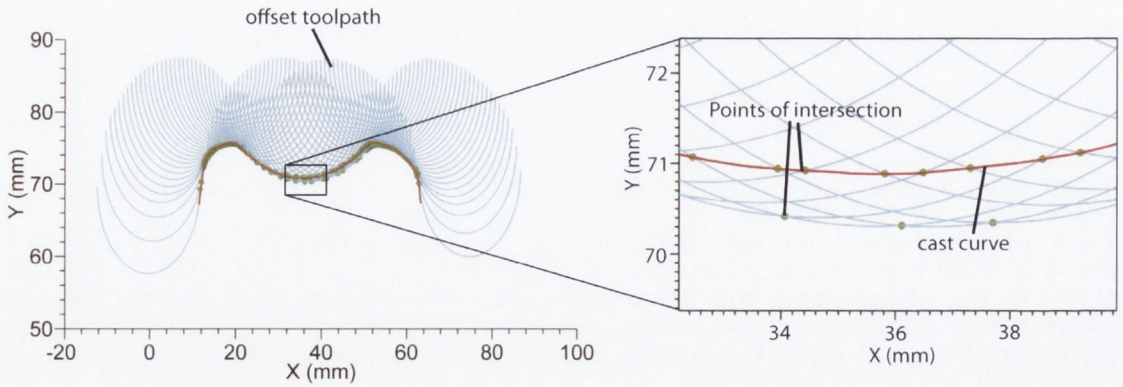


Figure 5.16: Example of offset toolpath generation and intersection with cast laser curve

The engaged area between the circular wheel cross-section and workpiece for $n > 1$ toolpaths is given by Equation 5.15 as the sum of area A_1 and A_2 as illustrated in Figure 5.17. The points of intersection between the cast laser curve, toolpath n and

toolpath *n+1* are first calculated, shown here as *a*, *b* and *c*. Point *b'* is found through interpolation from point *b* to toolpath *n+1*. The curve sections between the integration limits were approximated as cubic spline curves (*S*) based off the circular wheel-cross-section toolpath and cast laser curve. This meant that numerical integration could be performed with better resolution using the evenly spaced cubic spline curves. The area under the curve was therefore calculated using trapezoidal numerical integration through the *trapz()* function in Matlab. A_{Total} represents the total calculated area of integration for a given toolpath, n+1, and is also referred to as A_W during the course of this work.

$$A_{Total} = A_1 + A_2 \tag{5.13}$$

$$A_1 = \int_a^b S_1(x)dx - \int_a^{b\prime} S_2(x)dx \tag{5.14}$$

$$A_2 = \int_b^c S_3(x)dx - \int_{b\prime}^c S_4(x)dx \tag{5.15}$$

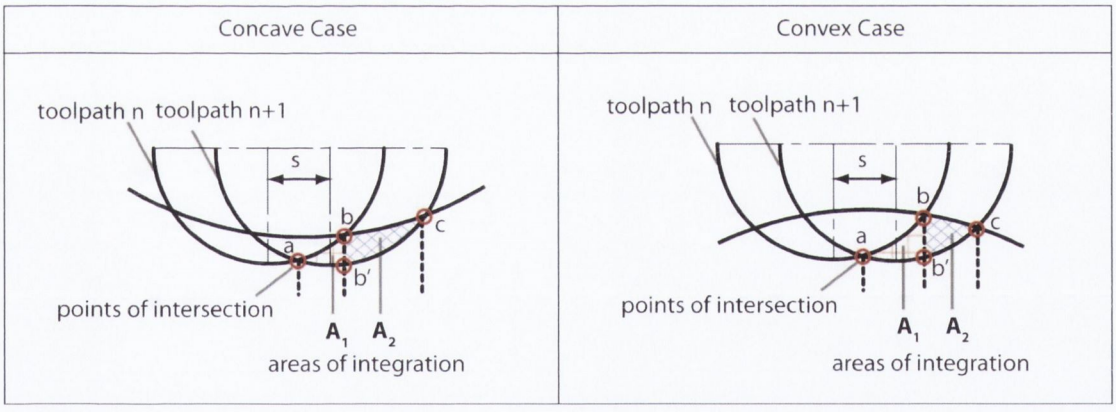


Figure 5.17: Method of calculating engaged area through integration with toolpaths & cast implant curve

5.2.1 Engagement analysis results

Initial results from engagement model based on laser measurements

Figure 5.18 illustrates calculated engaged tool-workpiece areas at various positions over the implants surface. As shown in Figure 5.18 the overall average amount

of material removal is rather small, generally less than 1 mm^2 and typically nearing 0.1 mm^2. In the example in Figure 5.18 it can also be seen that near concave areas such as the patella track, the area of engagement is increased to approximately 0.3 mm^2, whereas near convex areas such as the condyles the area of engagement remains quite small at less than 0.1 mm^2. Intuitively, the engaged area between two consecutive toolpaths can be seen to be greater for a concave workpiece radius than for a convex workpiece radius, for the range of parameters considered.

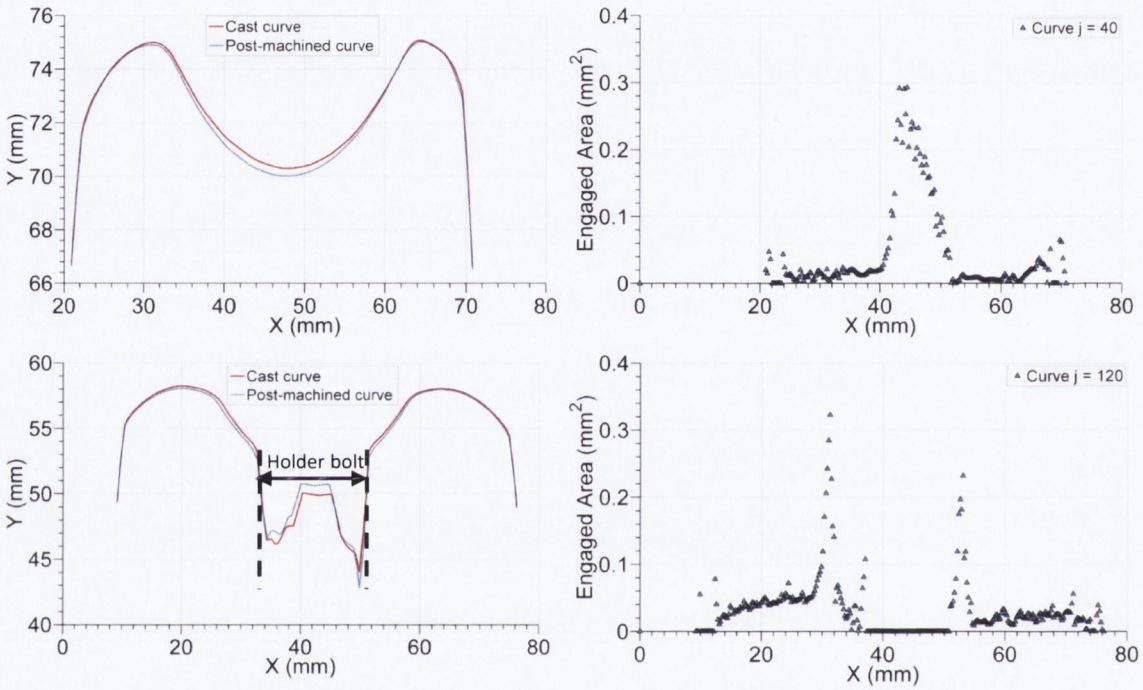


Figure 5.18: Engaged area calculation in X-direction at various positions over implant surface

Predicted engagement based on analytical model

An example of differences in engaged area with convex and concave workpiece shapes is shown in Figure 5.19, where the theoretical engaged area for two consecutive toolpaths is calculated for a variety of depths of cut and toolpath spacing between 0.1 and 2 mm. A workpiece radius, r = 22 mm, typical of what may be found on a femoral implant surface was chosen for this analysis. The theoretical engaged area shown here was calculated through the estimation of the area of intersection between three convex circles as described by Fewell, 2006 [212]. The analysis was extended to include the area of intersection between convex and concave workpiece circles with a circle representing the grinding wheel based on the minor grinding wheel toric radius.

Calculations shown in Figure 5.19 illustrate that in general a higher engaged area is to be expected with concave radiuses as compared to convex.

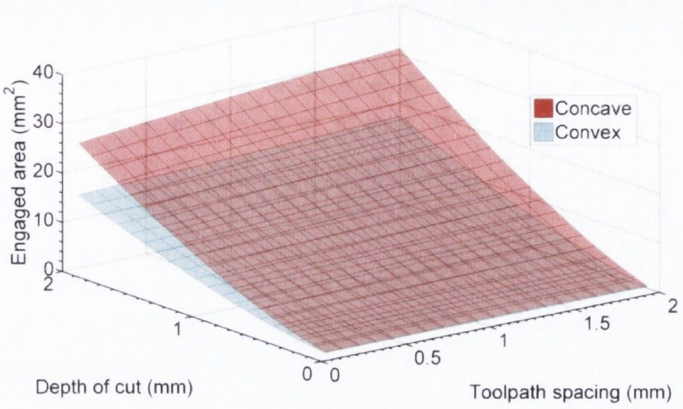


Figure 5.19: Calculated engaged area for two consecutive toolpaths, for a workpiece radius of r= 22 mm

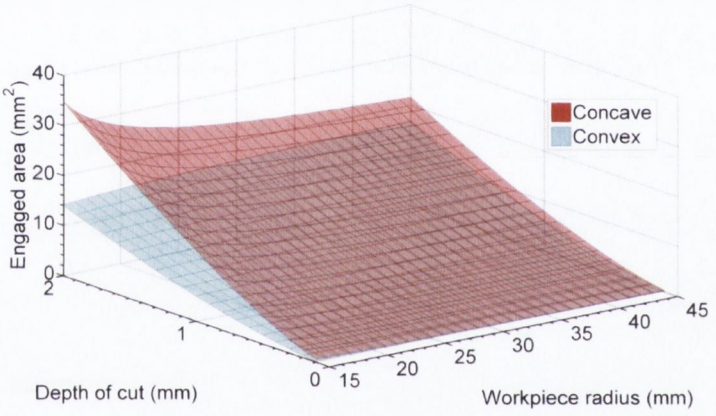


Figure 5.20: Calculated engaged area for two consecutive toolpaths for a toolpath spacing of s = 0.381 mm

The effect of an increase in workpiece radius for various depths of cut is illustrated in Figure 5.20, where the theoretical engaged area is calculated for a constant toolpath spacing of s = 0.381 mm. The radii used in these calculations correspond to radii that might be expected on a typical implant casting, and the toolpath spacing corresponds to that of a typical grinding toolpath for machining such an implant. As the workpiece radius increases the workpiece 'flattens' out, leading to a reduction in the engaged area. However, the theoretical engaged area for a concave workpiece still remains greater than for a convex-shaped workpiece, and as such is more influential on engaged area than the size of the workpiece radii. Though this model is useful for obtaining a general overview of how the engagement situation changes with convex and concave workpiece radii, the model is not refined enough to predict engagement

conditions over the course of abrasive machining of a freeform surface, therefore the method based on laser measurements and intersection with a model toolpath will be employed in order to explore engagement conditions during freeform grinding.

Results for estimated engagement model based on laser measurements

The engaged area over the surface of the implant was estimated using the method illustrated in Figure 5.17 for each of the 260 laser profile measurement curves. An example is shown in Figure 5.21, where the lower limit of estimated tool-workpiece engagement is compared to the lower limit of laser comparison measurements between a cast and post-machined implant. The error present in the laser measurements, where values less than 0.1 mm and close to 0 mm were calculated, is reflected in the estimation of engaged area, where estimates of no engagement or 0 mm^2 exist in the same locations as those in the laser measurements.

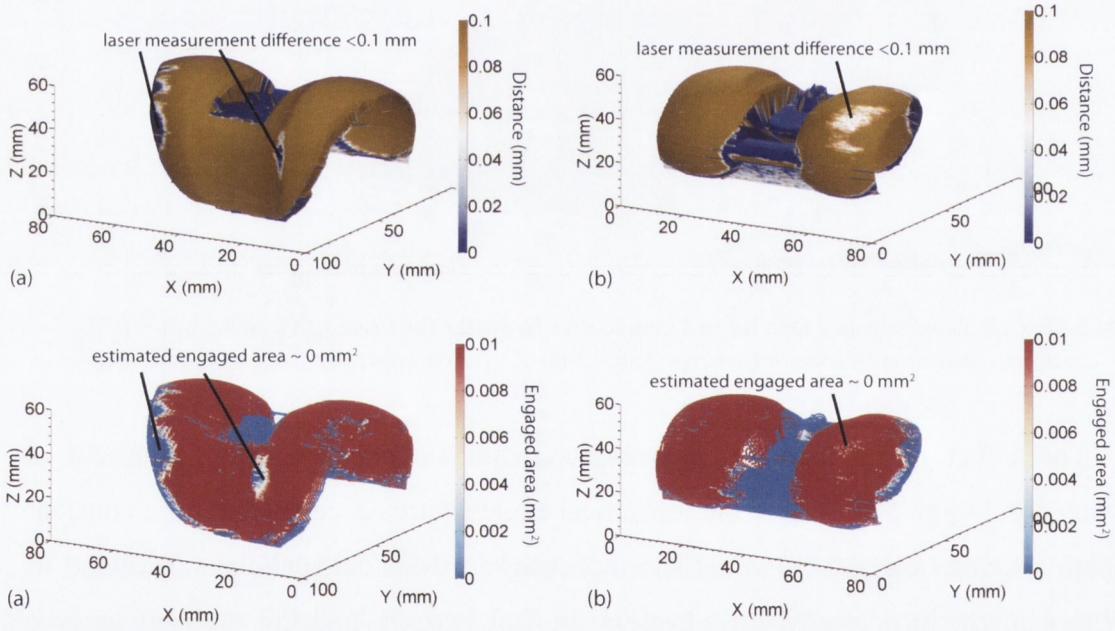


Figure 5.21: Laser measurement and engaged area estimate error propagation, (a) implant front view, (b) implant back view

Figure 5.22 illustrates estimated tool-workpiece engaged area over the surface of the implant the for a colormap limit of 1 mm^2. Areas of high tool-workpiece engagement are illustrated here at the patella track owing to the concave nature of the surface at this point, and at the casting gates which protrude over 1mm from the surface.

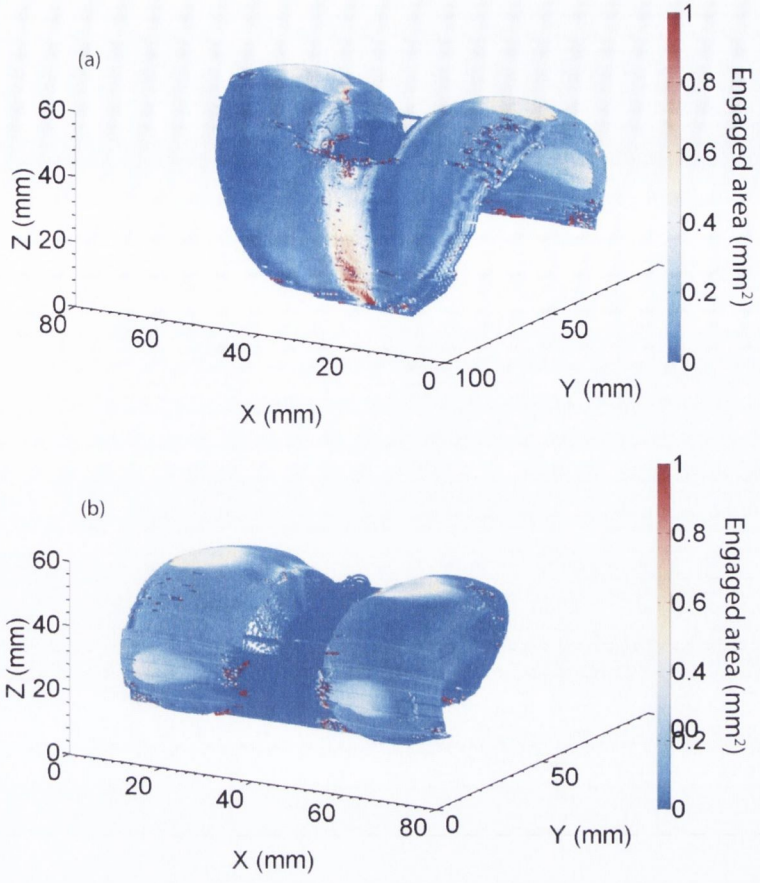


Figure 5.22: Calculated 2D tool-workpiece engagement area (mm^2), (a) implant front, (b), implant back

5.3 Position-oriented power monitoring

The significance of the variation in engagement over the surface of the part becomes apparent when power monitoring is applied to the process. In previous work, De Lacalle et al. have shown the benefit of generating a graphical representation of the forces during milling over the surface of a part in order to assist in diagnosing problems during the machining process [163]. Kratz went on to successfully apply this concept to vibration monitoring of milling of thin-walled components, where process disturbances could be detected through frequency map-based analysis [106]. The research shown here aims to extend the position-oriented analysis concept to power monitoring of freeform abrasive machining. Spindle power and tool position during machining were recorded directly from the numerical control on the machine during the process using the same process used in Chapter 4, as described in detail in Section 3.2.1. A schematic of the power monitoring process is illustrated in Figure 5.23.

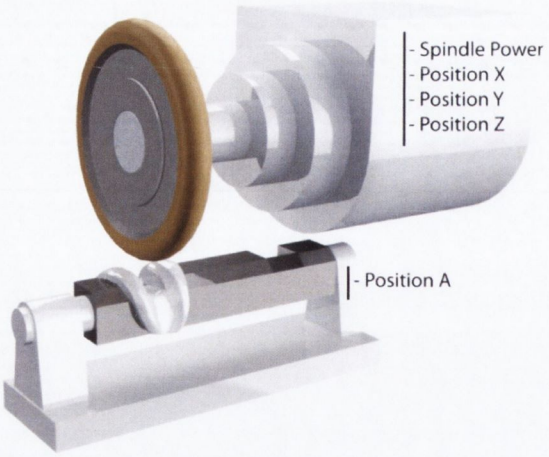


Figure 5.23: Position-oriented power monitoring parameters and schematic

A sample rate of 333Hz was used for these tests, the maximum sample rate available on the Siemens numerical control. As the A-axis is a rotary axis and the X- and Z-axes are both linear, the toolpath was reconstructed through a Polar to Cartesian coordinate transformation, with the A-axis representing ϑ in degrees and the Z-axis representing ρ in millimetres.

$$y_{Cartesian} = \rho \cos\theta \tag{5.16}$$

$$z_{Cartesian} = \rho sin\theta \tag{5.17}$$

For later correlation of the power and position data with the laser data it is necessary to have a sufficiently close starting point for the two scans, this is achieved through a heuristic mapping approach of moving and scaling the data based upon existing process knowledge. As the original toolpath data relates to the centre of the grinding spindle and is therefore larger than the actual implant, the data needed to be scaled down for visualisation and correlation to the laser data. The recorded machine power and position data was scaled down in the Z-direction by a factor of 7 and the X and Y-axis were centred on the laser data axis by subtraction of 1.5 mm and addition of 2 mm, respectively. Figure 5.24 illustrates the cutting power recorded over the course of the toolpath during machining of the same implant casting. It can be seen clearly in Figure 5.24 that power has a close resemblance to the previously calculated engaged area over the freeform surface as shown in Figure 5.19. The power shown is the power that relates directly to cutting as detailed in Section 3.1.2.

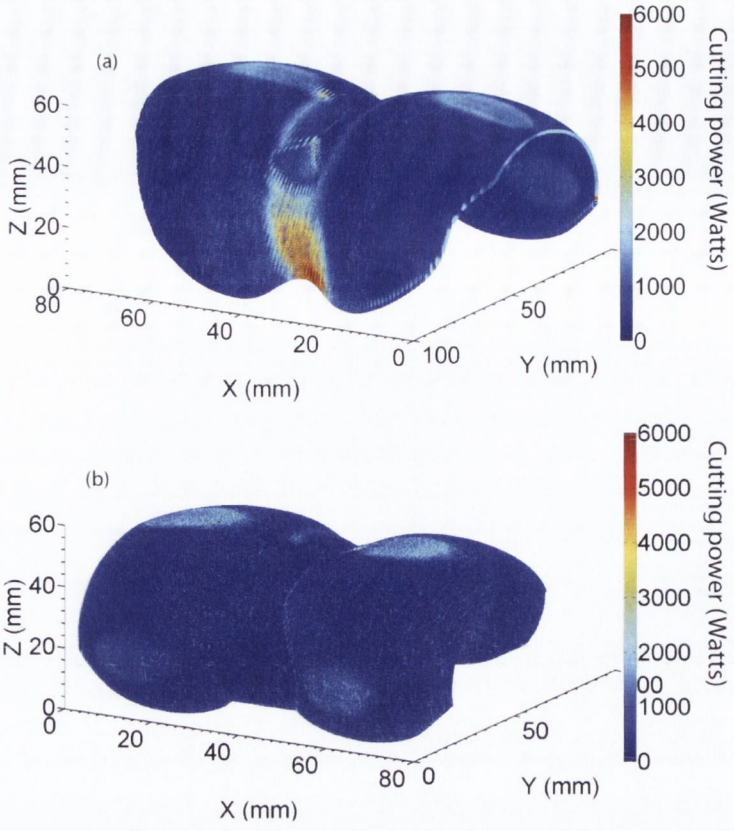


Figure 5.24: Modified toolpath data with cutting power (Watts), (a) Implant front, (b) Implant back

As the engaged area between the tool and workpiece increases so too does the spindle power. It is apparent from both the material removal and power measurements as shown in Figure 5.24 and Figure 5.22 that a positional relationship exists between the two quantities.

The method selected to perform a joint-analysis of the engaged area dataset and the machine power/positional dataset was data interpolation. The total number of data points for each set differs as the machining power/position was recorded at a higher sampling rate than the laser measurement data resulting in a total of 255,684 sample points, whereas the total number of sample points for the engaged area was 67,600. For the best results from data interpolation the sample size needs to be approximately the same for the two data sets, therefore it is necessary to reduce the power/position data set. A running root-mean-square filter was applied to the power/position data set with a window span of 3 points corresponding to approximately 5 ms. In order to reduce the dataset for joint-analysis with the engagement dataset, the power data was then downsampled by a factor of 4 by retaining every 4^{th} sample in the dataset. Figure 5.25 illustrates the preserved trend in the processed power data.

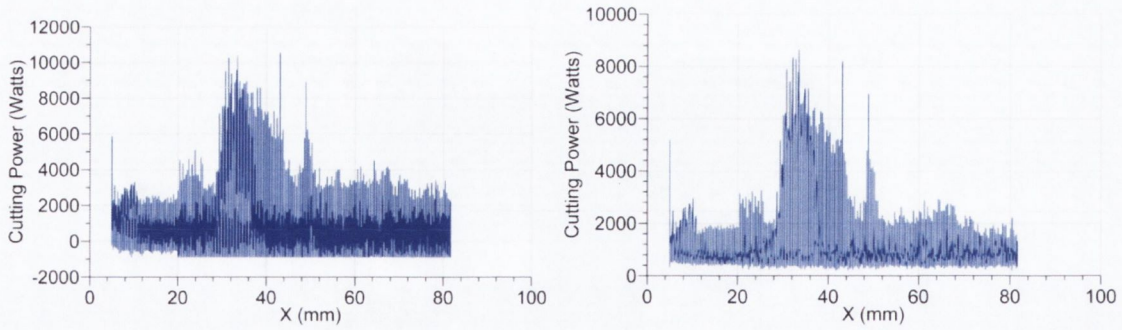


Figure 5.25: Original cutting power data (left), processed cutting power data (right)

The power data was then interpolated onto the laser data mesh surface through the use of the Matlab interpolation function triscatteredinterp(). The triscatteredinterp class has been used successfully previously in a number of different applications, including wave energy mapping, image reconstruction and mapping of magnetic particles [213-215]. Nearest neighbour was selected as the method for interpolation. Natural and linear interpolation were also attempted, however nearest neighbour providing the best results in terms of similarity to the original dataset shown in Figure 5.24 as the nearest neighbour method does not require the data for interpolation to be fully enclosed within a convex hull. The estimated engaged area as shown in Figure 5.22 was interpolated onto the laser point cloud surface in order to obtain a point-to-point correspondence between the power data and estimated engaged area data. Results for data interpolation are shown in Figure 5.26 where the similarity to the original data sets of power and engaged area is evident.

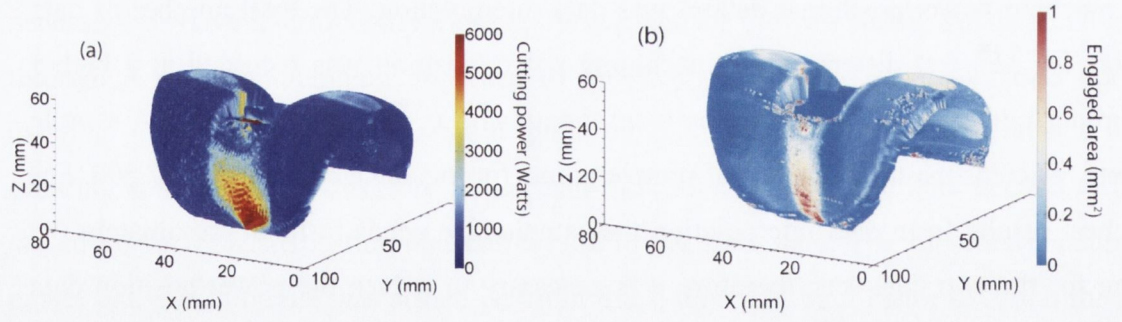


Figure 5.26: (a) Power data interpolated onto laser measurement mesh, (b) engaged area interpolated onto laser measurement mesh

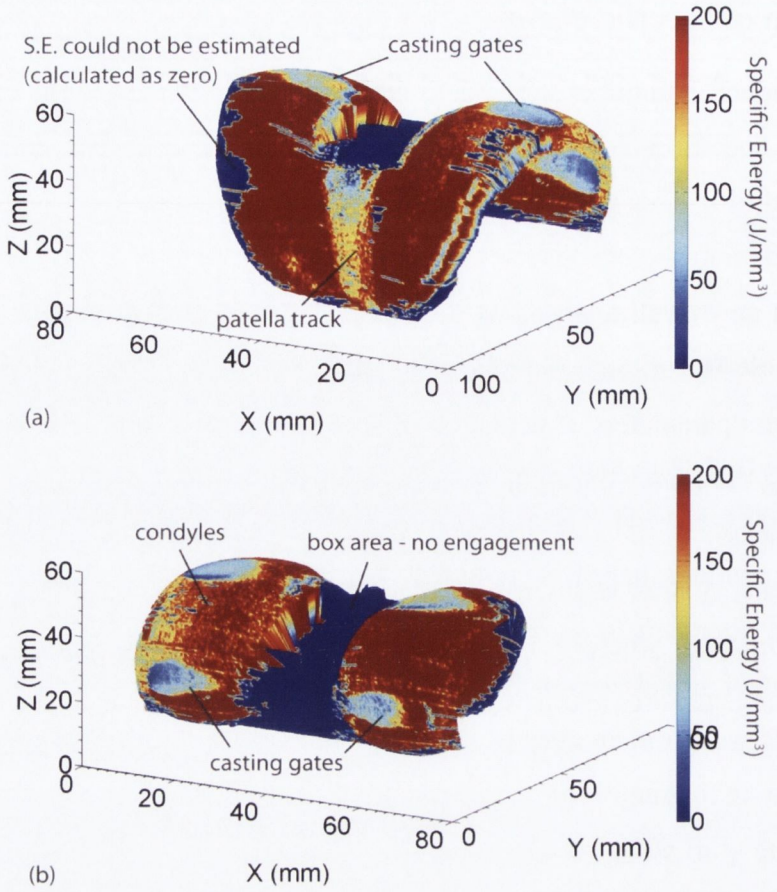
5.4 Estimation of specific energy

A fundamental parameter derived from the power and machining conditions in grinding is the specific energy, which is defined as the energy per unit volume of material removal [40]. This parameter includes the consideration of time related process feed rate and machining power as well as engaged cross-sectional area. Including these dependencies in an overall analysis of the machining toolpath with specific energy as the output analytic is a more comprehensive way of evaluating the effect of changing machining process parameters. Calculation of specific energy can provide an evaluation of the machining efficiency during a process which can be used as a suitable metric for optimizing a process.

Specific energy was estimated for each data point on the surface of the part through Equation 5.18, where P is the interpolated power matrix and A_W is the 2D-cross-sectional engaged area estimate as illustrated in Figure 5.22, and v_f is the feed rate.

$$u = \frac{P}{A_W v_f} \tag{5.18}$$

Figure 5.27 shows the specific energy estimate, u, over the surface of the femoral implant for a test where the feed rate was kept constant at $v_f = 55$ mm/s. It can be seen that where the tool-workpiece engagement and material removal rate is greater, the specific energy is reduced. This is illustrated in the casting gate and patella regions. Specific energy then rises to high levels where the amount of material being removed is very small. This can be reasoned through considering Equation 5.18; if a large amount of power is being directed into a very small volume of material then the specific energy is high as a result. It has been found to be the case that in general an abrasive machining process is efficient if material is removed quickly with low energy consumption, and inefficient processes require higher specific energy [216]. The specific energy result shown in Figure 5.27 illustrates clearly the dependency of the process efficiency on the engaged area between tool and workpiece experienced during abrasive machining.



Parameter:	Material:	Tool:	Coolant:
v_s = 84 m/s	CoCrMo F-75 Alloy	New Electroplated CBN B301 Grit	Henkel Multan CR10

Figure 5.27: Estimated specific energy, u (J/mm^3), (a) implant front, (b) implant back

5.5 Summary

A non-contact laser measurement system developed for this research was used to determine the material removed in the process. The developed system presented a resolution of at least 0.05 mm with a standard deviation of approximately 0.01 – 0.02 mm for flat and curved surfaces respectively. The developed system provides an insight into the varying cutting conditions during the grinding process. Measurements from the system were obtained from femoral implants pre- and post- abrasive machining. Scans were matched with the developed iterative closest point matching algorithm. Estimated depth of cut was obtained over the surface of the part with values shown to be within the range of 0 – 2 mm, with considerably more material removed in some areas such as concave shaped areas and casting gates, than other areas including the convex sections of the femoral condyles.

An algorithm was developed to estimate the 2D tool-workpiece engaged area over the surface of an implant utilizing laser part comparison measurements. The accuracy of the algorithm was found to depend on the accuracy of the laser measurements. Results shown provided an insight into the highly variable contact conditions encountered during abrasive machining. Typical engaged areas were found to be between 0 – 1 mm^2.

An advanced process monitoring technique was applied in order to further the understanding of abrasive machining of freeform surfaces. Internal machine signals including power and spindle position were utilized in monitoring the abrasive process and later analysed using a position-oriented approach. Typical cutting power values for a standard toolpath were found to be within 0 – 10 kW. The positional dependency between depth of cut and cutting power was highlighted through correlation between the laser and power measurements.

A joint analysis was performed correlating recorded power with calculated engaged area by means of nearest neighbour interpolation. Specific energy was estimated over the surface of the part providing an insight into the efficiency of the cutting process.

Chapter 6

Application of position-oriented monitoring approach for freeform surfaces

The abrasive machining parameters of depth of cut, toolpath spacing and feed rate have a significant effect on process power and machining efficiency. The position-oriented analysis method developed in Chapter 5 is extended to abrasive machining of femoral implants at varied tool-workpiece engagement and feed rate parameters. Sensitivity of the developed method is therefore tested, and the influence of changes in process parameters with respect to tool-workpiece engagement, power and specific energy for the freeform abrasive machining process is investigated.

6.1 Design of experiment with position-based analysis

A factorial experiment was undertaken examining the parameters of depth of cut and feed rate over the course of abrasive machining of femoral implants. This study utilized a 2^2 factorial array with analysis of variance (ANOVA). For ease of discussion in this chapter for the three-dimensional graphs, only the results for the first set of replicates are presented. The factors chosen are the parameters feed rate and engaged area. In order to achieve an increase in engaged area, both the tool path spacing and the radial machining offset were increased. The machining offset relates to the constant radial distance from the grinding wheel to the centre of the machining arbour. The test array is shown in Table 6.1 where cutting power, tool-workpiece engagement and specific energy are the response variables and three replicates of each set of test parameters are performed. The feed rate parameter of 90 mm/s is based upon an estimate of the onset of high efficiency deep grinding conditions, deemed to be over a specific material removal rate of 50 mm^2/s based upon an arbitrary depth of cut of 0.8 mm [21]. The wheel speed was maintained at 8000 rpm, or 84 m/s, the maximum available for all of the tests. The tool used was a new B301 electroplated steel hub wheel, as with previous tests. The primary objective of the machining trials is to explore

the sensitivity of the developed position oriented analysis method for the responses of cutting power and specific energy over the varied test parameters of feed rate and toolpath/engaged area. The sensitivity of the laser measurements towards differences in tool path spacing and depth of cut is also investigated.

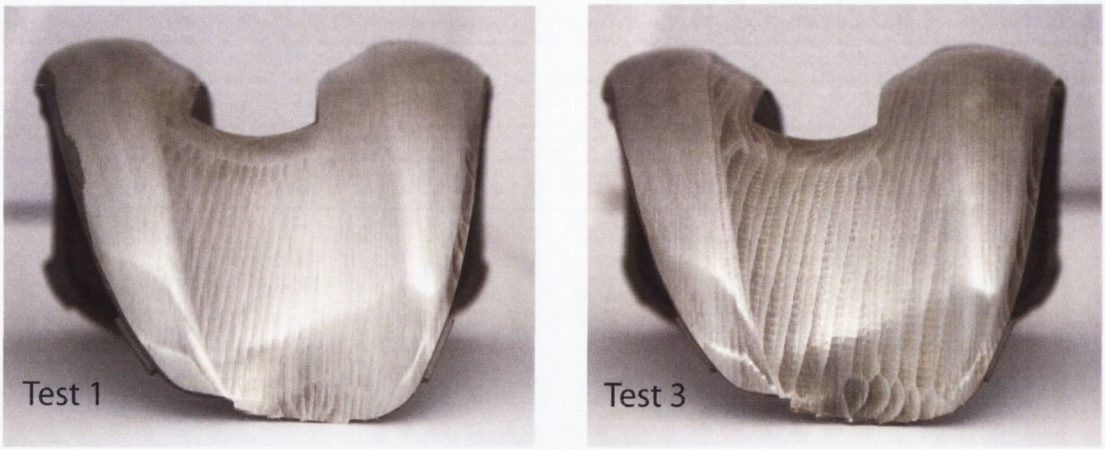
Toolpath	Tool Path Spacing, s (mm) *	Radial Machining Offset, d_0 (mm) *
A	0.381	0
B	0.762	-0.3
*Treated as 1 factor of engaged area Note: Radial Machining Offset of 0 mm refers to a standard machining toolpath, this is the set zero value, and any decrease in this value refers to an overall decrease in the distance between the centre of the grinding wheel and the centre of the machining arbour for the whole toolpath		

Test Number	Feed Rate, v_f (mm/s)	Toolpath
1	55	A
2	90	A
3	55	B
4	90	B
5	55	A
6	90	A
7	55	B
8	90	B
9	55	A
10	90	A
11	55	B
12	90	B

Table 6.1: 2^2 factorial array

Spindle active power was measured using the Sinucom Trace software on the Siemens 8400D sl control HMI, and acquired cutting power data was subsequently processed in Matlab (version R2010a). Each implant was laser scanned before and after abrasive machining and the difference between pre- and post- machining scans processed using algorithms developed in Matlab as detailed previously in Chapter 5.

Figure 6.1 shows an example of the post-machined parts for tests 1 and 3. The difference between the two tool paths can be seen with grinding tracks from the wider toolpath spacing clearly visible on test 3 in Figure 6.1. Although the surface finish is visibly smoother for abrasive machining with toolpath A than for toolpath B, the focus of the machining trials is not to improve surface finish but to explore the efficiency of the machining operation and the sensitivity of the position-oriented analysis method.



Material: CoCrMo F-75 Alloy	**Parameter:** v_s = 84 m/s	**Coolant:** Henkel Multan Cr10	**Tool:** New CBN B301 Grit
Test 1	v_f = 55 mm/s	s = 0.381 mm	d_o = 0 mm
Test 3	v_f = 55 mm/s	s = 0.762 mm	d_o = 0.3 mm

Figure 6.1: Femoral implant surface with visible difference between toolpath scallop height

6.2 Laser measurement results

A cross-section of the post-machined femoral implant was measured and the distance across a section of the part was examined for each of the tests in order to verify the sensitivity of the laser measurements towards differing amounts of material removal, as represented by the two toolpaths. A sample set of 30 measured points were taken as shown in Figure 6.2 and the mean of the selected points was calculated for each post-machined implant. The means are compared formally by specifying the null hypothesis of no difference, H_0, and carrying out a t-test based on Students t-distribution as given by Equation 6.1, where s is the average of the two sample standard deviations [200].

$$H_0 : \mu_2 - \mu_1 = 0$$

$$t = \frac{(\overline{y_2} - \overline{y_1}) - 0}{\sqrt{2s^2/n}} \tag{6.1}$$

As shown in Table 6.2 the null hypothesis is rejected for Test (i). This implies a statistically significant difference can be detected between the two toolpaths. Given that

significantly more material is removed for toolpath B than for toolpath A, this result is as expected. From this result the lasers ability to detect changes in material removal is also verified.

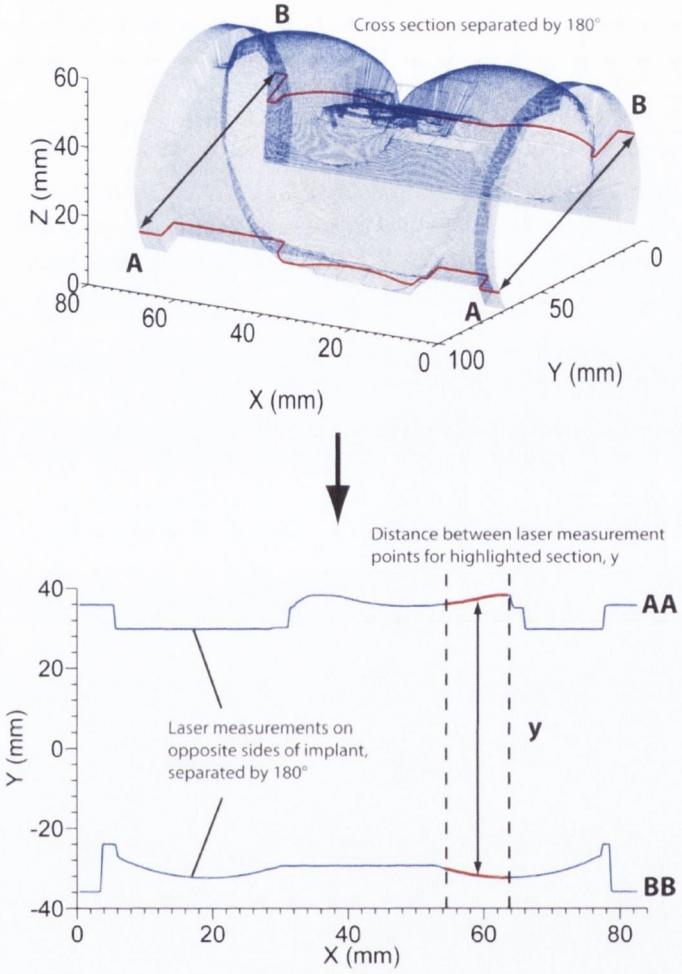


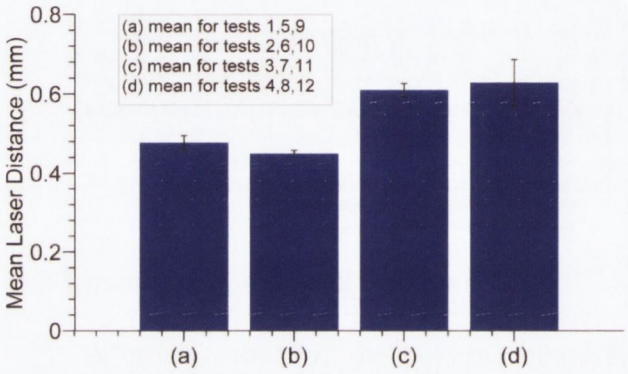
Figure 6.2: Selected profile scans on opposite sides of implant holder for t-test comparison highlighted in red, laser line scans from Test 1 shown

Test	Y_2 (mm)	Y_1 (mm)	S_1 (mm)	S_2 (mm)	n	t
(i) Difference between toolpaths A & B	68.94	68.29	0.07	0.12	6	3.45
(ii) Difference between feed rate for toolpath A	68.96	68.93	0.07	0.08	3	0.15
(iii) Difference between feed rate for toolpath B	68.29	68.30	0.12	0.12	3	0.02

Table 6.2: Results for t-test comparison between toolpaths and feed rates, where Y_1 and Y_2 are the mean distances for the chosen parameters, S_1 and S_2 are the standard deviations and n is the sample size

There are variations present in the laser measurements from implant to implant for the same machining parameters however they can largely be attributed to the casting process. Casting gates are cut off from the main casting tree with a manual band-saw, so their height may vary from part to part, and castings are not identical due to variation in

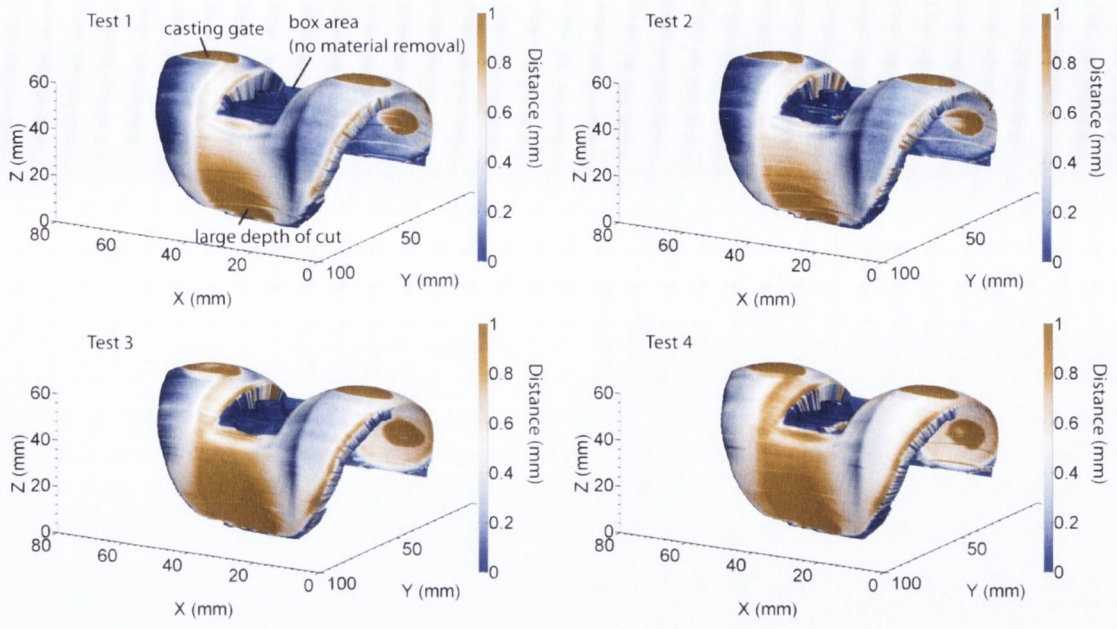
the wax moulds and investment casting process. Therefore material removed can vary by a small amount between implants. However, as the t-value for tests (ii) and (iii) is less than the critical value of +/- 2.07, the difference in implant width between the feed rates of 55 mm/s and 90 mm/s is not statistically significant, thus illustrating that the material removed for toolpath A and for toolpath B is repeatable and does not vary by a statistically significant amount when the feed rate is increased. An example of the calculated means and standard deviation between test replicates for the measured distance between cast and post-grinding implants is shown in Figure 6.3, again illustrating the difference in laser distance measurements between toolpaths A and B.



	Test Number	Feed Rate, v_f (mm/s)	Toolpath
(a)	1, 5, 9	55	A
(b)	2, 6, 10	90	A
(c)	3, 7, 11	55	B
(d)	4, 8, 12	90	B

Figure 6.3: Mean laser distance calculated for corresponding test replicates

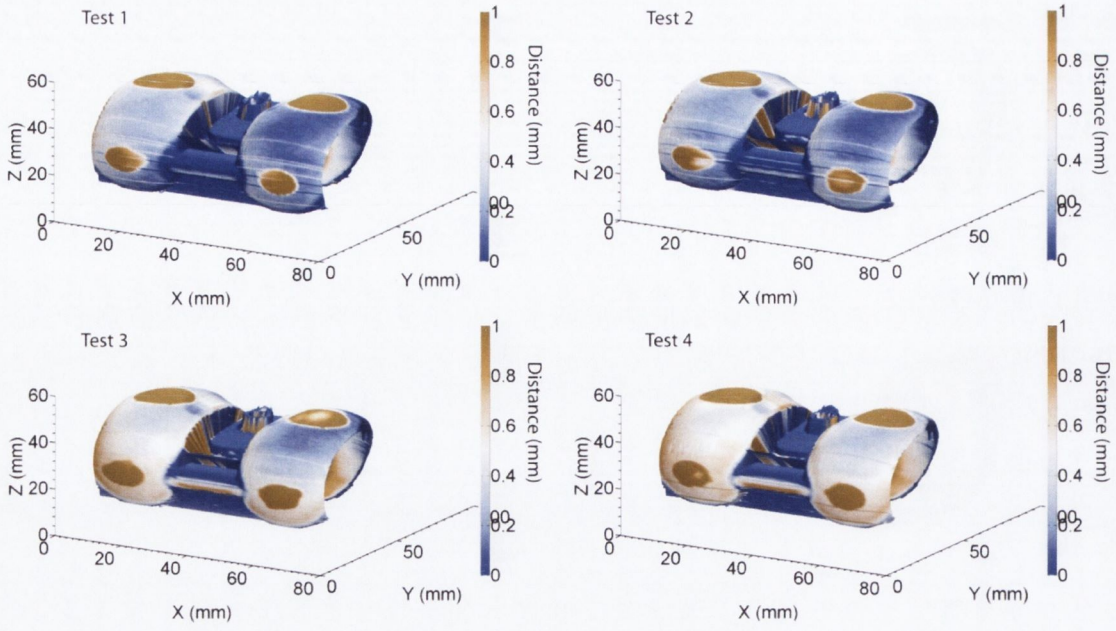
However, as the quantity of material removed varies considerably over the surface of the implant a position-oriented analysis is a more appropriate way of looking at the data. Figure 6.4 and Figure 6.5 show the laser scanning results and variation in material removed over the surface of the implant for experimental tests 1 - 4. The difference in material removed between the cast and post-machined implants was calculated through the method described in Section 5.1 and is represented by the corresponding distance map of colours in millimeters. In Figure 6.4 it can be seen that more material has been removed for the implants machined with toolpath B as shown in Test 3 and 4 as compared to Test 1 and 2 with toolpath A.



Material: CoCrMo F-75 Alloy	**Parameter:** v_s = 84 m/s	**Coolant:** Henkel Multan Cr10	**Tool:** New CBN B301 Grit
Test 1 v_f = 55 mm/s s = 0.381 mm d_o = 0 mm	**Test 2** v_f = 90 mm/s s = 0.381 mm d_o = 0 mm	**Test 3** v_f = 55 mm/s s = 0.762 mm d_o = 0.3 mm	**Test 4** v_f = 90 mm/s s = 0.762 mm d_o = 0.3 mm

Figure 6.4: Distance map laser measurements implant front view

The changing nature of the tool workpiece engagement during abrasive machining of the freeform surface is also illustrated by the wide range of distances or depths of cut over the surface of the part as shown in Figure 6.4 and Figure 6.5. Near the patella track and the casting gate regions over 1 mm of material has been removed for both toolpaths, whereas near the edges of the implant the material removed decreases to less than 0.2 mm for toolpath A and 0.4 mm for toolpath B. The amount of material removed for the condyle regions is also relatively low in comparison to the patella region and this can be attributed to the differing engagement conditions between the two regions and also to the original shape of the casting where more material needs to be removed in some areas as compared to others. Due to the variable material removed over the surface of the implant as shown in the results in Figure 6.4 and Figure 6.5, and the resultant alternating depths of cut and tool-workpiece engagement conditions, power and forces can be expected to fluctuate significantly during the grinding process.

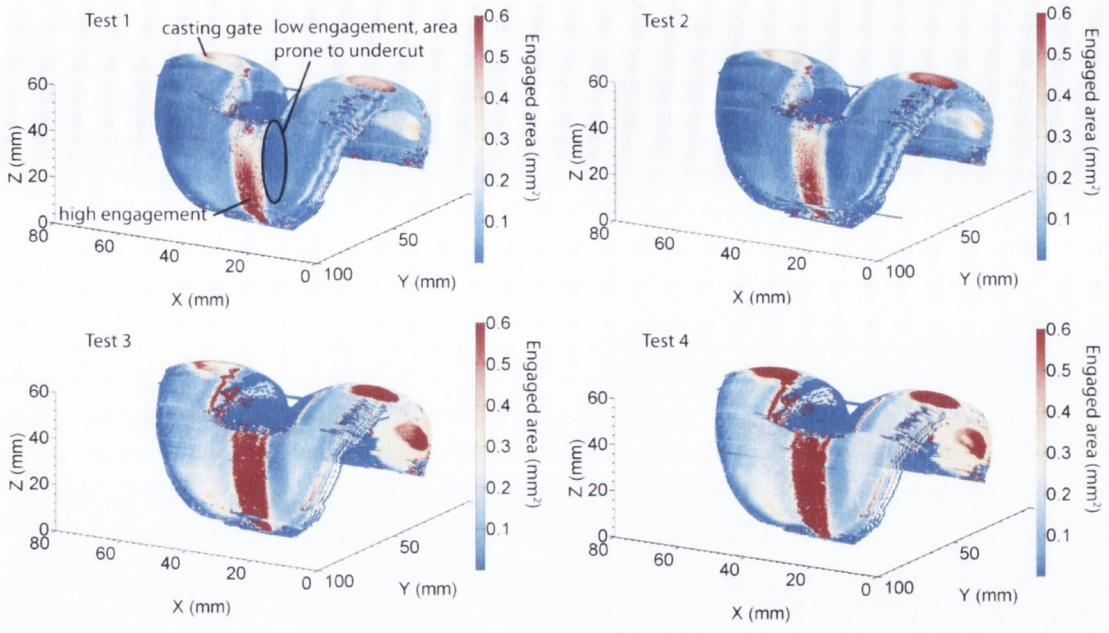


Material: CoCrMo F-75 Alloy	**Parameter:** v_s = 84 m/s	**Coolant:** Henkel Multan Cr10	**Tool:** New CBN B301 Grit
Test 1 v_f = 55 mm/s s = 0.381 mm d_o = 0 mm	**Test 2** v_f = 90 mm/s s = 0.381 mm d_o = 0 mm	**Test 3** v_f = 55 mm/s s = 0.762 mm d_o = 0.3 mm	**Test 4** v_f = 90 mm/s s = 0.762 mm d_o = 0.3 mm

Figure 6.5: Distance map laser measurements implant back view

6.3 Engagement analysis results

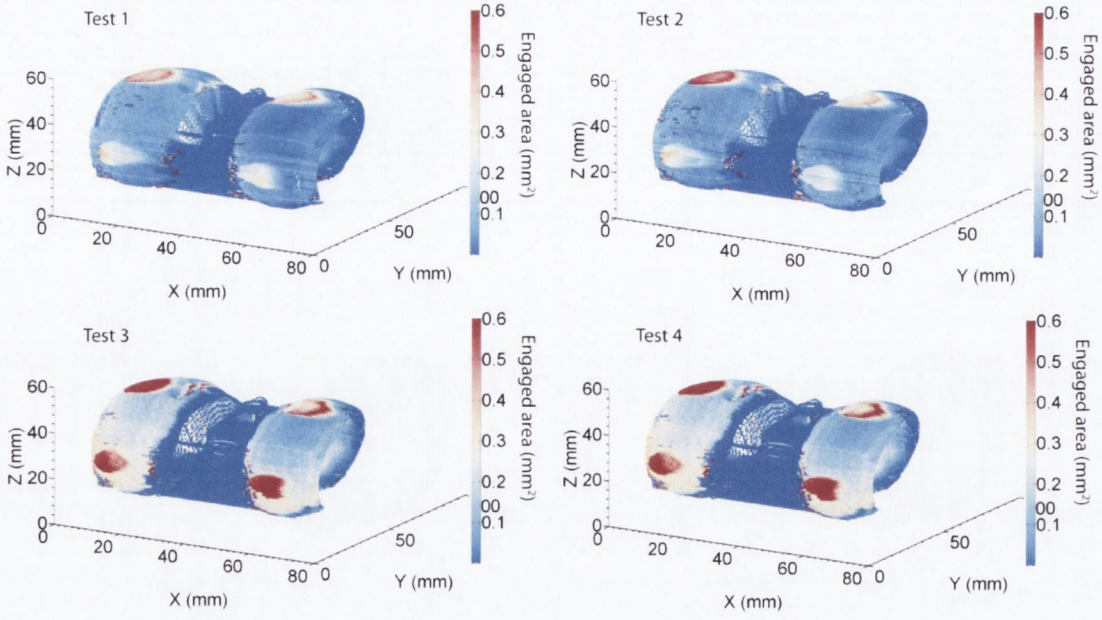
The cross-sectional tool-workpiece engagement for each of the machined implants was estimated as shown in Figure 6.6 based upon the method outlined previously in Section 5.2. The engaged cross-sectional area was shown to increase at the concave patella track and at the casting gates where a large amount of material to be removed is encountered.



Material: CoCrMo F-75 Alloy	**Parameter:** v_s = 84 m/s	**Coolant:** Henkel Multan Cr10	**Tool:** New CBN B301 Grit
Test 1 v_f = 55 mm/s s = 0.381 mm d_o = 0 mm	**Test 2** v_f = 90 mm/s s = 0.381 mm d_o = 0 mm	**Test 3** v_f = 55 mm/s s = 0.762 mm d_o = 0.3 mm	**Test 4** v_f = 90 mm/s s = 0.762 mm d_o = 0.3 mm

Figure 6.6: Engagement analysis, front view

The engaged cross-sectional area is also shown to increase for Tests 3 and 4 due to the increased toolpath spacing and increased radial depth of cut for toolpath B as illustrated in Figure 6.6. Areas on the implant prone to undercut are also illustrated through the engagement analysis and are highlighted by the dark blue areas in Figure 6.6 and Figure 6.7 near the edges of the patella track, near the edges of the implant and near the top of the left femoral condyle. Such areas are prone to undercut due to the small amount of material being removed and the low tool-workpiece engagement at these locations.

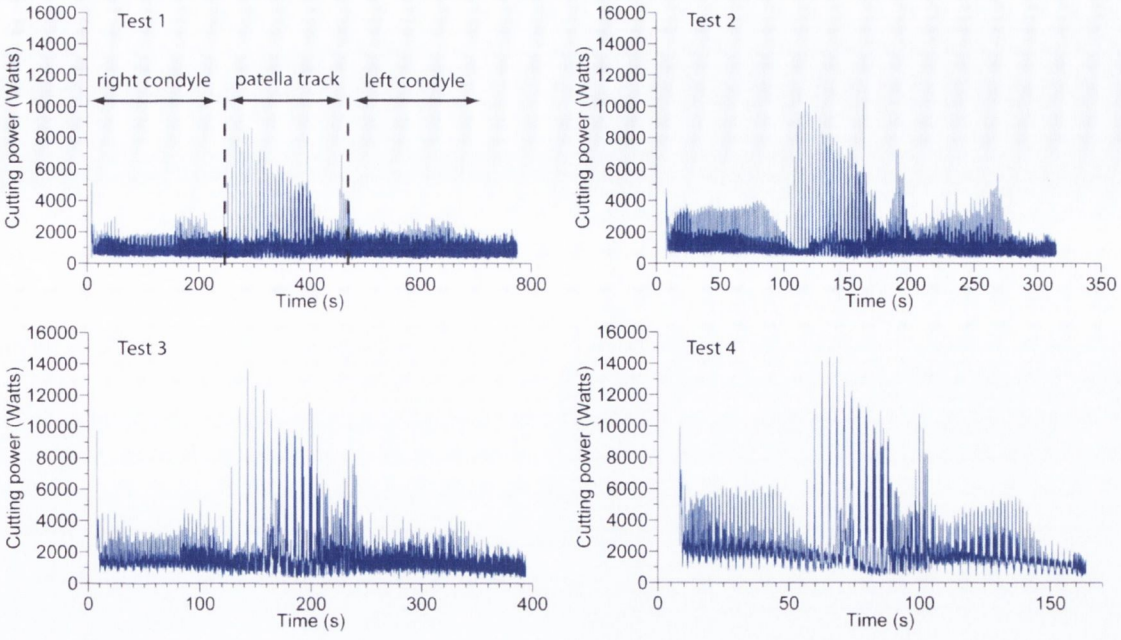


Material: CoCrMo F-75 Alloy	**Parameter:** v_s = 84 m/s	**Coolant:** Henkel Multan Cr10	**Tool:** New CBN B301 Grit
Test 1 v_f = 55 mm/s s = 0.381 mm d_o = 0 mm	**Test 2** v_f = 90 mm/s s = 0.381 mm d_o = 0 mm	**Test 3** v_f = 55 mm/s s = 0.762 mm d_o = 0.3 mm	**Test 4** v_f = 90 mm/s s = 0.762 mm d_o = 0.3 mm

Figure 6.7: Engagement analysis, back view

6.4 Power measurement results

Spindle power was measured directly from the machine NC using the method described in Section 3.1.2. The sample rate used was the maximum available at 333 Hz. Spindle active power recorded in this way was the total power including the power necessary for rotation of the spindle as well as the cutting power. The cutting power was therefore obtained by subtracting the rotary power components from the corresponding total. The power necessary for spindle rotation, was measured from multiple air cuts, and as the rotational grinding speed did not vary the mean air cut power was found to be 895 Watts.

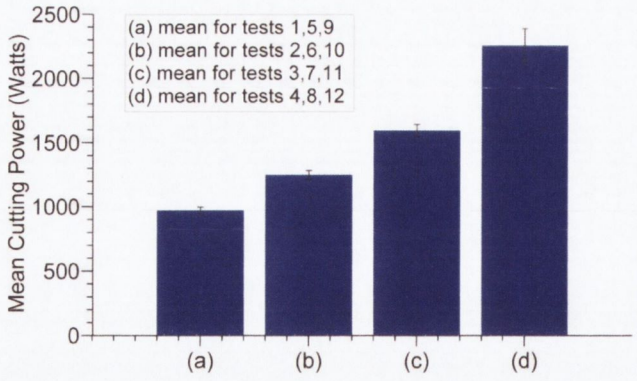


Material: CoCrMo F-75 Alloy	**Parameter:** v_s = 84 m/s	**Coolant:** Henkel Multan Cr10	**Tool:** New CBN B301 Grit
Test 1 v_f = 55 mm/s s = 0.381 mm d_o = 0 mm	**Test 2** v_f = 90 mm/s s = 0.381 mm d_o = 0 mm	**Test 3** v_f = 55 mm/s s = 0.762 mm d_o = 0.3 mm	**Test 4** v_f = 90 mm/s s = 0.762 mm d_o = 0.3 mm

Figure 6.8: Power measurements during freeform abrasive machining

Figure 6.8 illustrates processed cutting power for the first 4 tests. A large increase in power can be seen approximately half way through the cycle time. There are also noticeable increases in power particularly over the first and last 200 seconds. This can be attributed to the differing tool-workpiece engagement conditions at the patella track and femoral condyle regions.

Another source of variation is in the power requirement for rotation of the grinding spindle. This is largely accounted for through subtraction of a mean 'air cut' power value, though there still remains some variation in the power data as the spindle power oscillates naturally around a mean at a frequency given by the rotational speed of the spindle. This effect was illustrated previously in Section 4.1.



	Test Number	Feed Rate, v_f (mm/s)	Toolpath
(a)	1, 5, 9	55	A
(b)	2, 6, 10	90	A
(c)	3, 7, 11	55	B
(d)	4, 8, 12	90	B

Figure 6.9: Mean cutting power calculated for corresponding test replicates

Though there is considerable variability in the cutting power data over the course of one toolpath as shown in Figure 6.8 some initial conclusions can nonetheless be drawn from the data by examining mean values for each test. Figure 6.9 illustrates the variation between power measurement data means for each set of test parameters. The standard deviation between means calculated for the three replicates for each set of test parameters is shown to be small, and an increasing trend can be seen for the data.

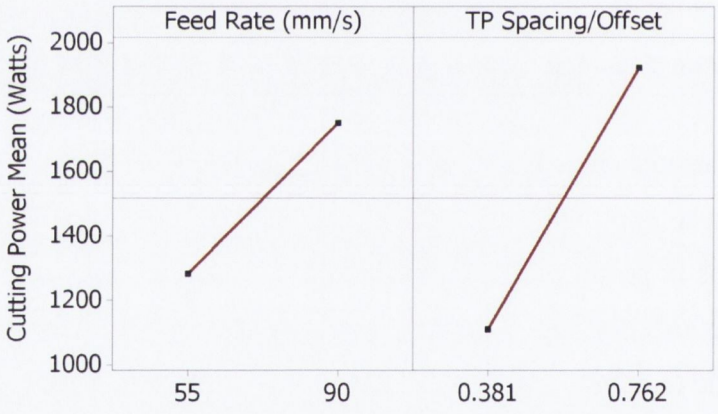


Figure 6.10: Main effects for cutting power response

Source	P-value
Feed Rate (mm/s)	0
TP Spacing / Offset	0
Feed Rate (mm/s)*TP Spacing/Offset	0.001

Table 6.3: ANOVA Results for mean cutting power

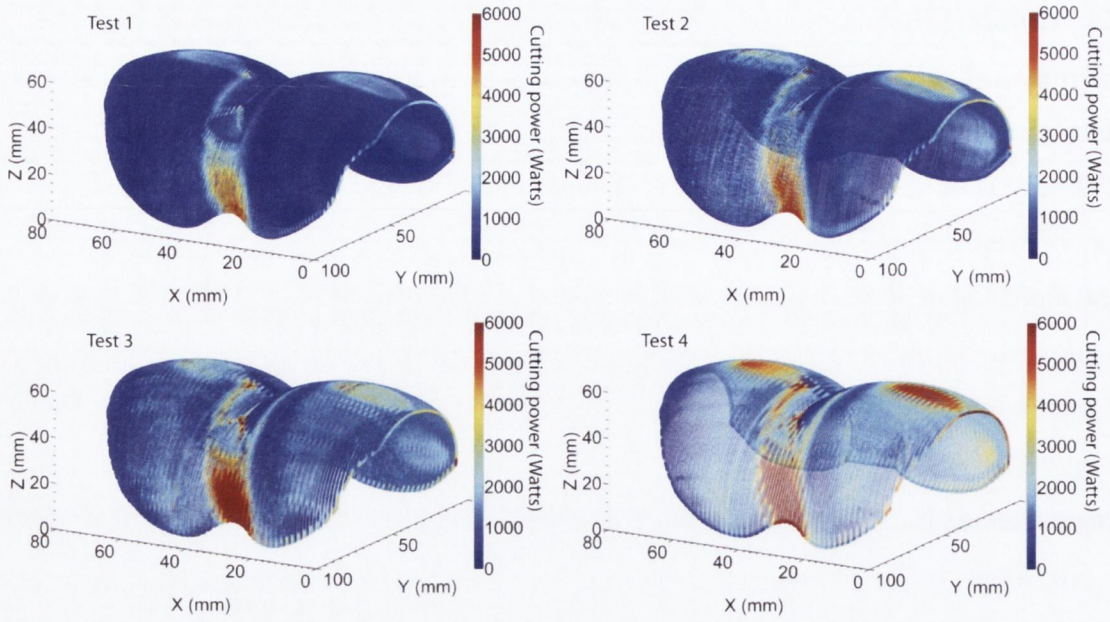
ANOVA analysis was therefore carried out on the means of the power data for each test in order to determine if varying the parameters of feed rate and toolpath/tool-workpiece engagement had a statistically significant effect on the cutting power signal

for the freeform grinding process. Figure 6.10 and Table 6.3 show the main effects plot and corresponding ANOVA results relating to means for cutting power for the duration of machining for the tests.

Analysis of variance also identified that for the cutting power response, the main factors of feed rate and combined tool path spacing/offset were statistically significant for the alpha value of 5% as denoted by the P-value shown in Table 6.3. An increase in feed rate from 55 mm/s to 90 mm/s was found to result in an increase of 469 Watts, or a 37% increase for the mean cutting power, whereas an increase in engaged area/toolpath spacing/offset was found to result in an increase of 813 Watts, or 73% for the mean cutting power, as illustrated in the main effect plot in Figure 6.10.

The analysis shown indicates that changing machining parameters of feed rate and toolpath has a statistically significant effect on the response variable of cutting power, and therefore a change in feed rate and/or tool-workpiece engaged area will have an effect on resulting process power and forces. However, the large variation in the results as illustrated in Figure 6.8 imply further analysis is necessary in order to fully understand the changes in the power signal with respect to the changing tool-workpiece engagement conditions for a freeform surface. A position-oriented analysis as demonstrated in Chapter 5 is of value in this case as the root cause of variations in the cutting power for abrasive machining of a freeform surface can be determined by analysis of the cutting power in combination with the position of cut during the toolpath.

Tool position and spindle power were therefore recorded simultaneously for the duration of each test. Results were processed as described in Section 5.4, and tool position and power were plotted for the course of each test. Figure 6.11 shows an example of position-oriented graphs for Tests 1 to 4, where a limit of 6000 Watts was chosen for the color map of power as this provided the best visualization of the power expended across the abrasive machining toolpath.



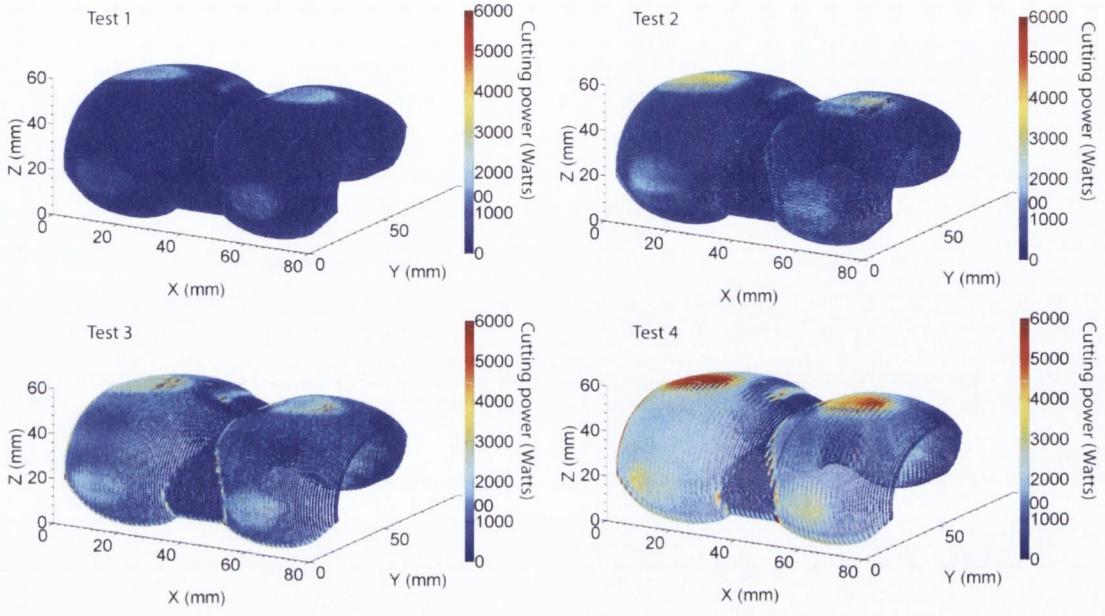
Material: CoCrMo F-75 Alloy	**Parameter:** v_s = 84 m/s	**Coolant:** Henkel Multan Cr10	**Tool:** New CBN B301 Grit
Test 1 v_f = 55 mm/s s = 0.381 mm d_o = 0 mm	**Test 2** v_f = 90 mm/s s = 0.381 mm d_o = 0 mm	**Test 3** v_f = 55 mm/s s = 0.762 mm d_o = 0.3 mm	**Test 4** v_f = 90 mm/s s = 0.762 mm d_o = 0.3 mm

Figure 6.11: Position oriented cutting power analysis, front view

Figure 6.11 and Figure 6.12 show the clear differences in cutting power between grinding at the various parameter settings. The recorded cutting power is shown to be highly positional dependent, with power increasing as the tool-workpiece engagement increases in concave areas as illustrated by the patella track and casting gate area. The more prevalent cutting condition of relatively low power of approximately 1000 Watts can also be observed over the convex shaped condyles as shown Figure 6.12. Both of these observations can be attributed to the tool-workpiece engagement conditions, where grinding of the convex shaped condyle regions results in low engagement, and grinding near the patella track concave regions results in increased engagement, as shown previously in Figure 6.6 and Figure 6.7.

Similar findings have been shown by other authors for grinding and milling with increases in power for corresponding increases in depth of cut [126, 196]. Cutting power is also observed to increase with increasing feed rate as illustrated in Figure 6.12. This is a well-known effect and agrees with findings in the literature where increases in material removal rate have been reported to be accompanied by an increase in power

[21, 126, 217, 218]. The large increase in power at the lower end of the patella track region is of concern however, and it may be concluded that perhaps the depth of cut and/or engagement conditions at this point in the toolpath are too high resulting in the large increase in power well above the mean value of less than 2 kW.



Material: CoCrMo F-75 Alloy	**Parameter:** v_s = 84 m/s	**Coolant:** Henkel Multan Cr10	**Tool:** New CBN B301 Grit
Test 1 v_f = 55 mm/s s = 0.381 mm d_o = 0 mm	**Test 2** v_f = 90 mm/s s = 0.381 mm d_o = 0 mm	**Test 3** v_f = 55 mm/s s = 0.762 mm d_o = 0.3 mm	**Test 4** v_f = 90 mm/s s = 0.762 mm d_o = 0.3 mm

Figure 6.12: Position oriented cutting power analysis, back view

6.5 Estimate of specific energy

Energy-related considerations can be called upon for an estimate of the efficiency of a process and the influence of thermal component stresses during grinding [18]. Given the engaged area estimate and the recorded cutting power, specific energy over the surface of the implant was estimated for each test using the method described previously in Section 5.5.

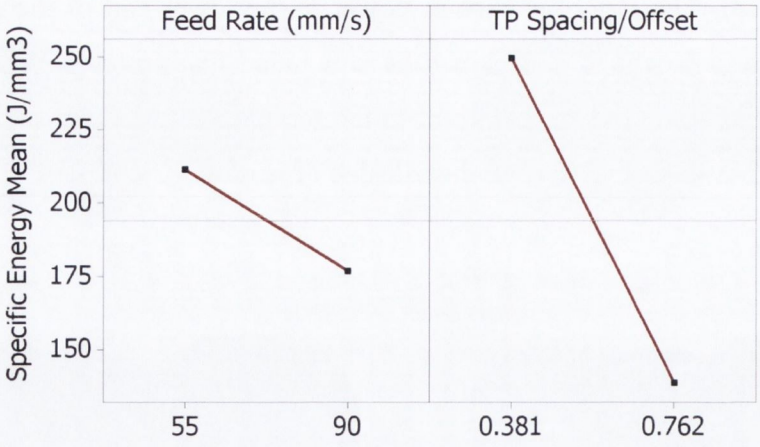


Figure 6.13: Main effects plot for specific energy (data means)

Source	P-value
Feed Rate (mm/s)	0.001
TP Spacing / Offset	0
Feed Rate (mm/s)*TP Spacing/Offset	0.143

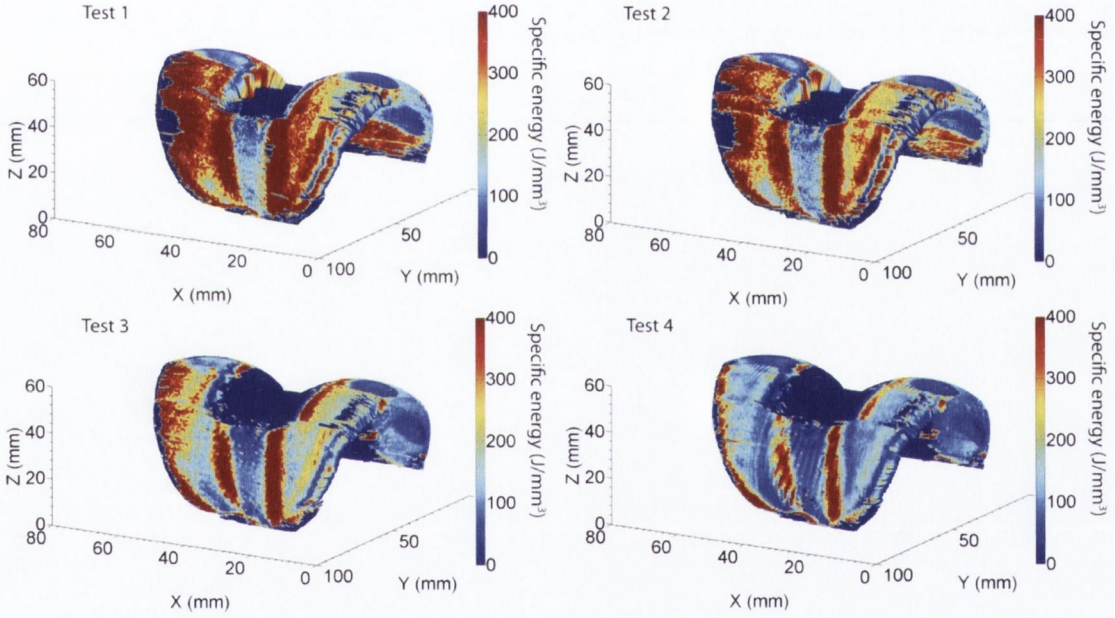
Table 6.4: ANOVA results for mean specific energy

Although there is considerable variability in the estimated specific energy over the course of one toolpath, as with cutting power, some initial conclusions can nonetheless be drawn from the calculations by examining mean values for each test. Figure 6.13 and Table 6.4 show the main effects plot and corresponding ANOVA results relating to means for mean specific energy for the duration of machining for the tests. Analysis of variance identified that for the specific energy response, the main factors of feed rate and combined tool path spacing/offset were statistically significant for the alpha value of 5%. Differences in the p-values between cutting power and specific energy can be attributed to the difference in data sets, as the power data set is reduced by a factor of 4 in order to correlate with engaged area calculations for estimation of the specific energy.

A significant decrease is also shown in specific energy for a corresponding increase in feed rate as well as tool-workpiece engagement through altering the toolpath. For example, an increase in the engaged area through changing the toolpath from A to B can be seen to result in a mean decrease in specific energy of approximately 111 J/mm^3, or 44%, for a given feed rate of 90 mm/s as shown by the main effect plot in Figure 6.13. Similarly, an increase in feed rate from 55 mm/s to 90 mm/s was found to result in a mean decrease of 34 J/mm^3, or 16% for specific energy.

The effect of a decrease in specific energy for an increase in material removal rate has been observed by numerous researchers for both grinding and milling processes. For example, Diaz et al. demonstrated an inverse relationship between specific energy and material removal rate for milling of a low carbon steel [123]. Linke et al. also found that for CBN grinding of hardened steel specific energy was found to decrease with increasing table speeds [70]. Similarly, Tawakoli and Stephenson et al. found that for high efficiency deep grinding specific energy reduced with increasing specific removal rate [21, 66].

However, mean values of specific energy can only provide an initial estimate of machining characteristics. To obtain a better understanding of the specific energy in relation to the alternating tool-workpiece engagement conditions, specific energy is plotted over the course of a full abrasive machining toolpath.



Material: CoCrMo F-75 Alloy	**Parameter:** v_s = 84 m/s	**Coolant:** Henkel Multan Cr10	**Tool:** New CBN B301 Grit
Test 1 v_f = 55 mm/s s = 0.381 mm d_o = 0 mm	**Test 2** v_f = 90 mm/s s = 0.381 mm d_o = 0 mm	**Test 3** v_f = 55 mm/s s = 0.762 mm d_o = 0.3 mm	**Test 4** v_f = 90 mm/s s = 0.762 mm d_o = 0.3 mm

Figure 6.14: Specific energy estimate over the surface of the part, front view

Figure 6.14 and Figure 6.15 illustrate specific energy calculated over the surface of the part for experimental tests 1 - 4. The effect of an increase in feed rate and engaged area is illustrated where in general an increase in feed rate or engaged area is accompanied with a decrease in specific energy. The magnitude of specific energy is also found to be at a minimum over the centre of the patella track and over the casting gates. This can be attributed to the large engagement area between tool and workpiece at these points as shown previously in Figure 6.6.

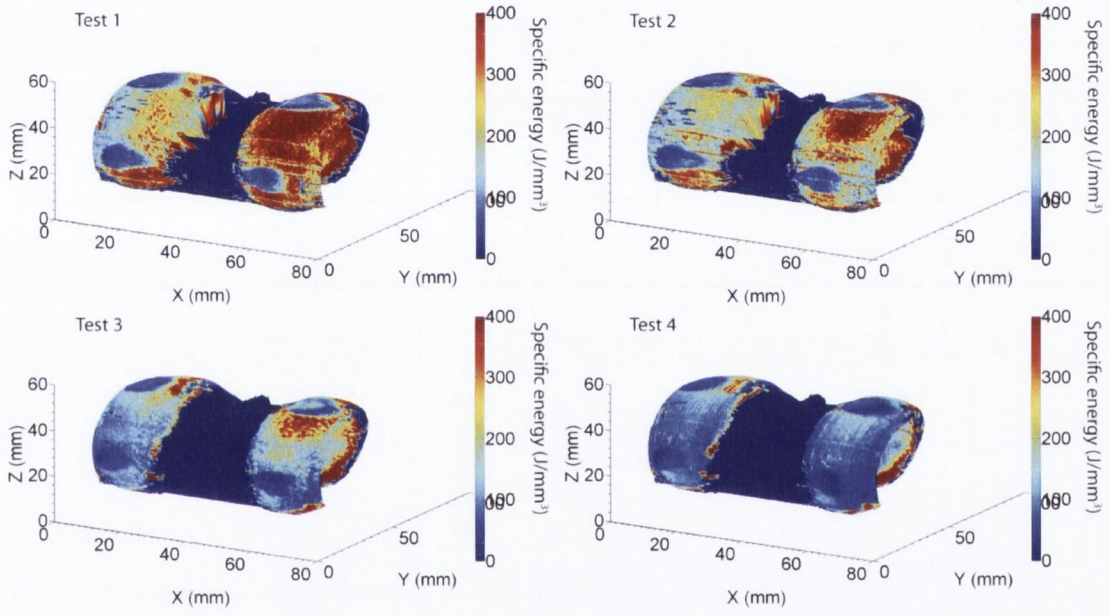
The specific energy analysis shown in Figure 6.14 and Figure 6.15 highlight regions over the surface of the femoral implant which could be considered to be inefficient. Low tool-workpiece engagement at the edges of the implant and edges of the patella track, and over the femoral condyles, result in high values of specific energy. This indicates a large amount of energy is entering a small area of material at these regions, therefore resulting in inefficient grinding conditions.

Specific energy near the convex shaped condyle regions is also shown to be approximately between 150 - 400 J/mm^3 for Toolpath A, and less than approximately 200 J/mm^3 for Toolpath B, illustrating that machining conditions are not ideal for the small engagement conditions given by Toolpath A.

Considering the results in context, specific energy for conventional surface grinding with typically low depths of cut have been found to be up to 200 J/mm^3, whereas low specific energy values of 10 – 50 J/mm^3 have been achieved with high efficiency deep grinding conditions for grinding of steels [21, 59, 216]. Specific energy values of 20 – 40 J/mm^3 have also been achieved for high efficiency deep grinding with electroplated CBN wheels for low alloy steel, with wheel speeds in excess of 100 m/s, depth of cut from 1 – 5 mm and feed rates of 2 – 125 mm/s used [66, 71].

High values of specific energy in abrasive machining processes are often to a low roughness requirement in a finishing operation coupled with a selection of inefficient process parameters [71]. The main goal of this abrasive machining process for femoral implants is to generate accurate and repeatable component dimensions, and to maintain surface integrity. Surface roughness of the components is reduced through later finishing processes of lapping and polishing. Therefore the focus of this process is efficient material removal, and machining parameters should be adjusted as such with respect to this primary goal of efficient material removal whilst maintaining a correct profile.

Low grinding temperatures can be achieved with high efficiency deep grinding as higher workspeeds can reduce the energy partition to the workpiece [61]. However, the thickness of the workpiece should also be considered as the thicker a workpiece is the more material there is for the heat to dissipate through as demonstrated in Appendix AI.3. Therefore feed rates and engaged area should not be increased by a large amount at regions of very thin workpiece thickness in order to avoid grinding burn. Also, when considering an increase in feed rate or depth of cut in order to reduce specific energy values, and therefore increase machining efficiency, the implications of tool wear, temperature and possibility of chatter vibration should be taken into account.



Material: CoCrMo F-75 Alloy	**Parameter:** v_s = 84 m/s	**Coolant:** Henkel Multan Cr10	**Tool:** New CBN B301 Grit
Test 1 v_f = 55 mm/s s = 0.381 mm d_o = 0 mm	**Test 2** v_f = 90 mm/s s = 0.381 mm d_o = 0 mm	**Test 3** v_f = 55 mm/s s = 0.762 mm d_o = 0.3 mm	**Test 4** v_f = 90 mm/s s = 0.762 mm d_o = 0.3 mm

Figure 6.15: Specific energy estimate over the surface of the part, back view

Regions of high specific energy shown in Figure 6.14 and Figure 6.15 could be reduced through an increase in depth of cut or a decrease in toolpath spacing, or alternatively an increase in feed rate. A significantly higher feed rate could likely be achieved particularly over the condyle regions without a significant risk of thermal damage in this region. Regions of lower specific energy of approximately 100 J/mm^3 or

less could be considered to be at an acceptable value and therefore increases in feed rate or tool-workpiece engagement at or near these areas are may be unnecessary and could run the risk of a deterioration in surface quality or tool wear.

6.6 Summary

In this chapter the influence of changes in process parameters with respect to tool-workpiece engagement, process power and specific energy for the abrasive machining process of femoral implants is investigated, and through this the developed algorithm and position-oriented monitoring method is tested. Results from a 2^2 factorial experiment with factors of feed rates of 55 mm/s and 90 mm/s and toolpaths with toolpath spacing of 0.381 mm, and 0.782 mm, and no radial offset and radial offset of -0.3 mm, respectively, are presented.

Laser measurement results detailing the difference between a cast and machined part were illustrated, and depth of cut was shown to vary between approximately 0.1 and 2 mm over the surface of the implant. A statistically significant difference in material removed between toolpath A and B was also detected by the laser measurements, illustrating the sensitivity of the measurement system to varying distance parameters.

An analysis of engaged area showed the majority of calculated values to be in the range of 0.01 – 1 mm^2. The regions of highest engagement were shown to be the patella track, which is concave in shape, as well as the casting gates due to their protrusion of up to 2 mm above the surface of the implant. Due to the alternating tool-workpiece engagement conditions it can be expected that process power and forces fluctuate significantly during the grinding process.

Power measurements from internal machine signals were shown to increase by approximately 813 Watts, or a 73% increase for a corresponding increase in tool-workpiece engagement between toolpath A and B. An increase of approximately 469 Watts, or a 37% increase was found for an increase in feed rate from 55 mm/s to 90 mm/s. The parameters of feed rate and toolpath were therefore shown to have a statistically significant effect on the response variable of cutting power. A position-oriented analysis of power showed power increasing with tool-workpiece engagement in concave areas such as the patella track as well as high depth of cut areas as encountered at the casting gate area.

An increase in the engaged area from toolpath A to toolpath B was shown to result in a mean decrease in specific energy of approximately 111 J/mm^3, or 44% decrease. Comparatively, an increase in feed rate from 55 mm/s to 90 mm/s was found to result in a mean decrease of 34 J/mm^3, or 16%, for mean specific energy. The regions of low specific energy over the surface of the part were found to be near the centre of the patella track and over the casting gates. This can be attributed to the large engagement area between tool and workpiece at these areas. In contrast, regions of high specific energy were found to be at the edges of the implant and edges of the patella track.

Specific energy could potentially be reduced in these regions through an increase in depth of cut or a decrease in toolpath spacing, or alternatively an increase in feed rate, in order to increase machining efficiency.

The results shown in this chapter verify that the developed process monitoring strategy, based upon correlation of machining position to the process metrics of power and material removed, is sensitive to changes in process parameters such as feed rate and toolpath/engaged area. By applying position-oriented monitoring, process characteristics can be better understood thus providing a knowledge base upon which process optimisation and control can be developed.

Chapter 7

Conclusion

The ability to monitor and control machining operations is of significant importance in guaranteeing long-term competitiveness in the manufacturing industry. However, not enough process monitoring knowledge makes the transition from research environments to real industrial machining applications due to the requirements for external sensors or modifications to machine structures. To date most devices are only suitable in one or two-axis manufacturing processes with few research studies investigating power monitoring of 3-axis or more freeform operations.

This research has explored the characteristics of an internal machine signal power and position-oriented monitoring strategy with a focus on development of a platform for process power monitoring for an industrial freeform machining operation. Internal machine signals of active power and position have been recorded and analysed under various grinding parameters for both flat surface and freeform grinding. In the case of freeform grinding, it has been attempted to correlate the signals with material removal measurements and model-based engagement over the full surface of the implant to form a position-related analysis on the efficiency of the process over the course of machining a freeform surface.

7.1 Process characterisation through power monitoring

Internal machine signals of active power and current from the spindle and servo drives as well as axis positions, and current from the servo drives were measured during flat surface grinding with toroidal shaped grinding wheels for Cobalt Chrome alloy under various machining parameters. Current from the A-axis drive was shown to be useful indicator of the material removed in the process. However, the active power signal from the main spindle was found to provide the most useful and sensitive information regarding the process, therefore the spindle active power was deemed be the most appropriate internal machine signal for monitoring and characterisation of the grinding process.

The behaviour of the internal machine active power signal from the spindle was shown to be sensitive to changes in depth of cut, with an almost linear rise in active spindle power between the values of 500 – 4000 Watts for depths of cut between 0.2 – 1.2 mm. The linearity in the signals behaviour provides an indication that the signal is reliable and repeatable and the sensitivity to depth of cut is a positive indication of power as a suitable metric for this process.

Furthermore, findings show that increased tool wear could be reliably detected through a rise in the power consumption. Increases of approximately 5000 Watts on average were experienced for depths of cut of 0.4 – 0.8 mm between a sharp and worn wheel with machining parameters of 84 m/s wheel speed and 55 mm/s feed rate analogous to those used in grinding of femoral implants. This indirect method of monitoring wheel wear has significant potential particularly for electroplated superabrasives. The slow wear increase of CBN can reliably be detected with power monitoring in order to avoid thermal damage of the workpiece due to excessive wheel wear.

During the Taguchi experiment the difference between a sharp wheel and worn wheel was quantified. Optical micrographs of the worn wheel surface taken with a USB microscope at 200X magnification revealed wear on the CBN grains by attrition, grain fracture and grain pullout, showing that a significant change in the grains morphology had taken place with wear. A difference in areal packing density of 0.7 grains/mm^2 was calculated between the sharp and worn wheel also indicating that a small amount of grain pullout has taken place during the wheels life. The wear flat area was also calculated from optical micrographs of replicas taken from the wheel surface and was found to be 2.1% for the worn wheel, further verifying the presence of wear flats on the individual CBN grains and noting that wear flats are typically responsible for increases in power and force during grinding.

Through a Taguchi L16 experimental design active spindle power was revealed to be sensitive to changes in process parameters including wheel speed and feed rate, whilst the sensitivity towards changes in depth of cut and wheel wear was further verified. In general, recorded cutting power for the various parameters varied between 3 – 13 kW. Further results from the Taguchi L16 test array showed the comparison between a new and sharp wheel had the highest contribution ratio of 52.3% for cutting power. Additionally, it was observed that wheel condition was the only statistically significant main effect for surface roughness, where a mean decrease in surface

roughness of 0.6 μm was found for grinding with a worn wheel, indicating that changes could be made to process parameters without a detrimental effect on workpiece surface roughness.

Depth of cut when varied between 0.5 and 1 mm has the second highest per cent contribution ratio of 42.1%. Wheel speed when varied between 52 – 84 m/s, and feed rate varied between 42 – 68 mm/s, both have a significant effect on the cutting power response, with their PCR value much lower, at 1.4% and 1.1% respectively. While the effect of changing wheel speed and feed rate on the cutting power was low in comparison to the effect of changes in wheel condition and depth of cut, it was still statistically significant, indicating a potential for process optimization through changes in these parameters.

Specific energy calculated for grinding with a worn wheel was observed to result in an increase of over 50 J/mm^3 with a per cent contribution ratio of 59%, illustrating a risk of thermal damage once significant wheel wear has taken place. Increases in depth of cut from 0.5 – 1 mm and feed rate from 42 – 68 mm/s resulted in a mean decrease in specific energy of 16 J/mm^3 for depth of cut and 11 J/mm^3 for feed rate. This indicates once more that changes made to these parameters can result in significant improvements in terms of reduction in specific energy and improvements in machining efficiency.

A power law trend was observed for specific energy calculated for depths of cut ranging from 0.1 – 1.2 mm for flat surface grinding of Cobalt Chrome alloy. It can be concluded that significant reductions of specific energy can be achieved through increases in the material removal rate up to a certain point, however after this point reductions in specific energy decrease in magnitude with increasing material removal rate. To avoid diminishing returns in efficiency for increases in material removal rate, it is important to identify the point at which this occurs, in order to prevent excessive and unnecessary tool wear and other associated issues.

7.2 Development of position-oriented process monitoring methodology

A custom laser measurement system designed and built in TCD as described in Section 3.4 was developed for this research and was used to determine the material removed in the process. The system comprised of two servo motors, a linear displacement laser and a custom built base. The developed system presented a resolution of at least 0.05 mm with a standard deviation of approximately 0.01 mm and

0.02 mm for flat and curved surfaces respectively, illustrating its potential as a flexible and economical solution for profile measurement.

Laser measurements using the system were obtained from femoral implants pre- and post- abrasive machining. The point clouds were matched using an iterative closest point matching algorithm that improved the alignment by reducing the overall root mean square distance between the pre- and post- abrasive machining point clouds.

The difference between the pre- and post- abrasive machining point clouds was obtained over the surface of the part and values were shown to vary between approximately 0 – 2 mm. Most significantly, there was considerable variation in the material removed over the surface of the implant, with more material removed in some areas such as concave shaped areas and casting gates, than other areas including the convex sections of the femoral condyles. Therefore, there is considerable potential for using the developed measurement system for the analysis of differences in material removal when toolpath or cutting conditions have changed.

While calculation of the distance between pre- and post-machined implants provides significant insights into the material removed during the process, an estimate of the engagement between the tool and workpiece over the course of the toolpath can provide a more in-depth insight into machining conditions and the effects of changes in toolpath spacing. This can be used also as a basis for the calculation of specific energy in order to provide an estimate of the efficiency of the toolpath over the entire surface of the part. An algorithm, as detailed in Section 5.2, was therefore developed in order to estimate the tool-workpiece engaged area over the surface of an implant utilizing laser part comparison measurements. Engagement is highly influential and dependent on the toolpath spacing and depth of cut in the X-direction, therefore a 2D analysis in the X-direction was selected in order to simplify the problem.

The accuracy of the developed algorithm was found to depend mainly on the accuracy and resolution of the laser measurements. The stated resolution of the laser measurement system is 0.003 mm. Repeat tests have shown that the system can produce results with standard deviations of less than 0.015 mm. A safe assumption is that the overall laser measurement system is accurate to 0.1 mm. Indeed, for power monitoring with a new wheel it becomes difficult to detect the change in the power signal for depths of cut of 0.1 mm or less. For this particular abrasive machining application however, where depths of cut are typically in the range of 0.1 mm – 2 mm, the process

monitoring combination of internal machine signal power monitoring and laser monitoring using the designed system.

The toolpath used to estimate the engaged area is a generated model toolpath based on the machined surface laser measurements. Results shown provide an insight into the highly variable contact conditions encountered during abrasive machining with typical estimates of engaged area ranging from 0 – 1 mm^2.

The internal machine signals of power and spindle position were used in order to monitor the abrasive machining process and were later analysed with a position-oriented approach. Typical cutting power values for a standard toolpath for machining a femoral implant were found to be within 0 – 10 kW. A plot of cutting power and position revealed an inter-positional dependency where power was notably higher than the mean value at certain points on the implants surface. Correlation of the power and material removed measurements from before and after machining further illustrated the positional dependency between the two quantities. Therefore, a joint analysis was performed in order to correlate the recorded cutting power with the calculated engaged area by first down-sampling the power data and then using nearest neighbour interpolation to match the two sets of data. Specific energy was then estimated over the surface of the part highlighting areas where abrasive machining conditions were not optimal.

7.3 Application of position-oriented monitoring approach for freeform surfaces

The method developed for position-oriented-analysis was applied and tested under different machining parameters with two feed rates and radial offset/tool path spacing. The femoral implant parts were measured with the laser measurement system before and after machining. The depth of cut and the estimated tool-workpiece engagement over the course of the toolpath was compared between experimental parameters. The internal power signal was examined between experimental parameters. Specific energy was estimated over the surface of the implant for each experimental trial and comparisons were drawn between the differing feed rates and radial offset/tool path spacing.

As shown previously, depth of cut for the abrasive machining trials was shown to vary between approximately 0.1 and 2 mm over the surface of the implant. This

illustrates the fact that material removal is not uniform over the course of the freeform toolpath, therefore it is necessary to consider the varying engagement conditions as part of any process optimisation strategy. Laser measurements also showed a statistically significant difference in material removed between toolpath A and B, highlighting the lasers sensitivity to varying distance parameters.

Internal machine signal power measurements demonstrated a significant increase in power of approximately 813 Watts, or 73%, for an increase in tool-workpiece engagement between the first and second toolpath. An increase of approximately 469 Watts, or 37%, was found for an increase in feed rate from 55 mm/s to 90 mm/s. A position-oriented power analysis revealed areas of significant power with power increasing as the tool-workpiece engagement increased in concave areas as illustrated by the patella track, and high depth of cut as encountered in the casting gate area. An interesting finding was that while the mean cutting power varied between approximately 1000 – 2500 Watts for each test, the maximum cutting power, particularly at the lower end of the patella track reached up to approximately 8000 – 14000 Watts for each test. This region, particularly due to the large depth of cut and tool-workpiece engagement at this point can therefore be considered to be anomalous.

An increase in the engaged area through an increase in toolpath spacing to 0.782 mm and radial offset decrease of 0.3 mm with toolpath B resulted in a mean decrease in specific energy of approximately 111 J/mm^3, or 44%. Comparatively, an increase in feed rate from 55 mm/s to 90 mm/s was found to result in a mean decrease of 34 J/mm^3, or 16%, for mean specific energy. The regions of low specific energy over the surface of the part were found to be near the centre of the patella track and over the casting gates. This can be attributed to the large engagement area between tool and workpiece at these areas. In contrast, regions of high specific energy were found to be at the edges of the implant and edges of the patella track, and over the condyle surface. Machining efficiency over the condyle surface for example, could potentially be improved through an increase in the material removal rate over this region.

The rationale behind pursuing a position-oriented monitoring and analysis strategy has been substantiated through the position-dependent results shown for specific energy. Anomalous high values of power and specific energy at certain positions of the part can be considered to be process disturbances. If a process optimization strategy was based only on the mean specific energy value, then the process disturbances would not be taken into account. Thermal damage could ensue as

the machining parameters that are suitable for the majority of the part may not be suitable for problem areas. Efficient machining conditions that do not compromise overall surface integrity can be achieved by considering differing engagement conditions separately. Such regions can be identified with a position-oriented monitoring and analysis strategy as investigated in this thesis.

7.4 Concluding remarks

It is generally accepted that there are significant opportunities associated with exploiting velocity effects in production processes, where the careful selection of process parameters can extend the existing process limits due to the production of a greater quantity of components in a shorter time. This can be achieved through increases in the material removal rate which can result in lower process specific energy. However, as an increase in process efficiency is typically accompanied by increased cutting power and risk of increased tool wear, it is critical to understand fully the effects of changing operating parameters before new grinding/abrasive machining strategies can be implemented without detrimental effect on surface integrity or tool wear [12, 21, 66-68]. One of the best ways of achieving this is through process monitoring where real process characteristics of complex freeform machining operations can be determined, allowing for more flexibility and certainty than perhaps process modelling would allow for.

Results shown in this thesis are of importance for the analysis of both machine parameter selection and toolpath planning in abrasive machining of femoral implants. As the engaged area decreases, the feed rate should be increased in order to maintain a constant material removal rate and in turn a constant specific energy. Inversely, it may be of benefit to reduce the feed rate at areas where the depth of cut/engaged area is particularly large. Furthermore, in order to achieve the most efficient machining conditions, it may be of benefit to increase the tool-workpiece engaged area where feasible by varying both the toolpath spacing as well as the engaged area.

The results shown in this thesis highlight the advantage of using two approaches towards process monitoring of freeform abrasive machining. First, monitoring and of internal machine power signals have been shown to be reliable, repeatable and to provide a deep insight into the grinding process characteristics [3, 15]. Second, the advantage of utilizing a position-oriented approach towards analysis of process power

and material removal data is illustrated, where machining characteristics and process disturbances can be identified and investigated in a more comprehensive manner [16, 106, 163]. This approach can serve as a basis for process optimization and offline control, where process efficiency is achieved through reducing specific energy over the generated surface of the part during abrasive machining.

7.5 Recommendations for future work

The four main areas of future work envisaged are -:

- Position-oriented analysis method
- Further characterisation of the abrasive machining process
- Laser measurement system
- Offline adaptive control loop for abrasive machining

Further improvement of the position-oriented analysis method can be achieved through development of a more refined data matching and interpolation method, as well as improvements of the efficiency of the algorithm. This may reduce computational time and improve accuracy, ease of use and accessibility of the algorithm.

Further testing of the abrasive machining process particularly focusing on characterization of the relationship between tool wear and feed rate may be beneficial. Assessment of the dynamic properties of the process at varying feed rates and engagement conditions through a modal analysis, and quantification of combinations of process parameters that carry a risk of regenerative chatter, could provide further insight into the dynamic characteristics of the process.

This thesis has highlighted the benefit of non-contact measurement of freeform surfaces for determination of material removed during a process. The laser measurement system developed for this project has considerable potential for future application integrated into a process control and inspection strategy/loop. Improvements could be made to the laser measurement system in terms of streamlining the control algorithms in order to reduce inspection time, as well as integration of a facility for comparison of acquired scans to CAD part models.

The development of a sensing and position-oriented sensor signal processing platform gives rise to the opportunity for process optimization and control. Given the

insight into process behaviour that power and material removal measurement can provide, an optimization strategy could be explored, with the ultimate goal of development into an offline or online adaptive control loop for abrasive machining. The approach could consist of a focus on the toolpath as well as the feed rate. The primary target is to maintain a consistent part profile. The toolpath could be optimized in order to maintain an increased and more consistent engaged area within the constraints of an acceptable part profile and macro surface roughness. The feed rate could then be adjusted with a position-oriented approach for the newly generated toolpath in order to maintain more efficient cutting conditions. Finally, surface integrity could be maintained through monitoring of the wheel wear through power monitoring, noting that a consistent increase in the power necessary to machine a part based upon the same machining parameters and engagement conditions is a reliable indicator of tool wear for electroplated CBN wheels.

Appendix I

Freeform abrasive machining investigations

AI.1 Macro surface roughness

Chapter 6 illustrates how with increased tool-workpiece engagement at certain feed rates corresponding specific energy can be low as a result. One method of increasing tool/workpiece engagement is to increase toolpath spacing. However, the macro surface roughness, also known as the scallop height, is closely related to the toolpath spacing. It is therefore of interest to know what effect changing toolpath spacing will have on the macro surface roughness. This effect can be estimated through approximating the scallop height analytically. The scallop height can be defined in terms of tool path spacing, the cutter radius and the local radius of curvature of the surface, as derived by Lin et al. [219]. As there are three main types of engagement; planar, convex and concave, theoretical scallop height was calculated through Equations AI.1 - AI.3.

$$s_h = R - \sqrt{R^2 - \left(\frac{s^2}{4}\right)} \tag{AI.1}$$

$$s_h = (R_w + R)\sqrt{1 - \left(\frac{s}{2R_w}\right)^2} - \sqrt{r^2 - \left[\frac{(R_w + R)s}{2R_w}\right]^2} - R_w \tag{AI.2}$$

$$s_h = R_w - (R_w - R)\sqrt{1 - \left(\frac{s}{2R_w}\right)^2} - \sqrt{r^2 - \left[\frac{(R_w + R)s}{2R_w}\right]^2} \tag{AI.3}$$

Tool path spacing is shown in Figure AI.1 versus the calculated scallop height. In order to maintain a good surface finish of the part it is necessary to ensure scallop height remains below the acceptable macro surface roughness value. It can be seen from Figure AI.1 that if for example, a theoretical scallop height of 0.02 mm is to be achieved

for a workpiece with a radius of 20 mm using a torus shaped grinding wheel with minor radius of 12 mm, it is necessary to have a toolpath spacing of approximately 0.83 mm, 1.10 mm and 1.39 mm for concave, convex and planar surfaces respectively. The difference in theoretical scallop heights for the different workpiece shape shown in Figure AI.1 also goes some way towards explaining the variation in visible scallop height between the concave patella track and the convex condyle regions shown previously on the surface of implants after abrasive machining. The shape of the workpiece is therefore an important consideration when increasing toolpath spacing in order to reduce overall cycle time.

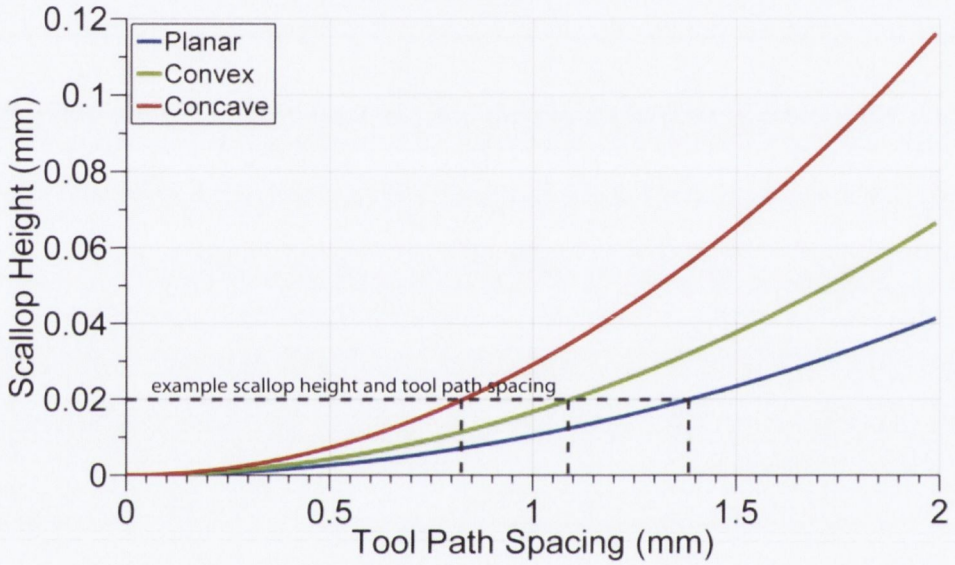


Figure AI.1: Scallop height for planar, convex and concave workpiece shapes of radius 20 mm

AI.2 Energy cost estimate

The abrasive machining process can also be evaluated from an energy cost point of view. Table AI.1 and Figure AI.2 demonstrate energy cost estimates for tests 1 – 4, where the machining parameters for tests 1 – 4 are described in Chapter 6 and in Figure AI.2.

The machine energy estimate refers to the machine overhead energy costs, with an approximation of 3.7 kW taken for the fixed energy consumption of the process. This is based upon a study by Herman et al. who investigated fixed power consumption of machine tools where a fixed power consumption of 3.7 kW was found for a Studer S40 universal grinding machine [220]. Electricity price was estimated at an average of €0.10/kWh [221]. Total energy expended by the spindle during machining was

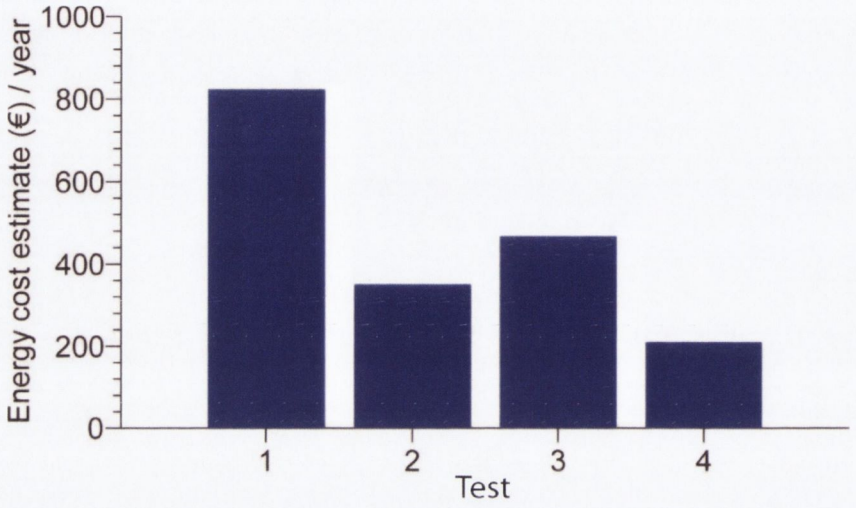
estimated through trapezoidal integration in Matlab. The energy estimate per year was estimated through an example of 24 parts machined per day, and the assumption that the machine operates 6 days a week, 52 weeks per year.

It is clear from Table AI.1 and Figure AI.2 that reduction in cycle time has a direct impact on energy cost reduction of the process. Grinding, or indeed any machining operation, is always accompanied by a fixed power demand from support equipment such as the spindle and servo drives, hydraulic and coolant supply system, control system and auxiliary systems such as the HMI, NC, fans and lighting [220]. An increase in the material removal rate therefore results in a decrease in overall cycle time and support equipment usage. The energy cost analysis shown in Figure AI.2 indicates it is generally beneficial in terms of cost to increase the material removal rate. The lowest estimated cost was for experimental test 4 at €210 per year, as compared to test 1 at €823 per year. Previous results shown for specific energy analysis also illustrate the benefit of an increase in material removal rate in order to reduce the magnitude of energy entering the part during grinding. Therefore it is generally beneficial when seeking an increase in process efficiency to increase the material removal rate.

While this analysis does not deal with the effect of the chosen process parameters on tool wear, the impact of an increase in process velocities on tool wear should also be taken into account for a more all-inclusive perspective on achieving efficiency in abrasive machining. Such an approach is described by authors Helu et al. and Mativenga et al. in their work on turning of titanium and steel alloys, who recommend taking a holistic perspective towards evaluating the total cost associated with a process time reduction strategy [222, 223]. Helu et al. found that material removal rates beyond 30 cm^3/min were unfeasible for turning of titanium alloy as the tool flank wear was too severe and tool life too short. This type of analysis should be performed when considering a change in process parameters, as although CBN is slow wearing due to its hardness there is likely a limit to which a benefit in energy costs and process efficiency is offset due to tool wear [79].

	Test time (hr)	Total Spindle Energy (kWh)	Machine Energy Estimate (kWh)	Energy Price (€/kWh)	Total Machine Energy Cost Estimate / Part (€)	Energy Cost Estimate (€) / Year
Test1	0.21	0.32	0.78	0.10	0.11	823
Test2	0.08	0.16	0.31	0.10	0.05	350
Test3	0.11	0.23	0.39	0.10	0.06	467
Test4	0.04	0.12	0.16	0.10	0.03	210

Table AI.1: Estimated energy costs



Material: CoCrMo F-75 Alloy	**Parameter:** v_s = 84 m/s	**Coolant:** Henkel Multan Cr10	**Tool:** New CBN B301 Grit
Test 1 v_f = 55 mm/s s = 0.381 mm d_o = 0 mm	**Test 2** v_f = 90 mm/s s = 0.381 mm d_o = 0 mm	**Test 3** v_f = 55 mm/s s = 0.762 mm d_o = 0.3 mm	**Test 4** v_f = 90 mm/s s = 0.762 mm d_o = 0.3 mm

Figure AI.2: Energy cost estimate per year

AI.3 Grinding burn marks

Figure AI.3 shows grinding burn marks at the back surface of the patella track. This was the only location where grinding burn marks were found on the implants. At this region on the implant the material thickness is very low, less than 1 mm at the area where grinding burn occurs. In a workpiece with a thin cross-section the heat entering the workpiece top surface from machining encounters a boundary before the heat energy has fully dissipated through the material. At this region the backside of the workpiece is not in contact with any of the arbour clamping system, therefore as air is a poor conductor the heat energy pools in this area. The grinding burn marks shown can be attributed to this effect.



Material: CoCrMo F-75 Alloy	**Parameter:** v_s = 84 m/s	**Coolant:** Henkel Multan Cr10	**Tool:** New CBN B301 Grit
Test 1 v_f = 55 mm/s s = 0.381 mm d_o = 0 mm	**Test 2** v_f = 90 mm/s s = 0.381 mm d_o = 0 mm	**Test 3** v_f = 55 mm/s s = 0.762 mm d_o = 0.3 mm	**Test 4** v_f = 90 mm/s s = 0.762 mm d_o = 0.3 mm

Figure AI.3: Grinding burn marks at back of patella track

The effect of increased feed rate is also shown in Figure AI.3. For the increased engaged area toolpath in Test 3 and 4 the effect is more noticeable, where it can be seen that the grinding burn is reduced as the heat energy had less time to sink into the part with the increased feed rate as shown in Test 4.

Appendix II

Flat surface grinding with toric wheels

AII.1 Temperature investigations

The objective of these tests was to investigate the range of temperatures the workpiece may experience at different depths of cut and with new and worn tool wear states.

Workpiece materials

Cobalt Chrome alloy (ASTM F-75) was used throughout the tests, details of the thermal properties are shown in Table AII.1. Workpiece material was initially supplied for the tests in the form of cast bars of Cobalt Chrome alloy with a bulk hardness of approximately 37 HRC. Test parts in the shape of T-bars were then cut and milled from the cast bars with thickness of 8 mm, flat surface area of 68 mm x 25 mm, designed to fit in the machine fixture. Blind holes of 0.6 mm diameter were drilled from the underside of the workpiece to a depth 0.1 mm below the track to be machined as shown in Figure AII.1. These holes were located in the centres of the tracks to be machined.

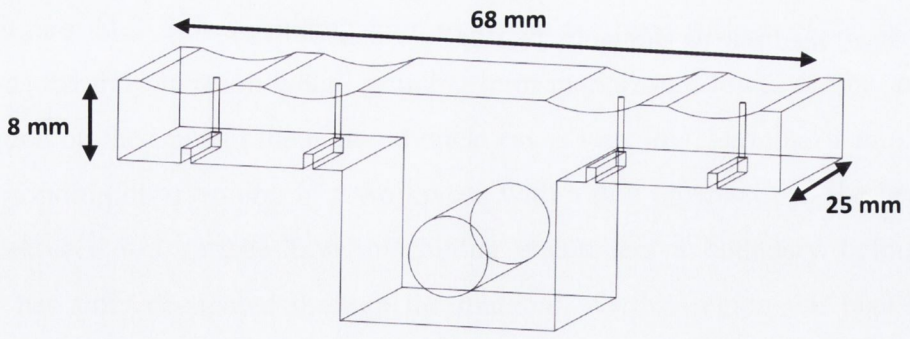


Figure AII.1: Cobalt Chrome alloy test piece with 4x thermocouples each placed beneath machined track

CoCrMo Alloy	ASTM F75
Thermal Conductivity, k (W/mK)	12-14
Specific Heat Capacity, c (J/kgK)	425-472
Density, ρ (kg/m^3)	8270-8320
Melting Point Temperature, T_m, for Co-Cr binary phase alloy (°C)	1397

Table AII.1: Thermal properties of Cobalt Chrome alloy [181, 224-226]

Test equipment

Tooling in the form of two sets of contoured twin wheels were used in these tests. Tools were 200 mm diameter electroplated CBN B301 grit grinding wheels with an inner toric radius of 12 mm. One of the sets was new, while the second set was worn. One wheel was chosen out of each set and used for the tests. All tests were carried out on a Haas Multigrind CB 5-axis grinding centre with a maximum spindle rotational speed of 8000 rpm and power rating of 29 kW. Figure AII.2 details the testing arrangement. Workpieces were held in a machining arbour with a secondary clamp.The oil used for coolant was a Henkel oil, Multan CR10.

Data acquisition equipment included a NI Hi-Speed USB Carrier NI USB-9162 in conjunction with NI Thermocouple DAQ NI 9213, connected via usb link to a Windows 7 laptop running Labview 2009. The DAQ unit was contained in a custom-made silicon sealed box with thermocouple and usb outputs. This was housed in the machine during testing. Thermocouples used in the tests were KMTXL-IM050U-150, Super OMEGACLAD® XL Sheath with 0.5 mm diameter, 150 mm length probes. Power was measured with Siemens Sinucom NC Trace software installed on the HMI of the machine on a Siemens 840Dsl controller. Machine variables including were recorded for each of the tests at a sample rate of 333 Hz.

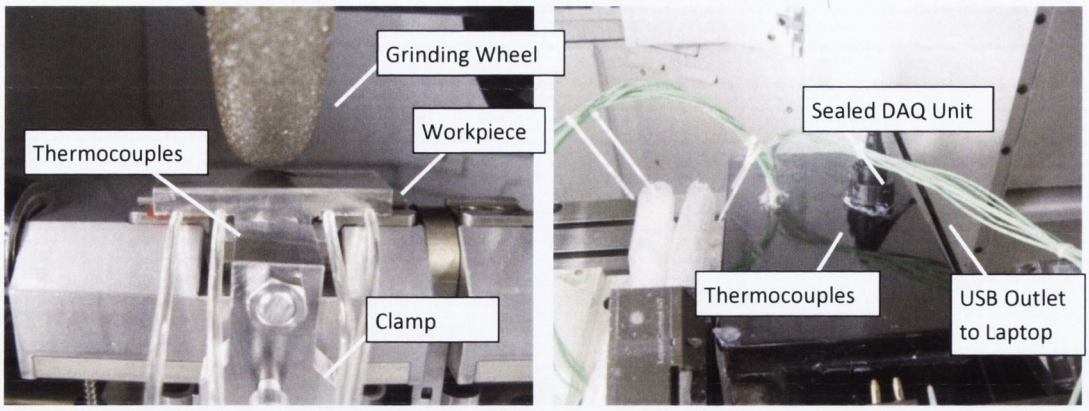


Figure AII.2: (Left) Cobalt Chrome t-bar with 4 thermocouples in place, (Right) Data acquisition equipment, silicon sealed box with NI 9213 thermocouple DAQ

Experimental Design and Test Parameters

A series of cuts were taken on the workpiece centred above each described thermocouple. Table AII.2 and Table AII.3 detail the test parameters. Two comparative tests between depths of cut of 0.5 mm and 0.9 mm and wheel condition of new and and worn were performed to assess their effect on workpiece temperature and machining power.

Test Parameters	
Wheel Speed	84 m/s (8000 RPM)
Feed Rate	55 mm/s (130 inch/min)
Depth of Cut	0.5mm/0.9mm
Coolant	Oil Based
Wheel Type	Electroplated CBN B301 grit
Wheel Condition	New/Worn
Workpiece Material	CoCr F-75 Alloy

Table AII.2: Test parameters

Test Parameters		
Depth of Cut	0.5mm	0.9mm
Wheel Condition	New	Worn

Table AII.3: Test parameters

Results & Discussion

Table AII.4 and Figure AII.3 show the temperature recorded during machining with new and worn wheel sets over two different depths of cut. Tests 3 and 4 for 0.9mm depth of cut with the new wheel set were not recorded due to incorrect parameter selection for the tests. Test 3 for 0.5 mm depth of cut with a worn wheel set

was a clear outlier, it is likely the thermocouple dislodged during the test and lost contact with the workpiece material. Despite the few missing tests there is still sufficient data present to examine the main trends.

A clear increase in temperature is shown when the depth of cut is increased from 0.5 mm to 0.9 mm for both the new and worn wheels. This is as expected, as the engagement area between the wheel and workpiece increases as the wheel moves deeper into the workpiece. A clear difference in temperature is also shown between the new and worn wheels. As the wheel wears the CBN grits develop wear flats and the contact area between the wheel and workpiece is increased leading to higher temperatures [84].

Temperature Results	New Wheel Set		Worn Wheel Set	
Depth of Cut	0.5mm	0.9mm	0.5mm	0.9mm
T1 (°C)	378	444	391	476
T2 (°C)	249	474	377	525
T3 (°C)	250		128	495
T4 (°C)	257		484	483
Mean	283	459	417	494
Std. Dev.	55	15	48	19

Table AII.4: Temperature measurements

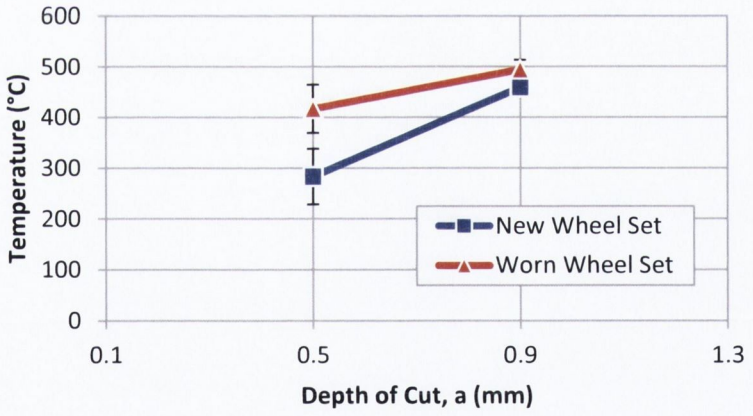


Figure AII.3: Temperature measurements for new and worn wheel at 0.5mm and 0.9mm depth of cut

When the depth of cut is 0.9mm depth of cut the temperature reaches up to 500°C with a worn wheel. In contrast, the coolant oil used, Henkel Multan CR-10 has a boiling point of 260°C [180]. Therefore it is possible that during machining of depths of cut above the 0.5 mm range the oil in the wheel-workpiece contact zone is vaporising. It is also important to note here that as the thermocouples were placed 0.1 mm below the surface of the machined track, it is clear that the actual temperature at the wheel-workpiece contact zone will be even higher. Therefore with increased wheel-workpiece

contact areas, large depths of cut, and a worn wheel, it is possible that the real cutting zone temperature could approach 1000°C or over.

Table AII.5 and Figure AII.4 shows the cutting power recorded for the tests. There is a relatively linear increase in cutting power when the depth of cut is increased from 0.5 mm to 0.9 mm. The cutting power is also significantly increased when a worn wheel is used. These results demonstrate a somewhat similar trend to the temperatures recorded during machining. Power monitoring also in this case appears to be a reliable indicator of tool wear over a variety of machining parameters.

Cutting Power Results (Watts)	New Wheel Set		Worn Wheel Set	
Depth of Cut	0.5mm	0.9mm	0.5mm	0.9mm
T1	3294	7286	10060	13692
T2	3342	7304	10142	13693
T3	3328		10225	13580
T4	3558		9889	13191
Mean	3381	7295	10079	13539
Std. Dev.	104	9	124	206

Table AII.5: Cutting power (Watts)

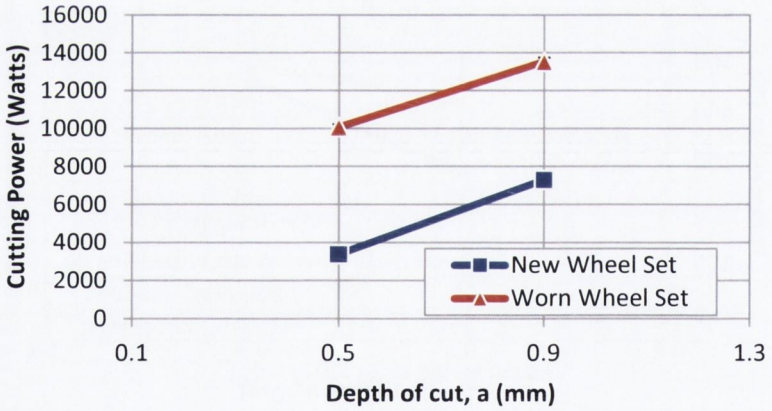


Figure AII.4: Cutting power (Watts)

Table AII.6 and Figure AII.5 show the specific energy calculated for the tests. For a new wheel, the power increases from 3.3 kW to 7.3 kW for a 0.5 mm and 0.9 mm depth of cut, however, specific energy remains relatively the same, from 26.8 J/mm^3 to 24.1 J/mm^3 for the two depths of cut. When grinding with a worn wheel the power is shown to increase from 10.1 kW to 13.5 kW for a 0.5 mm and 0.9 mm depth of cut, however there is a significant decrease in the specific energy, from 79.9 J/mm^3 to 44.6

J/mm^3 from 0.5 mm to 0.9 mm depth of cut. This can be attributed to the greater magnitude of power required for machining with a worn wheel.

Specific Energy Results (J/mm3)	New Wheel Set		Worn Wheel Set	
Depth of Cut	0.5mm	0.9mm	0.5mm	0.9mm
T1	26.1	24.0	79.7	45.1
T2	26.5	24.1	80.4	45.2
T3	26.4		81.0	44.8
T4	28.2		78.3	43.5
Mean	26.8	24.1	79.9	44.6
Std. Dev.	0.8	0.0	1.0	0.7

Table AII.6: Specific energy (J/mm^3)

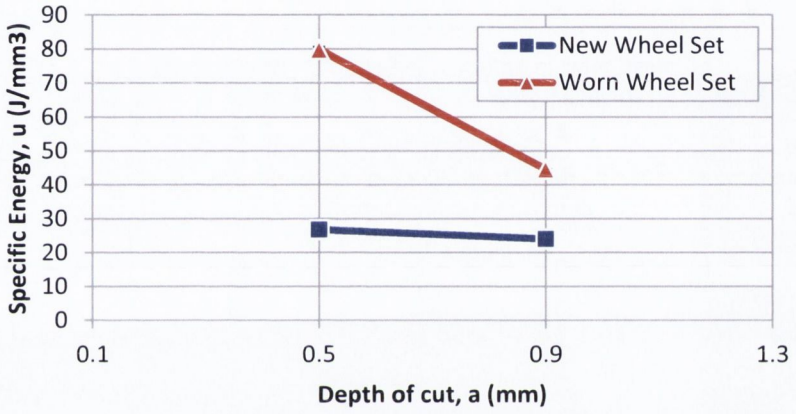


Figure AII.5: Specific energy (J/mm^3)

Appendix III

Machine Signal Evaluation

The available digital drive signals for process monitoring were evaluated and ranked under two main criteria; sensitivity to the material removal process and how closely the evaluated signal is related to known relationships for grinding process forces and energy. The analysis is summarized in Table AIII.1.

NC Trace variables	Sensitivity to surface grinding process	Relation to process forces and energy
Active Power SP1	●	●
Current SP1	●	◑
Active Power X	○	◑
Active Power Y	○	◑
Active Power Z	○	◑
Active Power A	○	◑
Current X	○	◑
Current Y	○	◑
Current Z	●	◑
Current A	●	◑
Actual Speed	○	◑

● Full agreement
◑ Partial agreement
○ No agreement

Table AIII.1: Evaluation of NC Trace variables

Spindle power is ranked as the most suitable machine drive internal signal for process monitoring as the signal is both sensitive to material removal and is also applicable in the evaluation of forces and energy in the abrasive process, where spindle power is a function of the tangential force and wheel speed. Specific energy and area specific power may also be subsequently derived from spindle power. Feed drive current remains a useful indicator for the material removal process as well as for identification of process anomalies.

Appendix IV

Machined surface 3D topographic maps

Figure AIV.1 shows an example of two 3D topographic maps taken for a 0.6 mm depth of cut with a new and worn wheel. Grinding marks can be seen running across the feed direction.

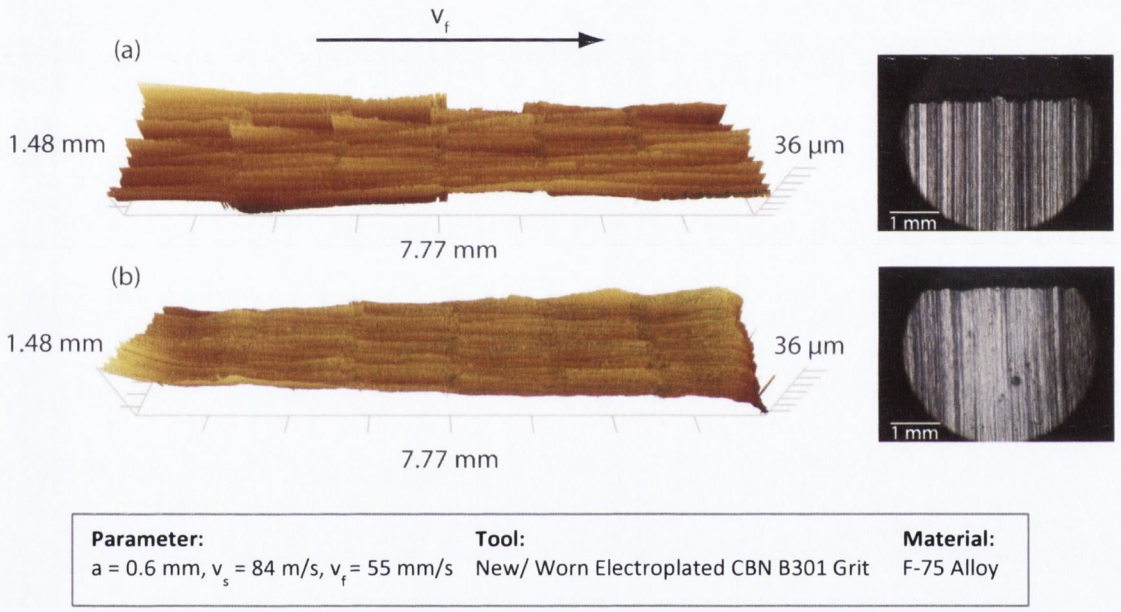


Figure AIV.1: 3D topography maps for (a) New wheel, Sa=2.93µm and workpiece surface microscopic image (right) and (b) Worn wheel, Sa=2.33µm and workpiece surface microscopic image (right)

References

[1] J. R. Duflou, J. W. Sutherland, D. Dornfeld, C. Herrmann, J. Jeswiet, S. Kara, M. Hauschild, and K. Kellens, "Towards energy and resource efficient manufacturing: A processes and systems approach," *CIRP Annals - Manufacturing Technology,* vol. 61, pp. 587-609, 2012.

[2] F. Klocke, S. Kratz, T. Auerbach, S. Gierlings, G. Wirtz, and D. Veselovac, "Process Monitoring and Control of Machining Operations," *International Journal of Automation Technology,* vol. 5, pp. 403-411, 2011.

[3] R. Teti, K. Jemielniak, G. O'Donnell, and D. Dornfeld, "Advanced monitoring of machining operations," *CIRP Annals - Manufacturing Technology,* vol. 59, pp. 717-739, 2010.

[4] G. Byrne, D. Dornfeld, I. Inasaki, G. Ketteler, W. König, and R. Teti, "Tool Condition Monitoring (TCM) -- The Status of Research and Industrial Application," *CIRP Annals - Manufacturing Technology,* vol. 44, pp. 541-567, 1995.

[5] G. Byrne, D. Dornfeld, and B. Denkena, "Advancing Cutting Technology," *CIRP Annals - Manufacturing Technology,* vol. 52, pp. 483-507, 2003.

[6] G. O'Donnell, P. Young, K. Kelly, and G. Byrne, "Towards the improvement of tool condition monitoring systems in the manufacturing environment," *Journal of Materials Processing Technology,* vol. 119, pp. 133-139, 2001.

[7] Espicom Business Intelligence Publications Limited, *Medistat: Worldwide Medical Market Forecasts to 2015*. Chichester, West Sussex, 2010.

[8] J. J. Ramsden, D. M. Allen, D. J. Stephenson, J. R. Alcock, G. N. Peggs, G. Fuller, and G. Goch, "The Design and Manufacture of Biomedical Surfaces," *CIRP Annals - Manufacturing Technology,* vol. 56, pp. 687-711, 2007.

[9] C. J. Evans, E. Paul, D. Dornfeld, D. A. Lucca, G. Byrne, M. Tricard, F. Klocke, O. Dambon, and B. A. Mullany, "Material Removal Mechanisms in Lapping and Polishing," *CIRP Annals - Manufacturing Technology,* vol. 52, pp. 611-633, 2003.

[10] M. Niinomi, *Metals for biomedical devices*: Woodhead Publishing, Oxford, 2010.

[11] B. Denkena, L. de Leon, A. Turger, and L. Behrens, "Prediction of contact conditions and theoretical roughness in manufacturing of complex implants by toric grinding tools," *International Journal of Machine Tools and Manufacture,* vol. 50, pp. 630-636, 2010.

[12] J. F. G. Oliveira, E. J. Silva, C. Guo, and F. Hashimoto, "Industrial challenges in grinding," *CIRP Annals - Manufacturing Technology,* vol. 58, pp. 663-680, 2009.

[13] B. Karpuschewski and I. Inasaki, "Monitoring Systems for Grinding Processes," in *Condition Monitoring and Control for Intelligent Manufacturing*: Springer London, 2006, pp. 83-107.

[14] H. K. Tönshoff, T. Friemuth, and J. C. Becker, "Process Monitoring in Grinding," *CIRP Annals - Manufacturing Technology,* vol. 51, pp. 551-571, 2002.

[15] C. Brecher, G. Quintana, T. Rudolf, and J. Ciurana, "Use of NC kernel data for surface roughness monitoring in milling operations," *The International Journal of Advanced Manufacturing Technology,* pp. 1-10, 2010.

[16] F. Klocke, S. Kratz, and D. Veselovac, "Position-oriented process monitoring in freeform milling," *CIRP Journal of Manufacturing Science and Technology,* vol. 1, pp. 103-107, 2008.
[17] E. Savio, L. De Chiffre, and R. Schmitt, "Metrology of freeform shaped parts," *CIRP Annals - Manufacturing Technology,* vol. 56, pp. 810-835, 2007.
[18] F. Klocke, *Manufacturing Processes 2; Grinding, Honing, Lapping* vol. 2. RWTHAachen University: Springer, 2009.
[19] S. Salmon, "What is Abrasive Machining?," *Manufacturing Engineering, SME,* vol. 144, 2010.
[20] M. Shaw, J. Crookall, and N. Suh, *Principles of Abrasive Processing.* Oxford: Clarendon Press, 1996.
[21] T. Tawakoli, *High efficiency deep grinding.* London: VDI-Verlag and Mechanical Engineering Publications Ltd., 1993.
[22] H. K. Tönshoff, B. Karpuschewski, T. Mandrysch, and I. Inasaki, "Grinding Process Achievements and their Consequences on Machine Tools Challenges and Opportunities," *CIRP Annals - Manufacturing Technology,* vol. 47, pp. 651-668, 1998.
[23] B. Denkena, A. Turger, L. Behrens, and T. Krawczyk, "Five-Axis-Grinding With Toric Tools: A Status Review," *Journal of Manufacturing Science and Engineering,* vol. 134, pp. 054001-6, 2012.
[24] B. Denkena, M. Reichstein, and M. van der Meer, "Production of complex medical implants with ceramic functional surfaces," in *5th International Conference of the european society for precision engineering and nanotechnology (euspen)*, Montpellier, 2005, pp. 759-762.
[25] B. Denkena, J. Köhler, and B. Wang, "Manufacturing of functional riblet structures by profile grinding," *CIRP Journal of Manufacturing Science and Technology,* vol. 3, pp. 14-26, 2010.
[26] L. N. L. de Lacalle and A. Lamikiz, *Machine tools for high performance machining* vol. 10: Springer Verlag, 2008.
[27] A. W. Khan and C. Wuyi, "Systematic Geometric Error Modeling for Workspace Volumetric Calibration of a 5-axis Turbine Blade Grinding Machine," *Chinese Journal of Aeronautics,* vol. 23, pp. 604-615, 2010.
[28] Z. Zhong and T. Nakagawa, "New Grinding Methods for Aspheric Mirrors with Large Curvature Radii," *CIRP Annals - Manufacturing Technology,* vol. 41, pp. 335-338, 1992.
[29] T. Kuriyagawa, M. S. S. Zahmaty, and K. Syoji, "A new grinding method for aspheric ceramic mirrors," *Journal of Materials Processing Technology,* vol. 62, pp. 387-392, 1996.
[30] S. Okuyama, T. Kitajima, and A. Yui, "Theoretical study on the effect of form error of grinding wheel surfaces under free form grinding," *Key Engineering Materials,* vol. 257, pp. 147-152, 2004.
[31] D. X. Feng and B. Hongzon, "CNC Rake Grinding for a Taper Ball-End Mill with a Torus-Shaped Grinding Wheel," *The International Journal of Advanced Manufacturing Technology,* vol. 21, pp. 549-555, 2003.
[32] K. Weinert, H. Blum, T. Jansen, and A. Rademacher, "Simulation based optimization of the NC-shape grinding process with toroid grinding wheels," *Production Engineering,* vol. 1, pp. 245-252, 2007.
[33] C. Brecher, M. Esser, and S. Witt, "Interaction of manufacturing process and machine tool," *CIRP Annals - Manufacturing Technology,* vol. 58, pp. 588-607, 2009.

[34] T. Jansen, "Entwicklung einer Simulation für den NC-Formschleifprozess mit Torusschleifscheiben," PhD, Institute of Machining Technology (ISF), TU Dortmund, 2008.
[35] D. Biermann, K. Weinert, T. Jansen, and M. Noyen, "Profile and shape grinding of high alloyed steels," *International Journal of Microstructure and Materials Properties,* vol. 3, pp. 413-423, 2008.
[36] B. Denkena, L. de Leon, and L. Behrens, "Contact Conditions in 5-Axis-Grinding of Double Curved Surfaces with Toric Grinding Wheels," *Advanced Materials Research,* vol. 126, pp. 41-46, 2010.
[37] B. Denkena and M. van der Meer, "Diamond tools for the grinding of complex ceramic implant surfaces," *Advanced Materials Research,* vol. 76, pp. 33-37, 2009.
[38] B. Denkena, J. Köhler, and M. van der Meer, "A roughness model for the machining of biomedical ceramics by toric grinding pins," *CIRP Journal of Manufacturing Science and Technology,* 2012.
[39] D. Graham and R. M. Baul, "An investigation into the mode of metal removal in the grinding process," *Wear,* vol. 19, pp. 301-314, 1972.
[40] S. Malkin and C. Guo, *Grinding technology: theory and applications of machining with abrasives*, second ed. New York: Industrial Press, 2008.
[41] E. Marshall and M. Shaw, "Forces in dry surface grinding," *Trans. Asme,* vol. 74, p. 51, 1952.
[42] H. K. Tönshoff, M. Zinngrebe, and M. Kemmerling, "Optimization of Internal Grinding by Microcomputer-Based Force Control," *CIRP Annals - Manufacturing Technology,* vol. 35, pp. 293-296, 1986.
[43] Y. Kita, M. Ido, and S. Hata, "The mechanism of metal removal by an abrasive tool," *Wear,* vol. 47, pp. 185-193, 1978.
[44] F. Klocke, E. Brinksmeier, and K. Weinert, "Capability Profile of Hard Cutting and Grinding Processes," *CIRP Annals - Manufacturing Technology,* vol. 54, pp. 22-45, 2005.
[45] S. Malkin and R. B. Anderson, "Thermal Aspects of Grinding: Part 1---Energy Partition," *Journal of Engineering for Industry,* vol. 96, pp. 1177-1183, 1974.
[46] W. Lortz, "A model of the cutting mechanism in grinding," *Wear,* vol. 53, pp. 115-128, 1979.
[47] S. M.C, "Energy Conversion in Cutting and Grinding*," *CIRP Annals - Manufacturing Technology,* vol. 45, pp. 101-104, 1996.
[48] S. Malkin and N. Joseph, "Minimum energy in abrasive processes," *Wear,* vol. 32, pp. 15-23, 1975.
[49] S. Kannappan and S. Malkin, "Effects of Grain Size and Operating Parameters on the Mechanics of Grinding," *Journal of Engineering for Industry,* vol. 94, pp. 833-842, 1972.
[50] A. J. Sedriks and T. O. Mulhearn, "Mechanics of cutting and rubbing in simulated abrasive processes," *Wear,* vol. 6, pp. 457-466, 1963.
[51] H. Sin, N. Saka, and N. P. Suh, "Abrasive wear mechanisms and the grit size effect," *Wear,* vol. 55, pp. 163-190, 1979.
[52] S. Malkin, "The attritious and fracture wear of grinding wheels," PhD, Massachusetts Institute of Technology, Dept. of Mechanical Engineering, 1968.
[53] S. Malkin and C. Guo, "Thermal Analysis of Grinding," *CIRP Annals - Manufacturing Technology,* vol. 56, pp. 760-782, 2007.
[54] M. C. Shaw, "The importance of temperature in grinding," *Journal of Mechanical Working Technology,* vol. 17, pp. 343-355, 1988.

[55] B. Karpuschewski, H. J. Knoche, and M. Hipke, "Gear finishing by abrasive processes," *CIRP Annals - Manufacturing Technology,* vol. 57, pp. 621-640, 2008.
[56] R. A. Irani, R. J. Bauer, and A. Warkentin, "A review of cutting fluid application in the grinding process," *International Journal of Machine Tools and Manufacture,* vol. 45, pp. 1696-1705, 2005.
[57] H. S. Carslaw and J. C. Jaeger, "Conduction of heat in solids," *Oxford: Clarendon Press, 1959, 2nd ed.,* vol. 1, 1959.
[58] J. Jaeger, "Moving sources of heat and the temperature of sliding contacts," in *Proc. R. Soc. New South Wales*, 1942, p. 202.
[59] W. B. Rowe, "Thermal analysis of high efficiency deep grinding," *International Journal of Machine Tools and Manufacture,* vol. 41, pp. 1-19, 2001.
[60] W. B. Rowe and T. Jin, "Temperatures in High Efficiency Deep Grinding (HEDG)," *CIRP Annals - Manufacturing Technology,* vol. 50, pp. 205-208, 2001.
[61] T. Jin and D. J. Stephenson, "Investigation of the heat partitioning in high efficiency deep grinding," *International Journal of Machine Tools and Manufacture,* vol. 43, pp. 1129-1134, 2003.
[62] E. Brinksmeier, J. C. Aurich, E. Govekar, C. Heinzel, H. W. Hoffmeister, F. Klocke, J. Peters, R. Rentsch, D. J. Stephenson, E. Uhlmann, K. Weinert, and M. Wittmann, "Advances in Modeling and Simulation of Grinding Processes," *CIRP Annals - Manufacturing Technology,* vol. 55, pp. 667-696, 2006.
[63] E. Brinksmeier, J. T. Cammett, W. König, P. Leskovar, J. Peters, and H. K. Tönshoff, "Residual Stresses -- Measurement and Causes in Machining Processes," *CIRP Annals - Manufacturing Technology,* vol. 31, pp. 491-510, 1982.
[64] X. Chen, W. B. Rowe, and D. F. McCormack, "Analysis of the transitional temperature for tensile residual stress in grinding," *Journal of Materials Processing Technology,* vol. 107, pp. 216-221, 2000.
[65] A. Bell, T. Jin, and D. J. Stephenson, "Burn threshold prediction for High Efficiency Deep Grinding," *International Journal of Machine Tools and Manufacture,* vol. 51, pp. 433-438, 2011.
[66] D. J. Stephenson, T. Jin, and J. Corbett, "High Efficiency Deep Grinding of a Low Alloy Steel with Plated CBN Wheels," *CIRP Annals - Manufacturing Technology,* vol. 51, pp. 241-244, 2002.
[67] R. Neugebauer, W. Drossel, R. Wertheim, C. Hochmuth, and M. Dix, "Resource and energy efficiency in machining using high-performance and hybrid processes," *Procedia CIRP 2012,* vol. 1, pp. 3-16, 2012.
[68] R. Neugebauer, K. D. Bouzakis, B. Denkena, F. Klocke, A. Sterzing, A. E. Tekkaya, and R. Wertheim, "Velocity effects in metal forming and machining processes," *CIRP Annals - Manufacturing Technology,* vol. 60, pp. 627-650, 2011.
[69] W. B. Rowe, M. N. Morgan, S. C. E. Black, and B. Mills, "A Simplified Approach to Control of Thermal Damage in Grinding," *CIRP Annals - Manufacturing Technology,* vol. 45, pp. 299-302, 1996.
[70] B. Linke, M. Duscha, F. Klocke, and D. Dornfeld, *Combination of Speed Stroke Grinding and High Speed Grinding with Regard to Sustainability*. UC Berkeley: Laboratory for Manufacturing and Sustainability, 2011.

[71] P. Comley, I. Walton, T. Jin, and D. J. Stephenson, "A High Material Removal Rate Grinding Process for the Production of Automotive Crankshafts," *CIRP Annals - Manufacturing Technology,* vol. 55, pp. 347-350, 2006.
[72] S. Malkin and N. H. Cook, *Wear of grinding wheels. Part 1. Attritious Wear.*: Univ. of Texas, Austin, 1971.
[73] A. A. Torrance, "Modelling abrasive wear," *Wear,* vol. 258, pp. 281-293, 2005.
[74] W. B. Rowe, *Principles of Modern Grinding Technology*: William Andrew Publishing, 2009.
[75] M. Groover, *Fundamentals Of Modern Manufacturing: Materials Processes and Systems*: John Wiley & Sons, 2007.
[76] M. J. Jackson and J. P. Davim, *Machining with abrasives*. New York, US: Springer, 2010.
[77] S. Hayden, *Manufactured Superabrasives An Art and a Science*. Worthington, Ohio: GE Superabrasives, 2000.
[78] J. Haines, J. Leger, and G. Bocquillon, "Synthesis and Design of Superhard Materials," *Annual Review of Materials Research,* vol. 31, pp. 1-23, 2001.
[79] Z. Shi and S. Malkin, "Wear of electroplated CBN grinding wheels," *Journal of manufacturing science and engineering,* vol. 128, p. 110, 2006.
[80] S. Malkin, "Current Trends in CBN Grinding Technology," *CIRP Annals - Manufacturing Technology,* vol. 34, pp. 557-563, 1985.
[81] D. K. Aspinwall, S. L. Soo, D. T. Curtis, and A. L. Mantle, "Profiled Superabrasive Grinding Wheels for the Machining of a Nickel Based Superalloy," *CIRP Annals - Manufacturing Technology,* vol. 56, pp. 335-338, 2007.
[82] W. B. Rowe, S. Ebbrell, and M. N. Morgan, "Process Requirements for Cost-Effective Precision Grinding," *CIRP Annals - Manufacturing Technology,* vol. 53, pp. 255-258, 2004.
[83] Q. Liu, X. Chen, and N. Gindy, "Assessment of Al2O3 and superabrasive wheels in nickel-based alloy grinding," *The International Journal of Advanced Manufacturing Technology, 33,* vol. 9, pp. 940-951, 2007.
[84] R. Upadhyaya and S. Malkin, "Thermal aspects of grinding with electroplated CBN wheels," *Journal of manufacturing science and engineering,* vol. 126, pp. 107-114, 2004.
[85] J. Webster and M. Tricard, "Innovations in Abrasive Products for Precision Grinding," *CIRP Annals - Manufacturing Technology,* vol. 53, pp. 597-617, 2004.
[86] R. P. Upadhyaya and J. H. Fiecoat, "Factors Affecting Grinding Performance with Electroplated CBN Wheels," *CIRP Annals - Manufacturing Technology,* vol. 56, pp. 339-342, 2007.
[87] W. A. Knight, *Fundamentals of Metal Machining and Machine Tools*, third ed.: CRC Press Taylor & Francis Group, 2006.
[88] Z. Shi and S. Malkin, "An Investigation of Grinding with Electroplated CBN Wheels," *CIRP Annals - Manufacturing Technology,* vol. 52, pp. 267-270, 2003.
[89] C. Guo, Z. Shi, H. Attia, and D. McIntosh, "Power and Wheel Wear for Grinding Nickel Alloy with Plated CBN Wheels," *CIRP Annals - Manufacturing Technology,* vol. 56, pp. 343-346, 2007.
[90] X. Chen, W. B. Rowe, and R. Cai, "Precision grinding using CBN wheels," *International Journal of Machine Tools and Manufacture,* vol. 42, pp. 585-593, 2002.

[91] T. Matsuo, H. Shibahara, and Y. Ohbuchi, "Curvature in Surface Grinding of Thin Workpieces with Superabrasive Wheels," *CIRP Annals - Manufacturing Technology,* vol. 36, pp. 231-234, 1987.
[92] H. K. Tönshoff, H. G. Wobker, and G. Brunner, "CBN Grinding with Small Wheels," *CIRP Annals - Manufacturing Technology,* vol. 44, pp. 311-316, 1995.
[93] M. Duscha, F. Klocke, and H. Wegner, "Residual stress model for speed stroke grinding of hardened steel with CBN grinding wheels," in *4th CIRP International Conference on High Performance Cutting*, Gifu, Japan, 2010, pp. 437 - 448.
[94] C. Brecher, *Integrative production technology for high-wage countries*: Springer Berlin Heidelberg, 2012.
[95] S. Liang, R. Hecker, and R. Landers, "Machining process monitoring and control: the state-of-the-art," *Journal of manufacturing science and engineering,* vol. 126, p. 297, 2004.
[96] G. E. O'Donnell, "Sensor Technology for Process Monitoring in Flexible Machining Systems," PhD, AMS Research Centre, UCD, Dublin, 2007.
[97] K. Jemielniak, "Commercial Tool Condition Monitoring Systems," *The International Journal of Advanced Manufacturing Technology,* vol. 15, pp. 711-721, 1999.
[98] H. K. Tönshoff, J. P. Wulfsberg, H. J. J. Kals, W. König, and C. A. van Luttervelt, "Developments and Trends in Monitoring and Control of Machining Processes," *CIRP Annals - Manufacturing Technology,* vol. 37, pp. 611-622, 1988.
[99] D. E. Dimla, "Sensor signals for tool-wear monitoring in metal cutting operations--a review of methods," *International Journal of Machine Tools and Manufacture,* vol. 40, pp. 1073-1098, 2000.
[100] E. Ahearne, D. Logan, and G. Byrne, "Dual mode control of the rotational grinding process," *CIRP Annals - Manufacturing Technology,* vol. 61, pp. 303-306, 2012.
[101] G. Byrne and G. E. O'Donnell, "An Integrated Force Sensor Solution for Process Monitoring of Drilling Operations," *CIRP Annals - Manufacturing Technology,* vol. 56, pp. 89-92, 2007.
[102] F. Klocke, S. Gierlings, O. Adams, T. Auerbach, S. Kamps, D. Veselovac, M. Eckstein, A. Kirchheim, M. Blattner, R. Thiel, and D. Kohler, "New Concepts of Force Measurement Systems for Specific Machining Processes in Aeronautic Industry," *Procedia CIRP,* vol. 1, pp. 552-557, 2012.
[103] I. Inasaki, B. Karpuschewski, and H. S. Lee, "Grinding Chatter – Origin and Suppression," *CIRP Annals - Manufacturing Technology,* vol. 50, pp. 515-534, 2001.
[104] G. Quintana and J. Ciurana, "Chatter in machining processes: A review," *International Journal of Machine Tools and Manufacture,* vol. 51, pp. 363-376, 2011.
[105] J. F. G. Oliveira, T. V. França, and J. P. Wang, "Experimental analysis of wheel/workpiece dynamic interactions in grinding," *CIRP Annals - Manufacturing Technology,* vol. 57, pp. 329-332, 2008.
[106] S. Kratz, "Position-Oriented Vibration Monitoring of Finish Milling Thin-Walled Components," PhD PhD Thesis, WZL RWTH Aachen, Aachen, 2011.
[107] M. A. Davies, T. Ueda, R. M'Saoubi, B. Mullany, and A. L. Cooke, "On The Measurement of Temperature in Material Removal Processes," *CIRP Annals - Manufacturing Technology,* vol. 56, pp. 581-604, 2007.

[108] X. Xu and S. Malkin, "Comparison of Methods to Measure Grinding Temperatures," *Journal of manufacturing science and engineering,* vol. 123, pp. 191-195, 2001.
[109] E. Brinksmeier, C. Heinzel, and L. Meyer, "Development and Application of a Wheel Based Process Monitoring System in Grinding," *CIRP Annals - Manufacturing Technology,* vol. 54, pp. 301-304, 2005.
[110] *Non Destructive Testing, Acoustic Emission.* Available: http://www.ndt-ed.org/. [Accessed on 20/Oct/2012].
[111] R. Babel, P. Koshy, and M. Weiss, "Acoustic emission spikes at workpiece edges in grinding: Origin and applications," *International Journal of Machine Tools and Manufacture,* vol. 64, pp. 96-101, 2013.
[112] Z. Yang and Z. Yu, "Grinding wheel wear monitoring based on wavelet analysis and support vector machine," *The International Journal of Advanced Manufacturing Technology,* vol. 62, pp. 107-121, 2012.
[113] R. Stoney, B. Donohoe, D. Geraghty, and G. E. O'Donnell, "The Development of Surface Acoustic Wave Sensors (SAWs) for Process Monitoring," *Procedia CIRP,* vol. 1, pp. 569-574, 2012.
[114] D. Lange, "New Strategies in Process Monitoring," presented at the 2nd International Workshop on Intelligent Manufacturing Systems, Leuven, Belgium, 1999.
[115] Y. Altintas, A. Verl, C. Brecher, L. Uriarte, and G. Pritschow, "Machine tool feed drives," *CIRP Annals - Manufacturing Technology,* vol. 60, pp. 779-796, 2011.
[116] Honeywell Sensing and Control, *Hall Effect Sensing and Application.* Golden Valley, MN, 2001.
[117] M. A. Mannan, S. Broms, and B. Lindström, "Monitoring and Adaptive Control of Cutting Process by Means of Motor Power and Current Measurements," *CIRP Annals - Manufacturing Technology,* vol. 38, pp. 347-350, 1989.
[118] X. Li and S. K. Tso, "Drill wear monitoring based on current signals," *Wear,* vol. 231, pp. 172-178, 1999.
[119] F. A. Al-Sulaiman, M. A. Baseer, and A. K. Sheikh, "Use of electrical power for online monitoring of tool condition," *Journal of Materials Processing Technology,* vol. 166, pp. 364-371, 2005.
[120] J. M. Lee, D. K. Choi, J. Kim, and C. N. Chu, "Real-Time Tool Breakage Monitoring for NC Milling Process," *CIRP Annals - Manufacturing Technology,* vol. 44, pp. 59-62, 1995.
[121] T.-Y. Kim, J. Woo, D. Shin, and J. Kim, "Indirect cutting force measurement in multi-axis simultaneous NC milling processes," *International Journal of Machine Tools and Manufacture,* vol. 39, pp. 1717-1731, 1999.
[122] D. Axinte and N. Gindy, "Assessment of the effectiveness of a spindle power signal for tool condition monitoring in machining processes," *International Journal of Production Research,* vol. 42, pp. 2679 - 2691, 2004.
[123] N. Diaz, E. Redelsheimer, and D. Dornfeld, "Energy Consumption Characterization and Reduction Strategies for Milling Machine Tool Use," in *Glocalized Solutions for Sustainability in Manufacturing*: Springer Berlin Heidelberg, 2011, pp. 263-267.
[124] C. Herrmann and S. Thiede, "Process chain simulation to foster energy efficiency in manufacturing," *CIRP Journal of Manufacturing Science and Technology,* vol. 1, pp. 221-229, 2009.

[125] E. Brinksmeier and E. Minke, "High-performance surface grinding-the influence of coolant on the abrasive process," *CIRP Annals-Manufacturing Technology,* vol. 42, pp. 367-370, 1993.
[126] J.-S. Kwak, S.-B. Sim, and Y.-D. Jeong, "An analysis of grinding power and surface roughness in external cylindrical grinding of hardened SCM440 steel using the response surface method," *International Journal of Machine Tools and Manufacture,* vol. 46, pp. 304-312, 2006.
[127] I. Inasaki, "Monitoring and Optimization of Internal Grinding Process," *CIRP Annals - Manufacturing Technology,* vol. 40, pp. 359-362, 1991.
[128] N. Subrahmanya and Y. Shin, "Automated Sensor Selection and Fusion for Monitoring and Diagnostics of Plunge Grinding," *Journal of manufacturing science and engineering,* vol. 130, pp. 0310141-11, 2008.
[129] W. B. Rowe, S. C. E. Black, and B. Mills, "Temperature control in CBN grinding," *The International Journal of Advanced Manufacturing Technology,* vol. 12, pp. 387-392, 1996.
[130] J. Webster, E. Brinksmeier, C. Heinzel, M. Wittmann, and K. Thoens, "Assessment of Grinding Fluid Effectiveness in Continuous-Dress Creep Feed Grinding," *CIRP Annals - Manufacturing Technology,* vol. 51, pp. 235-240, 2002.
[131] C. Guo, M. Campomanes, D. McIntosh, C. Becze, T. Green, and S. Malkin, "Optimization of Continuous Dress Creep-Feed Form Grinding Process," *CIRP Annals - Manufacturing Technology,* vol. 52, pp. 259-262, 2003.
[132] C. Guo, M. Campomanes, D. McIntosh, C. Becze, and S. Malkin, "Model-Based Monitoring and Control of Continuous Dress Creep-Feed Form Grinding," *CIRP Annals - Manufacturing Technology,* vol. 53, pp. 263-266, 2004.
[133] C. Guo and S. Malkin, "Model Based Simulation of Grinding Processes," presented at the 2nd European Conference on Grinding, 2007.
[134] C. Guo, S. Ranganath, D. McIntosh, and A. Elfizy, "Virtual high performance grinding with CBN wheels," *CIRP Annals - Manufacturing Technology,* vol. 57, pp. 325-328, 2008.
[135] C. Guo, "Modeling and Simulation of Mold and Die Grinding," *Journal of Manufacturing Science and Engineering,* vol. 134, pp. 0410071-4, 2012.
[136] J. Badger, "Factors affecting wheel collapse in grinding," *CIRP Annals - Manufacturing Technology,* vol. 58, pp. 307-310, 2009.
[137] V. R. Murray, F. Zhao, and J. W. Sutherland, "Life cycle analysis of grinding: a case study of non-cylindrical computer numerical control grinding via unit-process life cycle inventory approach," *Proceedings of the Institution of Mechanical Engineers, Part B: Journal of Engineering Manufacture,* 2012.
[138] G. Ketteler, " Influences on Monitoring Systems which Affect their Reliability," presented at the 2nd International Workshop on Intelligent Manufacturing Systems, Leuven, Belgium, 1999.
[139] J. Stein and C. H. Wang, "Analysis of power monitoring on AC induction drive systems," *Journal of dynamic systems, measurement, and control,* vol. 112, pp. 239-248, 1990.
[140] T.-Y. Kim and J. Kim, "Adaptive cutting force control for a machining center by using indirect cutting force measurements," *International Journal of Machine Tools and Manufacture,* vol. 36, pp. 925-937, 1996.
[141] P. W. Prickett and C. Johns, "An overview of approaches to end milling tool monitoring," *International Journal of Machine Tools and Manufacture,* vol. 39, pp. 105-122, 1999.

[142] D. Kim and D. Jeon, "Fuzzy-logic control of cutting forces in CNC milling processes using motor currents as indirect force sensors," *Precision Engineering,* vol. 35, pp. 143-152, 2011.
[143] A. Rivero, L. N. López de Lacalle, and M. L. Penalva, "Tool wear detection in dry high-speed milling based upon the analysis of machine internal signals," *Mechatronics,* vol. 18, pp. 627-633, 2008.
[144] L. A. Franco-Gasca, G. Herrera-Ruiz, R. Peniche-Vera, R. d. J. Romero-Troncoso, and W. Leal-Tafolla, "Sensorless tool failure monitoring system for drilling machines," *International Journal of Machine Tools and Manufacture,* vol. 46, pp. 381-386, 2006.
[145] L. Franco-Gasca, R. d. J. Romero-Troncoso, G. Herrera-Ruiz, and R. d. R. Peniche-Vera, "Reconfigurable filtering system for sensorless signal acquisition in machining processes," *The International Journal of Advanced Manufacturing Technology,* vol. 38, pp. 102-109, 2008.
[146] H. Y. Kim, J. H. Ahn, S. H. Kim, and S. Takata, "Real-time drill wear estimation based on spindle motor power," *Journal of Materials Processing Technology,* vol. 124, pp. 267-273, 2002.
[147] A. Verl, U. Heisel, M. Walther, and D. Maier, "Sensorless automated condition monitoring for the control of the predictive maintenance of machine tools," *CIRP Annals - Manufacturing Technology,* vol. 58, pp. 375-378, 2009.
[148] Haas Schleifmaschinen, "Multigrind CB Technical Manual," 2012.
[149] Siemens AG. 2010. *Sinumerik and Sinamics Equipment for Machine Tools Catalog NC61.* Available: http://www.automation.siemens.com/mcms/infocenter/dokumentencenter/mc/Documentsu20Catalogs/nc61_2010_e2.pdf. [Accessed on 01/Nov/2012].
[150] G. Pritschow, Y. Altintas, F. Jovane, Y. Koren, M. Mitsuishi, S. Takata, H. van Brussel, M. Weck, and K. Yamazaki, "Open Controller Architecture - Past, Present and Future," *CIRP Annals - Manufacturing Technology,* vol. 50, pp. 463-470, 2001.
[151] E. Silva, M. Biffi, and J. F. G. Oliveira, "The development of an open architecture control system for CBN high speed grinding," *Journal of the Brazilian Society of Mechanical Sciences and Engineering,* vol. 26, pp. 51-55, 2004.
[152] J. Oliveira, F. Ferraz Júnior, R. Coelho, and E. Silva, "Architecture for machining process and production monitoring based in open computer numerical control," *Proceedings of the Institution of Mechanical Engineers, Part B: Journal of Engineering Manufacture,* vol. 222, p. 1605, 2008.
[153] V. Plapper and M. Weck, "Sensorless machine tool condition monitoring based on open NCs," in *Proceedings ICRA. IEEE International Conference on Robotics and Automation, vol. 3,*, 2001, pp. 3104-3108.
[154] S. Mekid, P. Pruschek, and J. Hernandez, "Beyond intelligent manufacturing: A new generation of flexible intelligent NC machines," *Mechanism and Machine Theory,* vol. 44, pp. 466-476, 2009.
[155] C. da Silva, E. Nakao, T. de Souza, and E. Villani, "Analysis of Customized and Commercial Solutions for Remote Monitoring of Manufacturing Processes," presented at the ABCM Symposium Series in Mechatronics, 2008.
[156] Siemens AG, "SinuCom Installation/Service Tools Documentation," 2008.
[157] C. Brecher, W. Lohse, and M. Vitr, "CAx Framework for Planning Five-Axis Milling Processes," in *Proceedings of the 6th CIRP-Sponsored International*

Conference on Digital Enterprise Technology Advances in Intelligent and Soft Computing 2010, pp. 419-432.

[158] C. Brecher, W. Lohse, and M. Vitr, "CAM-NC planning with real and virtual process data," in *17th International Conference on Concurrent Enterprising (ICE)*, 2011, pp. 1-8.

[159] C. Brecher and T. Rudolf, "Adaptive logging module for monitoring applications using control internal digital drive signals," *Production Engineering,* vol. 3, pp. 305-312, 2009.

[160] G. Quintana, T. Rudolf, J. Ciurana, and C. Brecher, "Using kernel data in machine tools for the indirect evaluation of surface roughness in vertical milling operations," *Robotics and Computer-Integrated Manufacturing,* vol. 27, pp. 1011-1018, 2011.

[161] G. Quintana, T. Rudolf, J. Ciurana, and C. Brecher, "Surface roughness prediction through internal kernel information and external accelerometers using artificial neural networks," *Journal of Mechanical Science and Technology,* vol. 25, pp. 2877-2886, 2011.

[162] L. N. L. de Lacalle, A. Lamikiz, J. A. Sanchez, and I. F. de Bustos, "Simultaneous measurement of forces and machine tool position for diagnostic of machining tests," *Instrumentation and Measurement, IEEE Transactions on,* vol. 54, pp. 2329-2335, 2005.

[163] L. N. López de Lacalle, A. Lamikiz, J. Sánchez, and I. Fernández de Bustos, "Recording of real cutting forces along the milling of complex parts," *Mechatronics,* vol. 16, pp. 21-32, 2006.

[164] L. López de Lacalle, A. Lamikiz, J. Sanchez, and M. Salgado, "Toolpath selection based on the minimum deflection cutting forces in the programming of complex surfaces milling," *International Journal of Machine Tools and Manufacture,* vol. 47, pp. 388-400, 2007.

[165] F. Klocke, S. Kratz, and D. Veselovac, "Position-oriented process monitoring in freeform milling," presented at the 3rd International Conference on High Performance Cutting (HPC), Dublin, Ireland, 2008.

[166] X. J. Jiang and D. J. Whitehouse, "Technological shifts in surface metrology," *CIRP Annals - Manufacturing Technology,* vol. 61, pp. 815–836, 2012.

[167] Y. Li and P. Gu, "Free-form surface inspection techniques state of the art review," *Computer-Aided Design,* vol. 36, pp. 1395-1417, 2004.

[168] H. Schwenke, U. Neuschaefer-Rube, T. Pfeifer, and H. Kunzmann, "Optical Methods for Dimensional Metrology in Production Engineering," *CIRP Annals - Manufacturing Technology,* vol. 51, pp. 685-699, 2002.

[169] L. Zhu, J. Barhak, V. Srivatsan, and R. Katz, "Efficient registration for precision inspection of free-form surfaces," *The International Journal of Advanced Manufacturing Technology,* vol. 32, pp. 505-515, 2007.

[170] T. Rabbani, S. Dijkman, F. van den Heuvel, and G. Vosselman, "An integrated approach for modelling and global registration of point clouds," *ISPRS Journal of Photogrammetry and Remote Sensing,* vol. 61, pp. 355-370, 2007.

[171] *KD Tree - Searching in N-dimensions, Part I.* Available: http://www.codeproject.com/Articles/18113/KD-Tree-Searching-in-N-dimensions-Part-I. [Accessed on 08/03/2013].

[172] D. Shi and N. N. Gindy, "Tool wear predictive model based on least squares support vector machines," *Mechanical Systems and Signal Processing,* vol. 21, pp. 1799-1814, 2007.

[173] L. I. Smith, "A tutorial on principal components analysis," *Cornell University, USA,* vol. 51, p. 52, 2002.
[174] *Matlab Statistics Toolbox V7.3*. Natick, Massachusetts: The MathWorks Inc., 2010.
[175] A. McMaster, "Inspection report: comparison between cast and post-grinding implant SZ4 LT," Re-Tec Engineering Solutions, Queens University, Belfast2009.
[176] S. Martínez, E. Cuesta, J. Barreiro, and B. Álvarez, "Analysis of laser scanning and strategies for dimensional and geometrical control," *The International Journal of Advanced Manufacturing Technology,* vol. 46, pp. 621-629, 2010.
[177] I. Bešić, N. Van Gestel, J.-P. Kruth, P. Bleys, and J. Hodolič, "Accuracy improvement of laser line scanning for feature measurements on CMM," *Optics and Lasers in Engineering,* vol. 49, pp. 1274-1280, 2011.
[178] F. J. Brosed, J. Santolaria, J. J. Aguilar, and D. Guillomía, "Laser triangulation sensor and six axes anthropomorphic robot manipulator modelling for the measurement of complex geometry products," *Robotics and Computer-Integrated Manufacturing,* vol. 28, pp. 660-671, 2012.
[179] L. Qi, Z. Gan, C. Yun, and Q. Tang, "A novel method for Aero engine blade removed-material measurement based on the robotic 3D scanning system," in *International Conference on Computer, Mechatronics, Control and Electronic Engineering (CMCE)*, 2010, pp. 72-75.
[180] Henkel, "Material Safety Data Sheet, Henkel Multan CR10," 2008.
[181] G. E. Wnek and G. L. Bowlin, *Encyclopedia of Biomaterials and Biomedical Engineering*, second ed. vol. 2: Taylor & Francis, 2004.
[182] ASTM Standard, *Standard Specification for Cobalt-28 Chromium-6 Molybdenum Alloy Castings and Casting Alloy for Surgical Implants (UNS R30075)*. ASTM International Headquarters, US, 2007.
[183] J. R. Davis, *Handbook of Materials for Medical Devices*, first ed.: ASM International, 2003.
[184] J. Giacchi, C. Morando, O. Fornaro, and H. Palacio, "Microstructural characterization of as-cast biocompatible Co-Cr-Mo alloys," *Materials Characterization,* 2010.
[185] R. Rosenthal, B. Cardoso, I. Bott, R. Paranhos, and E. Carvalho, "Phase characterization in as-cast F-75 Co–Cr–Mo–C alloy," *Journal of Materials Science,* vol. 45, pp. 4021-4028, 2010.
[186] J. Cawley, J. E. P. Metcalf, A. H. Jones, T. J. Band, and D. S. Skupien, "A tribological study of cobalt chromium molybdenum alloys used in metal-on-metal resurfacing hip arthroplasty," *Wear,* vol. 255, pp. 999-1006, 2003.
[187] X. Xu, Y. Yu, and H. Huang, "Mechanisms of abrasive wear in the grinding of titanium (TC4) and nickel (K417) alloys," *Wear,* vol. 255, pp. 1421-1426, 2003.
[188] A. Igual Munoz and S. Mischler, "Effect of the environment on wear ranking and corrosion of biomedical CoCrMo alloys," *Journal of Materials Science: Materials in Medicine,* vol. 22, pp. 437-450, 2011.
[189] A. Warren and Y. Guo, "On the clarification of surface hardening by hard turning and grinding," *Trans. NAMRC/SME,* pp. 309–316, 2006.
[190] R. Cai, W. Rowe, M. N. Morgan, and B. Mills, "Measurement of Vitrified CBN Grinding Wheel Topography," *Key Engineering Materials,* vol. 238, pp. 301-306, 2003.
[191] L. Yan, Y. M. Rong, F. Jiang, and Z. Zhou, "Three-dimension surface characterization of grinding wheel using white light interferometer," *The*

International Journal of Advanced Manufacturing Technology, vol. 55, pp. 133-141, 2011.

[192] M. Barnes, *Practical variable speed drives and power electronics*: Newnes, 2003.

[193] O. I. Avram and P. Xirouchakis, "Evaluating the use phase energy requirements of a machine tool system," *Journal of Cleaner Production,* vol. 19, pp. 699-711, 2011.

[194] U.S. Department of Energy. 1997. *Technical Fact Sheet: Determining Electric Motor Load and Efficiency*. Available: http://www1.eere.energy.gov/manufacturing/tech_deployment/pdfs/10097517.pdf. [Accessed on 01/Nov/2012].

[195] Siemens AG, "Sinamics - Low Voltage Engineering Manual - Supplement to Catalogs D11 2011 and D21.3 2011," 2011.

[196] P. Chevrier, A. Tidu, B. Bolle, P. Cezard, and J. Tinnes, "Investigation of surface integrity in high speed end milling of a low alloyed steel," *International Journal of Machine Tools and Manufacture,* vol. 43, pp. 1135-1142, 2003.

[197] J. Aurich, M. Carrella, and M. Steffes, "Evaluation of Abrasive Processes and Machines with Respect to Energy Efficiency," in *Leveraging Technology for a Sustainable World*: Springer Berlin Heidelberg, 2012, pp. 329-333.

[198] I. Inasaki, H. K. Tönshoff, and T. D. Howes, "Abrasive Machining in the Future," *CIRP Annals - Manufacturing Technology,* vol. 42, pp. 723-732, 1993.

[199] P. J. Ross, *Taguchi Techniques for Quality Engineering*: McGraw-Hill, New York, 1996.

[200] E. Mullins, *Statistics for the quality control chemistry laboratory*: Royal Society of Chemistry, 2003.

[201] Minitab Inc., *Minitab 16 Technical Manual*, 2010.

[202] G. Taguchi, S. Chowdhury, and Y. Wu, *Taguchi's quality engineering handbook*: John Wiley & Sons, 2005.

[203] D. L. Butler, L. A. Blunt, B. K. See, J. A. Webster, and K. J. Stout, "The characterisation of grinding wheels using 3D surface measurement techniques," *Journal of Materials Processing Technology,* vol. 127, pp. 234-237, 2002.

[204] W. B. Rowe, J. A. Pettit, A. Boyle, and J. L. Moruzzi, "Avoidance of Thermal Damage in Grinding and Prediction of the Damage Threshold," *CIRP Annals - Manufacturing Technology,* vol. 37, pp. 327-330, 1988.

[205] R. Hood, F. Lechner, D. Aspinwall, and W. Voice, "Creep feed grinding of gamma titanium aluminide and burn resistant titanium alloys using SiC abrasive," *International Journal of Machine Tools and Manufacture,* vol. 47, pp. 1486-1492, 2007.

[206] A. Lasemi, D. Xue, and P. Gu, "Recent development in CNC machining of freeform surfaces: A state-of-the-art review," *Computer-Aided Design,* vol. 42, pp. 641-654, 2010.

[207] H. M. Kjer and J. Wilm, "Evaluation of surface registration algorithms for PET motion correction," BSc BSc Thesis, Information and Mathematical Modelling, Technical University of Denmark, 2010.

[208] J. H. Friedman, J. L. Bentley, and R. A. Finkel, "An algorithm for finding best matches in logarithmic expected time," *ACM Transactions on Mathematical Software (TOMS),* vol. 3, pp. 209-226, 1977.

[209] Z. J. Daruwalla, P. Courtis, C. Fitzpatrick, D. Fitzpatrick, and H. Mullett, "An application of principal component analysis to the clavicle and clavicle fixation devices," *Journal of Orthopaedic Surgery and Research,* vol. 5, p. 21, 2010.

[210] J. E. Jackson and J. Wiley, *A user's guide to principal components* vol. 19: Wiley Online Library, 1991.
[211] C. D. Meyer, *Matrix analysis and applied linear algebra*. Philadelphia: Society for Industrial and Applied Mathematics, 2000.
[212] M. Fewell, "Area of common overlap of three circles," DTIC Document2006.
[213] Z. Guangtao and Y. Xiaokang, "Image reconstruction from random samples with parametric and nonparametric modeling," in *Visual Communications and Image Processing (VCIP), 2011 IEEE*, 2011, pp. 1-4.
[214] A. E. David, A. J. Cole, B. Chertok, Y. S. Park, and V. C. Yang, "A combined theoretical and in vitro modeling approach for predicting the magnetic capture and retention of magnetic nanoparticles in vivo," *Journal of Controlled Release,* vol. 152, pp. 67-75, 2011.
[215] D. Dutykh, D. Mitsotakis, L. Chubarov, and Y. Shokin, "On the contribution of horizontal sea-bed displacements into tsunami generation processes," *Ocean Modelling,* vol. 56, pp. 43-56, 2012.
[216] J. D. Marinescu, W. B. Rowe, B. Dimitrov, and I. Inasaki, *Tribology of Abrasive Machining Processes*. Norwich, NY: William Andrew Publishing, 2004.
[217] A. J. Bell, "Temperatures in high efficiency deep grinding," PhD, School of Applied Sciences, Cranfield University, 2009.
[218] M. J. Jackson, C. J. Davis, M. P. Hitchiner, and B. Mills, "High-speed grinding with CBN grinding wheels — applications and future technology," *Journal of Materials Processing Technology,* vol. 110, pp. 78-88, 2001.
[219] Y. Koren and R. Lin, "Efficient tool-path planning for machining free-form surfaces," *ASME Trans. Journal of Engineering for Industry,* pp. 20-28, 1996.
[220] W. Li, A. Zein, S. Kara, and C. Herrmann, "An investigation into fixed energy consumption of machine tools," *Glocalized Solutions for Sustainability in Manufacturing,* pp. 268-273, 2011.
[221] Sustainable Energy Authority of Ireland, "Electricity and Gas Prices in Ireland 2nd Semester (July - December) 2011," 2012.
[222] M. Helu, B. Behmann, H. Meier, D. Dornfeld, G. Lanza, and V. Schulze, "Total Cost Analysis of Process Time Reduction as a Green Machining Strategy," in *Leveraging Technology for a Sustainable World*: Springer Berlin Heidelberg, 2012, pp. 299-304.
[223] P. Mativenga and M. Rajemi, "Calculation of optimum cutting parameters based on minimum energy footprint," *CIRP Annals-Manufacturing Technology,* 2011.
[224] E. b. A. International, *Materials and coatings for medical devices: cardiovascular*: ASM International, 2009.
[225] C. Guo, Y. Wu, V. Varghese, and S. Malkin, "Temperatures and energy partition for grinding with vitrified CBN wheels," *CIRP Annals-Manufacturing Technology,* vol. 48, pp. 247-250, 1999.
[226] Computational Thermodynamics Inc. *Co-Cr Phase Diagram*. Available: http://www.calphad.com/cobalt-chromium.html. [Accessed on 01/Nov/2012].